# Experimental Investigations on Thermal and Hydrodynamic Entrance Regions in Microchannels using μPIV and TLC Techniques

Tariq Ahmad

A Thesis

in

The Department

of

Mechanical and Industrial Engineering

Presented in Partial Fulfillment of the Requirements

for the Degree of Master of Applied Science (Mechanical Engineering) at

Concordia University

Montréal, Québec, Canada

March 2008

*Your file Votre référence*
*ISBN: 978-0-494-40906-0*
*Our file Notre référence*
*ISBN: 978-0-494-40906-0*

# Abstract

## Experimental Investigations on Thermal and Hydrodynamic Entrance Regions in Microchannels using µPIV and TLC Techniques

Tariq Ahmad

Micro-systems are expected to have abundant applicability in the biomedical industry, where operations such as medical diagnostics or DNA synthesis and sequencing, could potentially be carried out on a hand-held device. Fully integrated micro-systems consist of several processes needed to carry out the analysis, such as mixing, reaction, and detection. These systems are projected to have significant advantages over traditional testing methods, such as smaller footprint areas, portability, and shorter analysis times. Micro-systems are comprised of micro-devices, which perform the desired processes. Micro-devices themselves, such as micromixers or micro-heat exchangers, are an arrangement of microchannels, which span only a fraction of a millimeter. Consequently, microchannels have recently received much attention in the research community. Essential for advanced design applications are flow and heat transfer analyses of microchannels, which are used to transport fluid within micro-systems and their integrated components.

The entrance region of a channel, where the flow is hydrodynamically, thermally, or simultaneously developing, is very important since the flow and heat transfer mechanisms are enhanced due to the developing nature of the flow. Through the use

of state-of-the-art optical measurement techniques of micro-Particle Image Velocimetry (µPIV) and un-encapsulated Thermochromic Liquid Crystal (TLC) thermography, the hydrodynamic and thermal entrance regions in microchannels are experimentally investigated. New experimental data is obtained for both laminar and turbulent single-phase flow regimes, in microchannels ranging in hydraulic diameter from 100 µm to 1 mm. To investigate the effects of dimensional scaling, the results are compared to the physical mechanisms, observations, and existing data for developing flows in conventionally-sized ducts and pipes. In addition, new empirical laminar entrance length correlations are proposed for microchannels.

In microfluidic devices and systems, channel lengths are expected to be extremely short, in which case developing flow may dominate the flow field over the entire microchannel length. The present study broadens the knowledge into the mechanisms of developing flow and heat transfer in microchannels. With further understanding of micro flows through experimental evidence, the applicability of complete microfluidic systems can be realized on a practical level.

# Acknowledgements

Firstly, I would like to thank my supervisor Dr. Ibrahim Hassan, who has guided me throughout my university years at Concordia, both undergraduate and graduate. Dr. Hassan not only helped me grow on an academic and professional level, but also on a personal level through his working methods and helpful advice he has given me over the years.

I would also like to thank Dr. Roland Muwanga, a former Ph.D. student in our research group at Concordia. His development of TLC measurement methods and the microscale heat transfer experimental rig is much appreciated. In addition, Roland provided me with technical insight with his knowledge in thermo-fluids, and he is also a good friend.

Also thanks to Dr. Hassan's entire research group, composed of M.A.Sc. and Ph.D. students including Dino Bowden, Wael Saleh, Ayman Megahed, Chad Zhang, Mohamed Gaber, Mohamed Rahman, and Tarek Elnady. The friendships developed while working within the group will always be remembered.

In addition, I would like to thank my family for their continuous love and support. My Dad and Mom as well as my siblings, Tania, Farah, and Faisal, and extended family, in particular my aunt Tajie and brother-in-law Peter, provided much care and encouragement over the past years. I would also like to thank all my close friends, whose time together provided a path to relieve the stresses associated with graduate studies and everyday life.

# Contents

# List of Figures

# List of Tables

# Nomenclature

| | |
|---|---|
| $A$ | cross-sectional area, $m^2$ |
| $B$ | blue value, 0 to 1 |
| Cp | fluid specific heat at constant pressure, J/kg°C |
| $D$ | tube or pipe diameter, m, unless otherwise specified |
| $D_h$ | hydraulic diameter, m |
| $D_0$ | Stokes-Einstein diffusion coefficient, $m^2/s$ |
| $d_e$ | particle image diameter, m |
| $d_p$ | nominal particle diameter, m, unless otherwise specified |
| $d_s$ | diameter of the point-spread function, m |
| $f$ | Darcy friction factor |
| $G$ | Green value, 0 to 1 |
| $H$ | channel height, m |
| $h$ | hue angle, degrees |
| $h_x$ | local convective heat transfer coefficient, $W/m^2{}°C$ |
| $K_{loss}$ | minor loss coefficient |
| $k$ | fluid thermal conductivity, W/m°C |
| $L$ | channel length, m |
| Le | entrance length, m |
| $M$ | objective magnification |

| | |
|---|---|
| $\dot{m}$ | mass flowrate, kg/s |
| Nu | Nusselt number |
| $P$ | pressure, Pa, unless otherwise specified |
| $\Delta P$ | channel or tube pressure drop, Pa, unless otherwise specified |
| Pr | Prandtl number |
| $Q$ | volumetric flowrate, $m^3/s$, unless otherwise specified |
| $q''$ | heat flux, $W/m^2$ |
| $R$ | Red value, 0 to 1 |
| Re | Reynolds number |
| T | temperature, °C or K |
| Tw | wall temperature, °C |
| $\Delta t$ | time interval between laser pulses, s, unless otherwise specified |
| $U$ | average streamwise flow velocity, m/s |
| $u$ | local streamwise flow velocity, m/s |
| $W$ | channel width, m |
| $x$ | streamwise coordinate, m |
| $y$ | channel height coordinate, m |
| $z$ | spanwise coordinate, m |

## Acronyms

| | |
|---|---|
| BNC | bayonet Neill-Concelman |
| CCD | charge coupled device |
| CFD | computational fluid dynamics |
| CPU | central processing unit |

| | |
|---|---|
| DAQ | data acquisition |
| DRIE | deep reactive ion etching |
| DNA | deoxyribonucleic acid |
| EDL | electric double layer |
| FD | fully developed |
| GE | General Electric |
| IC | integrated circuit |
| ID | inner diameter |
| IMAQ | image acquisition |
| LCD | liquid crystal display |
| MEMS | micro-electro mechanical system |
| NA | numerical aperture |
| NTSC | National Television System Committee |
| OD | outer diameter |
| PDMS | polydimethylsiloxane |
| PIV | particle image velocimetry |
| μPIV | micro-particle image velocimetry |
| RAM | random access memory |
| ROI | region of interest |
| RPM | revolutions per minute |
| rgb | red-green-blue |
| SEE | standard error estimate |
| TAS | total analysis system |
| TIFF | tagged image file format |
| TLC | thermochromic liquid crystal |

## Greek Letters

| | |
|---|---|
| $\varepsilon_B$ | error due to Brownian motion |
| $\kappa$ | Boltzmann constant, 1.38065 x $10^{-23}$ J/K |
| $\lambda$ | wavelength, nm |
| $\mu$ | dynamic viscosity, $Ns/m^2$ |
| $\nu$ | kinematic viscosity, $m^2/s$ |
| $\rho$ | fluid density, $kg/m^3$ |

## Subscripts

| | |
|---|---|
| abs | absolute property value |
| b | bulk property |
| cl | centerline value |
| cl, FD | fully developed centerline value |
| exp | experimental value |
| emit | emission |
| Fluid | fluid parameter |
| Gniel | Gnielinski correlation |
| h | heated portion |
| hyd | hydrodynamic parameter |
| in | channel inlet condition |
| loc | local value |
| max, FD | maximum of fully developed value |

| | |
|---|---|
| out | channel outlet condition |
| turb | turbulent flow regime |
| w | wall condition |
| $x$ | streamwise coordinate |
| $xy$ | streamwise and spanwise coordinates |

# Chapter 1

# Introduction

Over the past decade, fluid flow and heat transfer in microchannels and micro-devices, with and without phase change, has been a strong focus of the research community. The relatively new area of microfluidics deals with the fluid mechanics and heat transfer disciplines, along with the microfabrication methods required at the microscale. Microchannels are prevalent in micro-devices, and in turn, these micro-devices will eventually be implemented in complete micro-systems. However, before the advanced development of these microfluidic systems, it is necessary to understand the fluid flow and heat transfer characteristics in their integrated components. With further understanding through experimental evidence, the applicability of these systems can be realized on a practical level. In terms of applications and fundamental understanding, single-phase flow remains important and there is a definite need for additional experimental investigations at the microscale.

Fundamental microchannel studies, analyzing both fluid flow and heat transfer, are meant to determine if the physical behavior is in agreement with classical theory, or if the effect of dimensional scaling requires new analysis methods as the geometry is reduced to microscale levels. These fundamental microchannel studies lay the ground work for the design and performance of micro-devices and their implementation in future micro-systems.

The application of microfluidics involves micro-devices and their integration with one another in developing a complete system. Micro-devices, such as micromixers, micro valves, and micro-heat exchangers, need to be designed, developed, analyzed, and produced in order to be incorporated in complete systems. Future micro-systems can have thermo-fluid applications, such as micro engines and micro reactors, or they can have biomedical applications in the form of Lab-on-a-Chip platforms and Micro-Total Analysis Systems (μ-TAS), such as DNA sequencing and synthesis and biological fluid sampling for medical diagnostics and drug testing.

Concerning the micro domain, experimental flow and heat transfer studies are a reliable method in analyzing the physics. In some instances the reaction of the flow in microscale circumstances may be unknown, and in these cases CFD could fail. Experimental analyses at micro dimensions may also require new experimental methods, not necessarily used for macroscale studies. Newer techniques such as micro-Particle Image Velocimetry (μPIV) and Thermochromic Liquid Crystal (TLC) thermography will further need to be relied upon to carry out more than adequate analyses.

From a comprehensive review into existing literature of single-phase microchannel flow and heat transfer, numerous research groups have carried out fundamental experimental analyses. Majority of these studies focused on the physics of fully developed flow. More recent studies, through improved experimental methods and accuracy, show that there is very good agreement for fully developed microchannel flow with conventional theory, for parameters such as pressure drop, laminar to turbulent transition, and heat transfer coefficient. However, there are still areas of microchannel flow that need to be investigated experimentally, which currently are very limited to non-existent.

The study of developing flow in microchannels, either thermally, hydrodynamically, or simultaneously, is very limited. Flow and heat transfer mechanisms within the entrance region of a channel is important, since its effect on transport properties, such as the pressure gradient and heat transfer coefficient, are significantly enhanced. Also, general correlations for friction factor, heat transfer coefficient, and laminar to turbulent transition are only valid if the flow is fully developed. It should be emphasized that in microfluidic devices and systems, microchannel lengths can be extremely short, in which case within a certain range of Reynolds numbers (Re), developing flow may dominate the flow field over the entire microchannel length.

The current experimental investigations are intended to present fundamental results into the entrance region of microchannels, with hydraulic diameters ranging from 100 μm to 1 mm. With regards to the hydrodynamic entrance region, for laminar flow there is very limited experimental data, whereas for turbulent flow experimental data is non-existent. Through the use of micro-PIV, a comprehensive experimental study into hydrodynamic developing flow is carried out for laminar flow and attempted for turbulent flow. The state-of-the-art, non-intrusive experimental technique of micro-PIV acquires both qualitative and quantitative velocity flow field data in micro geometries. The test-sections are designed to provide a fundamental inlet geometry where the flow is not pre-developed, as well as focus on the effect of scaling independent of cross-sectional aspect ratio. In addition, new empirical entrance length correlations for microchannels are proposed.

In terms of the thermal entrance region, there were many research efforts focused for laminar flow, where a wide majority of existing experimental data shows very good agreement with conventional theory. Instead, an extensive experimental study into the turbulent thermal entrance region is performed. Experimental data into the turbulent thermal entrance region of microchannels is non-existent. Through the use of un-encapsulated TLC's, experimental data is acquired for thermally developing turbulent flow. Un-encapsulated TLC's, whose non-intrusive, state-of-the-art characteristics include full surface temperature sensing at a very high resolution, is highly applicable to fine temperature measurements at the microscale, particularly in the turbulent thermal entrance region whose length is expected to be extremely short.

Chapter 2 presents an extensive literature review into experimental single-phase microchannel flow, including measurement and fabrication methods, applications, fully developed flow, and developing flows, both hydrodynamic and thermal. Chapter 3 presents the experimental test facilities and experimental methods (both μPIV and TLC) used the present analyses, including experimental procedures, general uncertainties, and measurement challenges. The results and discussion of hydrodynamic developing flow in microchannels is presented in Chapter 4, and that of thermally developing flow in microtubes is presented in Chapter 5. In addition, Chapter 6 presents a complete summary, including contributions and future directions.

# Chapter 2

# Literature Review

## 2.1 Overview

The following is a review into the open literature of single-phase liquid flow in microchannels with and without heat transfer, which includes experimental analysis methods, fluid driving mechanisms, and fabrication processes. A detailed review into previous experimental studies in both the fully developed and developing flow regions, both hydrodynamic and thermal, is presented.

## 2.2 Experimental Analysis Methods of Micro Flows

Concerning experimental work for single-phase liquid flow in microchannels, there are two primary classes of experimental methods to acquire flow data. Firstly, there is the classical bulk measurement approach, which consists of utilizing transducers to record bulk measurements of the flow, such as pressure drop (i.e. pressure sensors) and temperature (i.e. thermocouples), along with viscous flow theory to obtain flow characteristics while accounting for necessary losses. With the recent emergence of microfluidics, new experimental methods to quantify and measure the flow field were used. Bulk measurement methods are intrusive techniques that record bulk or average measurements of the flow, and difficulties arise as channel dimensions get to the microscale level. Measurement techniques, such as micro-Particle Image Velocimetry (μPIV) for flow field measurement and observation and un-encapsulated Thermochromic Liquid Crystals (TLC's) for surface temperature measurement, are attractive in microscale studies due to their non-intrusiveness and high spatial resolution. However, it should be pointed out that in many cases bulk measurements are required and combined with either micro-PIV or TLC thermography.

### 2.2.1 Bulk Measurements

Regarding the conventional approach in attaining fluid flow data in microchannels through transducers, there has been considerably more experimental work done and published in literature than the relatively new micro-PIV or TLC techniques. This is obviously due to its traditional nature in attaining flow data by means of transducers. The advantages of this method are the relative ease of understanding the experimental approach due to its classical nature, and secondly, the lower cost compared to a micro-PIV system or un-encapsulated TLC's. The main disadvantage associated with this method is the experimental uncertainty, particularly in the transducers themselves, their calibration, their positions, and the losses associated with introducing a measurement device in the flow field. It should also be emphasized that by using this method, bulk measurement devices measure averaged data in the vicinity of the transducer; local flow data cannot be obtained. A wide majority of the experimental microchannel pressure driven fluid flow studies using bulk measurements were on the laminar to turbulent transition region (i.e. Wu and Cheng, 2003; Lelea et al., 2004; Yang et al., 2003), the pressure drop and friction factor (i.e. Pfahler et al., 1990; Mala and Li, 1999; Judy et al., 2002; Hwang and Kim, 2006), and convection heat transfer coefficient (i.e. Yu et al., 1995; Adams et al., 1998; Celata et al., 2002; Bucci et al., 2003) over a wide range of Reynolds numbers and microchannel dimensions.

### 2.2.2 Micro-Particle Image Velocimetry

With regards to experimental fluid flow analysis in micro geometries, the relatively new method of micro-PIV is an attractive technique. Pioneered by Santiago et al. (1998), Koutsiaris et al. (1999), and Meinhart et al. (1999, 2000a, 2000b), this state-of-the-art, non-intrusive technique allows for a qualitative and quantitative analysis of flow visualization and flow field acquisition in micro-scale geometries using an experimental flow observation and particle tracking system. The local velocity fields are acquired by tracking the trajectories of fluorescent seeding particles. The particles are excited by a pulsed laser light, which illuminates the entire test-section volume, and imaging of the particles is done using an epi-fluorescent microscope. Images are recorded through a CCD camera and correlated to obtain two-dimensional velocity flow fields. Disadvantages associated with micro-PIV is the obvious need for an optically clear test section, as well as possible correlation problems due to laser light distortion and background noise. Previous micro-PIV studies focus on observation of the velocity flow field in micro-devices (i.e. Chariot et al., 2005; Hoffmann et al., 2006), as well as laminar to turbulent transition (i.e. Zeighami et al., 2000; Sharp and Adrian, 2004; Hao et al., 2005) and hydrodynamic entrance length (i.e. Lee and Kim, 2003; Hao et al., 2005) in microchannels.

### 2.2.3 Thermochromic Liquid Crystal Thermography

Thermochromic Liquid Crystals (TLC's) is an attractive technique for qualitative and quantitative local surface temperature measurement, due to its non-intrusiveness, spatial resolution, and full surface mapping. TLC's are basically a coating applied to a surface, and when the surface is heated, color contours are produced, which are photographed. The resulting images are then calibrated and quantified to produce temperature measurements and mapping. TLC's have been used since the late 1960's in non-destructive testing (i.e. Fergason, 1968; Woodmansee, 1968) and convection heat transfer applications (i.e. Cooper et al., 1975). However, these types of TLC coatings were in their micro-encapsulated form, where the spatial resolution is restricted for microscale dimensions due to tiny spherical capsules (10 μm to 20 μm) in the material (Ireland and Jones, 2000). Therefore, to obtain quantitative temperature measurements with high spatial resolution at the microscale, un-encapsulated TLC's should be applied (Muwanga and Hassan, 2006a). The successful use of un-encapsulated TLC's for thermal measurement on a micro geometry was pioneered by Höhmann and Stephan (2002), who investigated evaporation from a liquid meniscus. More recently, un-encapsulated TLC's were successfully applied by Muwanga and Hassan (2006a, 2006b, 2007) and Muwanga et al. (2007) in analyses regarding both single-phase flow and boiling flow in both microchannels and micro-heat sinks. Disadvantages associated with un-encapsulated TLC's are that they are unprotected and therefore easily contaminated by dust and solvents, and possible destruction of their response if exposed to ultraviolet light for long periods.

## 2.3 Microchannels

Microfluidic devices are made up, in large part, of a specific sequence, arrangement, or array of microchannels. Regardless of their simplicity compared with other microfluidic components, like micro valves and micro pumps, microchannels can be considered as the most important component in a microfluidic device (Liu, 2006). For completeness, a review into microchannels regarding their fluid driving mechanisms and fabrication procedures must be considered.

### 2.3.1 Fluid Driving Mechanisms

An important design consideration is concerning the choice of the method employed in driving the fluid through the microchannel or micro-device. The general microfluidic methods to drive fluid through microchannels and micro-devices are: Pressure Driven Flow and Electrokinetic Flow, which can be realized by either Electroosmotic Flow or Electrophoresis.

Forcing fluid through a microchannel by means of a pressure difference is the most common due to its simplicity, generality, and its classical nature carrying over from the macroscale (Liu, 2006). A difference in pressure from channel inlet to exit moves the fluid, and the flow will always move from a higher pressure to a lower pressure. There are a number of methods to create this pressure difference, basically to impose a greater pressure at the channel inlet relative to the channel exit (infusion), or a lower pressure at the channel exit relative to the channel inlet (withdrawal). Due to the no-slip condition imposed at the walls, where the velocity of the fluid particles adjacent to the wall is zero, pressure driven laminar flow is typically characterized by a parabolic velocity profile (Devasenathipathy and Santiago, 2005). The most classical method to move the fluid is through hydrostatic pressure due to a difference in height, however for most microchannel applications this method is insufficient to overcome the flow resistance within the channel. There are types of mini pumps derived from their macroscale counterparts, such as gear pumps, centrifugal pumps, and displacement pumps (i.e. syringe pumps). These pumps are separate from the device, and are not easily transported or portable; they are primarily used for laboratory work. Regarding "on-chip" pump designs, a widely researched pressure driving mechanism is the deformable membrane pump. The movement of the membrane can be produced a number of ways, including mechanical, piezo-electric, and thermal expansion (Liu, 2006).

The second mode of fluid transport in microchannels is through the use of electroosmotic pumping, which is a type of electrokinetic flow phenomena. An important category of microfluidic systems will require both processing and analysis steps implemented on a fluidic chip (Devasenathipathy and Santiago, 2005). Electroosmotic flow provides the mechanism to satisfy this task. Most channel wall materials, when brought into contact with any electrolytic solution (weak or strong), generate an electric charge at the liquid/solid interface (Liu, 2006). This region at the wall is known as the electric double layer (EDL), which is a region of high capacitance charged ions and the basis of electroosmotic flow. With an external electric field applied in parallel to the channel wall, ions in the electric double layer move in response to this applied field, in a direction towards the electrode of opposite polarity (Liu, 2006; Devasenathipathy and Santiago, 2005). The movement of these ions adjacent to the wall drags the surrounding liquid molecules with them through viscous forces, driving the bulk liquid within the channel. This is the concept of the electrokinetic flow phenomena. The direction of the flow can be controlled by the polarity of the externally applied electric field. An important characterization of electroosmotic flow is the distribution of the velocity profile across the channel, which is nearly uniform, as opposed to pressure-driven flow (Devasenathipathy and Santiago, 2005; Liu, 2006). Devasenathipathy and Santiago (2005) experimentally demonstrated the difference between electroosmotic and pressure-driven flows though the use of caged fluorescence visualization of their velocity profiles. This nearly uniform velocity profile has a very thin boundary layer, and can be generalized as a uniform velocity profile.

Another flow driving mechanism, which is also a type of electrokinetic flow phenomena, is known as electrophoresis. Devasenathipathy and Santiago (2005) define electrophoresis as the motion, relative to the bulk liquid, of colloidal particles or molecules suspended is a solution resulting from the application of an electric field. This method is useful for bioparticle transportation, separation, and characterization, and is particularly attractive in applications of separating charged biological macromolecules, such as DNA, proteins, and peptides according to their sizes and charges (Liu, 2006). The suspended charged particles, such as DNA (negative) or proteins (positive), have different charges, and will react differently with the application of an electric field. A charged particle experiences forces when placed in either a uniform or non-uniform electric field. However, a neutral particle, such as a cell, experiences net forces when placed in a non-uniform electric field, but experiences no net force when placed in a uniform electric field (Liu, 2006; Devasenathipathy and Santiago, 2005). Generally, different particles move at different speeds under a given electrical field, which is the basic mechanism of electrophoresis.

### 2.3.2 General Fabrication Materials and Processes

As previously stated, the choice in the material and fabrication procedure to carry out a specific design depends on numerous aspects. There are many materials one can use in microchannel fabrication, depending on the specific task of the design, and whether it is meant for research of a novel design, or commercial production. Microfluidic applications may require different materials and perhaps different manufacturing processes than those commonly found in MEMS. The fabrication of early microfluidic systems used inorganic materials frequently used in MEMS, such as silicon, silicon dioxide, polycrystalline silicon, or metal (Papautsky et al., 1998; de Boer et al., 2000; Yi et al. 2000; Liu, 2006). In accordance to these selections of materials, the common microfabrication processes were carried out, such as anisotropic or isotropic bulk micromachining, either wet or dry, surface micromachining, or wafer-to-wafer bonding. Bulk micromachining has evolved tremendously in the design of microchannels. Early methods used isotropic wet etching, which evolved toward anisotropic wet and dry etching along dominant crystallographic planes. Currently, a widely used method in bulk microchannel fabrication is Deep Reactive Ion Etching (DRIE), which basically relies on high energy gas ions to react as an etchant. DRIE etching produces high aspect ratio rectangular channels with relatively flat, uniquely profiled walls.

However, microfluidic designs developed in the chemistry and biology sector involve materials and fabrication techniques different from MEMS technology, such as glass and glass bonding. The reason for this is the many problems associated with silicon; in particular, silicon is not optically clear and therefore the flow is difficult to analyze (Liu, 2006). A microfluidic device fabricated using MEMS techniques in silicon requires a method to visualize the flow field. A common approach is the anodic bonding of glass to the top of the silicon wafer, which acts as a wall for the microchannel and allows for flow visualization as well. However, this may create some non-uniformity in the design, since one wall (glass) is a different material than the other three (silicon). Complete glass chips provide good surface characteristics, optical transparency, and relative ease of fabrication (Liu, 2006). Along with inorganic polymers, like glass and silicon, organic polymers are being applied in microchannel fabrication, such as parylene, acrylics, polycarbonate, polymide, and PMMA, which are less expensive and easier managed than their inorganic counterparts (Day and Gu, 2005).

For example, a rather popular approach in microchannel fabrication is PDMS (polydimethylsiloxane), due to its rapid, low cost fabrication and availability of material, which can be obtained by many vendors, such as GE and Dow Corning (Liu, 2006). The materials are in two parts, a base and curing agent, which are mixed at room temperature and result in a transparent elastromeric solid. The mixture can be poured into moulds fabricated using bulk etching or photorezist patterning. When hardened, the mould features are translated to the elastomeric solid. This piece can then be bonded to another PDMS material to enclose the channel (Erickson et al., 2003, Liu, 2006; Li and Olsen, 2006). Generally, there are many different methods researchers are exploring in the material selection and fabrication processes of microfluidic devices, which may or may not be similar to typical MEMS techniques.

### 2.3.3 Conceptual Microfluidic Applications

A conceptual look into microfluidic applications can provide an overall objective in the design of current microfluidic devices and systems as well as an understanding of how one would apply microfluidics in practice.

Possibly the pioneering work in microfluidics began with the application of heat removal of high speed micro-processors through a micro-heat exchanger (i.e. Tuckerman and Pease, 1981). Typically, a micro-heat exchanger, or heat sink, is a substrate where a series of microchannels are etched on the backside of the chip, opposite to the electronics. A standard substrate is silicon, since it is traditionally used in integrated-circuit (IC) technology in the fabrication of computer processors. The microchannels are micro-fabricated on the backside of the chip using traditional MEMS techniques, such as bulk or surface micromachining, which are derived from IC technology. The microchannels are meant to remove the heat dissipated by the electronics, using single-phase or boiling liquid flow, allowing future high-speed processors to function.

Future micro-systems that possibly have the greatest potential in terms of practical applications and the ability to eventually be commercialized are the Lab-on-a-Chip platforms and Micro-Total Analysis Systems (μ-TAS). These future microfluidic systems are typically applicable in the medical, biological, and chemical sectors, where complete automated testing and analysis is carried out on a fully integrated microfluidic chip (El-Ali, 2006; Chang and Yang, 2007). The microfluidic chip would incorporate several steps such as sample introduction, micromixing within a reaction chamber, detection, sensing, and waste. These future systems are to have great advantages over present methods of analysis, such as small sizes and footprints, portability and analysis on-site rather than at a laboratory, very small quantities of samples and reagents, reduction in consumption and waste, low cost and therefore disposable after use, simple so user must not be highly trained or qualified, and short analysis times while eliminating human error due to laboratory manipulations (Whitesides, 2006; Yager et al., 2006; Chang and Yang, 2007). In addition, the portability, low cost, and simple use of these future Lab-on-a-Chip systems will allow for advancement of the healthcare system in developing countries, where majority of the population resides, but are presently unable to afford simple healthcare, due to either financial reasons, a lack of trained staff, or the remote living conditions far from city centers (Yager, 2006; El-Ali, 2006). Applications associated with the Lab-on-a-Chip or µ-TAS are genetic analysis, drug testing, medical diagnostics, chemical testing and safety monitoring (i.e. biosensors), and drug delivery.

For example, in terms of medical diagnostics, the Lab-on-a-Chip should require very little user input, besides introducing the sample (i.e. blood, saliva, urine, etc.). The chip could perform routine testing, or detect the presence of an infectious agent, and provide guidance to the user (Yager et al., 2006). The chip would include different reagents, with the ability to detect a variety of diseases on the same platform, as well as provide guidance on what treatment should be given to the patient. Another example is the medical testing of drugs, which would be applicable to the pharmaceutical industry. With the implementation of cell biology, medical testing of drugs can be used to predict the performance of human clinical trials (Whitesides, 2006). The platform is to be packaged in a form that can be routinely used by technicians. Sample cells can be included or introduced within the microfluidic chip, and a medical drug sample would be introduced to the chip (El-Ali et al., 2006; Whitesides, 2006). The reaction of the biological cells to the drug, once analyzed within the chip, can provide data on the toxicology of the drug (deMello, 2006).

It should be emphasized that these applications are only concepts and much experimental and analytical work, both fundamental and practical, must be carried out prior to the design of such systems. Further work is required in microchannel fluid flow and heat transfer, in the design and efficiency of micro-devices, such as microfluidic mixers and micro-heat exchangers, and their implementation to form a complete micro-system. Also, studies into the control processes, quality control, operation, and commercialization eventually need to be carried out. However, these conceptual microfluidic applications provide an optimistic outlook towards future innovations.

## 2.4 Fully Developed Single-Phase Flow and Heat Transfer in Microchannels

Flow and heat transfer characteristics and parameters at the microscale level, such as velocity distribution, pressure drop, laminar to turbulent transition, and hydrodynamic and thermal entrance lengths are important in order to design efficient micro-systems. To better understand the nature of liquid flow in micro geometries and to aid in the design of microfluidic devices, it is advantageous to recognize if there is agreement between the conventional macroscale theories and microscale flow. Fundamental microchannel analyses such as these were widely investigated both experimentally and numerically, particularly in the fully developed region.

The fluid flow and heat transfer in microchannels has important applications, such as the thermal control of electronic devices. Early studies, such as that carried out by Tuckerman and Pease (1981), show that electronic chips can be cooled effectively using forced convection by running water through microchannels mounted directly on the back of a circuit board. This initial study has led to continued research on microchannel liquid flow and/or heat transfer that will eventually lead to the development of high performance micro-devices such as micromixers and micro-heat exchangers.

Early fully developed, single-phase laminar and turbulent flow and convective heat transfer studies in microchannels proposed a significant disagreement from conventional theory for issues such as pressure drop, laminar to turbulent transition, and heat transfer coefficients. Majority of these experimental analyses relied solely on bulk measurements to quantify the flow and heat transfer. Notable experimental investigations, who found disagreement with conventional theory regarding friction factors, laminar to turbulent transition, and convective heat transfer coefficients for microchannel flow include, Wu and Little (1983), Pfahler et al. (1990), Mala and Li (1999), Weilin et al. (2000), Pfund et al. (2000), Adams et al. (1998), Celata et al. (2002), and Brutin and Tadrist (2003). In addition, experimental transition studies carried out by Zeighami et al. (2000), Li et al. (2003), Yang et al. (2003), and Wu and Cheng (2003) concluded that in microchannel flow the lower bound of the transition range was below the generally accepted range of Reynolds numbers; however, their upper bound had good agreement.

Many research groups (i.e. Papautsky et al, 2001; Celata et al., 2004; Koo and Kleinstreuer, 2004 ; Ferguson et al., 2005; Celata et al., 2006a) carried out extensive reviews on literature regarding single-phase flow experiments in microchannels, and particular attention was attributed to experimental uncertainties and procedures. Papautsky et al. (2001) stated that there are several experimental microscale effects which become important on the microscale level. Effects such as momentum transport effects (i.e. surface roughness, channel size, channel geometry) and temperature variations (i.e. viscous dissipation) can possibly cause significant variations in fluid properties, leading to undetectable errors, undesirable levels of uncertainty, and complications in comparing microscale results with conventional theory. Papautsky et al. (2001), and more recently Celata et al. (2006a), identified these microscale effects as *scaling effects*, which describe the difference in importance of certain effects for microscale compared with macroscale, where these effects are negligible.

It can be seen that it is the early studies, as stated previously, which indicate deviation from conventional theory, whereas recent studies indicate good agreement with conventional theory. The recent experimental studies have recognized from past research efforts about the importance and accountability of experimental errors and uncertainties in microchannel flow. This is particularly true for bulk measurements at very small dimensions (less than 100 μm), such as the use of conventional thermocouples and pressure sensors, where bulk averaged flow properties are measured. Notable studies by Judy et al. (2002), Owhaib and Palm

(2004), Bucci et al. (2003), Lelea et al. (2004), Sharp and Adrian (2004), Steinke and Kandlikar (2005), Hao et al. (2005), Hwang and Kim (2006), Muwanga and Hassan (2006a, 2006b), and Celata et al. (2006b) found very good agreement with conventional flow theory for heat transfer and fluid flow in microchannels, due to improved experimental analyses and procedures, and experimental errors that were unaccounted for in earlier studies.

## 2.5 Hydrodynamically Developing Flow

Within the entrance region of a channel or tube, where the flow is hydrodynamically developing, there are significant effects on the flow field. In conventional experiments, analysis of the hydrodynamic entrance region was found either by measurement of the local pressure gradient or measurement of the local velocity profile. However, as reported by both Fleming and Sparrow (1969) and Wiginton and and Dalton (1970), the entrance length based on pressure underpredicts the entrance length based on velocity, where the magnitude of the difference depends on channel aspect ratio ($H/W$). A widely accepted notion of the hydrodynamic entrance length is the downstream location whereby the maximum local velocity approaches 99% of its fully developed value (Shah and London, 1978). Previous microchannel experimental studies, as well as general investigations carried out for conventional sized channels, are outlined for both laminar and turbulent flow.

### 2.5.1 Laminar Flow

In general, the laminar hydrodynamic entrance region can be defined as the length from the channel inlet over which the local velocity changes from a uniform inlet profile to a parabolic fully developed profile, after which there is minimal change in the velocity profile. The change in the velocity profile within the entrance region is caused by viscous effects from a drag disturbance at the channel walls, which in turn causes the center of the profile to accelerate, in order to satisfy continuity.

With regards to conventionally sized channels, numerous laminar hydrodynamic entrance length studies were carried out both experimentally and numerically. Regarding numerical studies for rectangular ducts or parallel plate channels, results found by groups such as Han (1960), Fleming and Sparrow (1969), Atkinson et al. (1969), Wiginton and Dalton (1970), and Chen (1973) are considered to be standard and accurate regarding the entrance length. Experimental entrance length studies for conventional ducts have been explored by numerous groups such as Sparrow et al. (1967), Goldstein and Kreid (1967), Beavers et al. (1970), and Muchnik et al. (1973). In these experimental investigations, majority used pressure sensor measurement within the entrance region, while others used visual techniques in observing the development of the velocity profile, such as a laser-doppler flowmeter (Goldstein and Kreid, 1967) or a hot wire method (Muchnik et al., 1973).

Very few laminar hydrodynamic entrance length studies have been carried out in microchannels, and of these, all have been analyzed using micro-PIV. Their geometries varied from one another and their studies of developing flows in the entrance region are limited, with varying agreement with conventional entrance length correlations.

Lee et al. (2002)'s micro-PIV experiments were carried out using deionized water with 1 μm particles flowing through a conventionally machined acrylic rectangular microchannel with a length of 120 mm, a height of 690 μm, and a width of 260 μm, over a range of Reynolds numbers from 250 to 2100. Images were taken at incremental distances from the microchannel entrance, where averaged correlation velocity profiles were recorded. Through observation, the entrance lengths were found to be shorter than correlations given by Shah and London (1978). The authors concluded that the entrance length is reduced by about 45% due to the pre-developed flow prior to entering the microchannel.

Lee and Kim (2003) investigated different inlet shapes of silicon etched microchannels using micro-PIV with deionized water flowing at about Re = 1. The microchannels were 30 mm in length, had a depth of 58 μm and a width of 100 μm. Overall, the researchers concluded that the entrance length for microchannels is much smaller than for macroscale channels.

Lee et al. (2004) experimentally investigated the entrance length in two rectangular microchannels of different aspect ratios ($H/W$), one with a hydraulic diameter ($D_h$) of 370 μm and an aspect ratio of 2.75 made of acrylic, and another with a hydraulic diameter of 56.4 μm and an aspect ratio of 0.37, made of silicon (DRIE). The authors used micro-PIV to measure the velocity profiles in the low Reynolds number range, from 1 to 100. The authors concluded that the present correlations showed a weaker dependence on Re than existing correlations in the linear portion of the entrance length. For the constant portion of the entrance length, there was agreement for the acrylic channel in comparison with existing correlations, while the silicon channel showed greater entrance values than existing correlations. According to the authors, this discrepancy was due to the different microchannel aspect ratios, and recommend that microchannel entrance studies be carried out without the influence of aspect ratio.

Oak et al. (2004) analyzed flow development characteristics of two co-flowing laminar streams in a high aspect ratio rectangular microchannel using micro-PIV. The two co-flowing streams are separated by 90° and are 9.1 mm long, and the Reynolds numbers are of 1 and 10. The development length of the merging flows was shown not to vary with Reynolds number between 1 and 10, and the authors concluded that high aspect ratio channels result in shorter development lengths.

Hao et al. (2005) showed the developing velocity profiles along various axial positions for water flow in a trapezoidal silicon microchannel with a hydraulic diameter of 237 μm. Using micro-PIV, centerline velocity distributions along the axial direction of the channel, over a range of Reynolds numbers between 50 and 1200, were investigated. The authors found the entrance length in their experiments to be about $Le/D_h = (0.08\text{-}0.09)Re$.

### 2.5.2 Turbulent Flow

In conventional-sized channels and ducts, turbulent flow is often practically applied, such as in mixing processes, heat-exchangers, and piping systems. Although decades of research has been focused on the subject both experimentally and analytically, from a review into literature the physics and mechanisms of turbulent flow generally remain very difficult to understand.

Turbulent flow can be characterized as disorderly, random movement and fluctuations of the local velocity components in the form of turbulent eddies. Notions such as the turbulence intensity, which describes the level of turbulence in a flow, and Reynolds stresses, which describes the turbulent shear stress using the fluctuating velocity components, attempt to describe the mechanisms of turbulent flow. The fully developed turbulent profile is typically broken into three regions: the viscous sub-layer, the overlap layer, and the turbulent outer layer. In the viscous sub-layer, viscous stresses dominate, whereas in the outer layer, Reynolds stresses dominate.

Regarding investigations of turbulent flow development in conventional ducts and pipes, numerous research efforts have been performed over the past decades. Both experimental and analytical studies were carried out in the entrance region for turbulent flow (i.e. Barbin and Jones, 1963; Lee and Park, 1971; Gabrianovic et al., 1979; Filippov, 1982; Hsieh et al., 2003; Lien et al., 2004; Doherty et al., 2007). However, most available works are scattered and conclusions vary from study to study.

In fact, there still remain questions into the entrance length required to achieve fully developed turbulent flow. For example, Gabrianovic et al. (1979) found that the entrance length is dependant on the initial turbulent level (intensity) at the inlet of the duct. Doherty et al. (2007) states that most experimental works cite the entrance length as being 'sufficiently long' however, the entrance length remains uncertain and no formal definition is widely accepted. The authors found that for their high air Re numbers ($Re \sim 10^5$) of their 0.1 m diameter pipe, the entrance length ranged from 50 to 80 diameters and is increased by the development of large-scale flow structures. Lien et al. (2004) found that for their rectangular channel, 1.17 m by 0.1 m, for their Reynolds air range of $40 \times 10^3$ to $185 \times 10^3$, the entrance length varied from

130 to 150 channel heights, and state that mean velocity profiles do not alone constitute as a through study of the development of turbulent flow.

Although a generally accepted conventional correlation for the turbulent entrance length is $Le/D_h = 4.4Re^{1/6}$, there is varying experimental agreement with this equation. For example, Hsieh et al. (2003) found good agreement with this correlation for a bare tube of 50 mm diameter and a Reynolds number range from 6500 to 19500. However, Barbin and Jones (1963) did not attain fully developed flow for a diameter of 200 mm and a Re number of $388 \times 10^3$ for a length of 40.5 diameters, due to the continuously changing velocities, turbulent intensities, and Reynolds stresses. Still, some authors state that there is very minimal influence of turbulent Reynolds number on the entrance length (i.e. Filippov, 1982; Lien, 2004).

With regards to microchannels, there are no experimental studies existing in literature for fully turbulent flow ($Re > 4000$). Possibilities could be due to the experimental methods and high hydrodynamic resistance for turbulent flow, which is amplified at microscale dimensions. Micro-PIV could perhaps be applied to microchannels by qualitatively and quantitatively observing the turbulent velocity profiles, as a first step towards analyzing turbulent developing flow at the microscale.

## 2.6 Thermally Developing Flow

From the beginning of a specified heated length for a uniformly heated walled channel or tube, where the flow is either developing or developed, there is development in the temperature profile. This development continues along a certain length, after which a fully developed temperature profile is achieved. Within the thermally developing region the effects of heat transfer mechanisms are increased. In general the thermal entrance length is defined as the length required for the local Nusselt number to come within 5% of its fully developed value (Shah and London, 1978). Previous experimental investigations into the thermal entrance region for microchannels, along with general studies for conventionally sized channels, are outlined for both laminar and turbulent flow.

### 2.6.1 Laminar Flow

Numerous laminar thermal entrance region studies, both experimental and numerical, were carried out in microchannels, with majority of the studies indicating good agreement with conventional correlations (i.e. Harms et al., 1999; Lelea et al., 2004; Lee et al., 2005; Gamrat et al., 2005; Muwanga and Hassan, 2006a, 2006b; Lee and Garimella, 2006). Conventionally for laminar flow, the theoretical trend of the thermal development length is a very high local Nusselt number at the inlet, which decreases with channel length toward some constant fully developed value. Experimentally, previous analyses were carried out using either bulk measurement or TLC techniques for microchannel wall temperature measurement.

For example, Lelea et al. (2004) carried out an experimental and numerical study of distilled water flowing through stainless steel microtubes of diameters of 0.1 mm, 0.3 mm, and 0.5 mm, in the laminar regime up to Re = 800. Thermocouples were used both in measuring the inlet and outlet bulk flow temperature, as well as the outer wall temperature along the channel lengths. Excellent agreement of the laminar thermal entrance length was found with comparison to their numerical results as well as the conventional correlation found in Shah and London (1978).

Lee et al. (2005) experimentally studied the laminar thermal entrance region of deionized water flowing in rectangular copper microchannels, with a width ranging from 194 μm to 534 μm and a depth five times the width in each case. Through the use of thermocouples, their experimental data of the convective heat transfer coefficient in the laminar thermal entrance region clearly showed a sharp decrease, in good agreement with classical theory.

Muwanga and Hassan (2006b) also measured the laminar thermal entrance region in microtubes. Their experiments were carried out using both water and FC-72 flowing through stainless steel tubes of diameters of 1 mm, 0.5 mm, and 0.25 mm. However, they used un-encapsulated TLC's to measure the local wall temperature along the channel length, and thermocouples to measure the inlet and outlet fluid bulk temperatures. Through their TLC results, very good agreement was found in comparing the laminar thermal developmental length with the analytical solution given in Shah and London (1978).

### 2.6.2 Turbulent Flow

Physically, for the turbulent thermal entrance length, the trends are similar to that of laminar flow, where there exists a very high Nusselt number at the entrance that decreases with the channel length towards a fully developed limit (Kays, 1966). Typically, as the Prantdl number is increased, the shorter the entrance length, however the thermal entrance length is typically much shorter for turbulent flow than for laminar flow.

In conventionally sized channels, turbulent thermal entrance length studies were carried out both experimentally and numerically (i.e. Sparrow et al., 1957; Malina and Sparrow, 1964; Allen and Eckert, 1964; Notter and Sleicher, 1972; Babus'haq, 1993). Numerical solutions for developed flow conditions were carried out for both a constant wall temperature and a uniform heat flux boundary condition. For experimental analyses, majority were investigated for a uniform heated wall condition, due to its ease of implementation in an experimental setup.

An example of a previous analytical work is that of Notter and Sleicher (1972). These authors numerically investigated turbulent thermal developing flow for both a constant temperature and a constant heat flux boundary condition for a circular tube. Their solution of the thermal entrance length for a uniform heat flux boundary condition, which had to be solved numerically, is found using 5% of the fully developed Nusselt value. They focused on very low Prandtl (Pr) numbers (i.e. liquid metals) ranging from 0.01 to 3.00, at very high Reynolds values above $10^4$ (i.e. conventional sized pipes). It was found that as Pr is increased toward high values, above 3, the entrance length is decreased, toward a constant value of 2 – 3 diameters, independent of Re number. Regarding these trends, there was good agreement with experimental data for conventional pipes (i.e. Malina and Sparrow, 1964; Allen and Eckert, 1964).

Concerning microchannels, there is currently no experimental turbulent thermal entrance region data available in literature. The reason for this is possibly due to the very short thermal entrance lengths for turbulent flow as opposed to laminar flow, where the use of thermocouples to measure local wall temperatures of a microchannel within this region is near to impossible. However, un-encapsulated TLC techniques may allow the possibility to capture localized temperature measurements within the thermal entrance.

## 2.7 Summary and Objectives

The above review shows that there were numerous fundamental studies carried out for single-phase liquid flow and heat transfer in microchannels in the fully developed region. Experimental investigations into laminar to turbulent transition, pressure drop and friction factors, and convective heat transfer coefficient were widely researched. However, there still remains a lack of experimental data concerning single-phase fundamental analyses as well as applications at the microscale. The entrance region, where the flow is either hydrodynamically developing, thermally developing, or both, is important because the effect on the flow field and heat transfer mechanisms is enhanced. In addition, for design purposes of future microfluidic devices, it is important to know which flow region, whether fully developed or developing, you are working in. However, the data available for the developing region of microchannels, either diabatic of adiabatic, is very limited or non-existent. The available experimental methods of micro-PIV and TLC provide the capabilities to perform analyses in the hydrodynamic or thermal entrance regions, respectively.

Fundamental data into the hydrodynamic entrance region for microchannels, both laminar and turbulent, is very limited. Only few experimental studies have been carried out for laminar flow, and no experimental data exists for turbulent flow. For the laminar hydrodynamic entrance region, particularly resulting from an inlet geometry where the flow is not pre-developed, experimental data is required to verify any scaling phenomena independent of channel aspect ratio. With the use of micro-PIV, a fundamental hydrodynamic entrance length study, both laminar and turbulent, are experimentally carried out and analyzed.

Concerning the thermal entrance region in microchannels, from the above literature review there were numerous laminar flow experiments carried out. A very wide majority of experimental studies performed for the laminar thermal entrance region show good agreement with conventional correlations. However, there is no heat transfer data available for the turbulent thermal entrance region. Due to the high pumping power required, turbulent flow is presently seen as impractical to apply in microchannels. Nonetheless, future microscale applications may necessitate a need for turbulent flow data in microchannels. Through the application of un-encapsulated TLC's, with its high spatial resolution, an experimental investigation into the turbulent thermal entrance region is investigated.

# Chapter 3

# Experimental Test Facilities and Methods

## 3.1 Micro-Particle Image Velocimetry

As previously outlined in Section 2.2 of Chapter 2, micro-PIV is a relatively recent experimental technique, having only widely been used in the last five years or so. This method allows for practical flow analysis in micro geometries, qualitative and quantitative, by acquiring velocity profile data of particles immersed in micro flows. In the following, the micro-PIV technique along with the experimental flow loop and its implementation with the micro-PIV system are explained. Also, the general operating procedure, data post-processing, and measurement challenges associated with the test facility are discussed.

### 3.1.1 Technique and Volume Illumination

The micro-PIV technique implements a similar method as conventional PIV in that velocity flow fields are acquired by tracking the trajectories of seeding particles immersed in the flow. However, where conventional PIV typically illuminates a single measurement plane 1 mm to 3 mm thick, micro-PIV illuminates the entire volume of the test section. Illuminating the entire volume is necessary due to the relative dimensions at the microscale, where the formation and aligning of a very thin light sheet would be extremely difficult (Meinhart et al., 2000a). Therefore, with the entire volume of the flow field illuminated, fluorescently dyed particles are necessary to track the flow. In micro-PIV, the depth of measurement volume is defined by aspects such as the depth of focus, magnification, numerical aperture and working distance of the microscope objective, particle diameter, and particle emission wavelength, and not the thickness of the laser sheet, as in conventional PIV (Olsen and Adrian, 2000). Due to this "volume illumination" all the particles in the flow field are illuminated (not just those in focus) and will contribute to the resulting image (Olsen and Adrian, 2000). The unfocused particles not in the focal plane can lead to background noise and uncertainty of the flow field data.

To implement the micro-PIV technique, the test-section must be optically accessible from at least one direction, as is the case with etched silicon microchannels. However, test sections which are entirely optically clear, such as those fabricated in glass or PDMS, possess advantages of increased illumination, ease in test section alignment with the microscope objectives, and a readily observable test setup. In addition, thin-walled clear microchannels with a flat surface provides good optical qualities ideal for micro-PIV laser emission.

### 3.1.2 System and Flow Loop

The experimental flow loop, along with a schematic of the micro-PIV system used in the present investigation, is shown in Figure 3.1. The flow loop consists of the test-

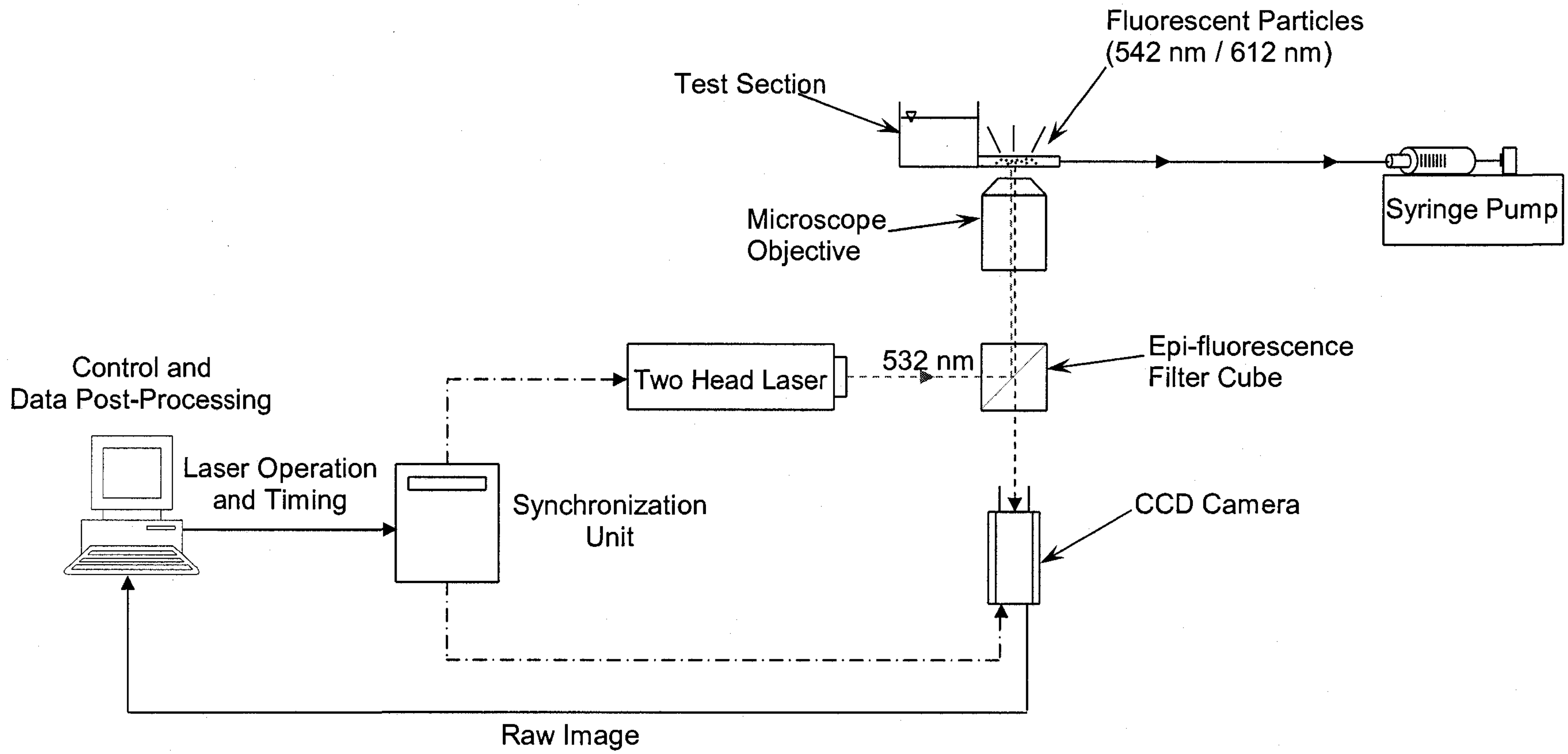


Figure 3.1: Experimental setup of micro-PIV system with flow loop

section and a syringe pump. The syringe pump (New Era Pump Systems model NE-1010) can be operated in either infusion or withdrawal modes and is programmed for desired flowrate and syringe diameter. Prior to operation, the working fluid is prepared by mixing the fluorescently dyed seeding particles (Duke Scientific) with distilled water, at a specified concentration. The particles were chosen to have a suspension density (1000 $kg/m^3$ to 1050 $kg/m^3$) very close to that of distilled water, so the particles accurately track the flow and do not interfere with the flow due to buoyancy effects.

The concentration of particles is based on a trial process and is measured in terms of volume percentage of the working fluid (i.e. distilled water). The concentration, as well as particle size, depends on the relative size of the microchannel or micro-device channels where the flow is to be analyzed. The particle concentration should be great enough to measure the flow fields with adequate signal strength, but not too great to interfere with the flow field or produce inaccuracies due to unnecessary amounts of background noise caused by unfocused particles. However, if the particle concentration is lowered, larger interrogation areas may be required. Particle concentration must be adequately chosen so that desired spatial resolution may be obtained, while maintaining adequate image quality. The particles used presently have an excitation/emission wavelength of 542 nm / 612 nm, and the available mean particle diameters are 3 μm, 2 μm, and 1 μm. The choice of particle size depends on channel dimensions, and is typically sized at 1% of the hydraulic diameter of the microchannel. The size of the particles must be large enough to dampen the effects of Brownian motion and provide a sufficient fluorescent signal, however small enough to follow the flow without disrupting the flow field (Santiago et al., 1998).

Figure 3.1 includes a schematic of the micro-PIV system, which was acquired as a commercial package from Dantec Dynamics and includes both image and data acquisition, as well as post-processing. The primary components associated with the micro-PIV system are a pulsed laser light, an inverted epi-fluorescent microscope, a CCD camera, a Synchronization Unit, and a Dell Precision Workstation equipped with specialized computer software (FlowManager v4.50) to control flow field acquisition and processing.

A dual-pulsed Nd:YAG laser light at 532 nm (New Wave Research) is passed through a beam expander assembly, and directed into the inverted microscope (Nikon Eclipse TE2000-S), incorporating both coarse and fine focus knobs. The laser pulses are controlled through the FlowManager computer software. The test section is securely positioned on the stage of the inverted microscope, below which the objectives are located. The stage is a horizontal table, capable of fine movements in both the streamwise and spanwise directions. The objectives (of magnification 2X, 4X, 10X, 20X, 40X, and 60X) are all mounted on a turret below the stage, for simplicity in changing from one magnification to another. The microscope also incorporates an epi-fluorescent filter cube (Chroma Technology), necessary for tracking the fluorescent particles due to volume illumination. The filter cube is configured for excitation with green laser light (band pass at 535 nm, band width of 50 nm) and fluorescence emission in the orange part of the spectrum (band pass at 610 nm, band width of 75 nm). The filter cube also contains a dichoric mirror which ensures efficient transfer of laser light to the test section while providing transmission of the fluorescence signal to detect, as well as reducing background reflections. On one side of the microscope is a camera port to mount the HiSense

MkII CCD camera (Hamamatsu Photonics), which has a resolution of 1344x1024 pixels. The microscope image is delivered to the camera through a camera adapter (1X magnification). The camera operation is also controlled through the computer software, and synchronized with the laser through the Synchronization Unit (Figure 3.1).

The particles are excited by the dual-pulsed laser light at a wavelength of 532 nm, and emit fluorescent light at a wavelength of about 612 nm. Imaging of the particles is done using the inverted microscope fitted with the designated objective and the epi-fluorescent filter cube. Within a predetermined time sequence ($\Delta t$) depending on the flowrate, the CCD camera acquires two sequential images in unison with the two pulses from the laser, and transmits it to the computer workstation equipped with the FlowManager software for post-processing. The Dell Precision Workstation is equipped with two 3.60 GHz Intel Xeon processors, 4 GB of RAM, two 250 GB 7200 RPM hard disks, and a 128 MB video card. Installed in the workstation is a National Instruments NI-IMAQ PCI-1426 frame grabber card, which was used in conjunction with the camera to record the images. The camera and laser pulses were synchronized using a National Instruments NI-DQQ PCI-6601 timer board.

### 3.1.3 General Procedure and Processing

The general operating procedure of the micro-PIV system is as follows: 1– The test section is setup on the microscope stage, with the appropriate microscope objective, to adequately visualize the location to be analyzed; 2– The particle/water solution is then manually introduced through the test section with a syringe; 3– The location of the desired measurement plane is chosen through the fine and coarse focal knobs; 4–

Spatial calibration of the channel size is carried out through imaging; 5– Temporal calibration is carried out through sample image pairs to select the appropriate $\Delta t$; 6– With the syringe pump steadily operating in either withdrawal or infusion modes, numerous image pairs are recorded; 7– Resulting image pairs are analyzed and correlated through the FlowManager software.

Regarding the data analysis carried out by the FlowManager software, the acquired images are divided into "interrogation areas", which are correlated for average particle displacement. Images with smaller sized interrogation areas lead to more velocity vectors in a given image. Therefore, selection of the interrogation area size, which is on the order of pixels, is dependent on the resolution of the vector map and the relative size of the flow area. Typically, smaller interrogation dimensions should be chosen in the spanwise direction, where a high flow field resolution is desired, whereas larger dimensions should be chosen in the flow direction to reduce computing.

Correlation methods (i.e. cross, average, or adaptive) incorporated in FlowManager correlate the interrogation areas into quantitative velocity data, processing a velocity vector for each interrogation area. This is carried out using a validation method of the correlation signal peak, which identifies common particle displacement through sub-pixel interpolation. The time between the image pairs ($\Delta t$) is chosen to have mean particle displacement of 25% within the interrogation area, also known as the "¼ law". The vector's characteristics are based on the $\Delta t$ chosen by the operator, and the particle displacement within the interrogation region through the correlation signal peak. The largest peak defines the particles' greatest signal and the vector's probable displacement characteristics. The velocity vector of each interrogation area is used to produce a vector map of all interrogation areas within the image. To obtain an adequate display of the flow field, numerous image pairs are taken for the same flow condition. The resulting vector map of each image pair is then filtered and temporally averaged with the remaining image pairs, to produce a vector plot of the flow field. The software outputs quantitative and qualitative information regarding the velocity flow field.

### 3.1.4 Micro-PIV Uncertainty

All the particles in the flow field are illuminated and will contribute to the resulting image. The unfocused particles not in the focal plane can lead to background noise and uncertainty in the acquired data. The method in validating the micro-PIV data, as well as detailed causes for micro-PIV uncertainty depend on the experiment and flow region to be analyzed, and is therefore, in many instances, test-section dependant. These uncertainties will be addressed in the results and discussion of the micro-PIV experimental investigations, in Chapter 4. However, there are generally two sources of random error in micro-PIV measurements, random error due to Brownian motion and random error due to interrogation and resolution. These two sources of random error are typically estimated to present the accuracy of the micro-PIV measurements.

When sufficiently small seeding particles are immersed in a fluid, random particle movements become apparent, due to fluid-particle interactions on the molecular level. This phenomenon is termed as Brownian motion. Since the particle is sufficiently small, there is an unbalance in the surrounding fluid molecules colliding with the particle, causing it to randomly move. However, Brownian motion becomes of lesser importance as the seeding particle size increases or as the fluid velocity increases. Santiago et al. (1998) stated that Brownian motion becomes important at fluid velocities in the vicinity of 10 μm/s. Santiago et al. (1998) considered the error due to Brownian motion ($\varepsilon_B$) as,

$$\varepsilon_B = \frac{1}{U}\sqrt{\frac{2D_0}{\Delta t}}, \tag{3.1}$$

where $U$ is the fluid's average velocity, and $\Delta$t is the time interval during particle displacement, or in the case of micro-PIV, the time interval between laser pulses. $D_0$ is the Stokes-Einstein diffusion coefficient, given as,

$$D_0 = \frac{\kappa T_{abs}}{3\pi \mu d_p}, \tag{3.2}$$

where $\kappa$ is the Boltzmann constant, $T_{abs}$ is the absolute experimental temperature, $\mu$ is the fluid's dynamic viscosity, and $d_p$ is the particle diameter. In general, for microchannel flow where the fluid speed is considerable, even at very low Re numbers, Brownian motion is not expected to cause great inaccuracies. Nonetheless, it will be addressed quantitatively in Chapter 4.

The random error due to interrogation and resolution is due to the uncertainty in the seeding particle image displacement. Larger particles generally increase these random errors, since they have a larger particle image size and occupy more pixels. Also, since a CCD camera is used, the pixel size is fixed (i.e. 6.45 μm); therefore to reduce random errors due to interrogation, the particle image size must be reduced (Prasad et al., 1992). Prasad et al. (1992) stated that for conventional PIV, the error is minimized by selecting a particle image size so that a particle occupies about 2 pixels. However, for micro-PIV, as stated by Santiago et al. (1998), since the shape of the particles is known to be spherical, the relative position of the particles can be determined with a resolution 10 times greater than that of the microscope. In other words, the uncertainty in determining the particle displacement is within 10% of the particle image diameter projected back into the flow field. From Santiago et al. (1998), the particle image diameter, $d_e$, of a particle in focus can be found by,

$$d_e = \sqrt{M^2 d_p^{\ 2} + d_s^{\ 2}} \ , \tag{3.3}$$

where $M$ is the objective's magnification, and $d_s$ is the diameter of the point-spread function, given by,

$$d_s = 1.22(1+M)\frac{\lambda_{emit}}{NA} \ . \tag{3.4}$$

For micro-PIV, the diameter of the point spread function is caused by the diffraction of the fluorescent particles. In Eq. (3.4), $\lambda_{emit}$ is the emission wavelength of the fluorescent particles and NA in the numerical aperture of the objective. Since uncertainty in the seeding particle displacement depends on the measurement methods and particle size, it will be quantified in Chapter 4.

### 3.1.5 Experimental Challenges

Through experimental trials and analysis, experimental measurement challenges of the micro-PIV setup were recorded. Concerning the test-sections and flow loop measurement challenges, there were initial difficulties in the fabrication of cost-effective, optically clear test-sections, with the ability to function properly with the laser emission of micro-PIV. Test-sections possessing a flat geometry to reduce refractions and reflections of the laser light is preferable. Also, it was noticed that after some micro-PIV experiments, the particles fouled the test-sections due to the fluorescent dye of the particles. In addition, the syringe pump employs a stepper motor and worm gear, as well as a plunger-type syringe. The range of operating flowrates was limited, particularly for smaller channel widths (< 200 μm) due to the friction of the plunger and the operation of the stepper motor. Regarding the micro-PIV system, difficulties arose in acquiring the appropriate measurement plane through the microscope focus, as well as obtaining flow data very close to channel walls, where there was possible influence of the particles.

## 3.2 Thermochromic Liquid Crystals

Through thermochromic liquid crystal (TLC) coating of a surface, optical thermal measurement may be obtained locally. The temperature sensing ability can provide qualitative and quantitative thermal data, if the material is properly calibrated through their color response to temperature, as discussed in Section 2.2 of Chapter 2. TLC's are attractive due to their ability to coat a complete surface, their non-intrusiveness with the flow, and their spatial resolution, particularly in their un-encapsulated form. The following provides further detail into the molecular workings of liquid crystals, as well as the experimental test facility, TLC application and calibration, and measurement challenges.

### 3.2.1 TLC Material

The notion of thermochromic liquid crystal is generally a liquid crystal material being employed for thermal sensing. The liquid crystal state is an intermediate phase between liquid and solid states that occurs in some organic compounds. Liquid crystal molecules have orientational order, which allows it to display useful optical properties of crystalline solids, but lose their positional order which causes their fluidity (Hay and Hollingsworth, 1996). The ability to sense temperature comes from the different forms of the molecular structure within a range of temperatures (Ireland and Jones, 2000).

Two phases of liquid crystals are the *smectic* and *nematic* phases. In the smectic phase the molecules are layered and ordered with their longitudinal axes parallel. In the chiral nematic phase, on the other hand, the molecules are not layered, and intermolecular forces cause each molecule to be rotated slightly with respect to adjacent molecules, tracing a helical path (Hay and Hollingsworth, 1996). The observed reflected color is a function of the pitch of this helix, which is dependant on temperature (Ireland and Jones, 2000). As the temperature of the liquid crystal in its nematic phase decreases, more groups of molecules begin to arrange themselves in smectic layers, where there is no rotation between molecules. With continued cooling, all molecules eventually arrange themselves in the smectic phase, where there is no longer a color response and outside the temperature sensing range of the liquid crystals (Hay and Hollingsworth, 1996).

Depending on the type of liquid crystal material, the temperature relation with the pitch of the helix can provide broad (~20 °C) or narrow (~1 °C) thermal sensing ranges. Once the TLC temperature enters within its thermal sensing range, the TLC's turn from colorless to red. Sequentially, as the temperature is increased, the material turns to other colors within the spectrum (yellow, green, blue). Once the temperature increases outside of its temperature range, the TLC's turn back to colorless. Within the TLC thermal range, this process is reversible upon cooling.

To protect the liquid crystal material from contamination and to increase their longevity, manufacturers use micro-encapsulation. In micro-encapsulated TLC's, droplets of the liquid crystal material are surrounded by polymer coatings producing microcapsules 10 μm to 20 μm in diameter (Hay and Hollingsworth, 1996). However, it is obvious that these capsules impede the material's spatial resolution. At the microscale, where a high spatial resolution is desired, un-encapsulated TLC's should be used (Muwanga and Hassan, 2006a), which is the case with the present study.

### 3.2.2 Test Facility Flow Loop

The experimental flow loop used in the present study is shown in Figure 3.2, and is the same used by Muwanga and Hassan (2006a, 2006b). This test facility was built to distinctly acquire TLC wall temperature measurements of microchannels and micro-devices, and was designed for both single-phase and flow boiling experiments. However, the present discussion will focus only on the elements required for single-phase flow. In regards to single-phase flow, the facility is capable of incorporating a number of different fluids to be analyzed, such as distilled water, a variety of refrigerants, and air. The working fluid in the present investigation is FC-72 (3M), a low viscosity electronics cooling fluid widely used in industry. The physical properties of FC-72 are shown in Table 3.1.

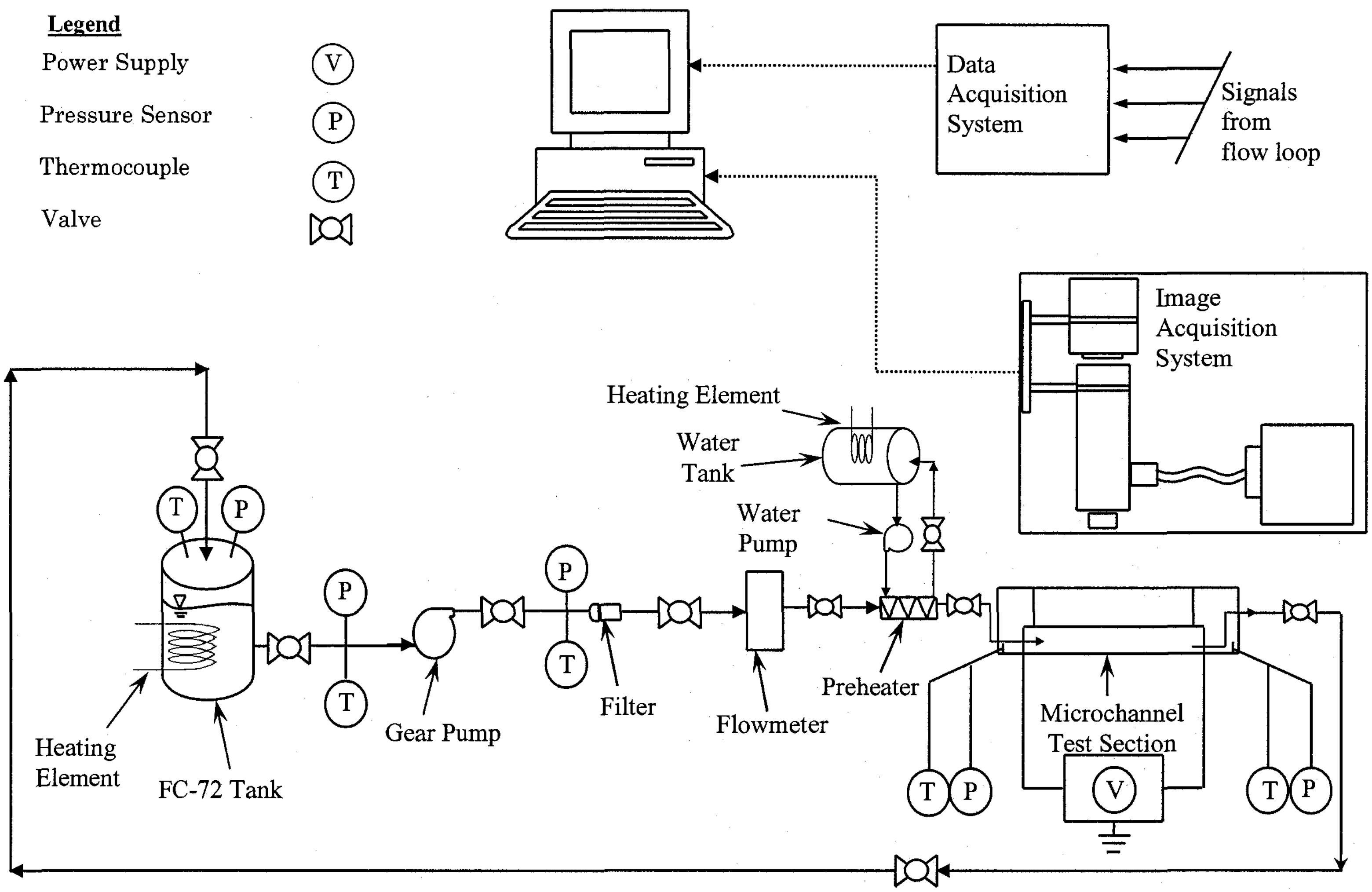


Figure 3.2: TLC experimental test facility flow loop (adapted from Muwanga, 2007)

Table 3.1: Physical properties of FC-72 at 25 °C and 1 atm

| Property | Value |
|---|---|
| $\rho$ | 1680 kg/m$^3$ |
| $\mu$ | 6.4 x 10$^{-4}$ Ns/m$^2$ |
| $C_p$ | 1100 J/kg°C |
| Pr | 12.35 |

The fluid operates in a closed system and is continuously circulated by means of a magnetically coupled gear pump (Cole-Parmer), as shown in Figure 3.2. The pump operates at a controlled speed and supplies a maximum flowrate of 290 ml/min, with a pressure of 517 kPa. Downstream from the pump is a 15 μm filter, to remove any particulates within the flow. The system flowrate was monitored by means of a nutating digital output flowmeter (DEA Engineering), equipped to handle corrosive refrigerants. Initial calibration of the flowmeter was carried out using a precise weighing method, and operates at a flowrate range from 10 to 250 ml/min. Prior to entering the microchannel test section, the fluid enters a preheater for additional flow temperature control. The preheater is a counter flow, tube-in-tube heat exchanger with distilled water as the heating fluid. As shown in Figure 3.2, the test section is heated by means of Joule heating with the use of a power supply. Heater power was provided by a Good Will (GW) Instruments power supply (Model GPC-1850) with a voltage range of 0 V to 20 V and a maximum current rating of 10 A. Also apparent from the figure are the image and data acquisition systems, details of which will be explained in a later section.

### 3.2.3 Un-encapsulated TLC Coating and Application

Concerning the heat transfer experiments, the measurement of local wall temperatures was achieved through the use of un-encapsulated thermochromic liquid crystals (TLC's). However, due to their fluidity, it was a challenging task to apply un-encapsulated TLC's to a curved surface, such as a microtube, rather than a flat surface.

The application of TLC's can, in some cases, be a challenging endeavor. The TLC's should be applied as a uniform coating capable of producing vibrant colors for surface temperature measurement. A thicker coating improves color vibrancy, however if the coating is too thick, the coating itself can produce non-negligible temperature gradients through the TLC layer. A relatively uniform application of the un-encapsulated TLC's was applied through the use of an airbrush using a similar method as Muwanga and Hassan (2006a).

The un-encapsulated liquid crystal material used is provided by LCR-Hallcrest. The TLC material nominally has a red-start of 40 °C with a bandwidth of 10 °C. The TLC material was applied onto the microtube surface using a Badger Model 100 independent action airbrush. In order to provide an improved uniform layer of coating, the TLC material was dissolved in acetone with concentrations by weight of 20:1 (solvent to TLC). Prior to the application of the TLC coating on the microtubes, a water-based, black paint coating was applied using the airbrush for improved color vibrancy of the TLC response.

### 3.2.4 Measurement Methods

Two 1.5 mm diameter Type-T (Omega special error limits material) thermocouples were placed in each plenum chamber of the test section (see Figure 3.2) to measure the bulk fluid temperature. Two static pressure transducers tracked the gage pressure in the inlet and outlet plenums. The pressure transducers, both manufactured by Omega, are model PX01C1 at the microtube outlet and model PX02C1 at the microtube inlet, with ratings of 517 kPa (75 psi) and 345 kPa (50 psi), respectively. The output from these and other sensors is monitored through an automated data acquisition system using the LabVIEW software. The data acquisition hardware consisted of National Instrument's SCXI 1000 signal conditioning unit, with the appropriate modules as well as the NI 6052E 16-bit 333 kHz data acquisition card.

A schematic of the data acquisition system is shown in Figure 3.3. The signals from the transducers (i.e. pressure, temperature) were transferred through the signal conditioning unit to reduce noise and/or improve signal strength, then through the data acquisition (DAQ) card to the computer (Dell). However, signals from the metering devices (i.e. flowmeter) were directly transferred to the computer through the DAQ card, without the use of the signal conditioner. Image acquisition was carried out in LabVIEW and the images were captured in Red-Green-Blue (rgb) format. The image size in pixels depends on the magnification and tube diameter. Hue planes were simultaneously extracted and saved in tagged image file format (TIFF). Image and data post-processing was carried out using an in-house program in MATLAB operating on the Dell workstation.

A schematic of the image acquisition system is shown in Figure 3.4. Light from an illuminator box (Optem Intl.) is directed through a fiber optic cable, keeping the heat generated from the light source away from the test section. Initial setup was to have the light from the illuminator to be passed through a polarizer prior to entering the zoom lens casing, where it was to be deflected to the test surface by a beam splitter. However, even though the test facility has this capability, it was not used in acquiring the microtube TLC images, due to the reduced intensity obtained when voltage was applied to the tube. Therefore, the fiber optic illumination source directly illuminated the surface by fixing it onto the zoom lens at a fixed angle, as

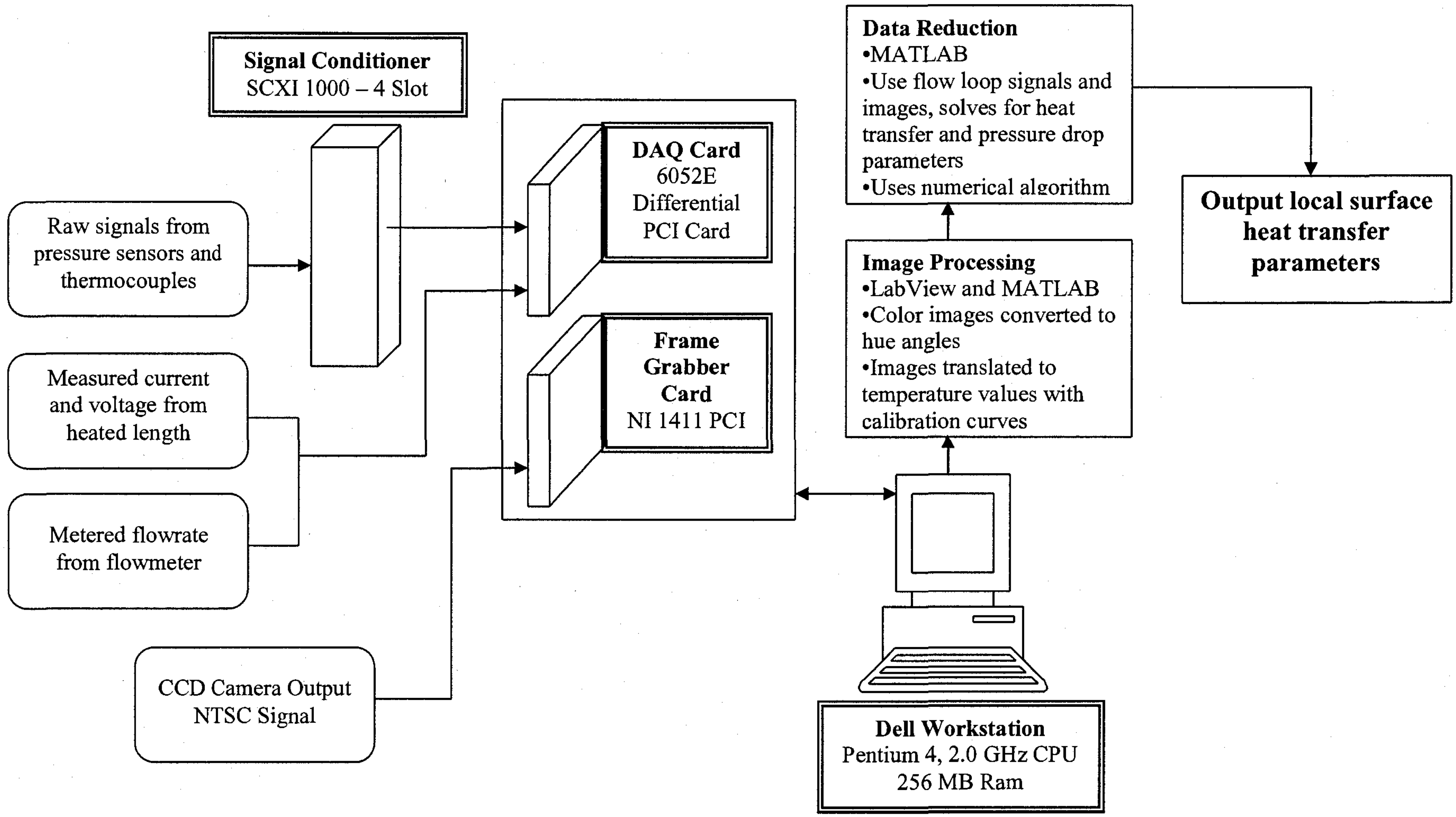


Figure 3.3: TLC data acquisition system schematic (adapted from Muwanga, 2007)

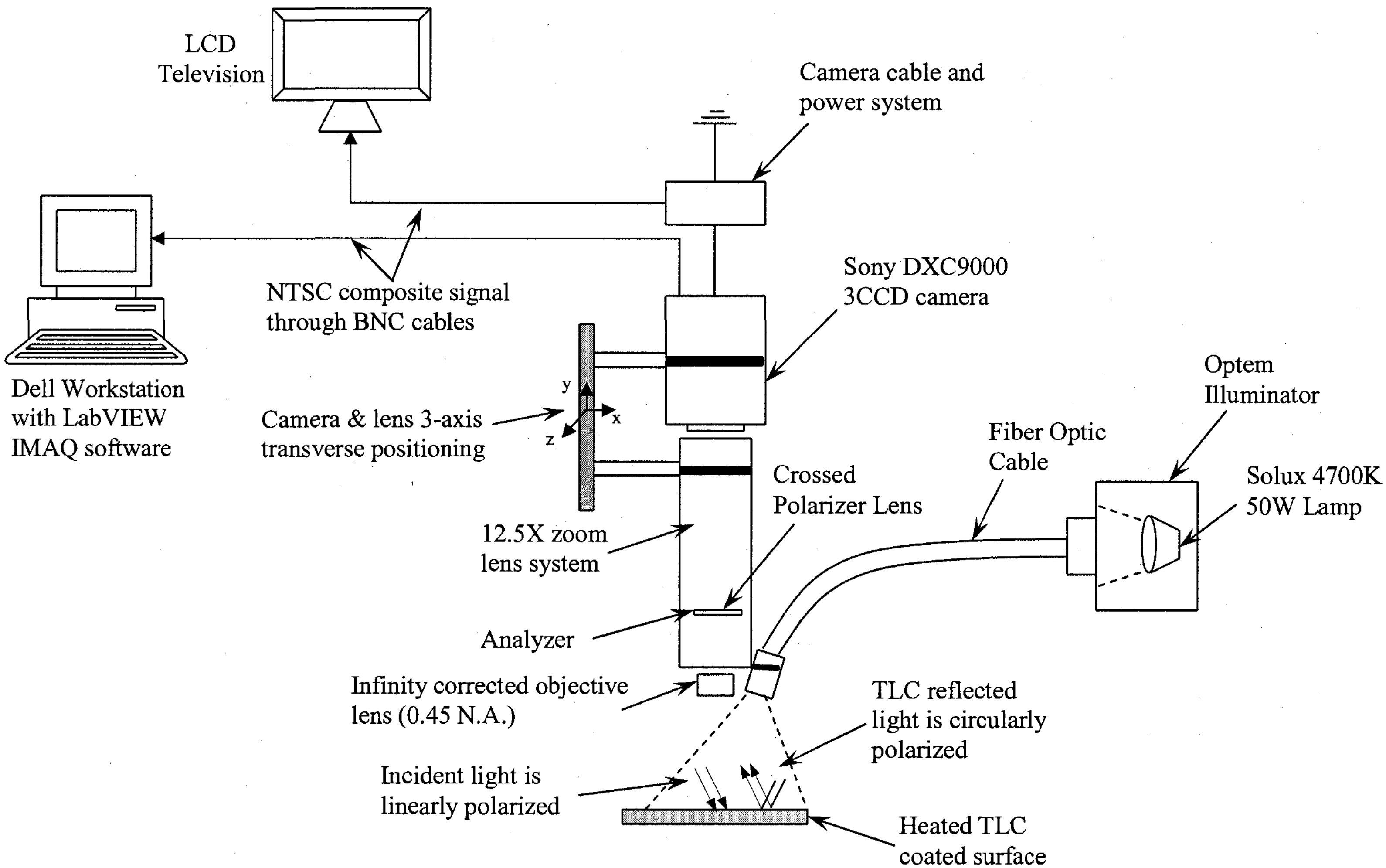


Figure 3.4: TLC image acquisition system schematic (adapted from Muwanga, 2007)

shown in Figure 3.4 and later in Figure 5.2. Upon reflection from the coated surface, the light is circularly polarized and is passed into the zoom lens through the analyzer, and is directed to the 3-CCD camera. Since the reflected light is circularly polarized, it travels through the crossed polarizing pair unaffected. The acquired TLC image is then transferred directly to the computer as a NTSC signal through a BNC cable.

Through the use of an LCD television, real time monitoring and positioning of the test section was possible. This allowed the operator to precisely align the test-section, as well as observe the colors of the TLC coated surface. The video signal used in the television loop comes from a separate output line directly from the camera. Image acquisition is obtained using a Sony 3-CCD analog camera, which is connected to a variable zoom microscopic lens. This combination is mounted onto a three-axis traverse, equipped with variable length stages with 1 μm resolution. The lateral and vertical axis stages allow for fine-tuning of both positioning and focusing.

### 3.2.5 TLC Calibration

To acquire quantitative temperature data from TLC thermal colors on the surface of the microtube, it is required that the TLC material be calibrated to relate the observed color to a temperature value. There are many different available methods to quantify the observed color. In the present study, similar to Muwanga and Hassan (2006a, 2006b) the hue angle was taken as the color descriptor in order to reduce the color response to a single value. The hue angle, given by Hay and Hollingsworth (1996) is defined as,

$$Hue = \arctan\left(\frac{\sqrt{3}(G-B)}{2R-G-B}\right), \tag{3.5}$$

where $R$, $G$, and $B$ are red, green, and blue values, respectively. The observed TLC color depends on many aspects, such as background lighting, camera distance, camera viewing angle, primary lighting angle and distance, and the time the TLC coating was applied to the specimen. In order for a valid and confident calibration to be carried out, all the above aspects must be maintained the same for both the calibration and the experiment.

The calibration is based on circulating the fluid through the channel and was selected due to its ease of incorporation into the setup. With the use of thermocouples, the bulk temperatures at the inlet and outlet of the channel were measured and remained to within 0.5 °C of each other. Through the use of the preheater, the fluid was slowly heated and images were captured at incremental changes in temperature, to cover the whole bandwidth of the TLC material (~10 °C). Also, if the wall temperature along the entire length of the tube had to be recorded and hence calibrated, then the camera would need to be transversed at different axial positions. However, as it will be discussed in Chapter 5, the present experimental heat transfer study dealt only with the thermal entrance region of a microchannel, therefore only one axial position had to be recorded. This simplified the process, since there was no need to traverse the camera axially along the microtube.

Processing of the calibrated images was carried out as follows. Each calibration curve, which is a curve of Temperature vs. Hue Angle, represents a certain region of interest (ROI) on the tube surface, which is made up of only a few pixels. This eliminates aspects such as viewing angle and light distortion between different regions on the tube. Therefore, a size of the ROI must be selected. In the present heat transfer study, a ROI of 4 x 3 pixels was selected, giving over 3000 calibration curves covering the entire image, depending on the tube size. The size of the ROI should be large enough to account for noisy pixels using statistics, but small enough to capture the local variability in the color change.

Through the use of MATLAB, an automated calibration curve fitting was utilized to fit the calibration data points. The MATLAB coding was developed by Muwanga (2007) where a sample of the calibration coding can be found. Initially a polynomial of order five was utilized to fit the calibration points, however if any local extensive fluctuations were present within a predefined region, the polynomial order was reduced to three. An example of this case is shown in Figure 3.5a, which shows a calibration curve with the data points originally set at a fifth order fit, then corrected to a third order fit. Figure 3.5b shows a typical calibration curve that shows a good fit between the calibrated data and a fifth order polynomial.

### 3.2.6 TLC Uncertainty and Challenges

The uncertainty in TLC wall temperature depends on factors such as the sensitivity (slope) in the calibration curve (Temperature vs. Hue Angle), the uncertainty in the hue value, and the error in the polynomial curve fit of the calibration points. Wall temperature uncertainty measurements were calculated using similar methods as Hay and Hollingsworth (1996) and Muwanga and Hassan (2006a, 2006b). The wall temperature uncertainty, $\delta T_w$, for an ROI can be calculated as,

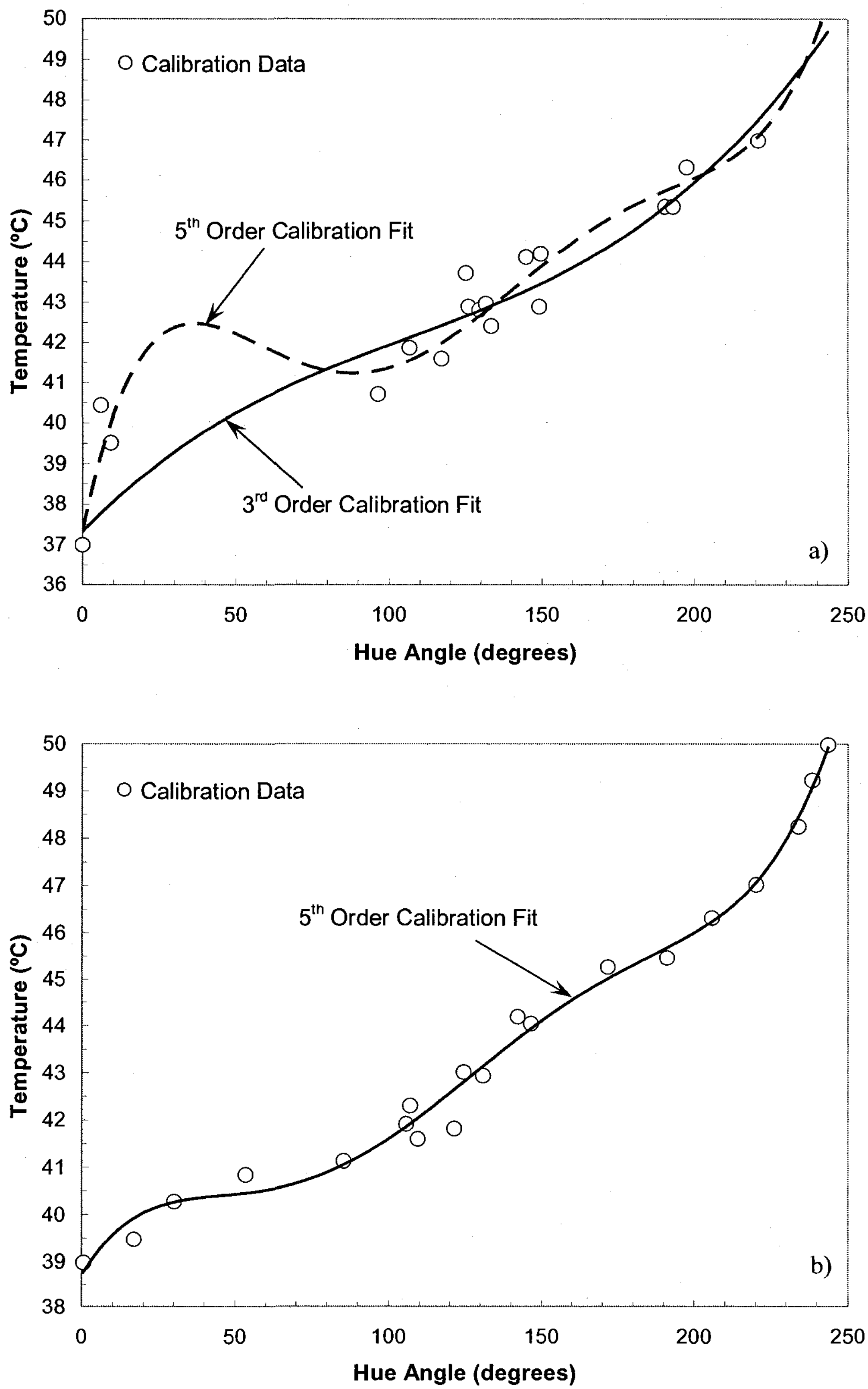


Figure 3.5: Examples of calibration curves: (a) corrected calibration curve with 3rd and 5th order fits, and (b) a typical good-fit calibration curve with a 5th order fit

$$\delta T_w = \left[ \left( \frac{dT}{dh} \delta h \right)^2 + \delta T_{Fluid}^{\ 2} + (2SEE)^2 \right]^{1/2}, \tag{3.6}$$

where $dT/dh$ is the sensitivity in the calibration curve, which can either be a third order or fifth order polynomial fit, as previously discussed. The parameter $\delta h$ is the uncertainty in hue for the ROI, and since the ROI's were very small, a constant value of 1 degree was chosen, through visual observation, instead of the scatter. Also, an additional 2 degrees was added to account for the conversion uncertainty from rgb to the composite signal. The parameter $\delta T_{Fluid}$ is the uncertainty of the thermocouples used to measure the fluid bulk temperature at the inlet and outlet plenum chambers during calibration, and was taken as 0.7 °C. The standard error estimate (SEE), given by Hay and Hollingsworth (1996) is defined as,

$$SEE = \left[ \frac{\sum_{i=1}^{n} \left[ T_i(h) - T_{fit,i}(h) \right]^2}{n - j - 1} \right]^{1/2}. \tag{3.7}$$

The standard error estimate is a measure of the accuracy of the predicted polynomial used in fitting the calibration points, and takes into account the error of the curve fit. However, it was noticed that since some calibrated points had large scatter, calculation of SEE was altered unreasonably. Therefore, instead of calculating SEE, a constant value of 0.5 °C was selected for SEE based on repeated observations of the calibration curves. The uncertainty of the TLC wall temperature was found to be 1.1 °C. The remaining experimental uncertainties are dependant on the experiment and test section, and are outlined in Chapter 5.

Experimental challenges associated with the TLC experimental process primarily resulted from the application and calibration of the un-encapsulated TLC coating. The spraying of an ideal amount of TLC as well as obtaining a proper thickness for color vibrancy with a negligible temperature gradient was challenging, in addition to avoiding contamination of the coated surface from dust and room lighting, as well as the fluidity of the TLC. In regards to TLC calibration, difficulties arose in curve fitting the calibrated data points to preferred polynomials of fifth order rather than third order.

# Chapter 4

# Hydrodynamic Entrance Region in Microchannels

## 4.1 Overview

The understanding of fluid flow behavior in microchannels and micro-devices has been a strong focus of the research community over the past decade. Microchannels are prevalent in micro-devices, such as micro-heat-exchangers (i.e. Tuckerman and Pease, 1981; Mishan et al., 2007; Muwanga et al., 2007), and micro-mixers (i.e. Nguyen and Wu, 2005, deMello, 2006; Chang and Yang, 2007). In turn, these microfluidic components are to be implemented in complete micro-systems, such as micro power-plants (i.e. Epstein, 2004; Suzuki et al., 2008) and Lab-on-a-Chip platforms (i.e. Whitesides, 2006; Yager et al., 2006; Chaw et al., 2007). However, prior to the advanced development of such micro systems, it becomes necessary to further understand the flow characteristics in microchannels and micro-devices incorporated in these systems. Also, single-phase liquid flow remains important in terms of applications and fundamental understanding.

From the literature review in Chapter 2, it was summarized that there were numerous experimental fluid flow studies carried out for fully developed microchannel flow. These studies focused on pressure drop, friction factors, and laminar to turbulent transition. Early studies indicated large deviations from conventional theory, however more recent studies found good agreement with convention due to the required accountability of experimental errors and uncertainties at the microscale, such as dimensional tolerances, entrance and exit losses, and surface roughness. From the improved experimental data, the present general consensus is that conventional theory is applicable for channel dimensions down to hydraulic diameters of 100 μm.

However, as outlined in Chapter 2, the study of the entrance region in microchannels and micro-devices is very limited. The entrance region, where the flow is hydrodynamically developing, can be very important because transport properties such as pressure gradient, wall shear stress, and heat transfer coefficient depend strongly on the flow region. Also, it should be stressed that general correlations for friction factor, heat transfer coefficient, and laminar to turbulent transition are only valid if the flow is fully developed. Generally, the hydrodynamic entrance length can be defined as the length from the inlet of a channel to a location over which the maximum local flow velocity has attained 99% of its fully developed value (Shah and London, 1978). However, a uniform inlet velocity profile is seldom achieved in practice, and is somewhat difficult to simulate in experimental investigations, particularly at the microscale.

An experimental study has been carried out to explore the laminar hydrodynamic development length in the entrance region of adiabatic square microchannels. As well, an attempt has been carried out to experimentally study the turbulent hydrodynamic development region in microchannels. Flow field measurements are acquired through the use of micro-Particle Image Velocimetry (μPIV), a non-intrusive particle tracking and flow observation technique.

## 4.2 Laminar Flow

In practical applications of microchannel flow, the majority of micro system flows are laminar, due to the high pressure drop in microchannels caused by relatively small channel dimensions. To apply many conventional laminar correlations it is necessary that the flow be fully developed or errors will result. Conventionally in the laminar regime, the lower the Reynolds number, the shorter the entrance region to achieve fully developed flow. But, it should be emphasized that in microfluidic devices and systems, microchannel lengths can be extremely short, in which case within a certain range of Reynolds numbers (Re), hydrodynamic developing flow may dominate the flow field over the entire microchannel length.

There is limited fluid flow data available for the laminar entrance region of microchannels, particularly resulting from a fundamental inlet geometry where the flow is not pre-developed. A general entrance length study from a very large reservoir, relative to the microchannel hydraulic diameter, is a significant contribution in the area of microchannel fluid flow. The laminar hydrodynamic development length in the entrance region of adiabatic square microchannels is experimentally investigated. With the application of micro-PIV, test sections of three different square microchannel hydraulic diameters of 500 µm, 200 µm, and 100 µm are employed. The working fluid is distilled water, and velocity profile data is acquired over a laminar Reynolds number range from 0.5 to 200. The test sections were designed with a sharp-edged inlet from a large reservoir, at least 100 times wider, higher, and longer than the microchannel hydraulic diameter, and all microchannels have a length-to-diameter ratio ($L/D_h$) of at least 100, to assure fully developed flow at the channel exit. The micro-PIV procedure is validated in the fully developed region with comparison to the Navier-Stokes momentum equations. In addition, to analyze the effect of dimensional scaling, the experimental data is compared with conventional entrance length correlations for ducts and parallel plates. New laminar entrance length correlations are proposed, which account for both creeping and high laminar Reynolds number flows.

### 4.2.1 Test Section

In order to fundamentally study microchannel entrance region characteristics from a very large reservoir, general fabrication methods were applied to satisfy this geometrical constraint. Three test sections, as shown in Figure 4.1, were designed to provide a sharp-edged microchannel inlet from a very large reservoir relative to the hydraulic diameter of the channel. For each of the 500 µm, 200 µm, and 100 µm microchannels, an appropriate test section was fabricated, dimensions of which are also given in Figure 4.1. The borosilicate thin-walled glass microchannels used in fabricating the present test sections are commercially available, manufactured and cut to length by Friedrich & Dimmock Inc. All microchannels possess a square cross-

| Length | 500 µm Test Section (mm) | 200 µm Test Section (mm) | 100 µm Test Section (mm) |
|---|---|---|---|
| A | 68 | 35 | 25 |
| B | 50 | 25 | 25 |
| C | 54 | 30 | 30 |
| D | 126 | 76 | 76 |
| E | 60 | 26 | 26 |
| F | 50.8 | 20 | 20 |

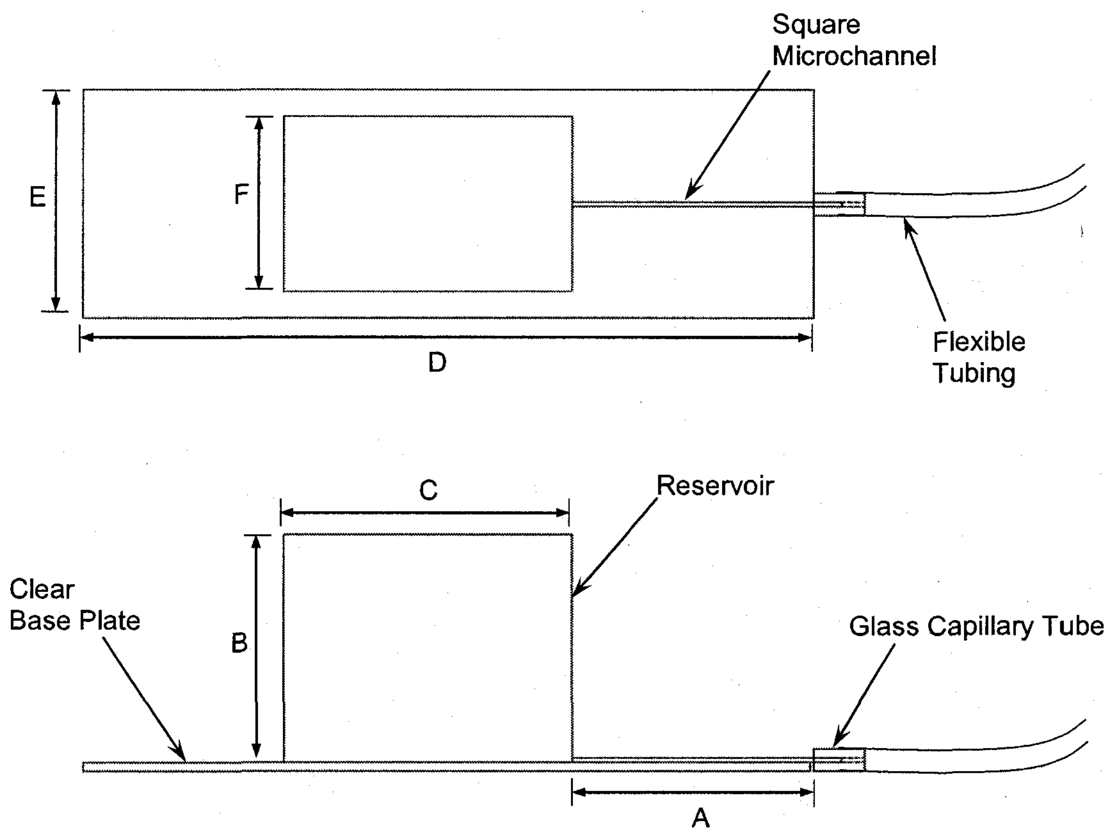


Figure 4.1: Top and side views of the test section configuration used in hydrodynamic entrance length studies

section ($H/W = 1$) in order to remove any influence of aspect ratio and to distinctly study the geometric influence of scaling in the microchannel entrance region.

As stated in Chapter 3, in micro-PIV the entire volume of the flow field is illuminated, and fluorescently dyed particles are necessary to track the flow through the use of microscope objectives. Therefore, to implement the micro-PIV technique, the test-section must be optically accessible from at least one direction, as is the case with etched silicon microchannels. However, in the present study the entire test sections are optically clear, having advantages of increased illumination, test section alignment with the microscope objectives, and a readily observable test setup. In addition, the thin-walled glass microchannels provided good optical qualities ideal for micro-PIV laser emission.

All test sections were fabricated using a similar method. Depending on microchannel dimension and objective working distance, either a 3 mm thick clear polycarbonate sheet (500 µm channel) or 1 mm thick clear glass slide (200 µm and 100 µm channels) was used as a base plate for the test section (Figure 4.1). The base plate provided rigidity for the test setup, as well as provided an optically clear flat surface for laser emission, necessary for micro-PIV. Four vertical polycarbonate walls were then bonded onto one end of the base plate using general purpose clear epoxy (Permatex), and sealed with silicone. These four walls, along with the base plate, served as the open air inlet reservoir to the microchannel, as shown in Figure 4.1. The walls were bonded together and sealed only on the exterior, as not to interfere with the flow inside the reservoir. Using a sawing technique, a small grove (on the order of the external dimensions of the microchannel) was machined at the bottom center of the reservoir wall bordering the microchannel inlet to provide a slot to seat the microchannel. Once the reservoir had been sealed and cured, the respective microchannel was carefully slid into the machined grove until the channel inlet was flush with the interior wall of the reservoir. Also, similar to an etched microchannel in a silicon substrate, the base of the inlet reservoir was on the same plane as the microchannel base. The microchannel was then bonded to the base plate and reservoir wall using the clear epoxy. A capillary tube was slid onto the microchannel exit and bonded to the base plate. Flexible tubing (Tygon) was then fixed firmly to the capillary tube, to provide an adaptable path to the syringe pump.

With the syringe pump operating in withdrawal mode, the fluid is steadily withdrawn from the inlet reservoir through the microchannel and into a syringe incorporated with the syringe pump, as was illustrated in the schematic of Figure 3.1. The fluid is a mixture of distilled water and micro-PIV particles. Mean particle diameters used in the test sections were 3 µm (500 µm channel), 2 µm (200 µm channel), and 1 µm (100 µm channel). The fluorescent particles (Duke Scientific) are excited by the green laser light (532 nm) and emit fluorescent light in the orange part of the spectrum (612 nm). Through the designated microscope objective (i.e. 10X for 500 µm channel, 20X for the 200 µm and 100 µm channels) and epi-fluorescent filter cube, imaging of the particles in the microchannel is carried out.

### 4.2.2 Experimental Parameters and Procedure

Micro-PIV data sets were recorded for the three microchannels at the center plane at incremental axial distances from the microchannel inlet. The overlapping incremental axial distances were at 0.5 mm for the 500 µm channel, and 0.25 mm for the 200 µm and 100 µm channels. There was considerable overlap in the axial images, as to considerably reduce the error associated with the process. The particle concentration in the distilled water for the 500 μm channel (3 μm particles) was ~0.0141% by volume, for the 200 μm channel (2 μm particles) was ~0.0168% by volume, and for the 100 μm channel (1 μm particles) was ~0.0223% by volume. These concentrations were chosen based on a trial process and are very low; hence the mixture can be considered as a single-phase liquid. The desired flowrates were programmed into the syringe pump operating in withdrawal mode. With a known volume flowrate, $Q$, the Reynolds (Re) number was calculated as,

$$\mathrm{Re} = \frac{Q D_h}{\upsilon A}, \tag{4.1}$$

where $D_h$ is the hydraulic diameter, $\upsilon$ in the kinematic viscosity, and $A$ is the cross-sectional area of the channel. The kinematic viscosity was assumed constant at room temperature.

Spatial calibration was carried out with the use of the FlowManager software for each axial position recorded. The maximum energy the laser can supply is 120 mJ/pulse, where 9.6 mJ was employed for the 100 μm channel, 10.8 mJ was employed for the 200 μm channel, and 12 mJ was employed for the 500 μm channel. The number of recorded sequential image pairs for a given flow condition must be large enough to collect an adequate amount of data to accurately describe the flow field, but not too great as to reduce the computing time. Based on an initial trial process, thirty sequential image pairs were used for each data set, and were recorded three times, to assure repeatability in the data. Interrogation areas of 32 x 64 pixels were used for all channels, and the time between the image pairs ($\Delta t$) was chosen as to have mean particle displacement of 25% within the interrogation area. The thirty image pairs were correlated using the adaptive correlation technique (Dantec Dynamics), then filtered (3 x 3 window) and temporally averaged, to produce a vector plot of the flow field. Prior to the entrance length measurements, vector plots for each Re number were recorded in the fully developed region to assure validation with the two-dimensional Navier-Stokes momentum equations for a rectangular duct at the center plane.

### 4.2.3 Experimental Uncertainties

The uncertainties in the process, which are tabulated in Table 4.1, resulted from the syringe pump (i.e. flowrate), the width of the channels, the channel center plane, transversing along the channel length, as well as the random errors associated with the micro-PIV system. The syringe pump employs a stepper motor and worm gear, as well as a plunger-type syringe. The uncertainty was higher at low flowrates due to the friction of the plunger and the operation of the stepper motor. Regardless, the highest uncertainty in the flowrate was observed to be 2 – 4% using the nominal channel widths. The uncertainty in the channel widths, provided by the manufacturer was ±10% for all channels, giving an uncertainty in Re of ~10.8%. The micro-PIV data was validated at the center plane in the fully developed region using the Navier-Stokes equations, with an uncertainty of less than 4%. However the uncertainty in Re, as well as the uncertainty in validation with the Navier-Stokes equations, is due largely to the high uncertainty in the widths of the channels.

The random errors due to micro-PIV, as explained in Chapter 3, are random error due to Brownian motion and random error due to interrogation and resolution.

Table 4.1: Uncertainties in the experimental parameters of the laminar hydrodynamic entrance length

| Parameter | Maximum Uncertainty | | |
|---|---|---|---|
| | 100 μm test section | 200 μm test section | 500 μm test section |
| Channel width | ± 10 % | ± 10 % | ± 10 % |
| Flowrate | 2 % – 4 % | 2 % – 4 % | 2 % – 4 % |
| Reynolds number | 10.8 % | 10.8 % | 10.8 % |
| Navier-Stokes validation | 3.8 % | 3 % | 3 % |
| Brownian motion | 1.51 % | 1.28 % | 1.24 % |
| Particle image displacement | 200.9 nm | 265.2 nm | 444.9 nm |

These are also tabulated in Table 4.1. Regarding Brownian motion, a large error was not expected, since the flow velocities are large for microchannels, even at small Re numbers. The largest error due to Brownian motion was 1.51%, which was for the 100 μm channel at Re = 0.476. The error associated with interrogation and resolution is due to the uncertainty in the particle image displacement from micro-PIV imaging. The largest uncertainty in particle image displacement was estimated to be approximately 445 nm, which was for the 500 μm channel, since it used the largest particles.

### 4.2.4 Entrance Flow Observations

Experimental velocity flow field data has been acquired in the entrance region of microchannels using micro-PIV. Three square cross-sectional microchannels were investigated in order to remove any effect of cross-sectional aspect ratio. The microchannels have hydraulic diameters ($D_h$) of 100 μm, 200 μm, and 500 μm, over a laminar Reynolds number range of 0.5 to 200. The microchannel inlets were sharp-edged from an infinitely-sized reservoir relative to the microchannel hydraulic diameter. The fluid at the reservoir interface is stagnant, as to impose minimal pre-development upstream of the microchannel entrance, and to obtain a relatively flat inlet velocity profile. Figure 4.2 shows the coordinate system used in the present analysis. Since micro-PIV images are acquired through the use of the microscope objectives beneath the test section, flow field data is attained at the center plane, at half the microchannel height. The height is denoted by the $y$ coordinate, the spanwise direction is denoted by the $z$ coordinate, and the axial direction is denoted by the $x$ coordinate, where the origin is at the microchannel inlet. It should be noted

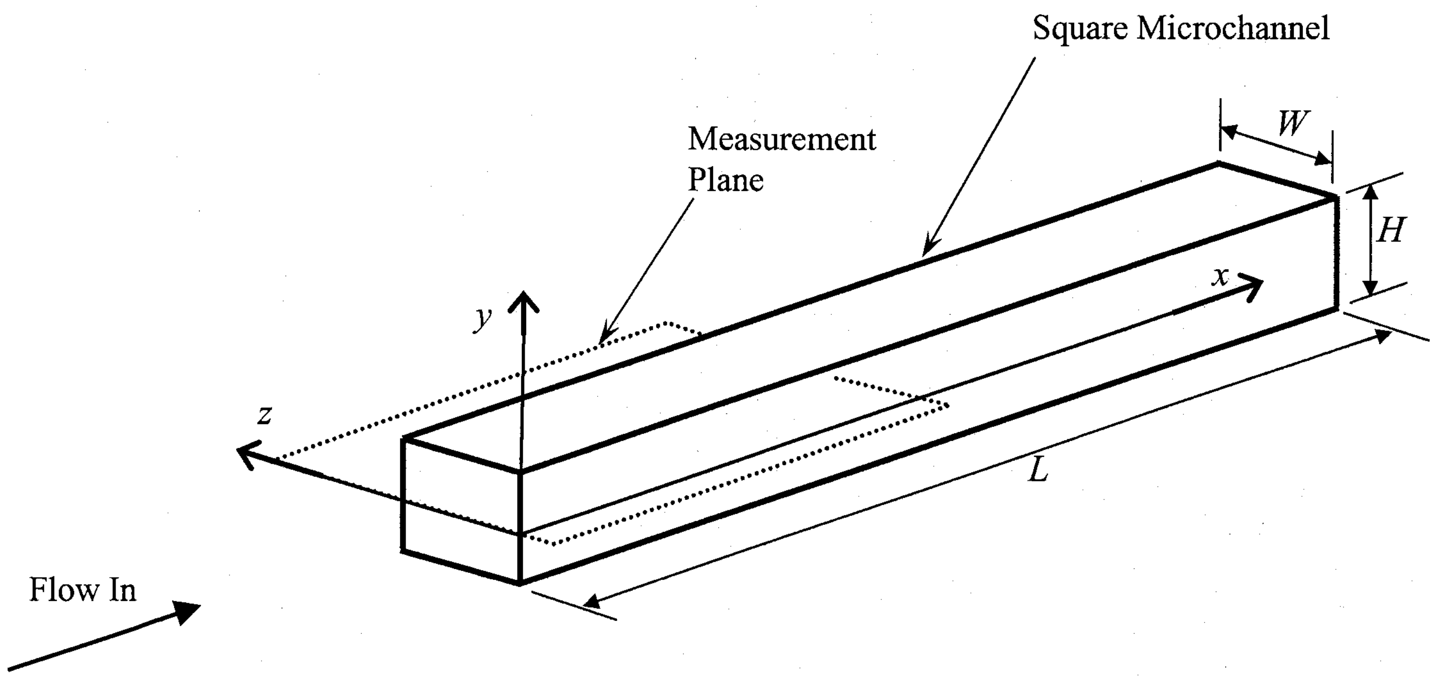


Figure 4.2: Experimental coordinate system used in present investigation

that since the cross sectional aspect ratio is one, the microchannel width, $W$, is identical to the microchannel height, $H$.

Figures 4.3a and 4.3b depict the flow separation effects produced by the corners of a sharp edged inlet. Figure 4.3a shows a schematic of the theoretical flow pattern that is found in the entrance region when the flow enters a channel that is flush with the inlet reservoir, thereby producing sharp edged corners and acting as an orifice. The corners have a physical effect on the flow field thereby producing a vena contracta, which is characterized by the point of minimum area and maximum flow contraction. As the flow contracts just downstream of the channel inlet, flow separation regions form, as shown in Figure 4.3a. Figure 4.3b shows the experimental vector flow field produced using micro-PIV for the 200 μm microchannel at Re = 50. It is possible to see the very low velocity flow in the inlet reservoir accelerating as it approaches the sharp-edged inlet of the microchannel. The inlet corners produce a disturbance on the flow field and force the fluid to contract, producing the vena contracta effect, demonstrating the inability of the flow to turn the 90° sharp corner. The flow then diverges to occupy the entire channel area. This figure is useful in demonstrating both the capability of micro-PIV in terms of visualizing the flow field, as well as a qualitative comparison with the conventional physical mechanism associated with the corner effects on the entrance region.

### 4.2.5 Developing Velocity Profiles

Figures 4.4 (a – d), 4.5 (a – d), and 4.6 (a – d) show the developing velocity profiles at incremental axial locations along the microchannel length, for the 100 μm, 200 μm,

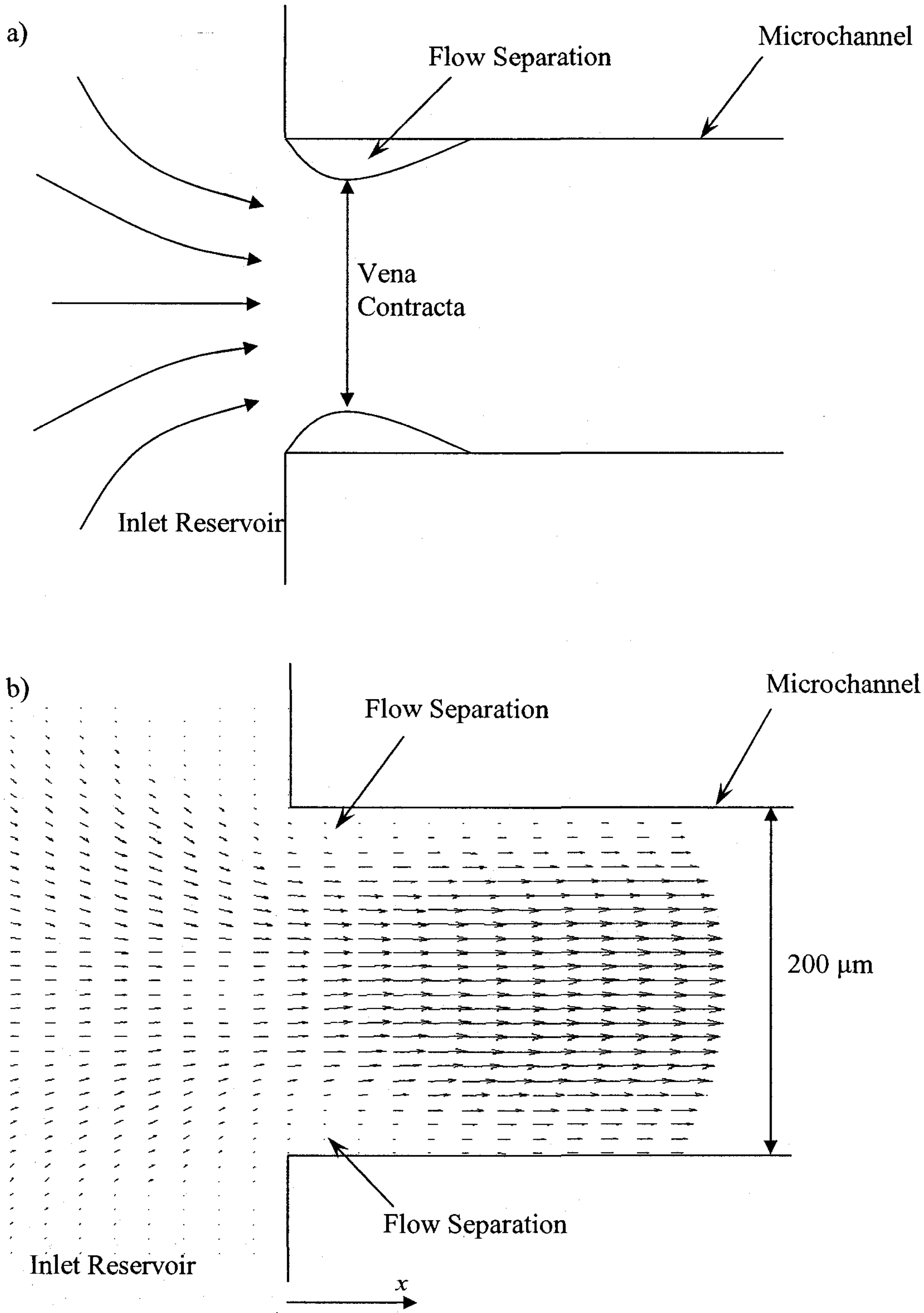


Figure 4.3: Flow separation effects produced by sharp edge corners at the entrance region of the microchannel: (a) Theoretical flow pattern and (b) experimental vector flow field for the 200 μm channel at Re = 50

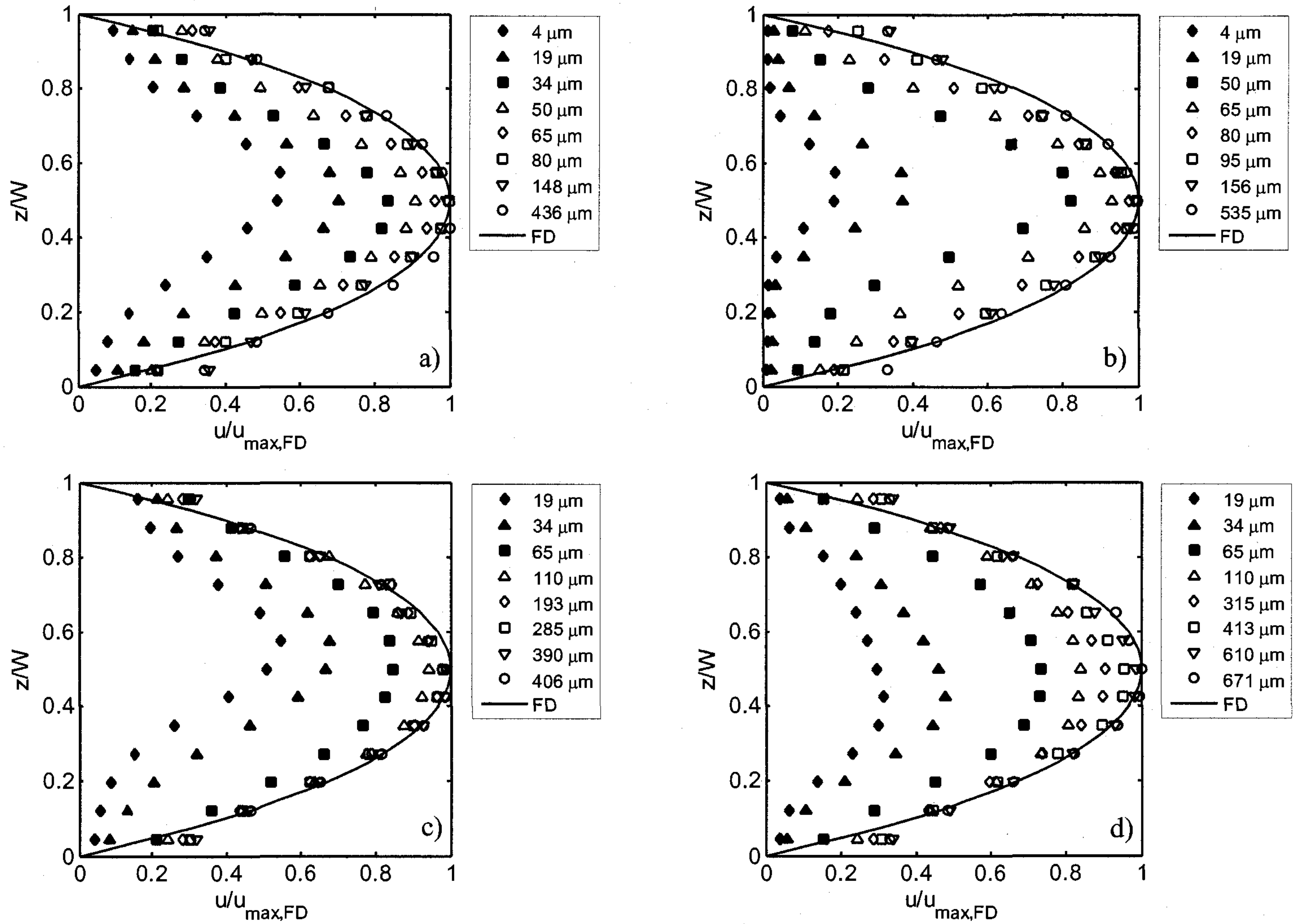


Figure 4.4: Developing velocity profiles for the 100 μm channel at Re of (a) 0.476, (b) 4.76, (c) 50, and (d) 89

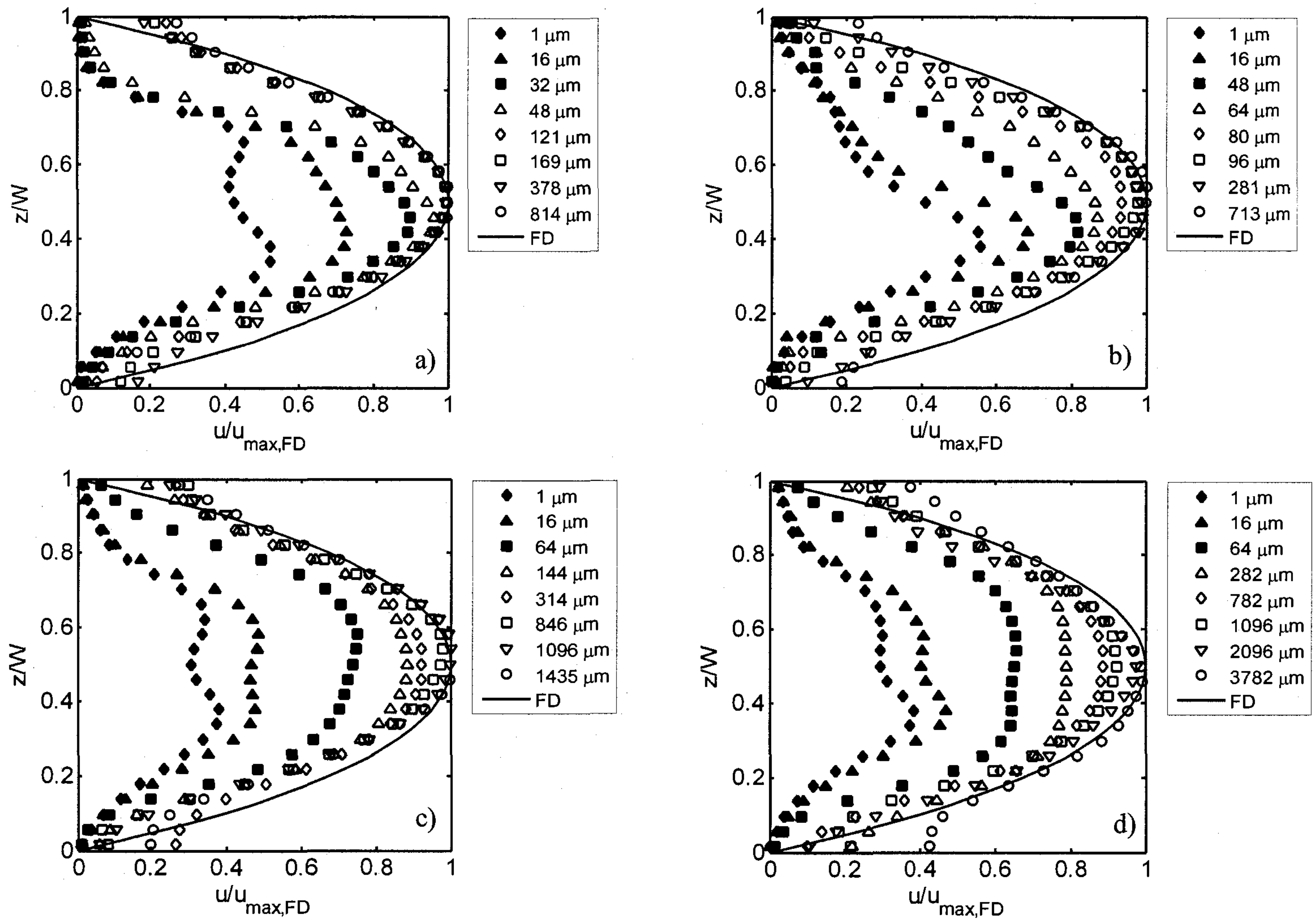


Figure 4.5: Developing velocity profiles for the 200 μm channel at Re of (a) 0.5, (b) 5, (c) 50, and (d) 200

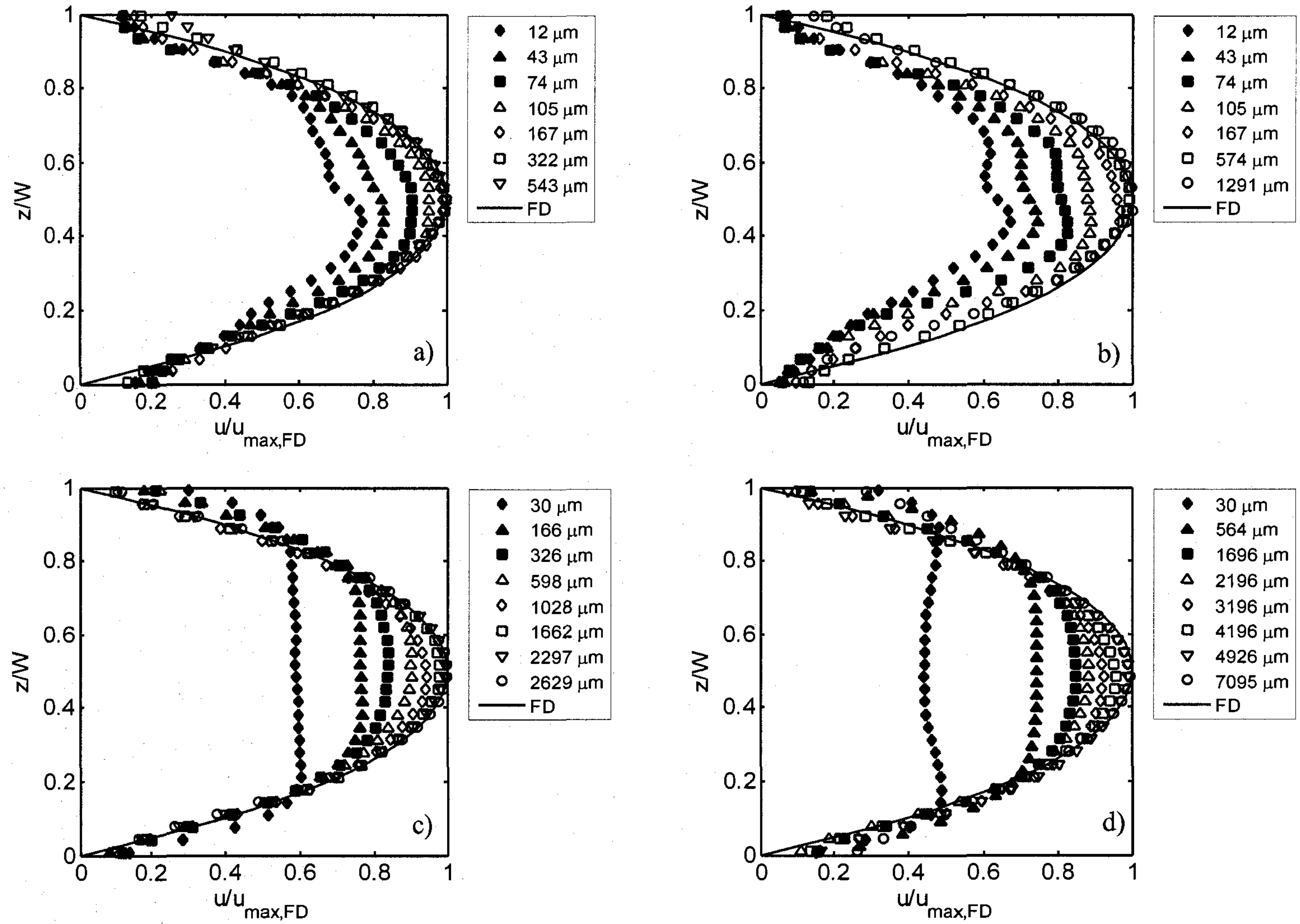


Figure 4.6: Developing velocity profiles for the 500 µm channel at Re of (a) 0.5, (b) 5, (c) 50, and (d) 200

and 500 μm microchannels, respectively. These figures serve to demonstrate the qualitative data obtained using micro-PIV, by observing the developing velocity profiles. The plots are normalized in the spanwise direction ($z$) with the microchannel width ($W$) on the y-axis, and with the theoretical maximum (centerline) fully developed axial velocity on the x-axis ($u/u_{max,\,FD}$). In addition, each plot shows the theoretical fully developed velocity profile with a solid line, given by the 2-D Navier-Stokes equations.

The plots demonstrate the theoretical physical mechanism for fluid from a reservoir entering a channel. As the flow enters the channel, the velocity of the fluid coming in contact with the inner channel walls is immediately reduced to zero. This drag disturbance creates shear waves that propagate from all walls toward the center of the channel. The presence of these shear waves cause the adjacent fluid layers to adjust, while the fluid at the center of the channel that is not yet affected by the disturbance, begins to accelerate in order to satisfy continuity. This process continues along the length of the channel, altering the velocity profile within the channel. Once the entire flow field adjusts to the no-slip boundary condition at the channel walls, the flow is said to be fully developed, and there is minimal change in the velocity profile downstream. As the experimental data shows for the three investigated microchannels, it is evident that there is faster development at lower Re numbers, and far downstream from the inlet, there is very little, if any, change in the experimental profile, indicating fully developed flow and good agreement with the theoretical profile. In addition, the inlet flow path is also influenced by the corner effects at the microchannel inlet, causing a vena contracta.

From Figure 4.4, it can be seen that for the 100 μm channel the profile just downstream from the inlet (at 4 μm (Re = 0.476 and 4.76) or at 19 μm (Re = 50 and 89)) is already in its developing shape, since the center velocity is beginning to accelerate. Failure to observe a more flat profile just downstream of the inlet is probably due to the interrogation area size in the axial direction, where a smaller size may be necessary. In addition, these initial profiles are slightly skewed, and then sequentially level out towards a more uniform shape as the flow develops downstream. This initial skewed inlet flow was also experimentally observed by Lee et al. (2004). The authors explained that it was due to the asymmetric flow path from the reservoir to the channel entrance, which is more evident at smaller channel dimensions. A similar observation can be seen in Figure 4.5 for the 200 μm channel, however the skewness of the inlet profiles is less evident than for the 100 μm channel. In most test cases for this channel size, a certain degree flatness of the early developing profiles can be seen, however there is an indent at the center, possibly caused by the flow contraction effects at the inlet. For the 500 μm channel, from Figure 4.6, a more classical development can be observed, particularly at higher Re numbers of 50 and 200. At these higher Re numbers, a flat profile just downstream from the inlet is evident, where the drag disturbance from the presence of the channel walls has not yet entirely altered the velocity profile. The profiles then sequentially develop downstream. For low Re numbers (0.5 and 5), similar observations can be seen for the early profiles as stated for the 200 μm channel, with slight skewness and flow contraction effects. Qualitatively then, for all three investigated channels, there is good agreement with the physical mechanisms for hydrodynamically developing flow.

### 4.2.6 Centerline Velocity Development

Figures 4.7 (a – d), 4.8 (a – d), and 4.9 (a – d), show the centerline velocity development along the microchannel axial distance for the 100 µm, 200 µm, and 500 µm channels, respectively. The y-axis shows the local centerline velocity ($u_{cl}$) normalized with the theoretical fully developed centerline velocity ($u_{cl,\,FD}$), whereas the x-axis shows the non-dimensional axial distance, normalized with the channel hydraulic diameter, as well as Re ($x/\mathrm{Re}D_h$), to incorporate its effect. The plots show the general hydrodynamic entrance length criterion, which is the location where the local centerline velocity has attained 99% of its fully developed value. It should be emphasized that theoretically speaking, the velocity continually increases and the distance required to attain the fully developed profile is infinitely large (Han, 1960). However, for engineering applications, the 99% criterion is suitable in defining the entrance length in a channel.

From all plots, a common trend can be seen; it is evident that there is a definite increase in the centerline velocity, which levels out toward a somewhat constant value at $u_{cl}/u_{cl,\,FD} \sim 0.99$. For the 100 µm channel, from Figures 4.7c and 4.8d, it can be seen that at higher Re numbers of 50 and 89, both trends reach $u_{cl}/u_{cl,\,FD} \sim 0.99$ at relatively the same non-dimensional axial distance, between 0.065 and 0.085. A similar observation can be seen from Figures 4.8c and 4.8d for the 200 µm channel, and from Figures 4.9c and 4.9d for the 500 µm channel, at Re numbers of 50 and 200, respectively. Regarding the plots at lower Re numbers of 0.476 and 4.76 for the 100 µm channel (Figures 4.7a and 4.7b), the non-dimensional axial distance at which the data reaches $u_{cl}/u_{cl,\,FD} \sim 0.99$ is observed to be rather high, at about 0.17 for Re = 4.76, and increases to about 1.7 for Re = 0.476. Similarly for the 200 µm channel

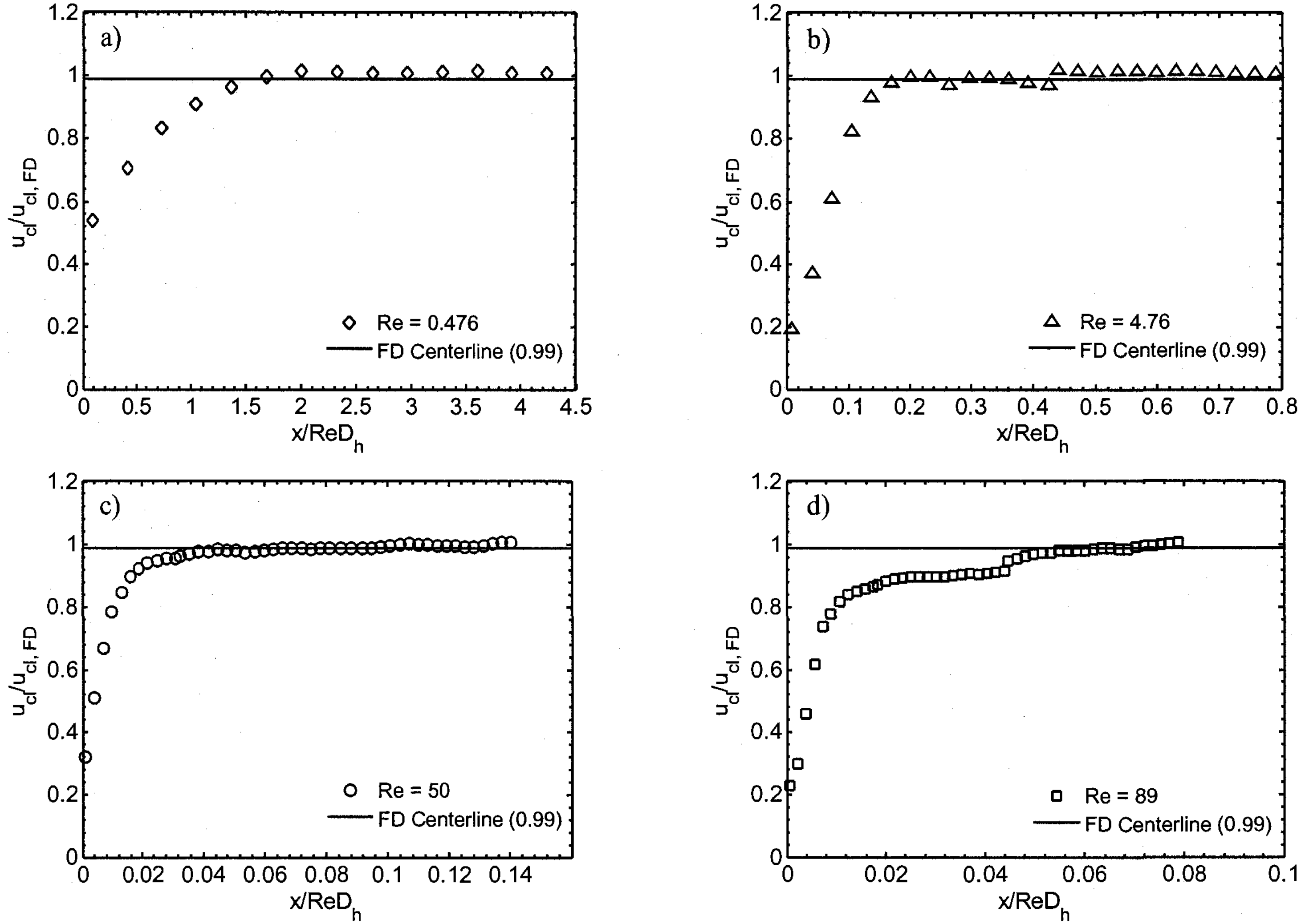


Figure 4.7: Centerline velocity development for the 100 μm channel at Re of (a) 0.476, (b) 4.76, (c) 50, and (d) 89

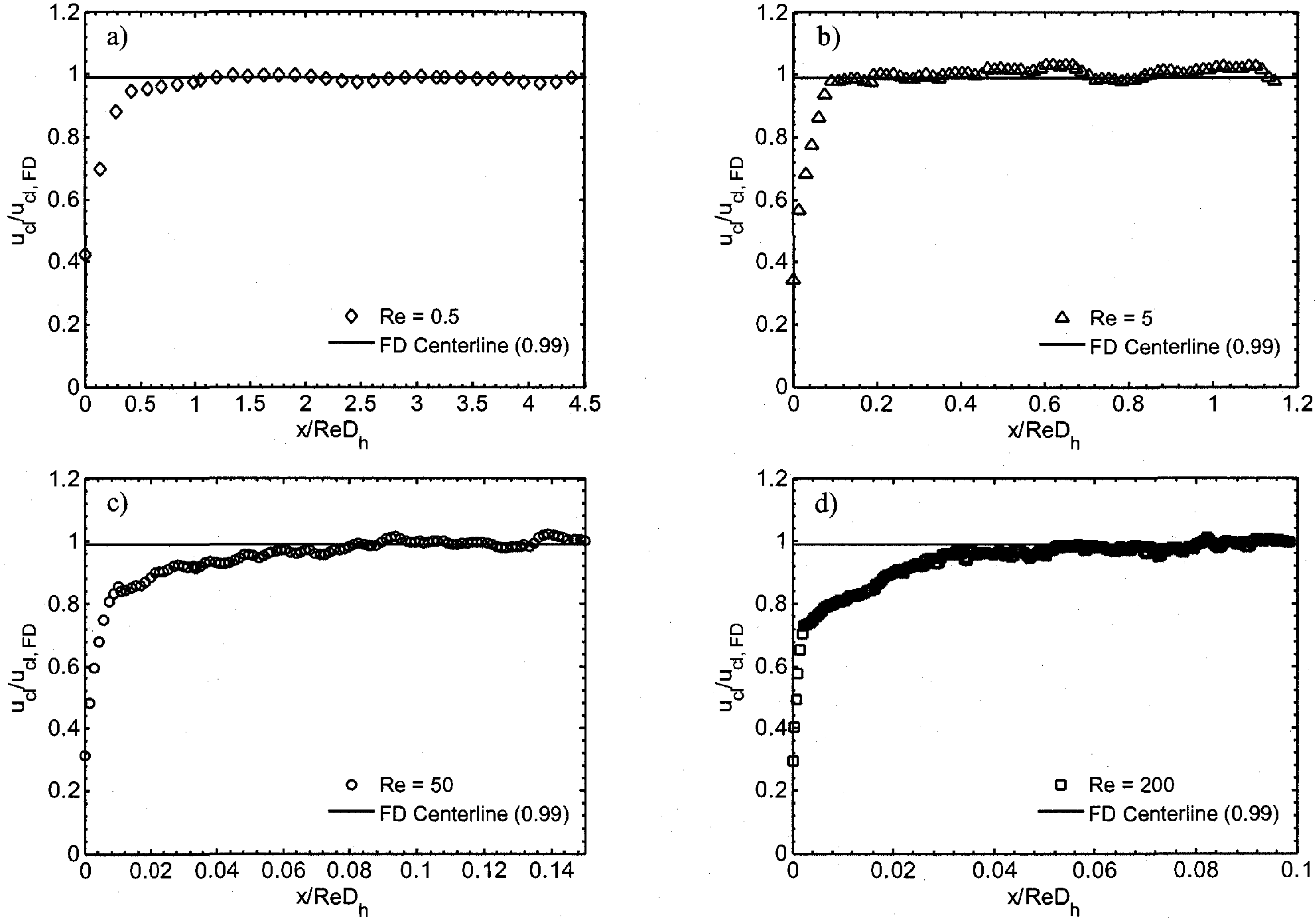


Figure 4.8: Centerline velocity development for the 200 μm channel at Re of (a) 0.5, (b) 5, (c) 50, and (d) 200

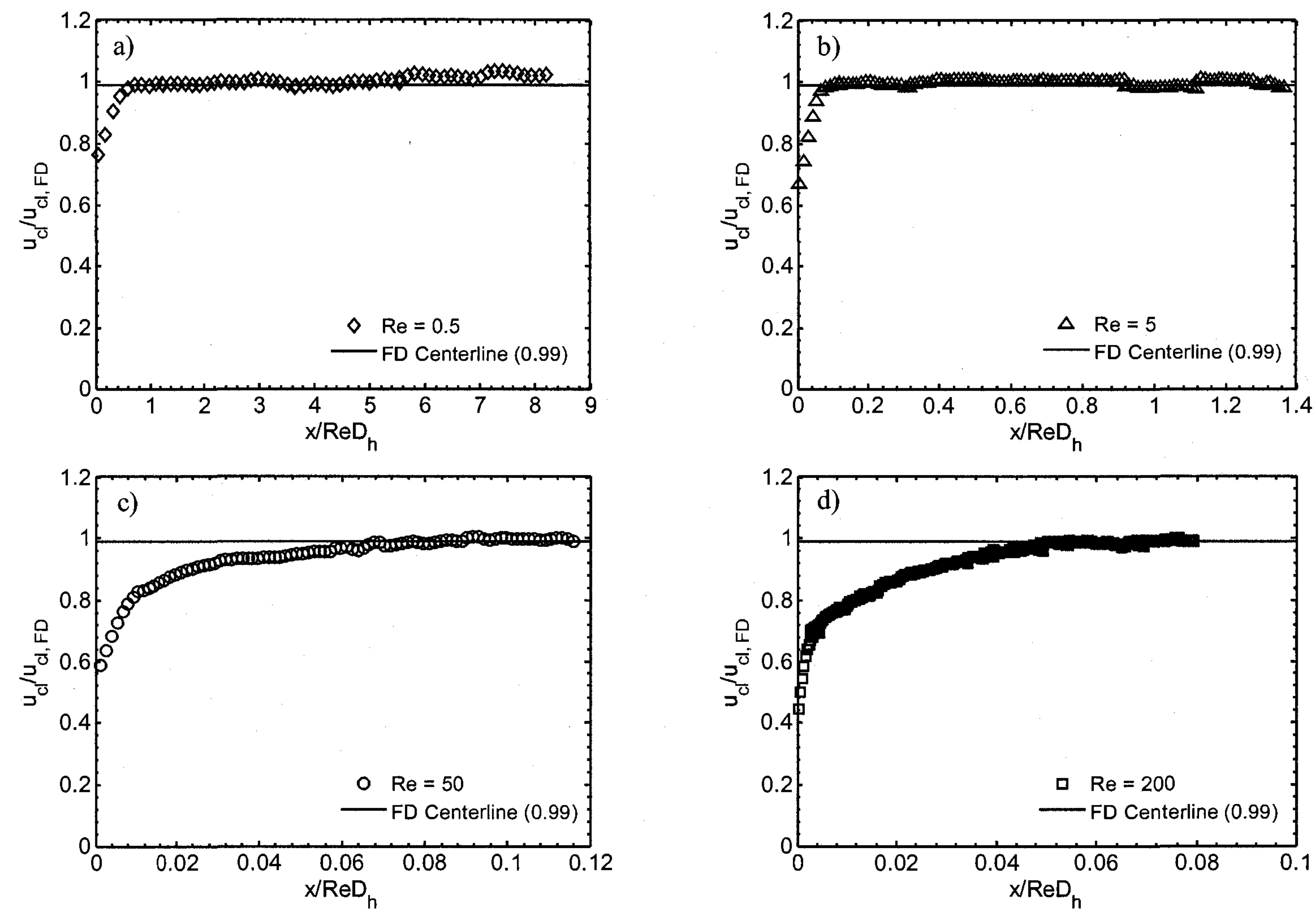


Figure 4.9: Centerline velocity development for the 500 μm channel at Re of (a) 0.5, (b) 5, (c) 50, and (d) 200

(Figures 4.8a and 4.8b), at Re = 0.5 and Re = 5, the normalized axial distances at which fully developed flow (0.99) is reached are high at 0.19 and 1.2, respectively. A similar observation can be made for the 500 µm channel at Re = 0.5 and Re = 5 (Figures 4.9a and 4.9b), where the axial distance is roughly 0.7. With these results, it can be seen that there is little influence of dimensional scaling for the three investigated channels, but a higher dependence of the entrance length on the Reynolds number, particularly at low values.

One can conclude that, similar to Lee et al. (2004)'s statement, since the channel bottom wall and reservoir bottom wall lie on the same plane, the inlet velocity profile is not completely uniform, and because of this, as stated by Shah and London (1978) and Atkinson et al. (1969), the entrance length at higher Re numbers are less affected by the inlet velocity profile. However, for lower Re numbers, as stated by Vrentas et al. (1966), there is a high dependence of the entrance length on the inlet velocity profile, due to the axial diffusion of vorticity. Vrentas et al. (1966) numerically showed the effect of vorticity for a pipe with an upstream inlet reservoir. The fluid in the inlet reservoir, initially free of vorticity, develops a vorticity field as it enters the pipe. This vorticity is generated at the walls of the pipe, and then transmitted from the walls to the fluid by convection and diffusion. The authors found that the vorticity transfer from the walls to the fluid is influenced by the Re number. At very low Re numbers, vorticity appears in the reservoir causing some flow development upstream from the tube entrance, and hence not a uniform velocity profile at the inlet. The degree of centerline velocity profile development upstream from the channel inlet increases as Re is decreased, particularly below 50 (Re < 50) which will have an effect on the entrance length.

This can be the case for the lower Re numbers of 0.5 and 5 for the three investigated channels.

### 4.2.7 Hydrodynamic Entrance Length

Figure 4.10 depicts the entrance length ($Le/D_h$) for the 100 µm, 200 µm, and 500 µm channels, versus the Re number, in logarithmic scale in order to amplify the effects at low Re numbers. There are four data points for the 100 µm channel (Re = 0.476, 4.76, 50, 89), four data points for the 200 µm channel (Re = 0.5, 5, 50, 200), and four data points for the 500 µm channel (Re = 0.5, 5, 50, 200). The entrance length was taken from the data collected in Figures 4.7, 4.8, and 4.9, for the 100 µm, 200 µm, and 500 µm channels, respectively, and it is the length (Le) at which $u_{cl}/u_{cl,\ FD}$ ~ 0.99. Regarding this criterion experimentally, the entrance length was taken as the length at which $u_{cl}/u_{cl,\ FD}$ remained relatively steady at 0.99 or crossed 0.99, depending on the trend of data. To analyze any effect of scaling, the overlapping range of data points for the investigated channels was also compared. From Figure 4.10, it can be seen that for high Re numbers (Re > 10) there is no influence of dimensional scaling. However, it can be seen that at lower Re numbers (Re < 10), there is a minor discrepancy between the entrance lengths of the 100 µm and 200 µm channels, compared with that of the 500 µm channel. This can lead to a slight dimensional scaling effect at low Re numbers for the 500 µm channel. In addition, the experimental data is compared with conventional entrance length correlations.

The numerical correlations given by Han (1960) and Wiginton and Dalton (1970) are linear correlations where the entrance length is proportional to the Reynolds

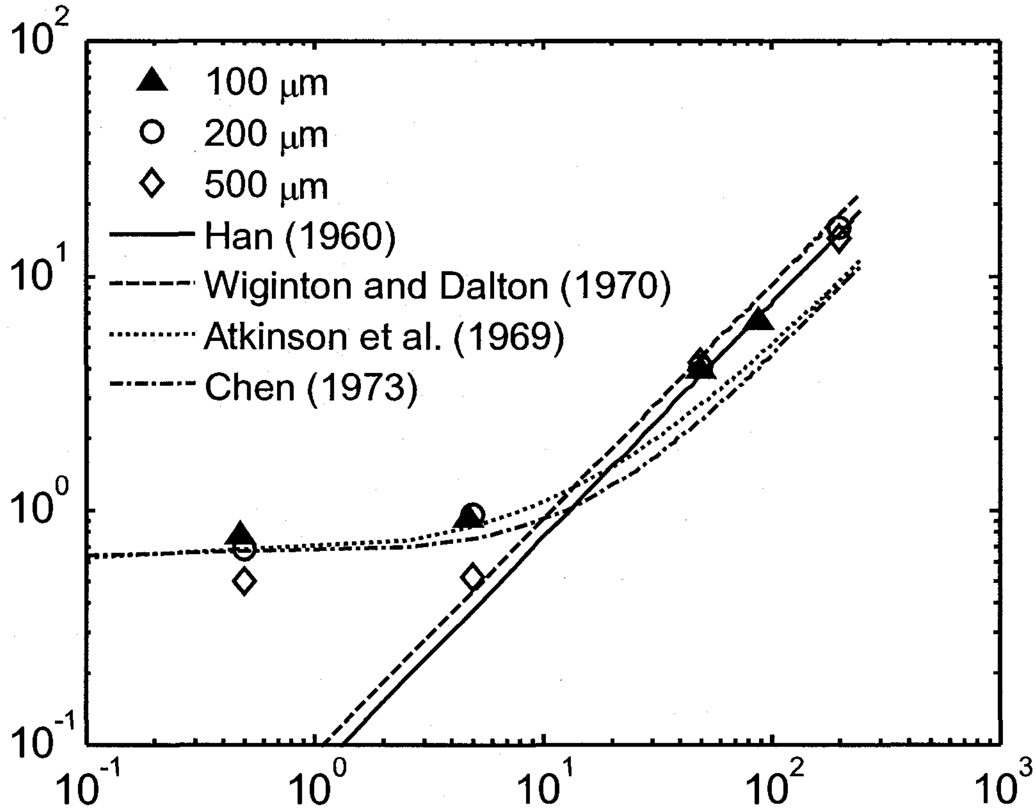


Figure 4.10: Entrance length comparison between present data and conventional correlations

number by some constant, depending on the cross-sectional aspect ratio. For an aspect ratio of one, Han (1960)'s correlation is given by,

$$\frac{L_e}{D_h} = 0.0752\,\mathrm{Re}, \tag{4.2}$$

whereas Wiginton and Dalton (1970)'s correlation, for an aspect ratio of one, is given by,

$$\frac{L_e}{D_h} = 0.09\,\mathrm{Re}\ . \tag{4.3}$$

According to Shah and London (1978), the equation given by Wiginton and Dalton (1970)'s model is more accurate, whereas that of Han (1960) is low since he calculated rapid flow development. From Figure 4.10, it can be seen that at high Re numbers (Re > 10), there is good agreement between the experimental data and the correlations given by Han (1960) and Wiginton and Dalton (1970). However, at low Re numbers, below 10, there is not good agreement. This is due to the fact that since these correlations are linear, and at very low Re numbers, $L_e/D_h$ goes towards zero. This may have little effect in conventional ducts where modest Reynolds numbers are applied. However, at the microscale, very low Reynolds numbers can be practically applied, where there indeed exists a finite value for the entrance length. This is apparent from the data, where at low Re numbers (i.e. Re = 0.5 or 5), there is a definite entrance length value.

For low Re numbers one can consider entrance length correlations given by Atkinson et al. (1969) and Chen (1973), both for parallel plates. Atkinson et al. (1969)'s parallel plate correlation is given by,

$$\frac{L_e}{D_h} = 0.625 + 0.044\,\text{Re}, \tag{4.4}$$

whereas Chen (1973)'s correlation given for parallel plates is given by,

$$\frac{L_e}{D_h} = \frac{0.63}{0.035\,\text{Re}+1} + 0.044\,\text{Re}. \tag{4.5}$$

It should be noted in Eqs. (4.4) and (4.5) the hydraulic diameter of a square channel ($D_h = W = H$) is used in the definitions of Re and $D_h$. Looking at these two above correlations, when Re is high, a linear curve is depicted. However, when Re is low, both correlations level out to a constant value and are independent of Re. This is shown in Figure 4.10. Comparison of the present experimental data with these two parallel plate correlations reveals very good agreement for the 100 µm and 200 µm channels, particularly at low Re numbers (0.5 an 5). Regarding the 500 µm channel, adequate agreement is found at lower Reynolds numbers; however the error is greater than for the 100 µm and 200 µm channels (a possible scaling effect). At the higher Re range (>10) there is adequate agreement for all investigated channels, however better agreement was found with comparison to the conventional correlations for ducts, notably that of Han (1960). From the present experimental data, these parallel plate correlations are better suited for the prediction of the entrance length in microchannels at very low Reynolds numbers (<10).

### 4.2.8 Entrance Length Correlations

In light of the previous discussion, with comparison of the present entrance length experimental data with conventional correlations, new entrance length correlations are proposed. These new correlations are applicable in predicting the entrance length in microchannels and will aid in the design of future microfluidic devices. As was seen in Figure 4.10, there was very good agreement at high Reynolds (Re > 10) numbers with conventional correlations for ducts, notably that of Han (1960) from Eq. (4.2). For lower Re numbers (Re < 10), there was very good agreement with parallel plate correlations, given by Atkinson et al. (1969) and Chen (1973) from Eqs. (4.4) and (4.5). These two entrance length parallel plate correlations were established by numerically solving for the creeping flow solution at low Re numbers, and adding the result to a high Re number asymptote provided by Bodia and Osterle (1961), which is 0.044Re. However, from Figure 4.10, it can be seen that at higher Re numbers there is poor agreement with these parallel plate correlations, but better agreement with conventional duct correlations, particularly that of Han (1960).

Applying a similar method and form of equation as Chen (1973), but replace the high Reynolds number asymptote with Han (1960)'s correlation, the following empirical correlation is obtained,

$$\frac{L_e}{D_h} = \frac{0.63}{0.035\,\mathrm{Re}+1} + 0.0752\,\mathrm{Re}\,. \tag{4.6}$$

Figure 4.11a shows Eq. (4.6) plotted along with the present experimental entrance length data for the 100 μm and 200 μm channels. From the figure, excellent agreement can be seen over the whole range on Re numbers, and quantitatively, from Figure 4.11b, the correlation fits all the data to within 15%. This correlation however, does not fit well with the experimental data obtained for the 500 μm

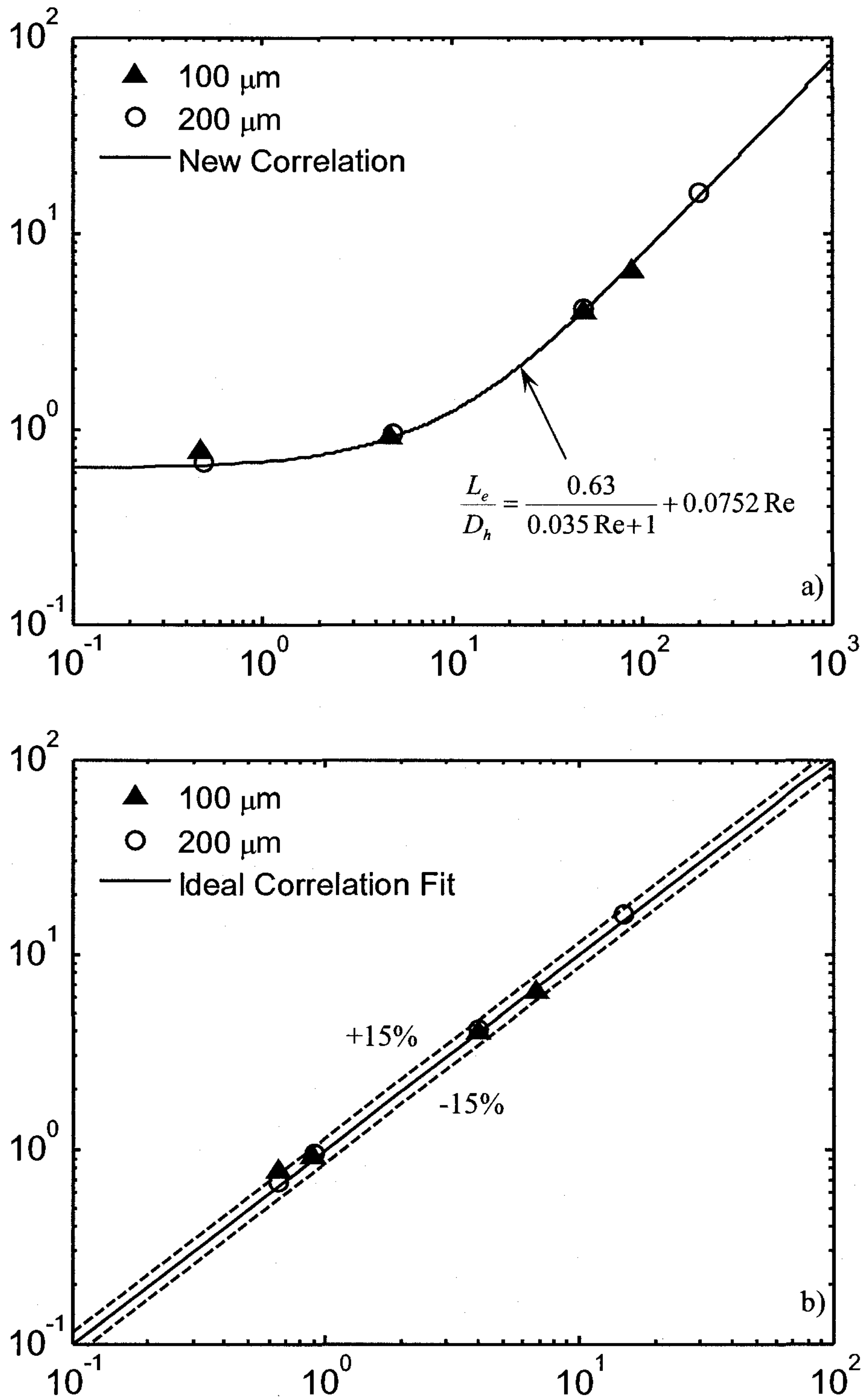


Figure 4.11: Proposed entrance length correlation for square microchannels below 500 μm with present experimental data of the 100 μm and 200 μm channels and the error in the fit

channel. Therefore, it can be said that Eq. (4.6) is well suited in predicting the entrance length in square microchannels ($H/W = 1$) for hydraulic diameters below 500 μm, over a wide range of laminar Reynolds numbers from 0.5 to 1000.

In finding an empirical correlation that fits all the present experimental data for the 100 μm, 200 μm, and 500 μm channels, another correlation is developed. Once again, an equation in the form of Chen (1973)'s correlation is applied. From Figure 4.10, it can be seen that at high Re numbers (Re > 10), all present experimental data fits Han (1960)'s correlation very well, therefore once again it will be used for the high Reynolds number asymptote. Applying a curve fit in the form of Chen (1973)'s correlation at the low Re numbers, the following correlation is found,

$$\frac{L_e}{D_h} = \frac{0.6}{0.14\,\mathrm{Re}+1} + 0.0752\,\mathrm{Re}. \tag{4.7}$$

Figure 4.12a shows Eq. (4.7) plotted with the present experimental data (100 μm, 200 μm, and 500 μm channels) along with conventional experimental data produced from Goldstein and Kreid (1967) for a square duct within a Re range of 69 to 387. These authors investigated flow development using a laser-Doppler flowmeter in a square duct with a hydraulic diameter of 1 cm, as shown in Table 4.2. From Figure 4.12b, it can be seen that the experimental data fits the empirical correlation to within 30%. Equation (4.7) shows to fit well with all the data over the whole range of Re numbers, and can be used as a general entrance length correlation for channels of square cross-section ($H/W = 1$) at both the micro and macro scales.

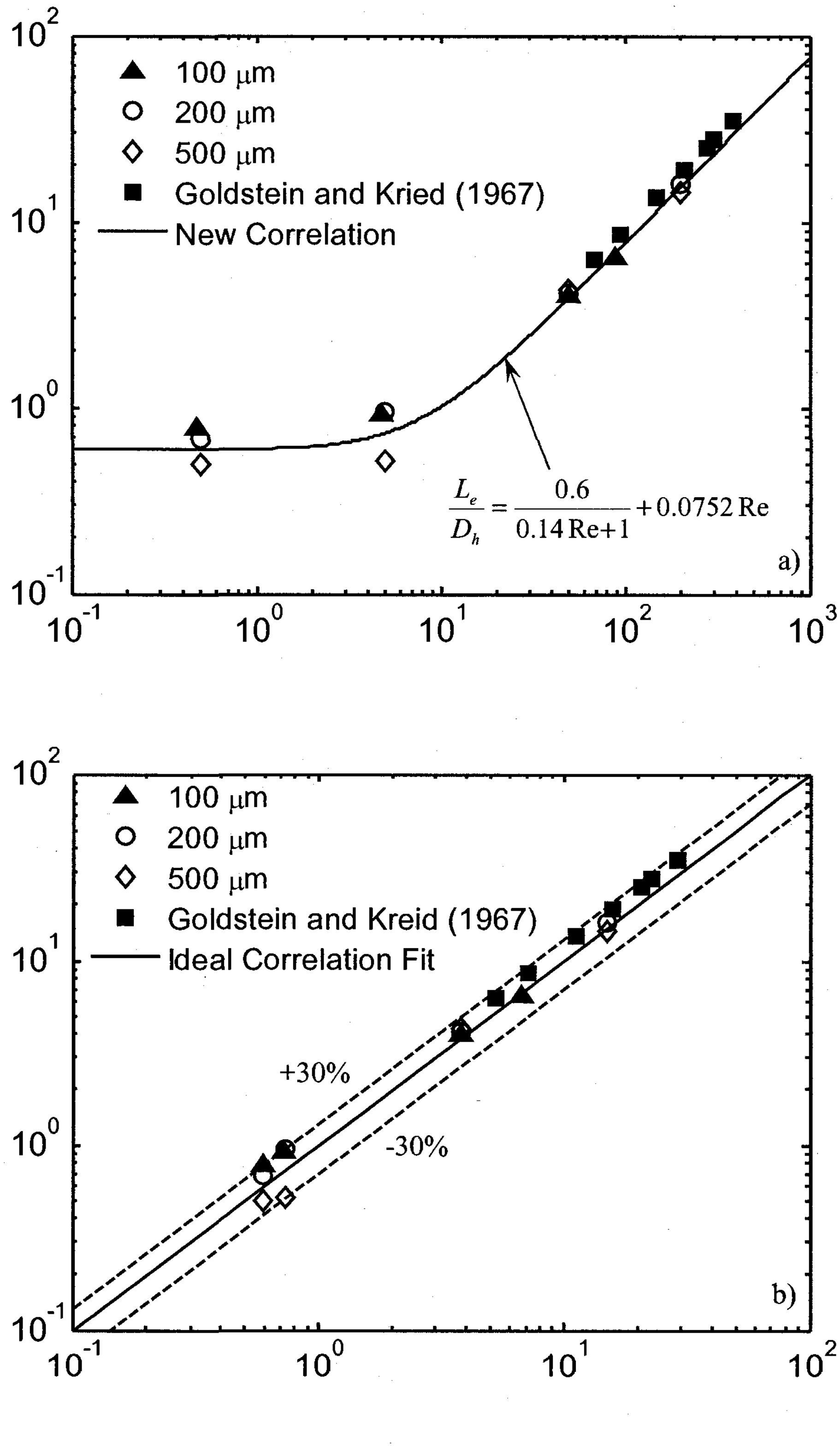


Figure 4.12: Proposed entrance length correlation for square channels at the micro and macro scales and the error in the fit

Table 4.2: Experimental entrance length geometries used in previous studies

| **Authors** | **$D_h$** | ***H/W*** |
|---|---|---|
| Goldstein and Kreid (1967) | 1 cm | 1 |
| Muchnik et al. (1973) | 1.33 cm | 2 |
| Lee et al. (2002) | 380 μm | 2.65 |
| Lee et al. (2004) – 1 | 370 μm | 2.75 |
| Lee et al. (2004) – 2 | 56.4 μm | 0.37 |
| Hao et al. (2005) | 237 μm | Trapezoidal |

Theoretically, the hydrodynamic entrance length of a channel is dependent on its cross-sectional aspect ratio ($H/W$). This is shown in analytical studies by Han (1960), Fleming and Sparrow (1969), and Wiginton and Dalton (1970). This is due to the proximity of the walls relative to the internal flow field, the drag disturbance they impose, and the shear waves they cause to propagate toward the center of the channel. Therefore the height and width of the solid walls of a channel, and their relative size to each other, have a great influence on the flow development. However, since there are not many experimental works associated with the hydrodynamic entrance region in micro geometries, a correlation applicable to microchannels regardless of aspect ratio would be useful where practical applications are concerned.

In light of this, previous experimental works for the hydrodynamic entrance length in microchannels (Lee et al., 2002; Lee et al., 2004; Hao et al., 2005), in addition to the present experimental data, are used in developing an empirical correlation. Also, conventional experimental data for the entrance length in ducts given by Goldstein and Kreid (1967) and Muchnik et al. (1973) is included to broaden the analysis. Table 4.2 shows the geometric parameters associated with the previous experimental data. Also, it should be noted that where conventional sized ducts are concerned, all available experimental data is above a Reynolds number of 10, due to reasons of practicality at the macroscale. However, where microchannels are concerned, there is available experimental data well below Re = 10, since these low Reynolds numbers are applicable at the microscale, primarily due to the pressure drop imposed at higher Reynolds numbers. In order to determine an empirical correlation to fit the data, an equation in the form of Chen (1973) is once again applied; however both the high Reynolds number asymptote, as well as the low Reynolds number solution are found using a curve fit. The following correlation is obtained,

$$\frac{L_e}{D_h} = \frac{0.55}{0.13\mathrm{Re}+1} + 0.065\mathrm{Re}. \tag{4.8}$$

Figure 4.13a depicts Eq. (4.8) plotted with the aforementioned entrance length experimental data for ducts and microchannels. The figure also shows that the conventional experimental data given by Muchnik et al. (1973), at higher Re numbers (Re > 10), has good agreement between the present experimental data, where their aspect ratio (*H/W*) was 2. In addition, the experimental data given by Hao et al. (2005) also has very good agreement with the present data at high Re values, where interestingly their microchannels had a trapezoidal cross-section. As shown in Figure 4.13b, the error between the proposed correlation and the experimental data is high, where the correlation fits majority of the data to within 60%. However, the high error results from the experimental data for the entrance length in microchannels from Lee et al. (2002) and Lee et al. (2004), where a high error can be expected due to the cross-sectional aspect ratio of the microchannels and pre-development of the flow prior to entering the microchannel. Nonetheless, this proposed correlation can be used as a general correlation for the entrance length in microchannels for aspect ratios below 3 ($H/W < 3$) and possibly trapezoidal microchannels, as shown by Hao et al. (2005)'s data.

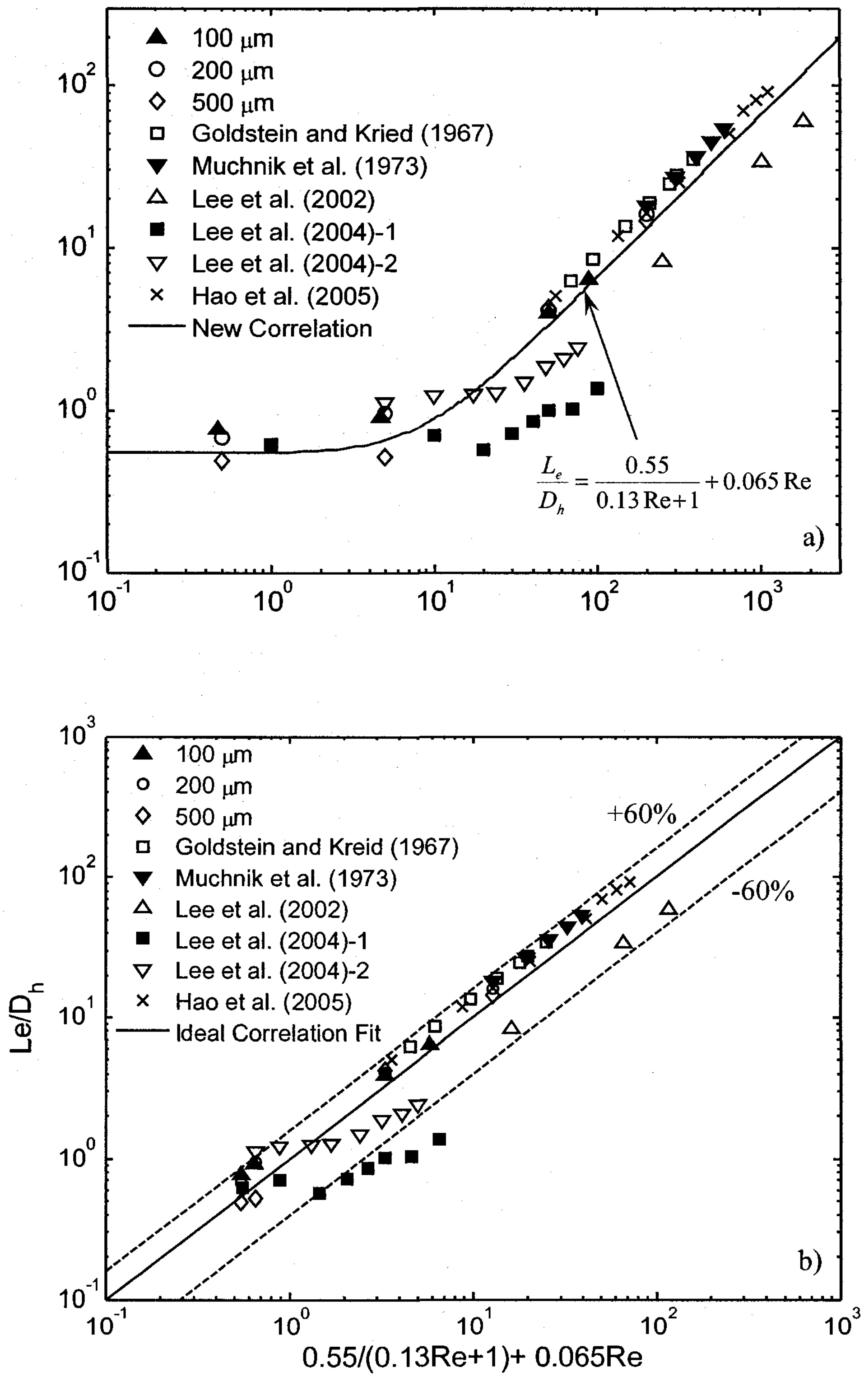


Figure 4.13: Proposed general entrance length correlation for microchannels, independent of cross-sectional aspect ratio, and the error in the fit

## 4.3 Turbulent Flow

Over the past century, numerous experimental studies were carried out in conventionally-sized pipes and ducts for hydrodynamic developing turbulent flow, as was outlined in Chapter 2. Notable experimental studies by groups such as Barbin and Jones (1963), Filippov (1982), Lien et al. (2004), and Doherty et al. (2007), emphasize that there is large scatter in results from study to study. Unlike laminar flow, turbulent flow is characterized by disorder and randomness. There still remain questions regarding the length required for turbulent flow to become fully developed, and the definition of fully developed turbulent flow in itself; whether analysis of the mean velocity profiles are sufficient to constitute the flow as being developed, or if steadiness in the flow structures, Reynolds stresses, and turbulence intensities constitute the flow as being fully developed.

As mentioned, there is no fundamental experimental data available for hydrodynamically developing turbulent flow (Re > 4000) in microchannels. The prime reasons for this are the practicality involved in forcing turbulent flow inside microchannels, where the hydrodynamic resistance is typically increased as hydraulic diameters move towards the microscale range, and due to experimental methods in analyzing turbulent flow in micro geometries. However, due to the lack of fundamental experimental data, an investigation into developing turbulent flow in microchannels was attempted using micro-PIV.

The turbulent entrance region experiments were attempted using the same test sections as those for laminar flow. Three test sections, one with a 100 µm channel width, one with a 200 µm channel width, and another with a 500 µm channel width, were considered, as shown in Figure 4.1. Each test section has a square cross-section microchannel with a very large inlet reservoir relative to microchannel size, to carry out fundamental hydrodynamic entrance region studies at the microscale. With respect to the expected pressure drop increase for turbulent flow, particularly at the dimensional scale of the present microchannels, the 100 μm test section was not attempted. From the laminar flow experiments, the highest Reynolds number achieved in the 100 μm channel, with the syringe pump operating in withdrawal mode, was Re = 89. Therefore, it was conveyed that the pumping power of the syringe pump, particularly in withdrawal mode, was insufficient to achieve turbulent flow in the 100 μm channel. Instead, only the 200 μm and 500 μm test sections were considered.

At first, flowrate calculations were carried out to determine the required flowrates to obtain turbulence (Re > 4000), and verify whether the syringe pump is capable in providing the necessary flowrates. The maximum possible flowrate from the syringe pump is 102 ml/min, due to the limit on the syringe size was 60 cc. However, this limit is for infusion mode and it was observed that the limit is much lower when withdrawal mode is applied. Figure 4.14 shows the capability of the syringe pump plotted with the possible flowrates for specific transition and turbulent Re numbers, using Eq. (4.1). From the figure, it can be seen that the flowrate capabilities of the syringe pump are insufficient to provide fully turbulent flow in the 500 μm channel, where the maximum Re number that can be achieved is Re~3000. However, in terms of possible flowrate, the syringe pump is theoretically capable to provide the required flowrate to obtain turbulence in the 200 μm channel, up to Re~7600. Therefore, only the 200 μm test section was attempted for turbulence experiments.

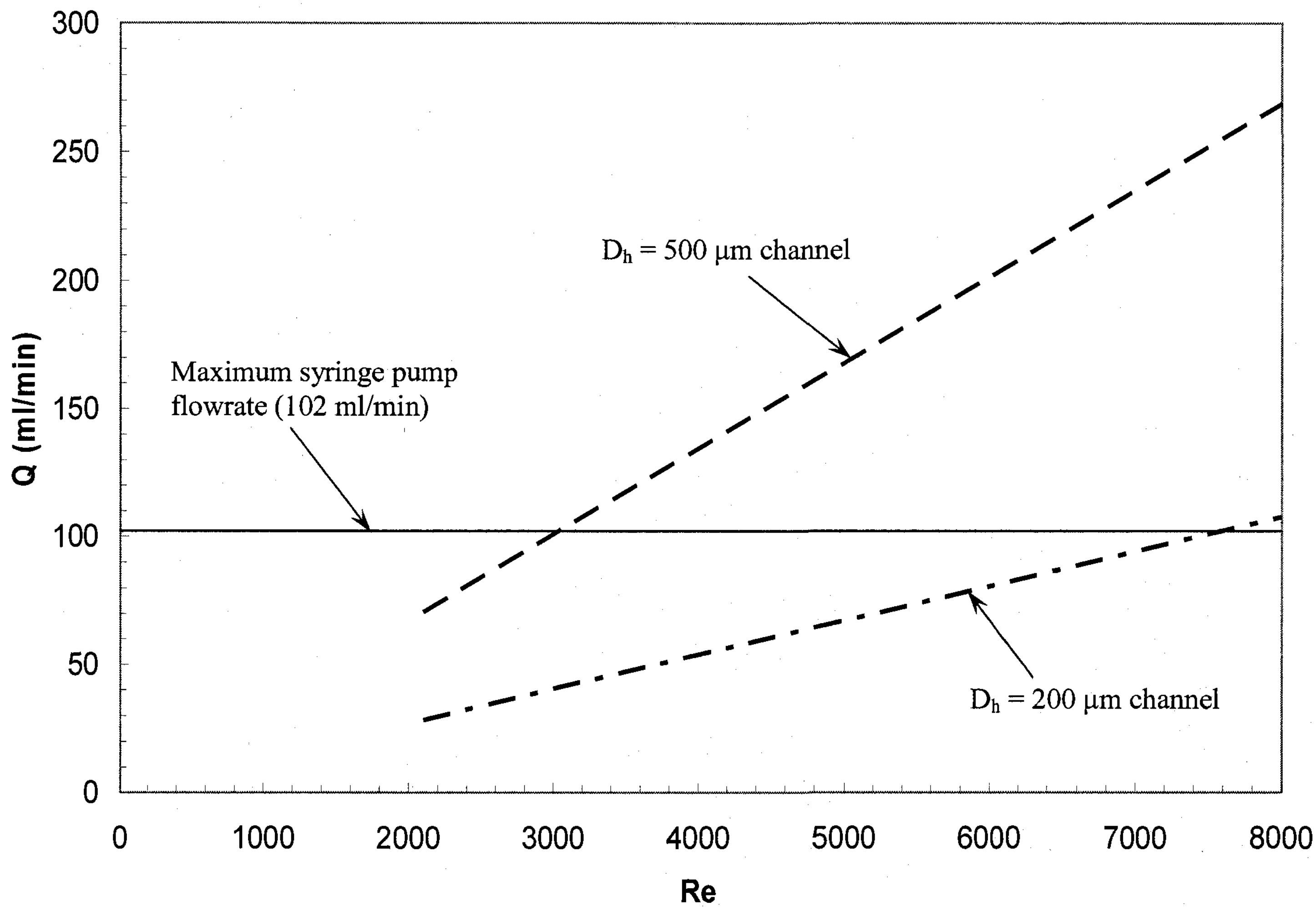


Figure 4.14: Flowrate capability of the syringe pump and its applicability to turbulent flow in the 200 μm and 500 μm microchannels

Since the rated flowrate of the syringe pump covered the flowrate range to achieve turbulence in the 200 μm channel, this test section was used in micro-PIV experiments to attempt to obtain turbulent entrance region data. With the syringe pump operating in withdrawal mode, after numerous trials, the maximum possible flowrate achieved was ~12 ml/min, which corresponds to Re~870, which is laminar. This was due to the immense pressure drop in the channel, and it was observed that with the syringe pulling out, a vacuum was created within the syringe. Therefore there was actually a limit of maximum flowrate in withdrawal mode. Another trial was attempted with the syringe pump operating in infusion mode, simply to verify the maximum flowrate possible through the microchannel. It was found that a Re number above 3500 was possible, however due to the high pressure drop and force required to push the flow through the channel, the worm gear in the pump was beginning to skip, potentially damaging the stepper motor.

To get an idea of the pressure drop involved, the theoretical turbulent pressure drop was plotted against the Reynolds number for both the 200 μm and 500 μm channels, as shown in Figure 4.15. The pressure drop was calculated using the Blasius formula to calculate the turbulent Darcy friction factor ($f_{turb}$) as,

$$f_{turb} = \frac{0.316}{\mathrm{Re}^{1/4}} . \tag{4.9}$$

The Blasius formula, found in 1913 for smooth pipes, is a conventional empirical solution acquired through a dimensional analysis. It is applicable to predict the friction factor and hence pressure drop in smooth pipes for turbulent flow over a Reynolds range of $4000 < \mathrm{Re} < 10^5$ (White, 1991). Although the present test sections

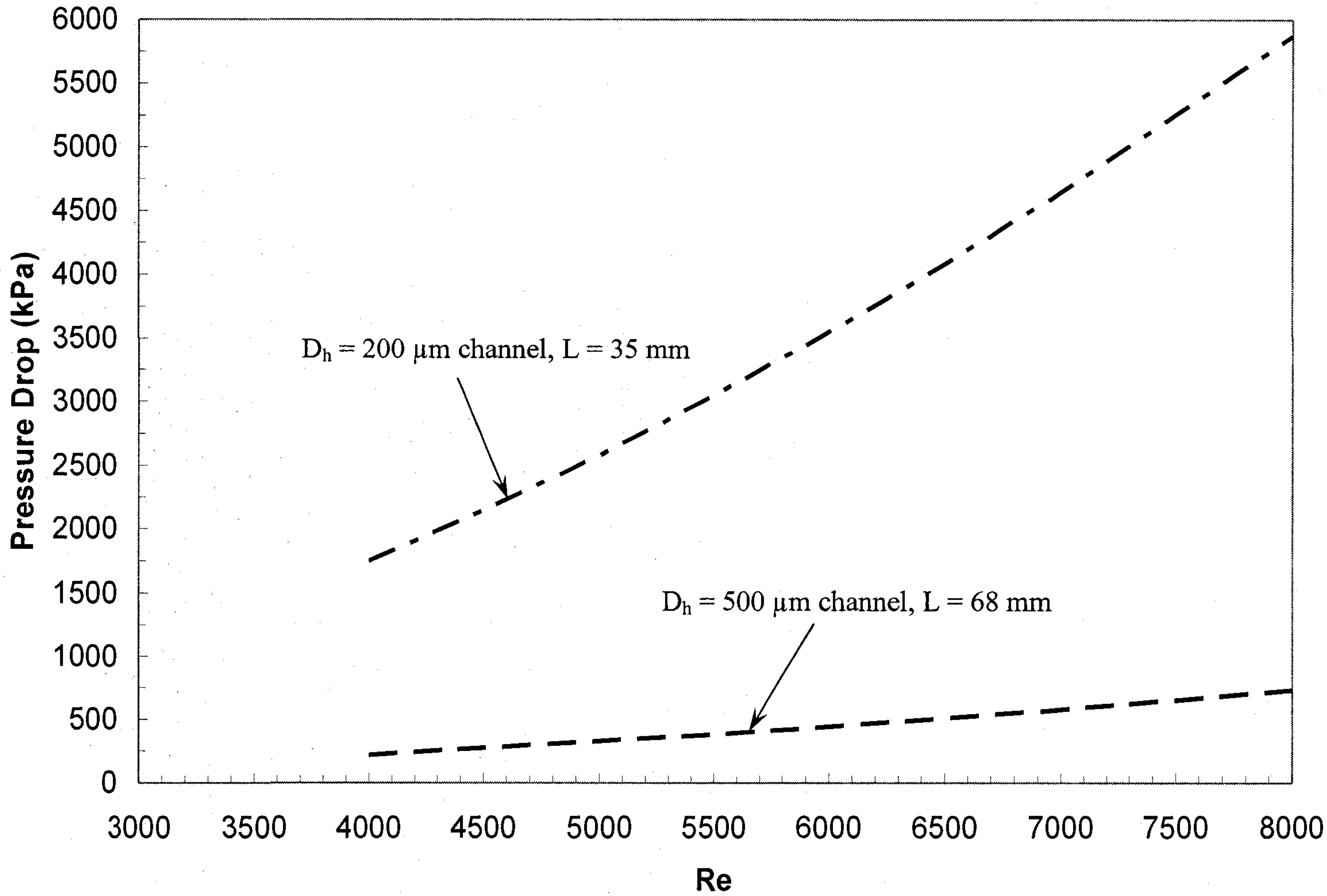


Figure 4.15: Empirical turbulent pressure drop in the 200 µm and 500 µm channels using the Blasius formula

have square cross-section channels, the Blasius equation has been used simply to get a sense of the pressure drop involved.

Looking at the curve for the 200 µm channel in Figure 4.15, the pressure drop is immense, even at low turbulent Re numbers of 4000 where the pressure drop is about 1750 kPa. As the Re number increases, it can be seen that the pressure drop increases tremendously to impractical values. Due to this, it is fundamentally unfeasible, particularly with the syringe pump, to achieve turbulent flow in the 200 µm channel. As a means for comparison, the theoretical pressure drop in the 500 µm channel was also plotted. It can be seen that the pressure drop is not as great as in the 200 µm channel, as expected. With a pressure drop of about 250 kPa at Re~4000, turbulence could be fundamentally possible in the 500 µm channel. However, as stated previously, the syringe pump is limited to flowrates which correspond to Re~3000, which limits the experimental practicality.

It can be asked why another pump was not chosen as opposed to a syringe pump, such as a gear pump. For a typical pump, such as a gear pump, these high pressures are possible, however since micro-PIV is to be applied, a syringe pump is required. Given that micro-PIV uses fluorescent particles mixed with water, a syringe pump is needed since there is no interference between the fluorescent particles and the mechanics of the pump. Also, with a gear pump, there is a possibility of damage due to the fouling the fluorescent particles impose after long periods of operation. Another advantage of a syringe pump is that since there is no direct interaction between the fluid and the pump's mechanics, there is minimal heat introduction into the fluid, which is required for adiabatic experiments.

Another concern in operating at such high pressures is safety. Since micro-PIV is an optical technique, it is required that the channels be clear. In this case, the only available commercial channels that were found at micro dimensions were made of borosilicate glass. Therefore, working at very high pressures there was a possibility of channel rupture.

## 4.4 Summary

An experimental investigation regarding the laminar hydrodynamic entrance length in square microchannels was carried out over a laminar Reynolds number range of 0.5 to 200. Three microchannels with hydraulic diameters of 100 μm, 200 μm, and 500 μm were used to investigate scaling effects. The micro-PIV experimental technique was utilized to obtain flow field data at different axial locations from the microchannel inlet. To remove any effect of cross-sectional aspect ratio, square microchannels were used, whose inlet reservoir was infinitely large, compared to the hydraulic diameter of the channels.

Good agreement was found regarding the conventional physical mechanism describing laminar developing flow, in terms of the observed developing velocity profiles downstream from the microchannel inlet. A slight influence of dimensional scaling was observed in comparing the entrance length of the 500 μm channel with the 100 μm and 200 μm channels at low Reynolds numbers. However, at higher Reynolds numbers, above 10, there was no effect of scaling. Also, very good agreement was found in comparing the entrance length data with conventional correlations developed for ducts at high Reynolds numbers (above 10) for all microchannels studied, and for parallel plates at lower Reynolds numbers (below 10), particularly for the 100 μm and 200 μm channels. At very low Reynolds numbers, below 10, the parallel plate correlations are well suited for the prediction of the entrance length in microchannels. This is important since for practical applications of microscale flow in microchannels and micro devices, the flow is highly laminar, due to the high pressure drop. Therefore, conventional entry pressure loss correlations developed for ducts may not be applicable for microchannels at very low Reynolds numbers.

In addition, three new empirical laminar entrance length correlations were proposed, whereby both creeping and high laminar Reynolds number correlations are combined. The first correlation applies the experimental data for the 100 μm and 200 μm channels, and is applicable to square microchannels with hydraulic diameters below 500 μm, with an error of less than 15%. The second correlation includes all present experimental data, along with conventional experimental data for square ducts, and can be applied as a general entrance length correlation for channels of square cross-section at both the micro and macro scales. This correlation fit the experimental data to within 30%. The third correlation proposed includes all previous microchannel experimental entrance length data and some conventional experimental data, regardless of cross-sectional aspect ratio. Despite the large error in fitting the data to this new correlation, it can be used as a general entrance length correlation for microchannels of aspect ratios below three.

An experimental attempt was carried out to acquire fundamental data on the turbulent hydrodynamic entrance region in microchannels using micro-PIV. The same test-sections as those used for the laminar entrance region experiments were considered (i.e. 100 μm, 200 μm, and 500 μm microchannels). However, due to an excessive increase in the hydraulic resistance at fully turbulent flow (Re > 4000), which poses limitations on the pumping power required to overcome the large pressure drop at microscale dimensions, and restrictions on the flowrate range of the syringe pump, only the 200 μm microchannel test-section was actually attempted. Fully turbulent flow was not achieved in the 200 μm test section, due to the excessive pressure drop, which was calculated in the range of 1700 kPa for Re = 4000 using the Blasius formula. This pressure drop was too high for the syringe pump to overcome. In addition, since the channels were made of glass, safety was a concern due to the possibility of rupture.

# Chapter 5

# Thermal Entrance Region in Microchannels

## 5.1 Overview

A strong focus of the research community has been on fluid flow and forced convection heat transfer in micro geometries with and without phase change. The fundamental understanding of forced convection heat transfer in microchannels is important, since they are to be incorporated in micro-devices which would require high heat transfer rates within a very small footprint area. An example of micro-devices required for high heat removal is the microchannel heat sink (i.e. Tuckermann and Pease, 1981; Muwanga et al., 2007) used in cooling micro-processors for future supercomputers. The micro-heat sink is typically a conducting block with a sequence of microchannels micro-machined within the substrate, whose widths are on the order of 100 μm to 300 μm. Another example is in the micromixing reaction chamber of future Lab-on-a-Chip platforms for portable and rapid on-site DNA synthesis and sequencing (i.e. Whitesides, 2006; Yager et al., 2006; El-Ali et al., 2006). Certain DNA processes, such as DNA amplification through the use of PCR (Polymerase Chain Reaction) and DNA hybridization, contains a sequence of steps controlled through heating and cooling. Here, heat transfer can be combined with a mixing process within a reaction chamber, implemented on a single, portable biological chip. For the advanced design of such systems, it becomes necessary to study the thermo-fluid fundamentals of the integrated components, such as single-phase flow and heat transfer in microchannels.

As previously stated in Chapter 4 and outlined in Chapter 2, experimental fundamental studies on fully developed microchannel flow and heat transfer were widely researched over the past fifteen years. For parameters such as pressure drop, forced convection heat transfer coefficient, and laminar to turbulent transition, the more recent studies generally indicate good agreement with conventional theory, due to their improved and careful experimental methods at the microscale, compared with the earlier studies. Therefore, it is implied that the general physics of fully developed fluid flow and heat transfer are applicable at the microscale.

Within the entrance region of a closed channel, the effects on the flow field and heat transfer mechanisms are significant. However, where microchannels and micro-devices are concerned, there are limited heat transfer studies into this region, and those available are for laminar flows. The entrance region, where the flow or the temperature profile are either developing independently or simultaneously, can be very important because the transport properties such as pressure gradient and heat transfer coefficient depend strongly on the flow region. For thermally developing flow, heat transfer coefficients are characteristically at their highest and typically level down to some constant value within the fully developed region. Therefore, much higher heat transfer rates are possible within the thermal developmental length. The thermal entrance length can be defined as the length from the inlet of a channel to a location where the local Nusselt number is within 5% of its fully developed value (Shah and London, 1978).

From the literature review in Chapter 2, it was seen that there were numerous experimental studies carried out for the laminar thermal entrance length in microchannels. For completeness of the thermal entrance region, previous works for laminar flow in microchannels are outlined in detail, with results and conclusions from past research in literature. There is, however, currently no heat transfer data available on the turbulent entrance region of microchannels. An experimental investigation has been carried out to explore turbulent convection heat transfer in the entrance region of uniformly heated microtubes. The measurement of local wall temperatures is achieved through the use of un-encapsulated thermochromic liquid crystals (TLC's), a state-of-the-art, non-intrusive thermal measurement technique.

## 5.2 Laminar Flow

In terms of applications in micro geometries, particularly at very low Reynolds numbers ($Re < 1$), laminar flow is highly practical. This is primarily due to the typically low hydraulic resistance, and hence pressure drop, that laminar flow offers compared to turbulent flow. The low pressure drop is favorable as channel dimensions enter the microscale, since less pumping power is required to drive the flow. In practical applications, where, for example, a micro-pump would be implemented on a small microfluidic chip on the order of 3 $cm^2$, if less pumping power is required, less energy is needed to run the pump and hence the pump should typically have a smaller geometric size and simplify its portability.

Fundamentally, thermally developing laminar flow in microchannels was widely investigated in previous works, as stated in Chapter 2. These studies covered a wide range of laminar Reynolds numbers and covered both rectangular microchannels (i.e. Gamrat et al., 2005; Lee et al., 2005; Lee and Garimella, 2006;) and circular microtubes (i.e. Lelea et al., 2004; Muwanga and Hassan, 2006b; Yang and Lin, 2007; Li et al., 2007) for fully developed and simultaneously developing laminar flow, as well as analyses in the entrance region of micro-heat exchangers (i.e. Jiang et al., 2001; Mishan et al., 2007). These authors attempted to validate the laminar thermal entrance length with analytical solutions, as a fundamental comparison of scaling phenomena with microchannels compared with conventional sized pipes and ducts. For example, for a constant wall heat flux boundary condition for fully developed laminar flow, the thermally developing local Nusselt number along the non-dimensional axial heated length of the channel ($x/D_h RePr$) can be found by solving a series given by Shah (1975), which is found in Shah and London (1978). In general, a wide majority of the studies carried out for thermally developing laminar flow found excellent agreement with theory.

For example, Figure 5.1 shows experimental Nusselt number data from previous microtube studies for thermally developing laminar flow, compared with an analytical solution found in Shah and London (1978) for circular ducts. The experimental microscale studies are that of Lelea et al. (2004), for a microtube diameter of 0.3 mm using thermocouples to measure the local wall temperatures, Muwanga and Hassan (2006b), for a diameter of 0.25 mm using un-encapsulated

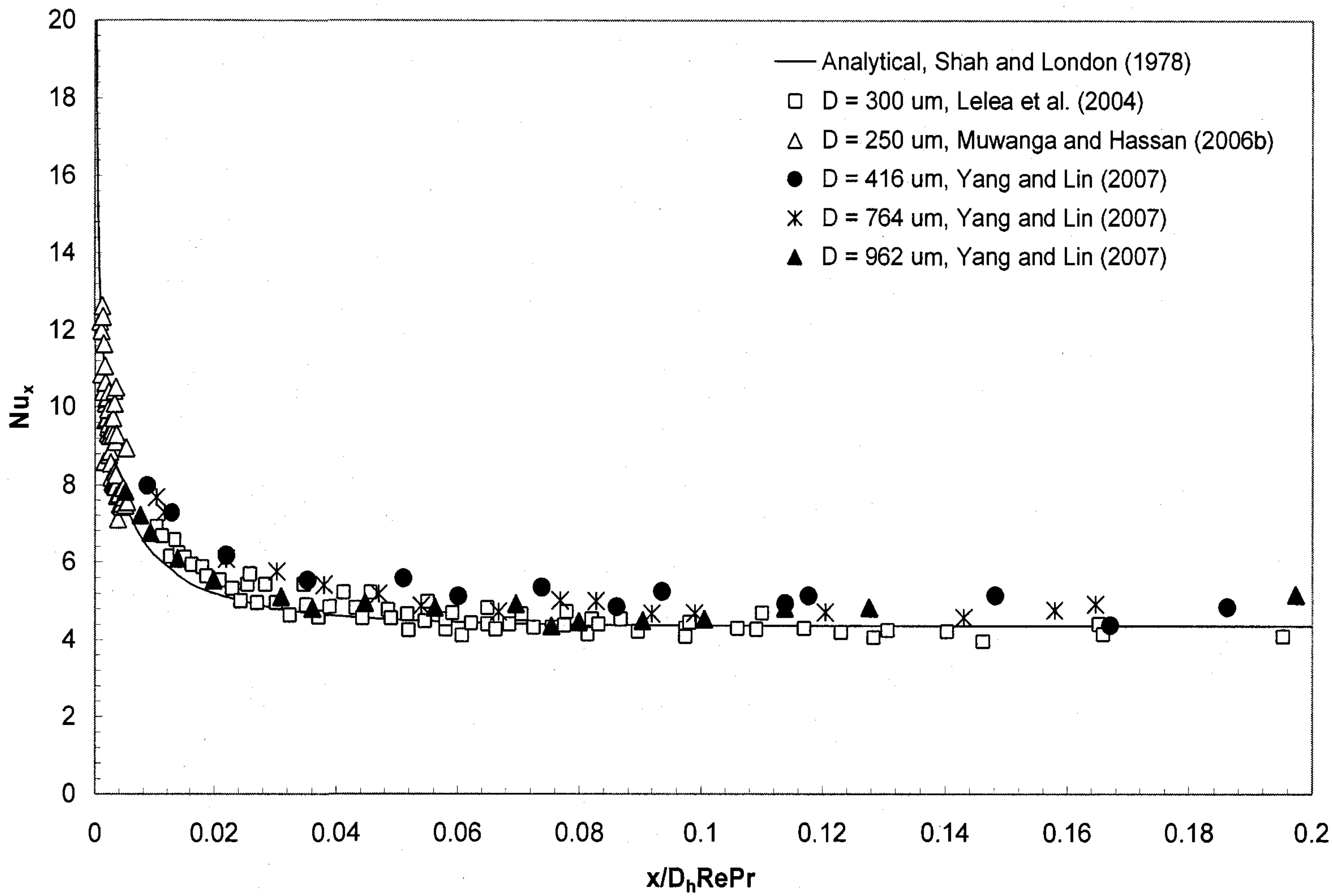


Figure 5.1: Comparison of experimental data and theory for thermally developing laminar flow for a constant wall heat flux

TLC's, and Yang and Lin (2007) for diameters ranging from 0.4 to 1 mm using micro-encapsulated TLC's. From Figure 5.1, it is apparent that there is good agreement in the trend of all the microscale experimental studies and the analytical solution given in Shah and London (1978). For Yang and Lin (2007), their trend is in agreement however there is a slightly higher error than the other two experimental studies when compared to the analytical result, particularly as the diameter is decreased. The authors did not provide any explanation for this discrepancy; however it is possibly due to their experimental setup or methods. From the figure, it can also be seen that the experimental data goes toward the theoretical Nu value for thermally developed laminar flow in a circular pipe, which is 4.364.

In addition, most data, except that from Muwanga and Hassan (2006b), was found using conventional techniques, such as thermocouples used by Lelea et al. (2004) and encapsulated TLC's used by Yang and Lin (2007). For these studies, even though there was agreement with the analytical solution of thermally developing flow, there is little data very close to the entrance of the microtube heated length, at very low $x/D_h RePr$ values. This can be due to the actual size and difficulty in positioning the thermocouple junctions close to the entrance or the encapsulation of the TLC's. It can be seen that the data given by Muwanga and Hassan (2006b), who used un-encapsulated TLC's, achieved thermal entrance data at very low $x/D_h RePr$ values below 0.005. This is due to the high spatial resolution and complete surface mapping of un-encapsulated TLC coating.

There exists thermal entrance region microtube data for laminar flow from many other publications that were not included here for sake of presentation. Further, even though laminar flow is a practical option, in terms of a fundamental experimental study it was widely investigated within the research community, with good agreement compared to conventional analytical solutions.

## 5.3 Turbulent Flow

Where conventionally-sized pipes and channels are concerned, turbulent flow is typically more likely to occur than laminar flow in practical situations, such as the flow process in a heat exchanger (Munson et al., 2002). Fully turbulent flow is present at high Reynolds numbers, above 4000, and is characterized by random, disorderly flow. A distinguishing feature of turbulent flow is the unsteadiness of the local velocity components. This irregular, randomness of turbulent flow has an effect on the flow properties, such as heat transfer and pressure drop (Munson et al., 2002). Compared to laminar flow, heat transfer processes are largely improved for turbulent flow, due to its randomness of flow.

At the microscale, it is widely conveyed that where practical applications are concerned, majority of micro system flows are laminar, due to the high pressure drop in microchannels caused by relatively small channel dimensions. In the turbulent regime, compared to laminar flow, the friction losses are conventionally increased, requiring very high pumping power to drive the flow. Nonetheless, future microscale applications may necessitate a need for turbulent flow data in microchannels. There is currently no data available on the turbulent thermal entrance region of microchannels. A fundamental study of this nature is a novel and significant contribution in the area of microchannel heat transfer.

An experimental study investigating the turbulent thermal entrance region, for developed hydrodynamic turbulent flow conditions was performed. The study was carried out for forced convective heat transfer in uniformly heated stainless steel microtubes with nominal inner diameters of 1.067 mm and 0.508 mm, over a turbulent Reynolds number range from 4000 to 9000. The working fluid is FC-72, an electronics cooling fluid, and adequate tube entry length is provided for hydrodynamic flow development prior to heating. The un-encapsulated TLC measurement technique for fine wall temperature measurements in the thermal entrance region of the microchannels will be applied, where local temperature data and Nusselt values are obtained. Although the application of un-encapsulated TLC's on a microchannel is challenging, these characteristics are attractive in resolving fine thermal entrance measurements.

### 5.3.1 Test Section

The present test sections used in evaluating the heat transfer characteristics in the thermal entrance region had the same manufacturing method for both the 1.067 mm and 0.508 mm microtubes. The primary test section component is a circular cross-section microtube (Small Parts), manufactured from stainless steel. Figure 5.2 shows a schematic of the test section, which incorporates the microtube along with the inlet and exit plenum/measurement chambers. The nominal inner diameters (ID) of the microtubes are 1.067 mm and 0.508 mm, whose outer diameters (OD) are 1.27 mm and 0.635 mm, respectively. The hydraulic length of both microtubes is 76 mm, and the heated length is 25 mm. Prior to the heated portion of the microtube, sufficient length was provided to assure hydrodynamic developed flow throughout the heated length.

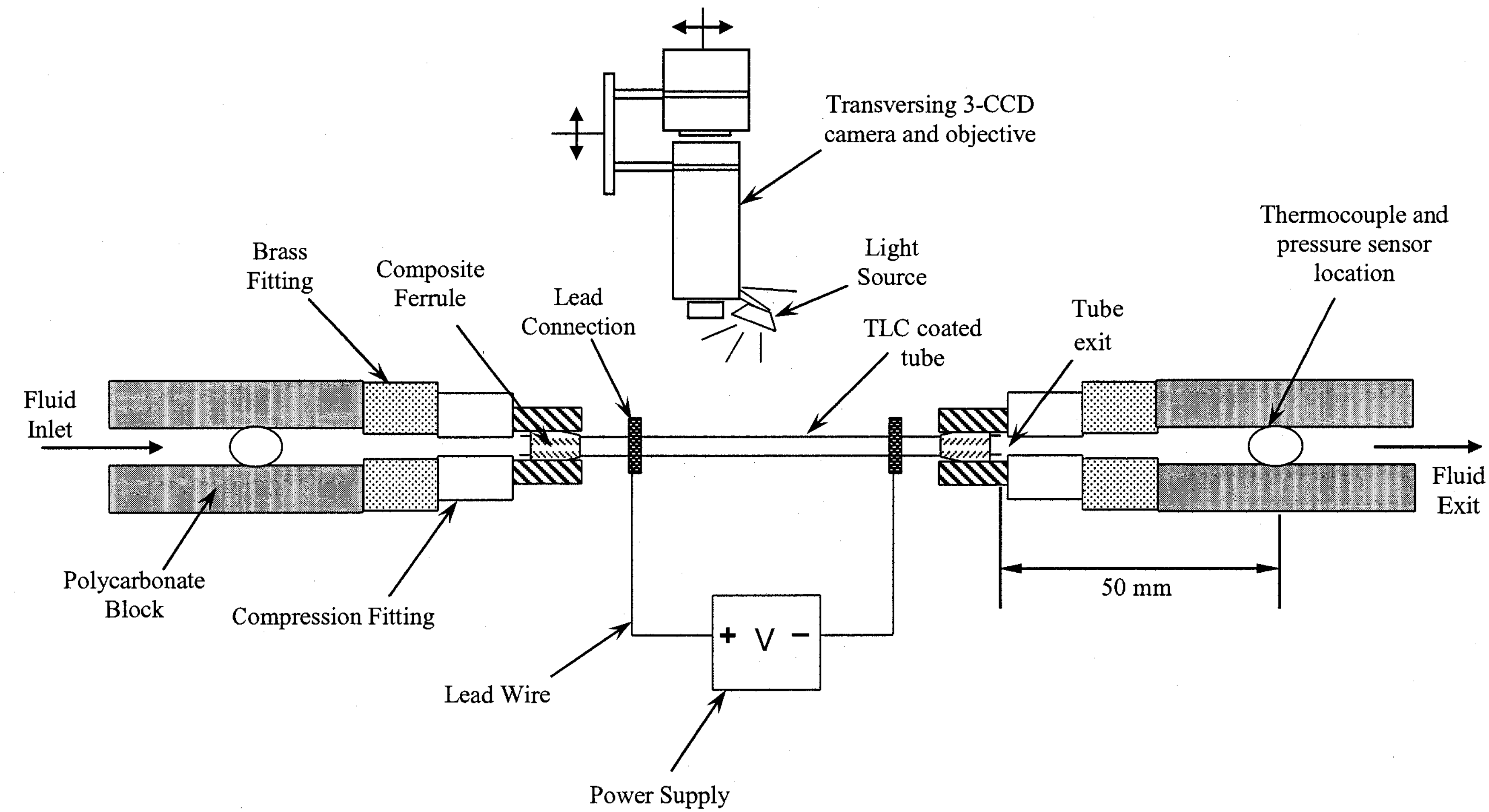


Figure 5.2: Test section setup with inlet/exit plenum chambers and TLC coated stainless steel microtube

In manufacturing the test-sections, shown in Figure 5.2, a polycarbonate sheet was machined to produce the measurement chambers (inlet and outlet) for bulk pressure and thermocouple temperature measurements. The tubes were connected to these chambers using standard 0.0625 mm stainless steel compression fittings with specialty ferrules to accommodate the small diameter microtubes. Fabricated from a composite of graphite and polyimide, the ferrules have a high electrical resistance. Other advantages of using compression fittings are that they provide an excellent seal to both gas and liquid, can withstand high pressures (up to 690 kPa) and are re-sealable for repeated use. Copper stranded wire (14 AWG) was soldered at each end of the tube to provide the electrical lead connection necessary for Joule heating from the power supply. The inside edge of this lead connection provided a flat edge for the beginning of the heated length, necessary for thermal entry length observation using the TLC measurement technique. There was no cover in direct contact with the TLC coated surface of the microtube, due to the small diameter of the tube. In order to protect the TLC coated surface from dust and room lighting, a non-contacting, optically clear plastic cover was placed over the tube.

### 5.3.2 Experimental Procedure

Through the use of un-encapsulated TLC thermography, wall temperature data was obtained through images taken at a single measurement location for the thermal entrance region of the microtube's heated length. Forced convection experiments were carried out for both the 0.508 mm and 1.067 mm microtubes, and regardless, the same calibration and measurement procedure was carried out for each test section.

As explained in Chapter 3, prior to each experiment it was necessary to calibrate the coated TLC material. Also, since the experimental aspects (i.e. room lighting, test section position, etc.) must be maintained for both the calibration and measurements, the calibration and measurements were performed on the same day. To begin the measurements, the flowrate was set and the system was allowed to run for about 10 minutes. Measurements were carried out for a flow range of 35–70 ml/min for the 0.508 mm tube, and 85–155 ml/min for the 1.067 mm tube. Using the preheater, the fluid temperature was raised until the inlet fluid bulk temperature was just under to the red-start of the TLC material (~40 °C). After running the flow through the system, measurements were ready to be taken and the protective non-contacting cover was removed. The illumination system was turned on and the voltage from the power supply (Joule heating) was adjusted until the TLC color response was predominantly in the green range of the fully developed region (~42 °C – 46 °C). From observation, the color in the thermal entrance region was, for the most part, in the red range (~39 °C – 42 °C). The system was allowed to come to equilibrium (5 – 10 minutes), after which a measurement image was taken.

Three color images were taken at a speed of 30 frames per second using the CCD camera. Through the automated system, these images were converted to hue angle, scaled for temperature conversion, and then averaged for each ROI location. In addition, the bulk fluid temperature and gage pressure at the inlet and outlet, as well as flowrate measurements were simultaneously captured and recorded. Numerous images were recorded for each flowrate and voltage setting, however for data reduction only the best images were selected for final presentation, based on visual inspection. Figure 5.3 (a and b) shows an example of raw rgb images for the

a) 0.508 mm microtube

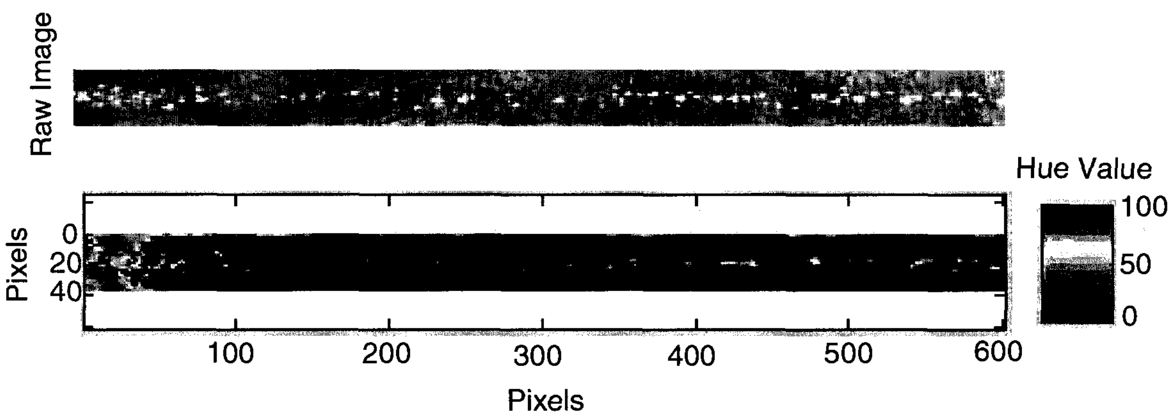


b) 1.067 mm microtube

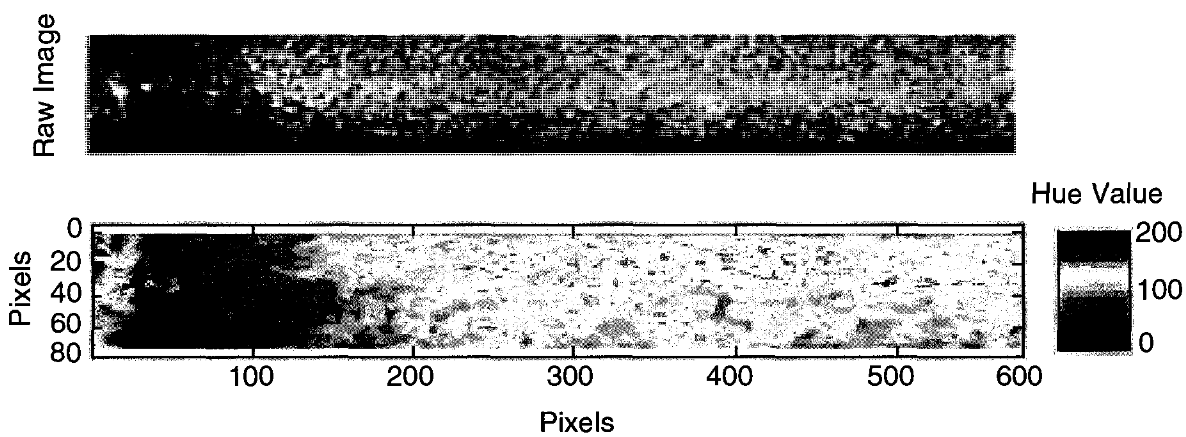


Figure 5.3: Examples of raw rgb images and their respective hue planes for the turbulent thermal entrance region of the (a) 0.508 mm and (b) 1.067 mm microtubes

0.508 mm and 1.067 mm microtubes and their converted hue planes taken for the present investigation. From the figure, the turbulent thermal entry region is evident.

### 5.3.3 Experimental Parameters and Uncertainty

The experimental parameters used in solving for the local values of the wall temperature, the heat transfer coefficient, and Nusselt values are similar to those developed in Muwanga and Hassan (2006a). The experimental friction factor, $f_{exp}$, was obtained from the pressure drop (ΔP) relation,

$$\Delta P = \left( f_{\exp} \frac{L_{hyd}}{D} + K_{loss} \right) \frac{\rho U^2}{2}, \tag{5.1}$$

where $L_{hyd}$ is the tube's hydraulic length, $D$ is the microtube's inner diameter, $\rho$ is the fluid's density, and $U$ the average velocity of the flow. The losses at the entrance and exit ($K_{loss}$) were estimated from Streeter (1961), considering the area changes at each location between the pressure sensor position and the tube entrance and exit. The heat flux to the fluid ($q$") was calculated based on the fluid enthalpy change given by,

$$q" = \frac{\dot{m} Cp(T_{out} - T_{in})}{\pi D L_h}, \tag{5.2}$$

where $T_{out}$ and $T_{in}$ are the outlet and inlet bulk fluid temperatures, respectively, and $L_h$ is the heated length. The local heat transfer coefficient ($h_x$) is obtained through the convective heat transfer relation,

$$h_x = \frac{q''}{(T_{w,xy} - T_{b,x})} \ , \tag{5.3}$$

where $T_{w,xy}$ is the inner wall temperature based directly on the TLC temperature measurement of the outer wall. $T_{w,xy}$ was estimated based on one-dimensional radial conduction (with heat generation) through the tube wall thickness. It was found that the differences in the inner and outer wall temperatures were less than 0.3 °C. $T_{b,x}$ is the local fluid bulk temperature, which was determined from an energy balance at each streamwise location given by,

$$T_{b,x} = T_{in} + \frac{\pi D q''}{\dot{m} Cp} x \ . \tag{5.4}$$

The local Nusselt number ($Nu_x$) was calculated as,

$$Nu_x = \frac{h_x D}{k_{loc}} \ , \tag{5.5}$$

where $k_{loc}$ is the local thermal conductivity of the fluid. Also, with a known volumetric flowrate, $Q$, the Reynolds number (Re) was calculated as,

$$\mathrm{Re} = \frac{\rho Q D}{\mu A} \ , \tag{5.6}$$

where $\mu$ is the fluid's dynamic viscosity and $A$ is the microtube's inner cross-sectional area. Except for the local Nusselt number, the fluid properties for the above calculations were taken through interpolation of the average fluid bulk temperature between the inlet and outlet. The properties of FC-72 were taken from the 3M product information sheet, and were shown in Table 3.1 for room temperature.

Experimental uncertainties were evaluated using standard methods outlined by Kline and McKlintock (1953). The experimental uncertainties of typical parameters are tabulated in Table 5.1. Based on the manufacturer's instrument specifications, the uncertainties in the pressure drop and thermocouple measurements are ± 0.73 kPa and ± 0.7 °C respectively. The uncertainty in flowrate was estimated at ± 2.25 ml/min and typical local Nusselt number uncertainty ranged from ± 20% to ± 30%. The high uncertainty in the local Nusselt number is due in part to the calculation of the heat flux to the fluid using an energy balance rather than using the power input from the power supply. However, using the change in enthalpy to calculate the heat flux input is more accurate since it eliminates the need to estimate the heat losses to the environment as well as the heat losses due to the resistance of the lead wires soldered to the tube. TLC measurement uncertainty, which was outlined in Chapter 3, was found to be to be estimated as ± 1.1 °C. Uncertainties in the microtubes' inner and outer diameters are based on the manufacturing tolerance and are also given in Table 5.1.

### 5.3.4 Pressure Drop

Experimental data has been developed for turbulent convection heat transfer in the thermal entrance region of uniformly heated microtubes with inner diameters of 0.508 mm and 1.067 mm, over a turbulent Reynolds number range of 4000 to 9000. Sufficient tube entrance length (~25 mm) was provided to assure hydrodynamic developed flow throughout the heated length. The cases that were considered for

Table 5.1: Uncertainty in experimental parameters of the turbulent thermal entrance region

| **Parameter** | **Uncertainty** |
|---|---|
| Local Nusselt number, $Nu_x$ | 20 % – 30 % |
| TLC wall temperature, $Tw_x$ | 1.1 °C |
| Inlet/Outlet temperatures, $T_{fluid}$ | 0.7 °C |
| Reynolds number, Re | 7.78 % |
| Volumetric flowrate, $Q$ | ± 2.25 ml/min |
| Microtube pressure drop, ΔP | ± 0.73 kPa |
| 0.508 mm microtube inner diameter, ID | – 0.0127 mm |
| 0.508 mm microtube outer diameter, OD | – 0.0000 mm |
| 1.067 mm microtube inner diameter, ID | ± 0.0254 mm |
| 1.067 mm microtube outer diameter, OD | ± 0.0127 mm |
| Non-dimensional axial heated distance, $x/D$ | 16.20 % |

analysis were at Re = 4717, 6645, 7912, and 8733, for the 0.508 mm microtube, and Re = 5399, 6287, 8035, and 8926, for the 1.067 mm microtube. The measurement of local wall temperatures was achieved through the use of un-encapsulated thermochromic liquid crystals (TLC's). The favorable characteristics of un-encapsulated TLC's, such as full surface mapping, high spatial resolution, and non-intrusiveness, are attractive in resolving fine thermal entrance measurements of a microchannel.

To assure the flow is indeed in the fully developed turbulent regime, the pressure drop was recorded over the microtube's length with the use of the inlet and exit static pressure transducers. From the experimental pressure drop, an experimental friction factor, $f_{exp}$, was obtained using Eq. (5.1) for all Re numbers studied for both microtubes, and compared to a conventional turbulent Darcy friction factor, given by Filonenko (1954) as,

$$f_{turb} = \left[1.82 \times \log(\mathrm{Re}) - 1.64\right]^{-2}. \tag{5.7}$$

Figure 5.4 shows the experimental friction factor, for both microtubes studied, compared with Filonenko (1954)'s correlation. This correlation was selected due to its use in the average fully developed turbulent Nusselt number relation, as will be shown later. It can be seen that, for the most part, the correlation slightly underpredicts the experimental data. However, taking into account the experimental uncertainty of the pressure transducers, there is adequate agreement with Filonenko (1954)'s friction factor correlation. Further, this data confirms that within the experimental Reynolds number range studied here (4000 – 9000), the flow is in the turbulent regime.

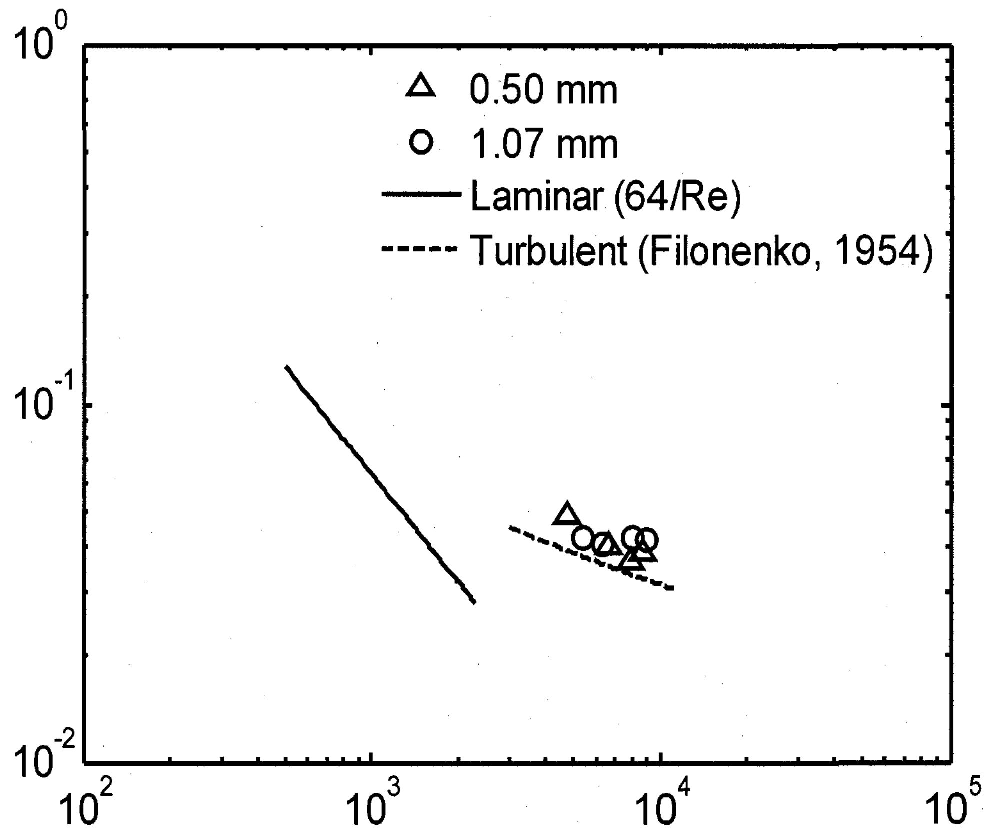


Figure 5.4: Comparison of the experimental friction factor with the Filonenko (1954) correlation

### 5.3.5 Local Wall Temperature Measurements

Figures 5.5 (a – d) and 5.6 (a – d) depict the local wall temperature ($Tw_x$) along the non-dimensional heated length ($x/D$), from the inlet lead connection (see Fig. 5.2) of the 0.508 mm and 1.067 mm microtubes, respectively, for each Reynolds number studied. It should be pointed out that it was difficult to distinctly distinguish the exact physical point at which tube heating begins, even with the use of the high magnification microscope apparatus. Identification of the heated length entrance was via visual selection of a pixel at the lead to tube contact. There is some uncertainty introduced by such a method, hence the zero location of the tube lies in the vicinity of zero $x/D$, rather than exactly at zero. This can be seen on the x-axis of Figures 5.5 and 5.6. As can be seen, all figures show a similar trend in accordance with the developing temperature profile of a uniformly heated tube. Even though the cases presented in these figures show the dimensionalized local wall temperatures which are dependant on the heat input, these figures serve to give a qualitative view at the trend of the wall temperature within the thermal entrance region.

In general from conventional observations, due to the high forced convection effects, turbulent thermal entrance lengths are much shorter than laminar thermal entrance lengths. At the start of the heated length, the wall temperature is lowest, however, along the axial distance of the heated microtube, the local wall temperature increases dramatically until a stable region, at 2 to 3 microtube diameters, where the temperature increase with $x/D$ is slight. From the trend of data, it can be said that for all turbulent Reynolds number test cases for both microtubes, the thermal entrance length is roughly 2 to 3 microtube diameters. In addition, since the heat input is, for the most part, variable for each case, the

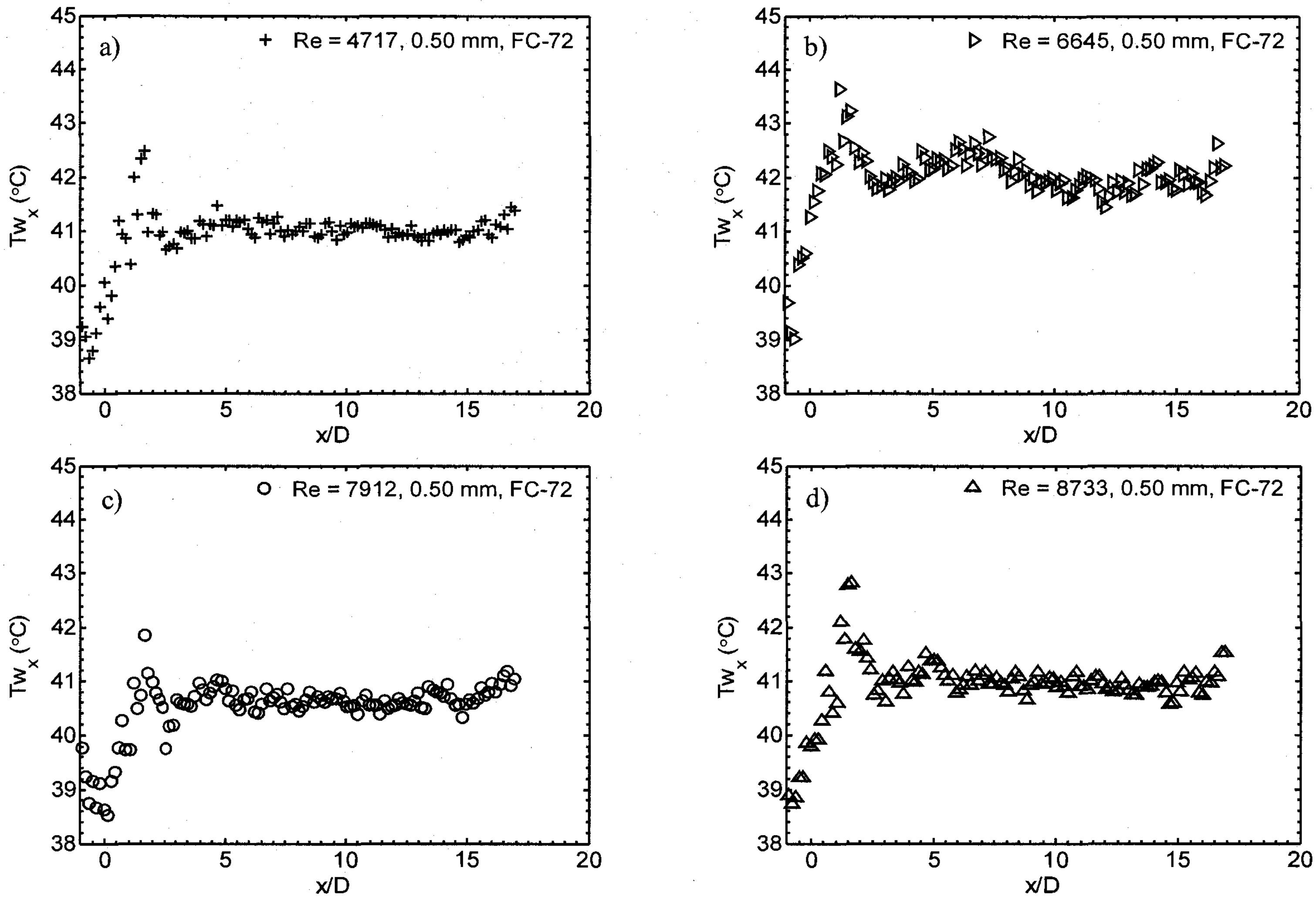


Figure 5.5: Local wall temperatures at the thermally developing region of the 0.508 mm microtube for different Reynolds numbers of (a) 4717, (b) 6645, (c) 7912, and (d) 8733

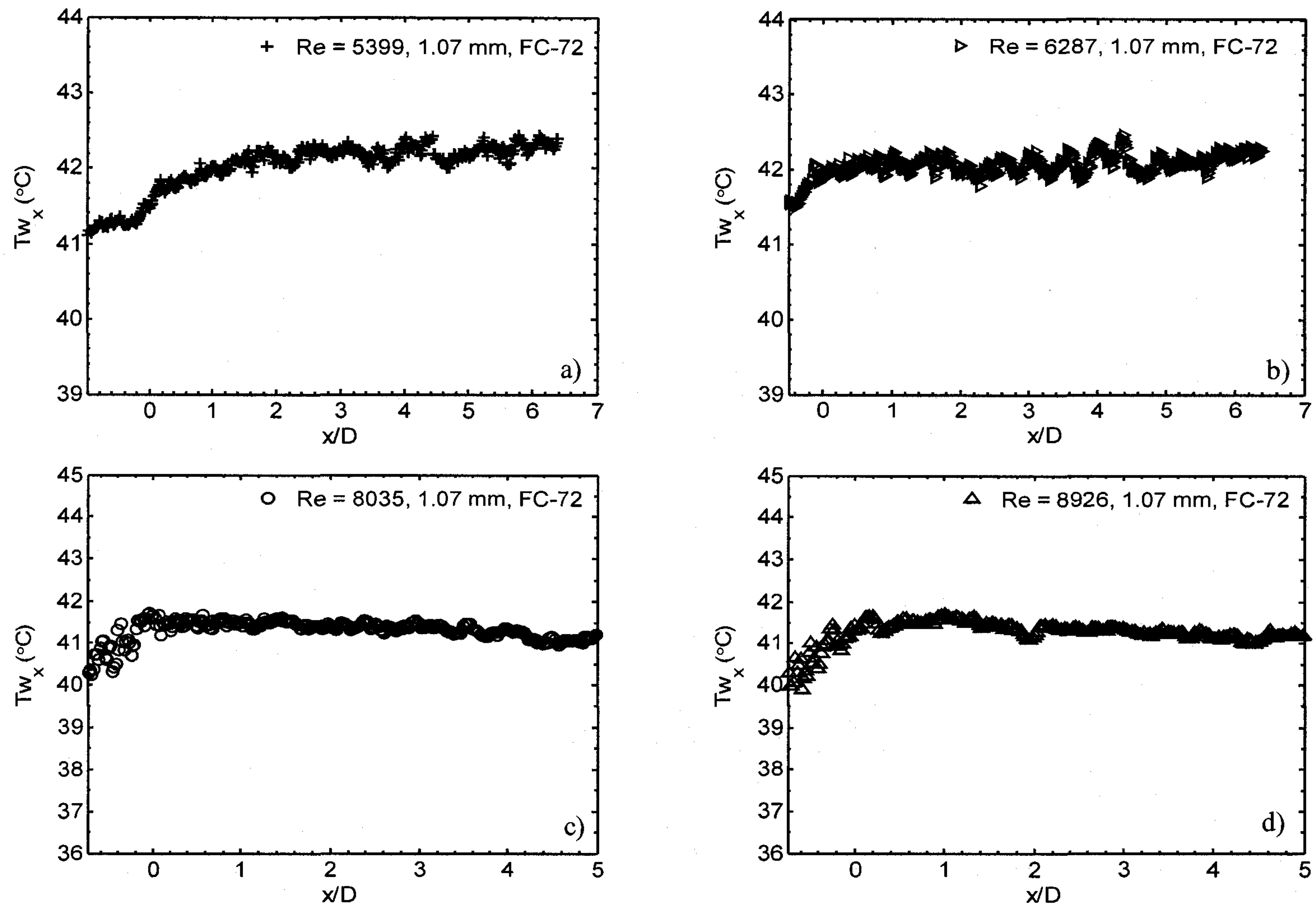


Figure 5.6: Local wall temperatures at the thermally developing region of the 1.067 mm microtube for different Reynolds numbers of (a) 5399, (b) 6287, (c) 8035, and (d) 8926

thermal entrance length is found to be independent of the heat flux. This indicates that for the Prandtl (Pr) number of our working fluid (FC-72, Pr = 12.35 at room temperature) and the Re range considered here (4000 – 9000), there is no effect on the thermal entrance length with turbulent Re number.

Conventionally for turbulent flow, the higher the Prandtl number the shorter the entrance length. However, there is a critical Pr number, above which the turbulence entrance length remains constant. This point is consistent with past researchers (i.e. Sparrow et al., 1957; Malina and Sparrow, 1964; Kays, 1966; Notter and Sleicher, 1972) who modeled the turbulent thermal entrance length in conventional tubes for a uniform wall heat flux boundary condition. Although these models were for high Re numbers (Re > $10^4$) impractical in their application to micro flows, these researchers concluded that there is little influence of Re on the turbulent thermal entry length for high Pr numbers, greater than 3. Also, at these high Pr numbers the turbulent thermal entrance length remained within a range of 2 to 3 diameters (i.e. Kays, 1966; Notter and Sleicher, 1972).

Regarding the local wall temperature for a developed temperature profile greater than 2 to 3 microtube diameters, it can be deduced that if the measurements were to extend along the axial distance of the tube throughout the entire heated length, one will observe a linear rise in the wall temperature, which is consistent for a fully developed temperature profile for a uniformly heated tube. Although measurements were confined to the thermal entrance region of the tube at low $x/D$ values, in some cases this trend is apparent. Looking at Figures 5.6a and 5.6b, for the 1.067 mm tube, this trend is highly evident; however, from the 0.508 mm tube of Figure 5.5 this trend is slight but detectable. From the local wall temperature plots, it is evident that there is a fair amount of noise associated with the data. Since TLC thermography is a local measurement technique with full surface mapping, many data points can be obtained. A data point is obtained for each region of interest (ROI), which is made up of only a few pixels. The data shown in the figures is down-sampled from the raw data, as a data reduction technique to obtain a viable trend. The scatter can be associated with the magnification, the large amount of data points, as well as the uncertainty of the TLC measurement technique.

### 5.3.6 Validation in the Thermally Developed Region

The local Nusselt number along the microtube axial heated length ($x/D$), for both the 0.508 mm and 1.067 mm tubes, are shown in Figures 5.7 (a – d) and 5.8 (a – d), respectively. These figures have similar implications as Figures 5.5 and 5.6. The turbulent thermal entrance length at 2 to 3 microtube diameters remains constant for our working fluid and Re range considered here. Along with this, other similarities with the previous two figures include the presentation of the plots, the axial range of the data, and the scatter in the data.

However, the relative significance associated with these figures is the inclusion in the non-dimensional analysis of the heat flux in presenting the Nusselt number, as well as validation of the analysis in the fully developed turbulent thermal region. Evident from the figures, the experimental data is compared with Gnielinski (1976)'s correlation for the average Nusselt number in the fully developed turbulent thermal region for large tubes given by,

$$Nu_{Gniel} = \frac{(f_{turb}/8)(\mathrm{Re}-1000)\mathrm{Pr}}{1+12.7(f_{turb}/8)^{1/2}(\mathrm{Pr}^{2/3}-1)}\ , \tag{5.8}$$

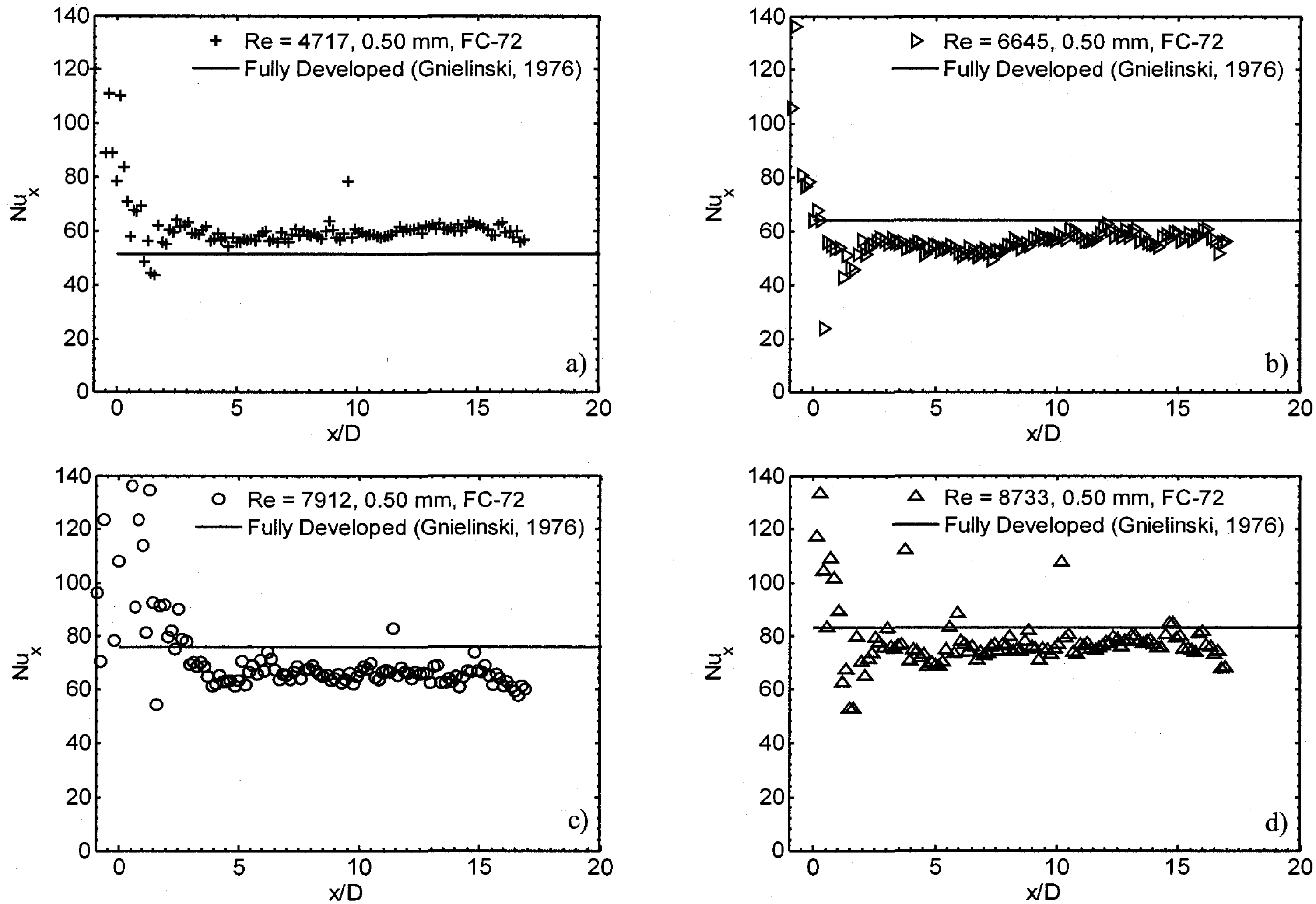


Figure 5.7: Local Nusselt values at the thermally developing region of the 0.508 mm microtube for different Reynolds numbers of (a) 4717, (b) 6645, (c) 7912, and (d) 8733

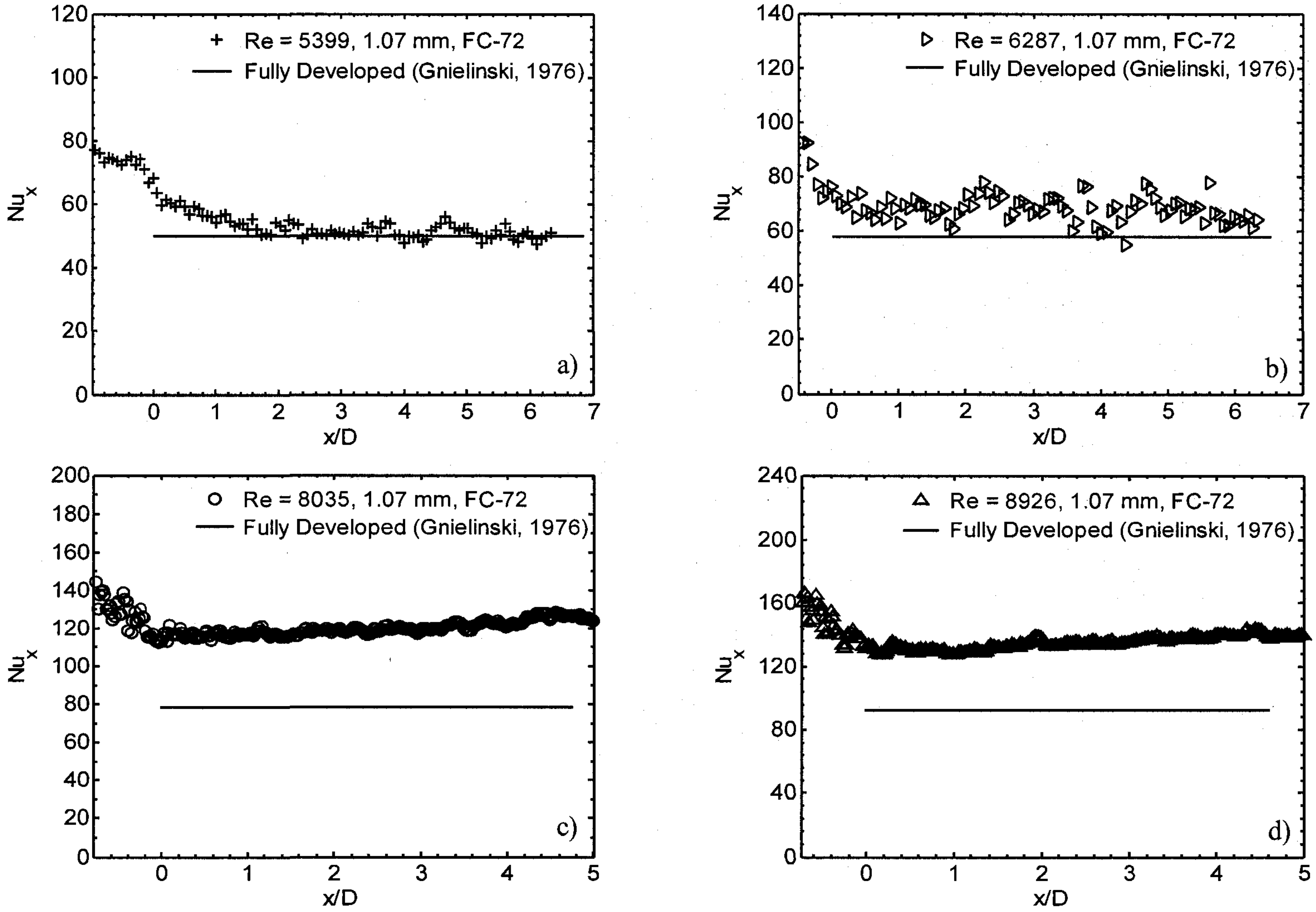


Figure 5.8: Local Nusselt values at the thermally developing region of the 1.067 mm microtube for different Reynolds numbers of (a) 5399, (b) 6287, (c) 8035, and (d) 8926

where Pr is the Prandtl number of the fluid and the turbulent Darcy friction factor, $f_{turb}$, is determined from Eq. (5.7). In solving Eq. (5.8), the fluid properties were taken at the average fluid bulk temperature between the tube inlet and outlet. Looking at Eq. (5.8), Gnielinski (1976)'s correlation is dependant not only on the Re and Pr numbers, but also on the theoretical friction factor, $f_{turb}$. Also, Eq. (5.8) is valid for $0.5 \leq Pr \leq 2000$ and $2300 \leq Re \leq 5x10^6$. This semi-empirical turbulent heat transfer correlation has some theoretical foundation, in that it is a combination of a functional form of a theoretically derived relation and empirically derived constants (Kays and Crawford, 1993). According to Kakaç et al. (1987), Eq. (5.8) is the recommended choice for turbulent heat transfer predictions in smooth tubes.

It can be seen from Figure 5.7 that for the four Re test cases for the 0.508 mm microtube, there is very good agreement of the experimental local Nusselt number data with the conventional fully developed correlation given by Gnielinski (1976). From Figure 5.8, for the 1.067 mm microtube, it is evident that there is very good agreement with Gnielinski (1976) at Reynolds numbers of 5399 and 6287 (Figs. 5.8a and 5.8b), however there is some deviation for Re of 8035 and 8926 (Figs. 5.8c and 5.8d). The deviation associated with these two cases is possibly due to the applied heat flux. In the calculation of Gnielinski (1976)'s correlation from Eq. (5.8), like many published correlations, the fully developed Nu number is found to be dependant on the Re and Pr numbers. However experimentally, the Nu number is dependant on the heat transfer coefficient, which in turn depends on the applied heat flux, although it should be noted that the error in Figures 5.8c and 5.8d is within the uncertainty of the experimental Nusselt number.

The conformity in the comparison of the experimental Nusselt number with theory validates the present investigation in defining the turbulent thermal entrance length at 2 – 3 microtube diameters. The Nusselt number is highest in the entrance region, then levels out to a somewhat constant value in the fully developed region at this entrance length, which is consistent for all Re numbers analyzed. Also, since there is no available data similar to the present investigation, it shows that the trend of the data from the start of the heated length through the turbulent thermal entrance region, and towards the fully developed turbulent temperature profile, does indeed make physical sense. In addition, it lays emphasis that un-encapsulated TLC's are a viable, valid, and attractive approach for wall temperature measurements at the microscale, particularly due to its fine spatial resolution suited for micro dimensions, and full surface mapping capability to obtain a continuous trend of experimental data. These characteristics were advantageous for measurements within the turbulent thermal entry region.

### 5.3.7 Data Trend of the Thermally Developing Nusselt Values

In comparing the experimental Nusselt number trend of the 0.508 mm tube in Figure 5.7 with that of the 1.067 mm tube of Figure 5.8, it can be seen that although there is good agreement in the overall experimental data in terms of the thermal entrance length, there is a slight difference in the trend of the two figures. From Figure 5.7 (a – d), as the wall temperature is sharply increasing in the entrance region, the forced convection Nusselt number is sharply decreasing. It can be seen that there is a noticeable undershoot in the Nu data, after which the data increases towards its fully developed value. This tendency is apparent for all Re cases for the 0.508 mm tube, and is also evident for the wall temperature measurements of Figure

5.5, where an overshoot in the temperature data is evident. However, looking at Figure 5.8 (a – d) for all Re cases of the 1.067 mm tube, there is no such occurrence, where the experimental Nu number trend decreases sharply and smoothly with no undershoot in the data. This trend is also observed in the wall temperature measurements of the 1.067 mm tube in Figure 5.6.

At first it was thought that this was a possible micro-scaling effect that becomes evident at microscale dimensions, but not apparent at conventional geometries, as with the 1.067 mm tube. To clarify this issue, and verify the repeatability in the TLC data, further turbulent thermal entrance region experiments were carried out in the 0.508 mm microtube. Figure 5.9 shows the local Nusselt number, $Nu_x$, versus the non-dimensional heated length, $x/D$, for two data sets for the 0.508 mm tube. The first data set, taken on January 18, 2007 for Re = 4717 is the same as that shown in Figure 5.7a. The second data set was taken nearly seven months later on August 8, 2007, on the same test section for Re = 4200. The difference in the experiments was that a new coating and calibration process was applied to the second data set. The minor dissimilarity in the Re numbers of the two data sets has a minor importance, and the Re values of 4717 and 4200 are close enough to compare the trend and the repeatability of the TLC data.

Both data sets have good agreement with Eq. (5.8) in their respective thermally developed regions; however this is not shown in the figure for reasons of simplicity. It can be seen from Figure 5.9 that there is very good repeatability in the data, in that both data sets show a definite entrance region spanning about 2 – 3 diameters, then level out to a constant Nu number in the fully developed region. However, it can be seen that there is a sharper negative slope for the January 18$^{th}$ case

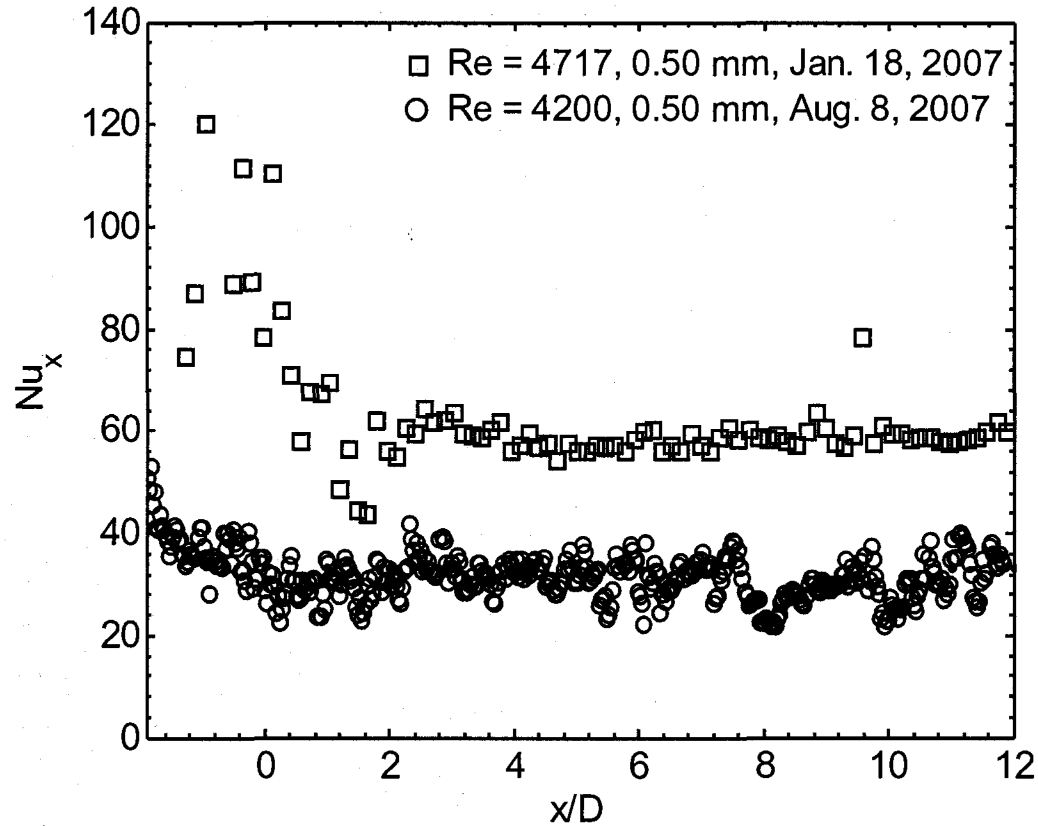


Figure 5.9: Evaluation of the repeatability in the experimental results at similar turbulent Reynolds numbers

compared with the August 8th case, where the entrance region data has a smoother shape. Also, from the figure, it can be seen that there is no undershoot in the data for the August 8th case as is the case for the January 18th case. Therefore, due to this observation it can be said that the overshoot in the $Tw_x$ data and the undershoot in the $Nu_x$ data at the entrance region for the 0.508 mm tube (Figs. 5.5 and 5.7, respectively) is due to the TLC coating and not a scaling phenomena.

Figure 5.10 shows two trends of data of the local experimental Nusselt number, $Nu_x$, versus the non-dimensional axial heated length, $x/D$, for Re = 5399. The data is for the 1.067 mm microtube at two different heat fluxes of 1.345 W and 0.784 W. This figure serves as to demonstrate the dependence of the turbulent thermal entrance length on the heat input at a given turbulent Re number, where there is no distinct significance in the choice of the actual value of the flowrate. From the figure, it can be seen that independent of the heat input, the turbulent thermal entrance length is at 2 – 3 diameters, consistent with the previous figures. This point further validates the present turbulent thermal entrance length analysis in that the entrance length is constant regardless of the heat flux and Re number for the Pr value studied. However, it is evident that there is a sharper drop (greater negative slope) in the local Nusselt number towards its fully developed value for the higher heat flux case of 1.345 W. This is expected since a higher heat flux produces a higher local convective heat transfer coefficient. Also, from Figure 5.10 it can be seen that there is better agreement with the fully developed Nusselt value given by Gnielinski (1976) for the higher heat flux case. However, the error associated with the lower heat flux case (0.784 W) is within the experimental uncertainty.

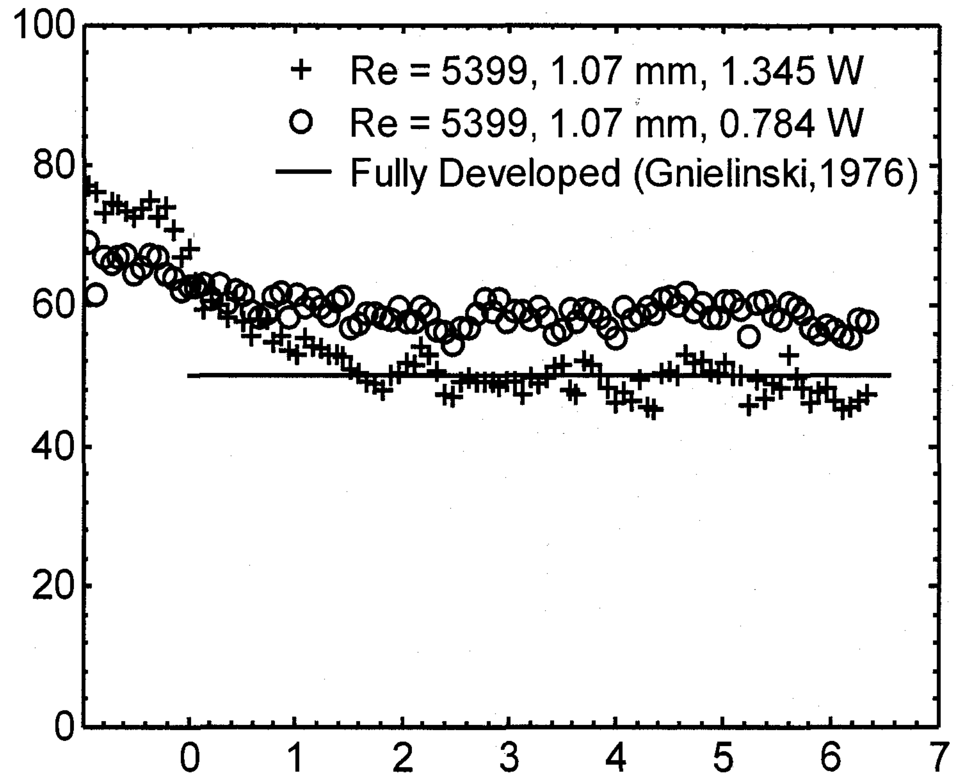


Figure 5.10: Thermal entrance length comparison of two data sets with different heat power input and the same flowrate (Re = 5399)

## 5.4 Summary

In regards to the laminar thermal entrance region, from a review into the open literature it was found that numerous experimental studies were carried out in microchannels and microtubes. Conventionally, thermally developing laminar flow has a significant effect on the flow and heat-transfer parameters, such as the convective heat transfer coefficient. Due to the relatively low pressure drop imposed for laminar flow compared to turbulent flow, particularly as channel dimensions enter the microscale range, laminar flow can be practically applied in microchannels and micro-devices. However, even though laminar flow is highly practical in microfluidics due to the low pumping power required to drive the flow, an experimental study was not carried out due to the amount of fundamental experimental data existing on the subject. Majority of the existing data found very good agreement with conventional correlations. Instead, an experimental study for thermally developing turbulent flow was performed.

An experimental investigation into the turbulent thermal entrance region of uniformly heated microtubes was carried out. Experimental heat transfer entrance data was presented for two stainless steel microtubes with inner diameters 0.508 mm and 1.067 mm, over a turbulent Reynolds number range of 4000 to 9000. Sufficient microtube length was given to allow the flow to develop prior to heating. Therefore turbulent thermal data was not obtained for simultaneously developing flow, but for fully developed hydrodynamic flow that is developing thermally.

The present fundamental experimental study was a first of its kind for flow in microchannels, with turbulent flow having possible future applications in microfluidics. High resolution measurements of local wall temperatures were possible through the use of un-encapsulated thermochromic liquid crystals (TLC's). TLC thermography is a non-intrusive surface temperature measurement technique, possessing high thermal resolution and full surface mapping in its un-encapsulated form. These characteristics are attractive in analyzing microscale heat transfer phenomena, and the complete surface mapping allows the collection of continuous temperature data.

The developing local wall temperature and local Nusselt number measurements showed good agreement with the physical mechanism describing thermally developing flow, and good agreement with conventional correlations was found in the thermally developed region of the microtubes. For the Reynolds number range considered, with Pr~10 (considering temperature effects), negligible variation in the entrance length was observed. The entry length was found to be ~2–3 microtube diameters under the conditions considered, which is consistent with conventional studies. Further, it was demonstrated that un-encapsulated TLC's are a viable approach for high resolution wall temperature measurements at the microscale.

# Chapter 6

# Conclusion

## 6.1 Summary and Contributions

Physically, the entrance region within a channel has a significant influence on the transport properties due to the developing nature of the flow. Within the hydrodynamic entrance region, where the velocity flow field is developing, the shear stress imposed by sudden drag effects of the channel walls, as well as the acceleration of the fluid at the center of the channel, has a profound effect on the pressure gradient. Similarly, for the thermal entrance region where the temperature profile is developing, the immediate increase in the wall temperature at the start of the heated length, and the heat transfer to the colder fluid through thermal diffusion has a great effect on the heat transfer coefficient. For reasons such as these, the entrance region within a channel, with or without heat transfer, has important implications on the flow field.

The relatively new area of microfluidics deals with thermo-fluid phenomena in microchannels and micro-devices, which are to be implemented in complete micro-systems. Prominent conceptual applications of these micro-systems are in the biomedical industry through Lab-on-a-Chip platforms, and the electronic sector through the cooling of processors using either single-phase or boiling flow. With regards to single-phase liquid flow in microchannels, much experimental research was previously carried out within the fully developed region, with recent studies indicating good agreement with conventional theory. However, there was a lack of experimental data concerning both the hydrodynamic and thermal entrance regions of microchannels. Fundamental entrance region data is required to experimentally verify if there is any effect of scaling on the entrance regions as channel dimensions enter the microscale, as well as provide data for future designs of micro-devices.

The present two part experimental investigation was carried out to provide new experimental evidence into the hydrodynamic and thermal entrance regions in microchannels, ranging in hydraulic diameters from 100 µm to 1 mm. The advantages associated with state-of-the-art experimental techniques of micro-PIV and un-encapsulated TLC's, allowed for the comprehensive analysis of the entrance regions in microchannels. In general, the results showed minimal influence of scaling on the physics of developing flow over the range of microchannel hydraulic diameters and Reynolds numbers studied.

Experiments were carried out for the laminar hydrodynamic entrance region and attempted for turbulent flow. New test sections were designed to provide fundamental entrance length data for microchannels from a very large inlet reservoir, to minimize pre-development in the flow upstream of the channel inlet. Three square microchannels, whose widths were 100 µm, 200 µm, and 500 µm, were investigated using micro-PIV to obtain extensive flow field data in the developing region. For laminar flow, a Reynolds number range from 0.5 to 200 was studied. There was a slight influence of dimensional scaling in comparing the entrance length of the 500 μm channel with the 100 μm and 200 μm channels at low Reynolds numbers, below 10. For all channels studied, good agreement was found in comparing the entrance lengths with conventional correlations developed for ducts at Re numbers above 10, and for parallel plates at lower Re numbers. Also, three new empirical laminar entrance length correlations were proposed, whereby both creeping and high laminar Reynolds number correlations are combined. Regarding the turbulent hydrodynamic entrance region, experiments were attempted in the 200 μm microchannel test section. However, due to the immense pressure drop for turbulent flow, the inability in providing the required pumping power from the syringe pump, and safety concerns, no experimental data was obtained.

Experiments were also performed for the thermal entrance region. For laminar flow, there are numerous studies available in literature investigating the laminar thermal entrance region, with majority indicating good agreement with conventional theory. Therefore, to provide new experimental data, only the thermal entrance region for turbulent flow was studied, since there was no available experimental data in microchannels. Experimental heat transfer entrance data was presented for two stainless steel microtubes with inner diameters of 0.508 mm and 1.067 mm, over a turbulent Reynolds number range of 4000 to 9000. Fine wall temperature entrance measurements were obtained through the use of un-encapsulated TLC's, whose spatial characteristics were desirable in carrying out the experiments. Developing local wall temperature and local Nusselt number measurements were presented and showed good agreement with the physical mechanism describing thermally developing flow. Also, agreement with conventional correlations was found in the thermally developed region of the microtubes. There was negligible change in the thermal entrance length for the turbulent Reynolds number range and working fluid ($Pr \sim 10$) considered. Consistent with conventional studies, the turbulent thermal entry length was found to be about 2 to 3 microtube diameters under the conditions considered.

## 6.2 Future Directions

Concerning experimental single-phase microchannel flow, experimental data is widely available for fully developed flow conditions, both diabatic and adiabatic, and limited data is available for the hydrodynamic and thermal entrance regions. From recent fully developed flow studies, along with the experimental data presented here for the entrance regions, it can be seen that for the most part there is minimal influence in dimensional scaling. Even though it was attempted, there were fundamental limitations in obtaining experimental data in microchannels for the turbulent hydrodynamic entrance region. Fundamental experimental data should be obtained for this region, even though there are many experimental difficulties associated with the study. A different flow loop or test section should be designed, to overcome the pressure drop and capabilities of the syringe pump, such as shorter channel lengths or operation of the syringe pump in infusion mode. Even though there are currently no conceptual applications of turbulent flow in microchannels due to the high pressure drop, future microfluidic applications may require fundamental experimental data for this regime.

The experimental methods used in analyzing the hydrodynamic and thermal entrance regions in the current study, showed the advantages associated with micro-PIV and un-encapsulated TLC techniques. Micro-PIV allowed for qualitative and quantitative analysis of the velocity flow field in the entrance region of square microchannels down to 100 μm in width. Un-encapsulated TLC's, due to their high spatial resolution, captured fine turbulent thermal entrance measurements, which are close to impossible to obtain using thermocouples due to extremely short entrance lengths. In accurate microfluidic measurements, optical techniques need to be relied upon as dimensions enter the microscale. Currently, many research groups use micro-PIV in the flow field analysis of microchannels and microchannel systems, as was seen in Chapter 2. However, with regards to un-encapsulated TLC's, very few groups apply this method for wall temperature measurements at the microscale. The characteristics of un-encapsulated TLC's compared with bulk measurements, such as full surface mapping and non-intrusiveness, make this method very attractive. Even though there are initial challenges and difficulties in the application of un-encapsulated TLC's compared to their micro-encapsulated form, their very high spatial resolution make them highly appropriate for microscale measurements, as was seen here.

With respect to microfluidic applications for single-phase liquid flow, the most prominent are those applicable to the biomedical sector through Lab-on-a-Chip platforms and μ-TAS. An important micro-device to be implemented into these micro-systems is a microfluidic mixer, which is used to mix two single-phase liquids at the microscale. In practical applications of microchannel flow, majority of micro-system flows are strongly laminar, due to the high pressure drop caused by relatively small channel dimensions. Due to these low Reynolds numbers, micromixers do not apply turbulent mixing as do conventional mixers, and laminar mixing must be efficiently applied. Typical micromixer applications include the mixing of reagents prior to chemical or biological reactions in chemical analyses and Lab-on-a-Chip platforms, drug delivery, and sequencing or synthesis of nucleic acids (Nguyen and Wu, 2005). In order for micromixers to efficiently and effectively operate in these applications, rapid mixing times are necessary.

From a brief review into literature on microfluidic mixers, there are definite advantages to passive mixers over active mixers in regards to implementation, practicality, and portability. The difference between passive mixers compared to active mixers, are that passive mixers use no external power sources or moving parts to carry out the mixing process; they solely rely on channel geometry for efficient mixing. Passive micromixers that have combined mixing mechanisms of both lamination and chaotic advection showed the most efficient mixing. From a fabrication point of view, in-plane micromixers are simple to fabricate compared with their out-of-plane counterparts, and are simpler to implement into a complete micro-system. Even though numerous experimental works have been carried out on microfluidic mixers, future works should focus on an in-plane micromixer that incorporates both lamination and chaotic advection. Also, it would provide an additional geometry designers can choose in the fabrication and design of complete micro-systems.

It is encouraging that the developing technology microfluidics brings will one day have a great impact on our day to day lives, whether it is in the cooling of our super computers through a micro-heat exchanger, or the direct medical diagnosis of an infectious disease using a Lab-on-a-Chip platform.

# References

Adams, T.M., Abdel-Khalik, S. I., Jeter, S. M., and Qureshi, Z. H., 1998, "An experimental investigation of single-phase forced convection in microchannels," *Int. J. Heat and Mass Transfer*, **41**, n 6 – 7, pp. 851–857.

Allan, R. W. and Eckert, E. R. G., 1964, "Friction and heat-transfer measurements to turbulent pipe flow of water (Pr = 7 and 8) at uniform wall heat flux," *J. Heat Transfer*, **86**, pp. 301–310.

Atkinson, B., Brocklebank, M. P., Card, C. C., and Smith J. M., 1969, "Low Reynolds number developing flows," *J. AIChE*, **15**(4), pp. 548–553.

Babus'haq, R. F., 1993, "Forced convection heat transfer in the entrance region of pipes," *Int. J. Heat and Mass Transfer,* **36**(13), pp. 3343–3349.

Barbin, A. R. and Jones, J. B., 1963, "Turbulent flow in the inlet region of a smooth pipe," *J. Basic Engineering*, **85**, pp. 29–34.

Beavers, G. S., Sparrow, E. M., and Magnuson, R. A., 1970, "Experiments on hydrodynamically developing flow in rectangular ducts of arbitrary aspect ratio," *Int. J. Heat Mass Transfer*, **13**, pp. 689–702.

Bodoia, J. R. and Osterle, J. F., 1961, "Finite difference analysis of plane poiseuille and couette flow development," *J. Applied Science Research*, Section A, **10**, pp. 265–276.

Brutin, D., and Tadrist, L., 2003, "Experimental friction factor of a liquid flow in microtubes," *J. Physics of Fluids*, **15**(3), pp. 653–661.

Bucci, A., Celata, G. P., Cumo, M., Serra, E., and Zummo, G., 2003, "Water single-phase fluid flow and heat transfer in capillary tubes," *J. Therm. Sci. & Eng.*, **11**(6), pp. 81–89.

Celata, G. P., Cumo, M., Guglielmi, M, and Zummo, G., 2002, "Experimental investigation of hydraulic and single phase heat transfer in 0.130-mm capillary tube," *J. Microscale Thermophysical Eng.*, **6**, pp. 85–97.

Celata, G. P., Cumo, M., and Zummo, G., 2004, "Thermal–hydraulic characteristics of single phase flow in capillary pipes," *J. Exp. Therm. and Fluid Sci.*, **28**, pp. 87–95.

Celata, G. P., Morini, G. L., Marconi, V., McPhail, S. J., and Zummo, G., 2006a, "Using viscous heating to determine the friction factor in microchannels – An experimental validation," *J. Exp. Therm. and Fluid Sci.*, **30**, pp. 725–731.

Celata G. P., Chmiel, K., Kulenovic, R., Martin-Callizo, C., McPhail, S., Mertz, R., Owhaib, W., Palm, B., Sobierska, E., and Zummo, G., 2006b, "Frictional pressure drop in single-phase flow in narrow channels," *Proc. ASME 4th International*

*Conference on Nanochannels, Microchannels and Minichannels (ICNMM06)*, ICNMM2006-96138.

Chang, C.-C. and Yang, R.-J., 2007, "Electrokinetic mixing in microfluidic systems," *J. Microfluidics and Nanofluidics*, **3**, pp. 501–525.

Chariot, P., Sullivan, P., and Ben Mrad, R., 2005, "Micro particle imaging velocimetry measurements in high aspect ratio passive microfluidic components," *Proc. ASME 3rd International Conference on Microchannels and Minichannels (ICMM05)*, ICMM2005-75137.

Chaw, K. C., Manimaran, M., Tay, E. H., and Swaminathan, S., 2007, "Multi-step microfluidic device for studying cancer metastasis," *J. Lab on a Chip*, **7**, pp. 1041–1047.

Chen, R.-Y., 1973, "Flow in the entrance region at low Reynolds numbers," *J. Fluids Eng.*, **95**, pp. 153–158.

Cooper, T. E., Field, R. J., and Meyer, J. F., 1975, "Liquid crystal thermography and its application to the study of convective heat transfer," *J. Heat Transfer*, **97** Ser C(3), pp. 442–450.

Day, D. and Gu, M., 2005, "Microchannel fabrication in PMMA based on localized heating by nanojoule high repetition rate femtosecond pulses," *J. Optics Express*, **13**(16), pp. 5939–5946.

de Boer, M. J., Meint, Tjerkstra, R. W., Berenschot, J. W., Jansen, H. V., Burger, G. J., Gardeniers, J. G., Elwenspoek, M., and van den Berg, A., 2000, "Micromachining of buried micro channels in silicon," *J. Microelectromechanical Sys.*, **9**(1), pp. 94–103.

deMello, A. J., 2006, "Control and detection of chemical reactions in microfluidic systems," *Nature*, **442**, pp. 394–402.

Devasenathipathy, S. and Santiago, J. G., 2005, "Electrokinetic Flow Diagnostics", in *Microscale Diagnostic Techniques*, ed. Breuer, K., Springer-Verlag, Berlin, Germany, pp. 113–154.

Doherty, J., Ngan, P., Monty, J., and Chong, M., 2007, "The development of turbulent pipe flow," *Proc. 16th Australasian Fluid Mechanics Conference*, Gold Coast, Australia, Dec. 2–7, pp. 266–270.

El-Ali, J., Sorger, P. K., and Jensen, K. F., 2006, "Cells on chips," *Nature*, **442**, pp. 403–411.

Epstein, A. H., 2004, "Millimeter-scale, micro-electro-mechanical systems gas turbine engines," *J. Engineering for Gas Turbines and Power*, **126**, pp. 205–226.

Erickson, D., Sinton, D., Nikolic, V., and Li, D., 2003, "Heat transfer and electrokinetic flow analysis in poly(dimethylsiloxane) microfluidic systems," *Proc. ASME International Mechanical Engineering Congress and Exposition (IMECE2003)*, **5**, Micro-Electro-Mechanical Systems (MEMS), pp. 537–544.

Ferguson, A. D., Bahrami, M., and Culham, J. R., 2005, "Review of experimental procedure for determining liquid flow in microchannels," *Proc. ASME 3rd*

*International Conference on Microchannels and Minichannels (ICMM2005)*, June 13–15, Toronto, Canada, ICMM2005-75126.

Ferguson, J. L., 1968, "Liquid crystals in nondestructive testing," *J. Applied Optics*, **7**(9), pp. 1729–1737.

Filippov, V. M., 1982, "Formation of a developed turbulent flow in a quadratic channel," *J. Eng. Physics and Thermophysics,* **42**(1), pp. 40–45.

Filonenko, G. K., 1954, "Hydraulic resistance in pipes," *Teploenergetika* (Russia), **1**, pp. 40–44.

Fleming, D. P. and Sparrow, E. M., 1969, "Flow in the hydrodynamic entrance region of ducts of arbitrary cross section," *J. Heat Transfer*, **91**, pp. 345–354.

Gabrianovich, B. N., Levchenko, Y. D., Trubakov, Y. P., and Ushakov, P. A., 1979, "Effect of entrance conditions on the development of turbulent flow in circular pipes," *J. Atomic Energy*, **47**(3), pp. 715–717.

Gamrat, G., Favre-Marinet, M., and Asendrych, D., 2005, "Conduction and entrance effects on laminar liquid flow and heat transfer in rectangular microchannels," *Int. J. Heat and Mass Transfer*, **48**, pp. 2943–2954.

Gnielinski, V., 1976, "New equations for heat and mass transfer in turbulent pipe and channel flow," *J. Int. Chem. Eng.*, **16**, pp. 359–368.

Goldstein, R. J. and Kreid, D. K., 1967, "Measurement of laminar flow development in a square duct using a laser-doppler flowmeter," *J. Applied Mech.*, **34**, pp. 813–818.

Han, L. S., 1960, "Hydrodynamic entrance lengths for incompressible laminar flow in rectangular ducts," *J. Applied Mech.*, **27**, pp. 403–409.

Hao, P.-F., He, F., and Zhu, K.-Q., 2005, "Flow characteristics in a trapezoidal silicon microchannel," *J. Micromech. and Microeng.*, **15**, pp. 1362–1368.

Harms, T. M., Kazmierczak, M. J., and Gerner, F. M., 1999, "Developing convective heat transfer in deep rectangular microchannels," Int. *J. Heat and Fluid Flow*, **20**, pp. 149–157.

Hay, H. L. and Hollingsworth, D. K., 1996, "A comparison of trichromic systems for use in the calibration of polymer-dispersed thermochromic liquid crystals," *J. Exp. Therm. and Fluid Sci.*, **12**, pp. 1–12.

Hoffmann, M., Schlüter, M, and Räbiger, N, 2006, "Experimental investigation of liquid–liquid mixing in T-shaped micro-mixers using μ-LIF and μ-PIV," *J. Chem. Eng. Sci.*, **61**, pp. 2968–2976.

Höhmann, C. and Stephan P., 2002, "Microscale temperature measurement at an evaporating liquid meniscus," *J. Exp. Therm. and Fluid Sci.*, **26**, pp.157–162.

Hsieh, S.-S., Wu, F.-Y., and Tsai, H.-H., 2003, "Turbulent heat transfer and flow characteristics in a horizontal circular tube with strip-type inserts. Part I. Fluid mechanics," *Int. J. Heat and Mass Transfer*, **46**, pp. 823–835.

Hwang, Y. W., and Kim, M. S., 2006, "The pressure drop in microtubes and the correlation development," *Int. J. Heat and Mass Transfer*, **49**, pp. 1804–1812.

Ireland, P.T. and Jones, T.V., 2000, "Liquid crystal measurements of heat transfer and surface shear stress," *J. Meas. Sci. and Tech.*, **11**, pp. 969–986.

Jiang, P.-X., Fan, M.-H., Si, G.-S., Ren, Z.-P., 2001, " Thermal-hydraulic performance of small scale micro-channel and porous media heat-exchangers," *Int. J. Heat and Mass Transfer*, **44**, pp. 1039–1051.

Judy, J., Maynes, D., and Webb, B. W., 2002, "Characterization of frictional pressure drop for liquid flows through microchannels," *Int. J. Heat and Mass Transfer*, **45**, pp. 3477–3489.

Kakaç, S., Shah, R. K., and Aung, W., 1987, *Handbook of Single-Phase Convective Heat Transfer*, Wiley, New York.

Kays, W. M., 1966, *Convective Heat and Mass Transfer*, McGraw-Hill, New York, pp. 186–191.

Kays, W. M. and Crawford, M. E., 1993, *Convective Heat and Mass Transfer*, 3rd ed., McGraw-Hill, New York.

Kline, J. and McClintock, F.A., 1953, "Describing uncertainties in single-sample experiments," *J. Mechanical Engineering*, 75, pp. 3-8.

Koo, J., and Kleinstreuer, C., 2004, "Viscous dissipation effects in microtubes and microchannels," *Int. J. Heat and Mass Transfer*, **47**, pp. 3159–3169.

Koutsiaris, A. G., Mathioulakis, D. S., and Tsangaris, S., 1999, "Microscope PIV for velocity-field measurement of particle suspensions flowing inside glass capillaries," *J. Meas. Sci. Technolo.*, **10**, pp. 1037–1046.

Lee, P.-S., Garimella, S. V., and Liu, D., 2005, "Investigation of heat transfer in rectangular microchannels," *Int. J. Heat and Mass Transfer*, **48**, pp. 1688–1704.

Lee, P.-S. and Garimella, S. V., 2006, "Thermally developing flow and heat transfer in rectangular microchannels of different aspect ratios," *Int. J. Heat and Mass Transfer*, **49**, pp. 3060–3067.

Lee, S.-J., and Kim, G.-B., 2003, "Analysis of flow resistance inside microchannels with different inlet configurations using micro-PIV system," *Proc. ASME 1st International Conference on Microchannels and Minichannels (ICMM2003)*, Apr. 21–23, Rochester, NY, ICMM2003-1108.

Lee, S.-Y., Wereley, S. T., Gui, L., Qu, W., and Mudawar, I., 2002, "Microchannel flow measurement using micro particle image velocimetry," *Proc. ASME International Mechanical Engineering Congress and Exposition (IMECE2002)*, Nov. 17–22, New Orleans, LA, ASME Fluids Engineering Division, **258**, pp. 493–500.

Lee, S.-Y., Jang, J., and Wereley, S. T., 2004, "Entrance length of low Reynolds number flow in microchannel," Proc. *ASME International Mechanical Engineering Congress and Exposition (IMECE2004)*, Nov. 13–20, Anaheim, CA, ASME Fluids Engineering Division, IMECE2004-61908, pp. 423–430.

Lee, Y. and Park, S. D., 1971, "Developing turbulent flow in concentric annuli: and analytical and experimental study," *J. Heat and Mass Transfer*, **4**(3), pp. 156–166.

Lelea, D., Nishio, S., and Takano, K., 2004, "The experimental research on microtube heat transfer and fluid flow of distilled water," *Int. J. Heat and Mass Transfer*, **47**, pp. 2817–2830.

Li, H., and Olsen, M. G., 2006, "MicroPIV measurements of turbulent flow in square microchannels with hydraulic diameters from 200 μm to 640 μm," *Int. J. Heat and Fluid Flow*, **27**, pp. 123–134.

Li, Z., He, Y.-L., Tang G.-H., and Tao, W.-Q., 2007, "Experimental and numerical studies of liquid flow and heat transfer in microtubes," *Int. J. Heat and Mass Transfer*, **50**, pp. 3447–3460.

Li, Z.-X., Du, D.-X., and Guo, Z.-Y., 2003, "Experimental study on flow characteristics of liquid in circular microtubes," *J. Microscale Thermophysical Eng.*, **7**, pp. 253–265.

Lien, K., Monty, J. P., Chong, M. S., and Ooi, A., 2004, "The entrance length for fully developed turbulent channel flow," *Proc. 15th Australasian Fluid Mechanics Conference*, Sydney, Australia, Dec. 13–17, paper no. AFMC00093.

Liu, C., 2006, *Foundations of MEMS*, Pearson Prentice Hall, New Jersey.

Mala, G. M., and Li, D., 1999, "Flow characteristics of water in microtubes," *Int. J. Heat and Fluid Flow*, **20**, pp. 142–148.

Malina, J. A. and Sparrow, E. M., 1964, "Variable-property, constant-property, and entrance region heat transfer results for turbulent flow of water and oil in a circular tube," *J. Chem. Eng. Sci*, **19**, pp. 953–962.

Meinhart, C. D., Wereley, S. T., and Santiago, J. G., 1999, "PIV measurements of a microchannel flow," *J. Exp. in Fluids*, **27**, pp. 414–419.

Meinhart, C. D., Wereley, S. T., and Gray, M. H. B., 2000a, "Volume illumination for two-dimensional particle image velocimetry," *J. Meas. Sci. Technolo.*, **11**, pp. 809–814.

Meinhart, C. D., Wereley, S. T., and Santiago, J. G., 2000b, "A PIV algorithm for estimating time-averaged velocity fields," *J. Fluids Eng.*, **122**, pp. 285–289.

Mishan, Y., Mosyak, A., Pogrebnyak, E., and Hestroni, G., 2007, "Effect of developing flow and thermal regime on momentum and heat transfer in micro-scale heat sink," *Int. J. Heat and Mass Transfer*, **50**, pp. 3100–3114.

Muchnik, G. F., Solomonov, S. D., and Gordon, A. R., 1973, "Hydrodynamic development of a laminar velocity field in rectangular channels," *J. Eng. Physics* (USSR), **25**(4), pp. 1268–1271.

Munson, B. R., Young, D. F., and Okiishi, T. H., 2002, *Fundamentals of Fluid Mechanics*, 4th ed., John Wiley & Sons, Hoboken, NJ.

Muwanga, R. S., 2007, *Experimental Study on Heat Transfer Characteristics of Microchannel Systems using Liquid Crystal Thermography*, Ph. D. thesis, Concordia University, Montréal, Québec, Canada.

Muwanga, R. and Hassan, I., 2006a, "Local heat transfer measurements in microchannels using liquid crystal thermography: Methodology development and validation," *J. Heat Transfer*, **128**, pp. 617–626.

Muwanga, R. and Hassan, I., 2006b, "Local heat transfer measurements on a curved microsurface using liquid crystal thermography," *J. Thermophysics and Heat Transfer*, **20**(4), pp. 884–894.

Muwanga, R. and Hassan, I., 2007, "A flow boiling heat transfer investigation of FC-72 in a microtube using liquid crystal thermography," *J. Heat Transfer*, **129**, pp. 977–987.

Muwanga, R., Hassan, I., and MacDonald, R., 2007, "Characteristics of flow boiling oscillations in silicon microchannel heat sinks," *J. Heat Transfer*, **129**, pp. 1341–1351.

Notter, R. H. and Sleicher, C. A., 1972, "A solution to the turbulent Graetz problem – III. Fully developed and entry region heat transfer rates," *J. Chem. Eng. Sci.*, **27**, pp. 2073–2093.

Nguyen, N.-T. and Wu, Z., 2005, "Micromixers – a review," *J. Micromech. and Microeng.*, **15**, pp. R1–R16.

Oak, J., Pence, D. V., and Liburdy, J. A., 2004, "Flow development of co-flowing streams in rectangular micro-channels," *J. Microscale Thermo.* Eng., **8**, pp. 111–128.

Olsen, M. G., and Adrian, R. J., 2000, "Brownian motion and correlation in particle image Velocimetry," *J. Optics & Laser Technology*, **32**, pp. 621–627.

Owhaib, W. and Palm, B., 2004, "Experimental investigation of single-phase convective heat transfer in circular microchannels," *J. Exp. Thermal and Fluid Sci.*, **28**, pp. 105–110.

Papautsky, I, Brazzle, J., Swerdlow, H., and Frazier, A. B., 1998, "A low temperature IC-compatible process for fabricating surface-micromachined metallic microchannels," *J. Microelectromechanical Sys.*, **7**(2), pp. 267–273.

Papautsky, I., Ameel, T., and Frazier, A.B., 2001, "A review of laminar single-phase flow in microchannels," *Proc. ASME International Mechanical Engineering Congress and Exposition (IMECE2001)*, November 11–16, New York, NY, **3**, Micro-Electro-Mechanical Systems (MEMS), pp. 495–503.

Pfahler, J., Harley, J., Bau, H., and Zemel, J., 1990, "Liquid transport in micron and submicron channels," *Proc. 5th International Conference on Solid-State Sensors and Actuators and Eurosensors III (Transducers '89)*, Part 3, June 25–30, Montreux, Switz., Sensors and Actuators, A:Physical, **22**, n 1-3, pp. 431–434.

Pfund, D., Rector, D., Shekarriz, A., Popescu, A., and Welty, J., 2000, "Pressure drop measurements in a microchannel," *AIChE Journal*, **46**, pp. 1496–1507.

Prasad, A. K., Adrian, R. J., Landreth, C. C., and P. W. Offutt, 1992, "Effect of resolution on the speed and accuracy of particle image velocimetry interrogation," *J. Experiments in Fluids*, **13**, pp. 105–116.

Santiago, J. G., Wereley, S. T., Meinhart, C. D., Beebe, D. J., and Adrian, R. J., 1998, "A particle image velocimetry system for microfluidics," *J. Exp. in Fluids,* **25**, pp. 316–319.

Shah, R. K., 1975, "Thermal entry length solutions for the circular tube and parallel plates," *Proc. 3rd National Heat and Mass Transfer Conference,* Bombay, India, **1**, HMT-11-75.

Shah, R. K., and London, A. L., 1978, *Laminar Flow Forced Convection in Ducts,* Advances in Heat Transfer – Supplement 1, Academic Press, New York.

Sharp, K. V., and Adrian, R. J., 2004, "Transition from laminar to turbulent flow in liquid filled microtubes," *J. Exp. in Fluids,* **36**, pp. 741–747.

Sparrow, E. M., Hallman, T. M., and Siegel, R., 1957, "Turbulent heat transfer in the thermal entrance region of a pipe with uniform heat flux," *Appl. Sci. Res.* (Sect. A), **7**, pp. 37–52.

Sparrow, E. M., Hixon, C. W., and Shavit, G., 1967, "Experiments on laminar flow development in rectangular ducts," *J. Basic Engineering,* **89**, pp. 116–124.

Steinke, M. E., and Kandlikar, S. G., 2005, "Single-phase liquid friction factors in microchannels," *Proc. ASME 3rd International Conference on Microchannels and Minichannels (ICMM2005)*, June 13–15, Toronto, Canada, ICMM2005-75112.

Streeter, V.L., 1961, *Handbook of Fluid Dynamics*, McGraw-Hill Book Company Inc, 1st ed., pp.3-8 – 3-22.

Suzuki, Y., Okada, Y., Ogawa, J., Sugiyama, S., and Toriyama, T., 2008, "Experimental study on mechanical power generation from MEMS internal combustion engine," *J. Sensors and Actuators: A Physical*, **141**, pp. 654–661.

Tuckerman, D.B. and Pease, R.F.W., 1981, "High-performance heat sinking for VLSI," *IEEE Electron Device Letters*, **vol. EDL-2**, no. 5, pp. 126-129.

Vrentas, J. S., Duda, J. L., and Bargeron, K. G., 1966, "Effect of axial diffusion of vorticity on flow development in circular conduits: Part I. Numerical solutions," *J. AIChE*, **12**(5), pp. 837–844.

Weilin, Q., Mala, G. M., and Li, D., 2000, "Pressure-driven water flows in trapezoidal silicon microchannels," *Int. J. Heat and Mass Transfer*, **43**, pp. 353–364.

White, F. M., 1991, *Viscous Fluid Flow*, 2nd ed., McGraw-Hill, New York, pp. 117, 422–424.

Whitesides, G. M., 2006, "The origins and the future of microfluidics," *Nature*, **442**, pp. 368–373.

Wiginton, C. L. and Dalton C., 1970, "Incompressible laminar flow in the entrance region of a rectangular duct," *J. Applied Mech.*, **37**, pp. 854–856.

Woodmansee, W. E., 1968, "Aerospace thermal mapping applications of liquid crystals," *J. Applied Optics*, **7**(9), pp. 1721–1727.

Wu, H. Y., and Cheng, P., 2003, "Friction factors in smooth trapezoidal silicon microchannels with different aspect ratios," *Int. J. Heat and Mass Transfer*, **46**, pp. 2519–2525.

Wu, P., and Little, W. A., 1983, "Measurement of friction factors for the flow of gases in very fine channels used for microminiature Joule-Thomson refrigerators," *J. Cryogenics*, **23**, pp. 273–277.

Yager, P., Edwards, T., Fu, E., Helton, K., Nelson, K., Tam, M. R., and Weigl, B. H., 2006, "Microfluidic diagnostic technologies for global public health," *Nature*, **442**, pp. 412–418.

Yang, C.-Y., Wu, J.-C., Chien, H.-T., and Lu, S.-R., 2003, "Friction characteristics of water, R-134a, and air in small tubes," *J. Microscale Thermophysical Eng.*, **7**, pp. 335–348.

Yang, C.-Y. and Lin, T.-Y., 2007, "Heat transfer characteristics of water flow in microtubes," *J. Exp. Thermal and Fluid Sci.*, **32**, pp. 432–110.

Yi, W., Jeong, T., Jin, S., Yu, S., Lee, J., and Kim, J. M., 2000, "Novel fabrication method of microchannel plates," *J. Review of Scientific Instruments*, **71**(11), pp. 4165–4169.

Yu, D., Warrington, R., Barron, R., and Ameel, T., 1995, "An experimental and theoretical investigation of fluid flow and heat transfer in microtubes," *Proc. ASME/JSME Joint Thermal Engineering Conference*, March 19–25, Maui, Hawaii, **1**, pp. 523–530.

Zeighami, R., Laser, D., Zhou, P., Asheghi, M., Devasenathipathy, S., Kenny, T., Santiago, J., and Goodson, K., 2000, "Experimental investigation of flow transition in microchannels using micro-resolution particle image velocimetry," *Proc. IEEE 7th Intersociety Conference on Thermomechanical Phenomena in Electronic Systems*, May 23–26, Las Vegas, NV, **2**, ITHERM.2000.866184, pp. 148–153.

# Appendix A

# Experimental Data for the Hydrodynamic Entrance Region

## A.1 Developing Velocity Profiles at Axial Locations from Channel Inlet

Table A.1: Velocity Profiles, $D_h$ = 100 μm, Re = 0.476, Distilled Water

| $z/W$ | 4 μm | 19 μm | 34 μm | 50 μm | 65 μm | 80 μm | 148 μm |
|---|---|---|---|---|---|---|---|
| | $u/u_{max,FD}$ | $u/u_{max,FD}$ | $u/u_{max,FD}$ | $u/u_{max,FD}$ | $u/u_{max,FD}$ | $u/u_{max,FD}$ | $u/u_{max,FD}$ |
| 0.0449 | 0.0495 | 0.1057 | 0.1579 | 0.2033 | 0.2145 | 0.2167 | 0.3587 |
| 0.1207 | 0.0780 | 0.1804 | 0.2752 | 0.3463 | 0.3742 | 0.3996 | 0.4675 |
| 0.1966 | 0.1408 | 0.2907 | 0.4249 | 0.5008 | 0.5507 | 0.5975 | 0.6144 |
| 0.2724 | 0.2406 | 0.4282 | 0.5880 | 0.6533 | 0.7162 | 0.7666 | 0.7768 |
| 0.3483 | 0.3524 | 0.5624 | 0.7351 | 0.7915 | 0.8518 | 0.8967 | 0.9028 |
| 0.4242 | 0.4610 | 0.6632 | 0.8197 | 0.8853 | 0.9392 | 0.9768 | 0.9790 |
| 0.5000 | 0.5398 | 0.7052 | 0.8340 | 0.9094 | 0.9625 | 0.9987 | 0.9926 |
| 0.5759 | 0.5460 | 0.6799 | 0.7783 | 0.8684 | 0.9270 | 0.9630 | 0.9653 |
| 0.6517 | 0.4559 | 0.5656 | 0.6631 | 0.7671 | 0.8435 | 0.8867 | 0.9028 |
| 0.7276 | 0.3233 | 0.4243 | 0.5265 | 0.6373 | 0.7243 | 0.7773 | 0.7768 |
| 0.8034 | 0.2073 | 0.2892 | 0.3841 | 0.4951 | 0.5954 | 0.6776 | 0.6144 |
| 0.8793 | 0.1398 | 0.2117 | 0.2847 | 0.3803 | 0.4712 | 0.3996 | 0.4675 |
| 0.9551 | 0.0955 | 0.1506 | 0.2054 | 0.2838 | 0.3125 | 0.2167 | 0.3587 |

Table A.2: Velocity Profiles, $D_h$ = 100 µm, Re = 4.76, Distilled Water

| $z/W$ | 4 µm | 19 µm | 50 µm | 65 µm | 80 µm | 95 µm | 156 µm |
|---|---|---|---|---|---|---|---|
| | $u/u_{max,FD}$ | $u/u_{max,FD}$ | $u/u_{max,FD}$ | $u/u_{max,FD}$ | $u/u_{max,FD}$ | $u/u_{max,FD}$ | $u/u_{max,FD}$ |
| 0.0449 | 0.0116 | 0.0234 | 0.0951 | 0.1523 | 0.1906 | 0.2156 | 0.2050 |
| 0.1207 | 0.0154 | 0.0264 | 0.1370 | 0.2492 | 0.3471 | 0.3957 | 0.3976 |
| 0.1966 | 0.0165 | 0.0203 | 0.1816 | 0.3656 | 0.5236 | 0.5969 | 0.6115 |
| 0.2724 | 0.0172 | 0.0367 | 0.2978 | 0.5219 | 0.6940 | 0.7558 | 0.7784 |
| 0.3483 | 0.0394 | 0.1114 | 0.4977 | 0.7094 | 0.8443 | 0.8876 | 0.8997 |
| 0.4242 | 0.1114 | 0.2475 | 0.6964 | 0.8581 | 0.9443 | 0.9701 | 0.9762 |
| 0.5000 | 0.1904 | 0.3716 | 0.8231 | 0.9304 | 0.9773 | 0.9956 | 0.9932 |
| 0.5759 | 0.1927 | 0.3698 | 0.8002 | 0.9002 | 0.9393 | 0.9540 | 0.9464 |
| 0.6517 | 0.1262 | 0.2632 | 0.6647 | 0.7886 | 0.8444 | 0.8636 | 0.8585 |
| 0.7276 | 0.0473 | 0.1372 | 0.4734 | 0.6213 | 0.7102 | 0.7444 | 0.7490 |
| 0.8034 | 0.0203 | 0.0696 | 0.2800 | 0.4018 | 0.5100 | 0.5836 | 0.6185 |
| 0.8793 | 0.0141 | 0.0423 | 0.1546 | 0.2316 | 0.3250 | 0.4113 | 0.4775 |
| 0.9551 | 0.0129 | 0.0296 | 0.0791 | 0.1138 | 0.1739 | 0.2537 | 0.3402 |

Table A.3: Velocity Profiles, $D_h$ = 100 µm, Re = 50, Distilled Water

| $z/W$ | 4 µm | 34 µm | 65 µm | 110 µm | 193 µm | 285 µm | 390 µm |
|---|---|---|---|---|---|---|---|
| | $u/u_{max,FD}$ | $u/u_{max,FD}$ | $u/u_{max,FD}$ | $u/u_{max,FD}$ | $u/u_{max,FD}$ | $u/u_{max,FD}$ | $u/u_{max,FD}$ |
| 0.0449 | 0.0412 | 0.0810 | 0.2131 | 0.2441 | 0.2837 | 0.3019 | 0.3194 |
| 0.1207 | 0.0575 | 0.1313 | 0.3596 | 0.4421 | 0.4350 | 0.4435 | 0.4586 |
| 0.1966 | 0.0848 | 0.2066 | 0.5172 | 0.6374 | 0.6237 | 0.6239 | 0.6445 |
| 0.2724 | 0.1534 | 0.3219 | 0.6604 | 0.7752 | 0.7882 | 0.7808 | 0.8106 |
| 0.3483 | 0.2629 | 0.4634 | 0.7657 | 0.8759 | 0.9012 | 0.8983 | 0.9265 |
| 0.4242 | 0.4066 | 0.5929 | 0.8248 | 0.9253 | 0.9653 | 0.9638 | 0.9850 |
| 0.5000 | 0.5102 | 0.6674 | 0.8469 | 0.9417 | 0.9780 | 0.9792 | 0.9891 |
| 0.5759 | 0.5469 | 0.6758 | 0.8375 | 0.9141 | 0.9405 | 0.9476 | 0.9419 |
| 0.6517 | 0.4902 | 0.6191 | 0.7951 | 0.8591 | 0.8863 | 0.8938 | 0.8679 |
| 0.7276 | 0.3806 | 0.5055 | 0.7010 | 0.7729 | 0.8439 | 0.8380 | 0.8106 |
| 0.8034 | 0.2698 | 0.3736 | 0.5542 | 0.6760 | 0.6237 | 0.6239 | 0.6510 |
| 0.8793 | 0.1957 | 0.2682 | 0.4123 | 0.4421 | 0.4350 | 0.4435 | 0.4586 |
| 0.9551 | 0.1640 | 0.2154 | 0.2985 | 0.2441 | 0.2837 | 0.3019 | 0.3194 |

Table A.4: Velocity Profiles, $D_h$ = 100 μm, Re = 89, Distilled Water

| $z/W$ | 4 μm | 34 μm | 65 μm | 110 μm | 193 μm | 285 μm | 390 μm |
|---|---|---|---|---|---|---|---|
| | $u/u_{max,FD}$ | $u/u_{max,FD}$ | $u/u_{max,FD}$ | $u/u_{max,FD}$ | $u/u_{max,FD}$ | $u/u_{max,FD}$ | $u/u_{max,FD}$ |
| 0.0449 | 0.0401 | 0.0585 | 0.1527 | 0.2421 | 0.2862 | 0.3082 | 0.3378 |
| 0.1207 | 0.0644 | 0.1074 | 0.2889 | 0.4393 | 0.4328 | 0.4439 | 0.4915 |
| 0.1966 | 0.1367 | 0.2102 | 0.4500 | 0.6147 | 0.5973 | 0.6186 | 0.6609 |
| 0.2724 | 0.2294 | 0.3438 | 0.5978 | 0.7345 | 0.7397 | 0.7794 | 0.8184 |
| 0.3483 | 0.2998 | 0.4428 | 0.6895 | 0.8057 | 0.8413 | 0.8969 | 0.9294 |
| 0.4242 | 0.3149 | 0.4794 | 0.7329 | 0.8341 | 0.9003 | 0.9519 | 0.9837 |
| 0.5000 | 0.2969 | 0.4598 | 0.7363 | 0.8400 | 0.9050 | 0.9553 | 0.9874 |
| 0.5759 | 0.2717 | 0.4209 | 0.7082 | 0.8198 | 0.8676 | 0.9130 | 0.9518 |
| 0.6517 | 0.2385 | 0.3669 | 0.6514 | 0.7791 | 0.8062 | 0.8547 | 0.8781 |
| 0.7276 | 0.1986 | 0.3083 | 0.5697 | 0.7108 | 0.7259 | 0.8184 | 0.8205 |
| 0.8034 | 0.1520 | 0.2386 | 0.4449 | 0.5912 | 0.6328 | 0.6186 | 0.6610 |
| 0.8793 | 0.0645 | 0.1075 | 0.2891 | 0.4393 | 0.4672 | 0.4440 | 0.4913 |
| 0.9551 | 0.0400 | 0.0586 | 0.1525 | 0.2421 | 0.2878 | 0.3080 | 0.3380 |

Table A.5: Velocity Profiles, $D_h$ = 200 μm, Re = 0.5, Distilled Water

| $z/W$ | 1 μm | 16 μm | 32 μm | 48 μm | 121 μm | 169 μm | 378 μm |
|---|---|---|---|---|---|---|---|
| | $u/u_{max,FD}$ | $u/u_{max,FD}$ | $u/u_{max,FD}$ | $u/u_{max,FD}$ | $u/u_{max,FD}$ | $u/u_{max,FD}$ | $u/u_{max,FD}$ |
| 0.0170 | 0.0040 | 0.0000 | 0.0169 | 0.0302 | 0.0551 | 0.1177 | 0.1700 |
| 0.0573 | 0.0094 | 0.0175 | 0.0429 | 0.0686 | 0.0683 | 0.1463 | 0.2113 |
| 0.0975 | 0.0522 | 0.0590 | 0.0844 | 0.1226 | 0.1381 | 0.2103 | 0.2745 |
| 0.1378 | 0.1076 | 0.1240 | 0.1528 | 0.2022 | 0.2786 | 0.3193 | 0.3662 |
| 0.1780 | 0.1843 | 0.2263 | 0.2682 | 0.3142 | 0.4413 | 0.4565 | 0.4884 |
| 0.2183 | 0.2858 | 0.3713 | 0.4371 | 0.4823 | 0.5947 | 0.5861 | 0.6139 |
| 0.2585 | 0.3886 | 0.5104 | 0.5994 | 0.6425 | 0.7063 | 0.7035 | 0.7264 |
| 0.2988 | 0.4775 | 0.6257 | 0.7280 | 0.7728 | 0.7997 | 0.7956 | 0.8215 |
| 0.3390 | 0.5202 | 0.6889 | 0.7961 | 0.8468 | 0.8759 | 0.8666 | 0.8884 |
| 0.3793 | 0.5228 | 0.7191 | 0.8542 | 0.9065 | 0.9328 | 0.9221 | 0.9347 |
| 0.4195 | 0.4875 | 0.7250 | 0.8908 | 0.9514 | 0.9727 | 0.9613 | 0.9573 |
| 0.4598 | 0.4459 | 0.7069 | 0.8970 | 0.9628 | 0.9976 | 0.9851 | 0.9797 |
| 0.5000 | 0.4226 | 0.6979 | 0.8799 | 0.9439 | 1.0086 | 0.9945 | 0.9920 |
| 0.5403 | 0.4103 | 0.6706 | 0.8400 | 0.9070 | 1.0006 | 0.9933 | 0.9961 |
| 0.5805 | 0.4149 | 0.6459 | 0.7994 | 0.8741 | 0.9769 | 0.9747 | 0.9750 |
| 0.6207 | 0.4386 | 0.6226 | 0.7582 | 0.8396 | 0.9408 | 0.9375 | 0.9361 |
| 0.6610 | 0.4513 | 0.5783 | 0.6870 | 0.7649 | 0.8962 | 0.8941 | 0.8820 |

| $z/W$ | 1 μm | 16 μm | 32 μm | 48 μm | 121 μm | 169 μm | 378 μm |
|---|---|---|---|---|---|---|---|
| | $u/u_{max,FD}$ | $u/u_{max,FD}$ | $u/u_{max,FD}$ | $u/u_{max,FD}$ | $u/u_{max,FD}$ | $u/u_{max,FD}$ | $u/u_{max,FD}$ |
| 0.7012 | 0.4079 | 0.4829 | 0.5635 | 0.6426 | 0.8372 | 0.8384 | 0.8168 |
| 0.7415 | 0.2871 | 0.3231 | 0.3832 | 0.4712 | 0.7544 | 0.7616 | 0.7401 |
| 0.7817 | 0.1606 | 0.1696 | 0.2082 | 0.2914 | 0.6582 | 0.6529 | 0.6423 |
| 0.8220 | 0.0716 | 0.0698 | 0.0911 | 0.1521 | 0.5373 | 0.5292 | 0.5296 |
| 0.8622 | 0.0336 | 0.0264 | 0.0355 | 0.0714 | 0.4313 | 0.4129 | 0.4152 |
| 0.9025 | 0.0145 | 0.0095 | 0.0200 | 0.0465 | 0.3345 | 0.3203 | 0.3256 |
| 0.9427 | 0.0076 | 0.0051 | 0.0139 | 0.0320 | 0.2820 | 0.2586 | 0.2553 |
| 0.9830 | 0.0043 | 0.0047 | 0.0110 | 0.0229 | 0.2426 | 0.2113 | 0.1837 |

Table A.6: Velocity Profiles, $D_h$ = 200 μm, Re = 5, Distilled Water

| $z/W$ | 1 μm | 16 μm | 48 μm | 64 μm | 80 μm | 96 μm | 281 μm |
|---|---|---|---|---|---|---|---|
| | $u/u_{max,FD}$ | $u/u_{max,FD}$ | $u/u_{max,FD}$ | $u/u_{max,FD}$ | $u/u_{max,FD}$ | $u/u_{max,FD}$ | $u/u_{max,FD}$ |
| 0.0170 | 0.0023 | 0.0000 | 0.0017 | 0.0077 | 0.0151 | 0.0396 | 0.0970 |
| 0.0573 | 0.0105 | 0.0056 | 0.0157 | 0.0326 | 0.0526 | 0.0870 | 0.1882 |
| 0.0975 | 0.0351 | 0.0370 | 0.1311 | 0.0469 | 0.0848 | 0.1230 | 0.2526 |
| 0.1378 | 0.0830 | 0.0405 | 0.1204 | 0.1834 | 0.2417 | 0.2766 | 0.3562 |
| 0.1780 | 0.1551 | 0.1438 | 0.2743 | 0.3458 | 0.4063 | 0.4376 | 0.4764 |
| 0.2183 | 0.2327 | 0.2582 | 0.4234 | 0.4869 | 0.5437 | 0.5716 | 0.5998 |
| 0.2585 | 0.3188 | 0.3765 | 0.5495 | 0.6015 | 0.6537 | 0.6785 | 0.7024 |
| 0.2988 | 0.4108 | 0.4957 | 0.6541 | 0.6973 | 0.7481 | 0.7731 | 0.7905 |
| 0.3390 | 0.5035 | 0.6037 | 0.7402 | 0.7728 | 0.8182 | 0.8443 | 0.8718 |
| 0.3793 | 0.5554 | 0.6689 | 0.7952 | 0.8281 | 0.8763 | 0.9040 | 0.9357 |
| 0.4195 | 0.5498 | 0.6815 | 0.8168 | 0.8595 | 0.9086 | 0.9406 | 0.9807 |
| 0.4598 | 0.4961 | 0.6506 | 0.8092 | 0.8700 | 0.9290 | 0.9656 | 0.9902 |
| 0.5000 | 0.4099 | 0.5644 | 0.7719 | 0.8625 | 0.9344 | 0.9767 | 0.9867 |
| 0.5403 | 0.3277 | 0.4530 | 0.7075 | 0.8344 | 0.9302 | 0.9743 | 0.9732 |
| 0.5805 | 0.2584 | 0.3395 | 0.6308 | 0.7958 | 0.9169 | 0.9624 | 0.9608 |
| 0.6207 | 0.2257 | 0.2832 | 0.5783 | 0.7541 | 0.8890 | 0.9337 | 0.9377 |
| 0.6610 | 0.1969 | 0.2402 | 0.5237 | 0.7011 | 0.8402 | 0.8920 | 0.8966 |
| 0.7012 | 0.1816 | 0.2164 | 0.4707 | 0.6358 | 0.7700 | 0.8230 | 0.8247 |
| 0.7415 | 0.1702 | 0.1814 | 0.3994 | 0.5505 | 0.6715 | 0.7267 | 0.7418 |
| 0.7817 | 0.1555 | 0.1388 | 0.3139 | 0.4446 | 0.5523 | 0.6074 | 0.6442 |
| 0.8220 | 0.1215 | 0.1148 | 0.2227 | 0.3328 | 0.4227 | 0.4768 | 0.5353 |
| 0.8622 | 0.0785 | 0.0839 | 0.1180 | 0.2136 | 0.2940 | 0.3478 | 0.4201 |
| 0.9025 | 0.0470 | 0.0442 | 0.1163 | 0.1201 | 0.1826 | 0.2298 | 0.3207 |
| 0.9427 | 0.0309 | 0.0236 | 0.0673 | 0.0513 | 0.1010 | 0.1435 | 0.2301 |
| 0.9830 | 0.0233 | 0.0198 | 0.0482 | 0.0130 | 0.0464 | 0.0774 | 0.1143 |

Table A.7: Velocity Profiles, $D_h$ = 200 µm, Re = 50, Distilled Water

| $z/W$ | 1 µm | 16 µm | 64 µm | 144 µm | 314 µm | 846 µm | 1096 µm |
|---|---|---|---|---|---|---|---|
| | $u/u_{max,FD}$ | $u/u_{max,FD}$ | $u/u_{max,FD}$ | $u/u_{max,FD}$ | $u/u_{max,FD}$ | $u/u_{max,FD}$ | $u/u_{max,FD}$ |
| 0.0170 | 0.0138 | 0.0101 | 0.0112 | 0.0584 | 0.2650 | 0.0804 | 0.0579 |
| 0.0573 | 0.0360 | 0.0329 | 0.0269 | 0.0870 | 0.2745 | 0.0644 | 0.1037 |
| 0.0975 | 0.0674 | 0.0676 | 0.0835 | 0.1614 | 0.3197 | 0.1643 | 0.1936 |
| 0.1378 | 0.1162 | 0.1290 | 0.2003 | 0.2869 | 0.3957 | 0.3012 | 0.3000 |
| 0.1780 | 0.1719 | 0.2009 | 0.3513 | 0.4474 | 0.5061 | 0.4477 | 0.4331 |
| 0.2183 | 0.2328 | 0.2811 | 0.4831 | 0.5842 | 0.6121 | 0.5668 | 0.5652 |
| 0.2585 | 0.2878 | 0.3507 | 0.5750 | 0.6894 | 0.7084 | 0.6731 | 0.6794 |
| 0.2988 | 0.3407 | 0.4172 | 0.6325 | 0.7583 | 0.7821 | 0.7684 | 0.7828 |
| 0.3390 | 0.3757 | 0.4618 | 0.6772 | 0.8071 | 0.8381 | 0.8453 | 0.8641 |
| 0.3793 | 0.3795 | 0.4777 | 0.7016 | 0.8389 | 0.8816 | 0.8965 | 0.9264 |
| 0.4195 | 0.3540 | 0.4700 | 0.7153 | 0.8638 | 0.9070 | 0.9279 | 0.9658 |
| 0.4598 | 0.3209 | 0.4624 | 0.7240 | 0.8806 | 0.9212 | 0.9537 | 0.9868 |
| 0.5000 | 0.3079 | 0.4679 | 0.7364 | 0.8840 | 0.9227 | 0.9714 | 0.9987 |
| 0.5403 | 0.3131 | 0.4809 | 0.7483 | 0.8820 | 0.9205 | 0.9807 | 1.0023 |
| 0.5805 | 0.3370 | 0.4849 | 0.7498 | 0.8692 | 0.9084 | 0.9714 | 0.9946 |
| 0.6207 | 0.3430 | 0.4687 | 0.7344 | 0.8540 | 0.8858 | 0.9472 | 0.9697 |
| 0.6610 | 0.3340 | 0.4306 | 0.7048 | 0.8221 | 0.8441 | 0.8964 | 0.9219 |
| 0.7012 | 0.2822 | 0.3688 | 0.6626 | 0.7790 | 0.7884 | 0.8297 | 0.8569 |
| 0.7415 | 0.2090 | 0.2688 | 0.5933 | 0.7187 | 0.7173 | 0.7474 | 0.7821 |
| 0.7817 | 0.1357 | 0.1727 | 0.4930 | 0.6375 | 0.6266 | 0.6621 | 0.6916 |
| 0.8220 | 0.0853 | 0.0990 | 0.3723 | 0.5429 | 0.5245 | 0.5553 | 0.5929 |
| 0.8622 | 0.0615 | 0.0676 | 0.2551 | 0.4330 | 0.4232 | 0.4454 | 0.4927 |
| 0.9025 | 0.0422 | 0.0410 | 0.1618 | 0.3413 | 0.3378 | 0.3537 | 0.3979 |
| 0.9427 | 0.0260 | 0.0209 | 0.0989 | 0.2620 | 0.2850 | 0.3059 | 0.3162 |
| 0.9830 | 0.0159 | 0.0144 | 0.0628 | 0.1901 | 0.2653 | 0.2979 | 0.2492 |

Table A.8: Velocity Profiles, $D_h$ = 200 µm, Re = 200, Distilled Water

| $z/W$ | 1 µm | 16 µm | 64 µm | 282 µm | 782 µm | 1096 µm | 2096 µm |
|---|---|---|---|---|---|---|---|
| | $u/u_{max,FD}$ | $u/u_{max,FD}$ | $u/u_{max,FD}$ | $u/u_{max,FD}$ | $u/u_{max,FD}$ | $u/u_{max,FD}$ | $u/u_{max,FD}$ |
| 0.0170 | 0.0000 | 0.0021 | 0.0140 | 0.2193 | 0.1007 | 0.2160 | 0.1075 |
| 0.0573 | 0.0193 | 0.0223 | 0.0352 | 0.2632 | 0.1386 | 0.1843 | 0.1779 |
| 0.0975 | 0.0405 | 0.0479 | 0.0841 | 0.3391 | 0.2287 | 0.2202 | 0.2827 |
| 0.1378 | 0.0737 | 0.0919 | 0.2060 | 0.4451 | 0.3573 | 0.3228 | 0.4191 |
| 0.1780 | 0.1149 | 0.1469 | 0.3529 | 0.5610 | 0.4923 | 0.4621 | 0.5449 |
| 0.2183 | 0.1750 | 0.2174 | 0.4883 | 0.6538 | 0.6141 | 0.5935 | 0.6574 |

| z/W | 1 µm | 16 µm | 64 µm | 282 µm | 782 µm | 1096 µm | 2096 µm |
|---|---|---|---|---|---|---|---|
| | $u/u_{max,FD}$ | $u/u_{max,FD}$ | $u/u_{max,FD}$ | $u/u_{max,FD}$ | $u/u_{max,FD}$ | $u/u_{max,FD}$ | $u/u_{max,FD}$ |
| 0.2585 | 0.2462 | 0.3024 | 0.5662 | 0.7128 | 0.7029 | 0.6983 | 0.7426 |
| 0.2988 | 0.3218 | 0.3901 | 0.6156 | 0.7479 | 0.7673 | 0.7766 | 0.8076 |
| 0.3390 | 0.3748 | 0.4548 | 0.6413 | 0.7678 | 0.8164 | 0.8345 | 0.8626 |
| 0.3793 | 0.3842 | 0.4702 | 0.6465 | 0.7796 | 0.8526 | 0.8757 | 0.9086 |
| 0.4195 | 0.3555 | 0.4498 | 0.6428 | 0.7863 | 0.8746 | 0.9000 | 0.9435 |
| 0.4598 | 0.3136 | 0.4171 | 0.6457 | 0.7891 | 0.8809 | 0.9139 | 0.9675 |
| 0.5000 | 0.2939 | 0.4042 | 0.6522 | 0.7871 | 0.8866 | 0.9214 | 0.9755 |
| 0.5403 | 0.2935 | 0.4064 | 0.6563 | 0.7855 | 0.8874 | 0.9200 | 0.9662 |
| 0.5805 | 0.3023 | 0.4080 | 0.6534 | 0.7835 | 0.8750 | 0.9117 | 0.9336 |
| 0.6207 | 0.2954 | 0.3888 | 0.6452 | 0.7795 | 0.8538 | 0.8891 | 0.8877 |
| 0.6610 | 0.2821 | 0.3615 | 0.6287 | 0.7656 | 0.8226 | 0.8558 | 0.8299 |
| 0.7012 | 0.2547 | 0.3250 | 0.6019 | 0.7380 | 0.7877 | 0.8058 | 0.7716 |
| 0.7415 | 0.2036 | 0.2558 | 0.5563 | 0.6986 | 0.7355 | 0.7382 | 0.6950 |
| 0.7817 | 0.1418 | 0.1779 | 0.4780 | 0.6443 | 0.6588 | 0.6535 | 0.5986 |
| 0.8220 | 0.0894 | 0.1081 | 0.3763 | 0.5680 | 0.5598 | 0.5565 | 0.4869 |
| 0.8622 | 0.0627 | 0.0761 | 0.2688 | 0.4658 | 0.4526 | 0.4670 | 0.3948 |
| 0.9025 | 0.0488 | 0.0543 | 0.1786 | 0.3609 | 0.3545 | 0.3893 | 0.3331 |
| 0.9427 | 0.0352 | 0.0357 | 0.1153 | 0.2685 | 0.2839 | 0.3254 | 0.2994 |
| 0.9830 | 0.0247 | 0.0241 | 0.0736 | 0.2068 | 0.2376 | 0.2729 | 0.2921 |

Table A.9: Velocity Profiles, $D_h$ = 500 µm, Re = 0.5, Distilled Water

| z/W | 12 µm | 43 µm | 74 µm | 105 µm | 167 µm | 322 µm | 543 µm |
|---|---|---|---|---|---|---|---|
| | $u/u_{max,FD}$ | $u/u_{max,FD}$ | $u/u_{max,FD}$ | $u/u_{max,FD}$ | $u/u_{max,FD}$ | $u/u_{max,FD}$ | $u/u_{max,FD}$ |
| 0.0046 | 0.1552 | 0.1677 | 0.2032 | 0.2099 | 0.2014 | 0.1330 | 0.1585 |
| 0.0356 | 0.1914 | 0.2044 | 0.2308 | 0.2442 | 0.2584 | 0.1783 | 0.2020 |
| 0.0666 | 0.2562 | 0.2601 | 0.2756 | 0.2920 | 0.3323 | 0.2548 | 0.2758 |
| 0.0975 | 0.3343 | 0.3344 | 0.3413 | 0.3545 | 0.4054 | 0.3543 | 0.3675 |
| 0.1285 | 0.3978 | 0.4059 | 0.4192 | 0.4330 | 0.4742 | 0.4622 | 0.4541 |
| 0.1594 | 0.4397 | 0.4687 | 0.5002 | 0.5225 | 0.5432 | 0.5500 | 0.5281 |
| 0.1904 | 0.4721 | 0.5211 | 0.5765 | 0.6126 | 0.6207 | 0.6248 | 0.5996 |
| 0.2214 | 0.5176 | 0.5844 | 0.6538 | 0.6944 | 0.6921 | 0.6887 | 0.6746 |
| 0.2523 | 0.5777 | 0.6502 | 0.7164 | 0.7581 | 0.7595 | 0.7480 | 0.7414 |
| 0.2833 | 0.6341 | 0.7076 | 0.7710 | 0.8119 | 0.8193 | 0.8017 | 0.7984 |
| 0.3142 | 0.6866 | 0.7522 | 0.8151 | 0.8552 | 0.8748 | 0.8485 | 0.8427 |
| 0.3452 | 0.7222 | 0.7876 | 0.8572 | 0.8971 | 0.9167 | 0.8916 | 0.8861 |
| 0.3762 | 0.7448 | 0.8092 | 0.8836 | 0.9265 | 0.9445 | 0.9282 | 0.9230 |
| 0.4071 | 0.7564 | 0.8218 | 0.8983 | 0.9456 | 0.9645 | 0.9585 | 0.9568 |

| $z/W$ | 12 µm $u/u_{max,FD}$ | 43 µm $u/u_{max,FD}$ | 74 µm $u/u_{max,FD}$ | 105 µm $u/u_{max,FD}$ | 167 µm $u/u_{max,FD}$ | 322 µm $u/u_{max,FD}$ | 543 µm $u/u_{max,FD}$ |
|---|---|---|---|---|---|---|---|
| 0.4381 | 0.7692 | 0.8269 | 0.9014 | 0.9483 | 0.9782 | 0.9803 | 0.9812 |
| 0.4690 | 0.7621 | 0.8279 | 0.9054 | 0.9514 | 0.9882 | 0.9944 | 0.9941 |
| 0.5000 | 0.7341 | 0.8209 | 0.9070 | 0.9529 | 0.9881 | 0.9986 | 0.9998 |
| 0.5310 | 0.6948 | 0.8016 | 0.9036 | 0.9534 | 0.9819 | 0.9910 | 0.9928 |
| 0.5619 | 0.6784 | 0.7857 | 0.8882 | 0.9440 | 0.9685 | 0.9783 | 0.9812 |
| 0.5929 | 0.6792 | 0.7737 | 0.8692 | 0.9249 | 0.9479 | 0.9620 | 0.9660 |
| 0.6238 | 0.6695 | 0.7595 | 0.8454 | 0.9033 | 0.9229 | 0.9435 | 0.9444 |
| 0.6548 | 0.6552 | 0.7400 | 0.8207 | 0.8726 | 0.8893 | 0.9129 | 0.9174 |
| 0.6858 | 0.6374 | 0.7116 | 0.7827 | 0.8323 | 0.8524 | 0.8777 | 0.8778 |
| 0.7167 | 0.6293 | 0.6872 | 0.7430 | 0.7815 | 0.8009 | 0.8418 | 0.8344 |
| 0.7477 | 0.6116 | 0.6563 | 0.6950 | 0.7243 | 0.7413 | 0.7986 | 0.7820 |
| 0.7786 | 0.5796 | 0.6170 | 0.6458 | 0.6648 | 0.6712 | 0.7423 | 0.7200 |
| 0.8096 | 0.5235 | 0.5525 | 0.5747 | 0.5958 | 0.5973 | 0.6765 | 0.6503 |
| 0.8406 | 0.4551 | 0.4755 | 0.4913 | 0.5100 | 0.5133 | 0.6068 | 0.5794 |
| 0.8715 | 0.3706 | 0.3738 | 0.3769 | 0.3951 | 0.4182 | 0.5305 | 0.5048 |
| 0.9025 | 0.2870 | 0.2677 | 0.2536 | 0.2644 | 0.3142 | 0.4319 | 0.4263 |
| 0.9334 | 0.2098 | 0.1781 | 0.1621 | 0.1721 | 0.2291 | 0.3242 | 0.3547 |
| 0.9644 | 0.1528 | 0.1303 | 0.1224 | 0.1334 | 0.1791 | 0.2313 | 0.3000 |
| 0.9954 | 0.1188 | 0.1160 | 0.1199 | 0.1293 | 0.1539 | 0.1732 | 0.2558 |

Table A.10: Velocity Profiles, $D_h$ = 500 µm, Re = 5, Distilled Water

| $z/W$ | 12 µm $u/u_{max,FD}$ | 43 µm $u/u_{max,FD}$ | 74 µm $u/u_{max,FD}$ | 105 µm $u/u_{max,FD}$ | 167 µm $u/u_{max,FD}$ | 574 µm $u/u_{max,FD}$ | 1291 µm $u/u_{max,FD}$ |
|---|---|---|---|---|---|---|---|
| 0.0046 | 0.0637 | 0.0518 | 0.0576 | 0.0658 | 0.0983 | 0.1316 | 0.1171 |
| 0.0356 | 0.0897 | 0.0739 | 0.0769 | 0.0913 | 0.1370 | 0.1745 | 0.1392 |
| 0.0666 | 0.1349 | 0.1118 | 0.1103 | 0.1273 | 0.1983 | 0.2399 | 0.1838 |
| 0.0975 | 0.1821 | 0.1600 | 0.1609 | 0.1841 | 0.2599 | 0.3360 | 0.2584 |
| 0.1285 | 0.2173 | 0.1995 | 0.2078 | 0.2409 | 0.3277 | 0.4437 | 0.3556 |
| 0.1594 | 0.2484 | 0.2481 | 0.2691 | 0.3112 | 0.4003 | 0.5381 | 0.4706 |
| 0.1904 | 0.2914 | 0.3075 | 0.3433 | 0.3982 | 0.5005 | 0.6119 | 0.5756 |
| 0.2214 | 0.3541 | 0.3920 | 0.4497 | 0.5169 | 0.6088 | 0.6793 | 0.6646 |
| 0.2523 | 0.4112 | 0.4696 | 0.5531 | 0.6415 | 0.7144 | 0.7447 | 0.7351 |
| 0.2833 | 0.4655 | 0.5450 | 0.6474 | 0.7425 | 0.7988 | 0.8019 | 0.7977 |
| 0.3142 | 0.5219 | 0.6104 | 0.7225 | 0.8069 | 0.8595 | 0.8479 | 0.8469 |
| 0.3452 | 0.5789 | 0.6683 | 0.7798 | 0.8477 | 0.9002 | 0.8887 | 0.8901 |
| 0.3762 | 0.6258 | 0.7094 | 0.8097 | 0.8685 | 0.9298 | 0.9241 | 0.9247 |
| 0.4071 | 0.6556 | 0.7348 | 0.8265 | 0.8876 | 0.9547 | 0.9549 | 0.9577 |
| 0.5000 | 0.6399 | 0.7252 | 0.8103 | 0.8810 | 0.9616 | 0.9926 | 1.0040 |

| $z/W$ | 12 μm | 43 μm | 74 μm | 105 μm | 167 μm | 574 μm | 1291 μm |
|---|---|---|---|---|---|---|---|
| | $u/u_{max,FD}$ | $u/u_{max,FD}$ | $u/u_{max,FD}$ | $u/u_{max,FD}$ | $u/u_{max,FD}$ | $u/u_{max,FD}$ | $u/u_{max,FD}$ |
| 0.5310 | 0.6106 | 0.7093 | 0.8024 | 0.8802 | 0.9545 | 0.9908 | 0.9969 |
| 0.5619 | 0.6029 | 0.7010 | 0.7979 | 0.8726 | 0.9432 | 0.9818 | 0.9904 |
| 0.5929 | 0.6103 | 0.7021 | 0.7971 | 0.8669 | 0.9330 | 0.9657 | 0.9822 |
| 0.6238 | 0.6187 | 0.7032 | 0.7940 | 0.8565 | 0.9136 | 0.9485 | 0.9689 |
| 0.6548 | 0.6133 | 0.6933 | 0.7755 | 0.8339 | 0.8803 | 0.9248 | 0.9459 |
| 0.6858 | 0.6014 | 0.6672 | 0.7367 | 0.7953 | 0.8355 | 0.8925 | 0.9088 |
| 0.7167 | 0.5710 | 0.6283 | 0.6890 | 0.7453 | 0.7812 | 0.8473 | 0.8647 |
| 0.7477 | 0.5313 | 0.5877 | 0.6437 | 0.6977 | 0.7242 | 0.7931 | 0.8107 |
| 0.7786 | 0.4800 | 0.5361 | 0.5901 | 0.6368 | 0.6535 | 0.7370 | 0.7479 |
| 0.8096 | 0.4357 | 0.4782 | 0.5205 | 0.5538 | 0.5688 | 0.6698 | 0.6698 |
| 0.8406 | 0.3717 | 0.3966 | 0.4258 | 0.4499 | 0.4736 | 0.5985 | 0.5773 |
| 0.8715 | 0.2987 | 0.3023 | 0.3103 | 0.3291 | 0.3670 | 0.5100 | 0.4741 |
| 0.9025 | 0.2143 | 0.1973 | 0.1897 | 0.2087 | 0.2566 | 0.4143 | 0.3698 |
| 0.9334 | 0.1453 | 0.1166 | 0.1051 | 0.1208 | 0.1617 | 0.3128 | 0.2804 |
| 0.9644 | 0.0990 | 0.0734 | 0.0656 | 0.0753 | 0.1021 | 0.2327 | 0.2048 |
| 0.9954 | 0.0714 | 0.0579 | 0.0568 | 0.0609 | 0.0735 | 0.1790 | 0.1454 |

Table A.11: Velocity Profiles, $D_h$ = 500 μm, Re = 50, Distilled Water

| $z/W$ | 30 μm | 166 μm | 326 μm | 598 μm | $z/W$ | 1028 μm | 1662 μm | 2297 μm |
|---|---|---|---|---|---|---|---|---|
| | $u/u_{max,FD}$ | $u/u_{max,FD}$ | $u/u_{max,FD}$ | $u/u_{max,FD}$ | | $u/u_{max,FD}$ | $u/u_{max,FD}$ | $u/u_{max,FD}$ |
| 0.0062 | 0.1386 | 0.08083 | 0.1164 | 0.1052 | 0.0107 | 0.1168 | 0.0990 | 0.1006 |
| 0.0402 | 0.2845 | 0.171308 | 0.2006 | 0.1914 | 0.0444 | 0.1946 | 0.1845 | 0.1731 |
| 0.0743 | 0.4248 | 0.287569 | 0.3092 | 0.3013 | 0.0782 | 0.3095 | 0.2993 | 0.2768 |
| 0.1084 | 0.5138 | 0.406238 | 0.4182 | 0.4098 | 0.1119 | 0.4319 | 0.4183 | 0.3956 |
| 0.1424 | 0.5642 | 0.508506 | 0.5115 | 0.5026 | 0.1457 | 0.5371 | 0.5243 | 0.5078 |
| 0.1765 | 0.5921 | 0.591919 | 0.5885 | 0.5869 | 0.1794 | 0.6249 | 0.6200 | 0.6088 |
| 0.2105 | 0.6036 | 0.65483 | 0.6551 | 0.6597 | 0.2132 | 0.6965 | 0.7014 | 0.6938 |
| 0.2446 | 0.6044 | 0.702226 | 0.7091 | 0.7221 | 0.2469 | 0.7575 | 0.7671 | 0.7628 |
| 0.2786 | 0.6001 | 0.731136 | 0.7519 | 0.7711 | 0.2806 | 0.8076 | 0.8198 | 0.8161 |
| 0.3127 | 0.5993 | 0.751272 | 0.7829 | 0.8097 | 0.3144 | 0.8443 | 0.8674 | 0.8639 |
| 0.3467 | 0.5966 | 0.762566 | 0.8047 | 0.8403 | 0.3481 | 0.8782 | 0.9032 | 0.9071 |
| 0.3808 | 0.5978 | 0.768089 | 0.8180 | 0.8637 | 0.3819 | 0.9055 | 0.9354 | 0.9429 |
| 0.4149 | 0.5970 | 0.769119 | 0.8290 | 0.8831 | 0.4156 | 0.9305 | 0.9562 | 0.9672 |
| 0.4489 | 0.5949 | 0.766451 | 0.8339 | 0.8949 | 0.4494 | 0.9399 | 0.9752 | 0.9837 |
| 0.4830 | 0.5905 | 0.765085 | 0.8374 | 0.9018 | 0.4831 | 0.9434 | 0.9787 | 0.9941 |
| 0.5170 | 0.5880 | 0.763919 | 0.8380 | 0.9012 | 0.5169 | 0.9396 | 0.9792 | 0.9944 |

| $z/W$ | 30 μm $u/u_{max,FD}$ | 166 μm $u/u_{max,FD}$ | 326 μm $u/u_{max,FD}$ | 598 μm $u/u_{max,FD}$ | $z/W$ | 1028 μm $u/u_{max,FD}$ | 1662 μm $u/u_{max,FD}$ | 2297 μm $u/u_{max,FD}$ |
|---|---|---|---|---|---|---|---|---|
| 0.5511 | 0.5872 | 0.763736 | 0.8383 | 0.9029 | 0.5506 | 0.9330 | 0.9745 | 0.9888 |
| 0.5851 | 0.5902 | 0.763745 | 0.8346 | 0.8994 | 0.5844 | 0.9200 | 0.9658 | 0.9765 |
| 0.6192 | 0.5901 | 0.763562 | 0.8271 | 0.8913 | 0.6181 | 0.8991 | 0.9446 | 0.9581 |
| 0.6533 | 0.5882 | 0.763783 | 0.8186 | 0.8749 | 0.6519 | 0.8711 | 0.9119 | 0.9254 |
| 0.6873 | 0.5841 | 0.759251 | 0.8069 | 0.8511 | 0.6856 | 0.8338 | 0.8714 | 0.8809 |
| 0.7214 | 0.5819 | 0.748494 | 0.7893 | 0.8199 | 0.7194 | 0.7862 | 0.8230 | 0.8287 |
| 0.7554 | 0.5811 | 0.729681 | 0.7594 | 0.7778 | 0.7531 | 0.7325 | 0.7710 | 0.7709 |
| 0.7895 | 0.5766 | 0.696791 | 0.7190 | 0.7278 | 0.7868 | 0.6690 | 0.7064 | 0.7046 |
| 0.8235 | 0.5744 | 0.648923 | 0.6677 | 0.6715 | 0.8206 | 0.5924 | 0.6236 | 0.6230 |
| 0.8576 | 0.5647 | 0.585068 | 0.6052 | 0.6024 | 0.8543 | 0.4993 | 0.5249 | 0.5303 |
| 0.8916 | 0.5422 | 0.506485 | 0.5290 | 0.5270 | 0.8881 | 0.3883 | 0.4109 | 0.4281 |
| 0.9257 | 0.4942 | 0.404162 | 0.4372 | 0.4375 | 0.9218 | 0.2754 | 0.2925 | 0.3153 |
| 0.9598 | 0.4188 | 0.291793 | 0.3321 | 0.3360 | 0.9556 | 0.1736 | 0.1796 | 0.2034 |
| 0.9938 | 0.3025 | 0.180824 | 0.2122 | 0.2254 | 0.9893 | 0.1042 | 0.0961 | 0.1161 |

Table A.12: Velocity Profiles, $D_h$ = 500 μm, Re = 200, Distilled Water

| $z/W$ | 30 μm $u/u_{max,FD}$ | $z/W$ | 564 μm $u/u_{max,FD}$ | $z/W$ | 1696 μm $u/u_{max,FD}$ | 2196 μm $u/u_{max,FD}$ | 3196 μm $u/u_{max,FD}$ | 4196 μm $u/u_{max,FD}$ | 4926 μm $u/u_{max,FD}$ |
|---|---|---|---|---|---|---|---|---|---|
| 0.0062 | 0.0062 | 0.0232 | 0.2692 | 0.0107 | 0.1541 | 0.1086 | 0.1613 | 0.1356 | 0.1654 |
| 0.0402 | 0.0402 | 0.0573 | 0.3828 | 0.0444 | 0.2271 | 0.1868 | 0.2644 | 0.2158 | 0.2700 |
| 0.0743 | 0.0743 | 0.0913 | 0.4863 | 0.0782 | 0.3391 | 0.3001 | 0.3881 | 0.3283 | 0.3880 |
| 0.1084 | 0.1084 | 0.1254 | 0.5705 | 0.1119 | 0.4520 | 0.4260 | 0.5005 | 0.4457 | 0.4996 |
| 0.1424 | 0.1424 | 0.1594 | 0.6314 | 0.1457 | 0.5523 | 0.5361 | 0.5930 | 0.5527 | 0.5924 |
| 0.1765 | 0.1765 | 0.1935 | 0.6761 | 0.1794 | 0.6329 | 0.6243 | 0.6710 | 0.6412 | 0.6776 |
| 0.2105 | 0.2105 | 0.2276 | 0.7060 | 0.2132 | 0.7013 | 0.6947 | 0.7358 | 0.7145 | 0.7454 |
| 0.2446 | 0.2446 | 0.2616 | 0.7231 | 0.2469 | 0.7509 | 0.7487 | 0.7878 | 0.7720 | 0.8036 |
| 0.2786 | 0.2786 | 0.2957 | 0.7319 | 0.2806 | 0.7856 | 0.7920 | 0.8306 | 0.8222 | 0.8509 |
| 0.3127 | 0.3127 | 0.3297 | 0.7374 | 0.3144 | 0.8071 | 0.8248 | 0.8626 | 0.8636 | 0.8890 |
| 0.3467 | 0.3467 | 0.3638 | 0.7408 | 0.3481 | 0.8219 | 0.8464 | 0.8887 | 0.8982 | 0.9229 |
| 0.3808 | 0.3808 | 0.3978 | 0.7430 | 0.3819 | 0.8343 | 0.8615 | 0.9034 | 0.9232 | 0.9458 |
| 0.4149 | 0.4149 | 0.4319 | 0.7440 | 0.4156 | 0.8428 | 0.8727 | 0.9149 | 0.9411 | 0.9660 |
| 0.4489 | 0.4489 | 0.4659 | 0.7445 | 0.4494 | 0.8481 | 0.8813 | 0.9193 | 0.9523 | 0.9780 |
| 0.4830 | 0.4830 | 0.5000 | 0.7439 | 0.4831 | 0.8497 | 0.8846 | 0.9243 | 0.9571 | 0.9875 |
| 0.5170 | 0.5170 | 0.5341 | 0.7440 | 0.5169 | 0.8485 | 0.8833 | 0.9203 | 0.9516 | 0.9879 |
| 0.5511 | 0.5511 | 0.5681 | 0.7438 | 0.5506 | 0.8468 | 0.8792 | 0.9121 | 0.9412 | 0.9780 |
| 0.5851 | 0.5851 | 0.6022 | 0.7439 | 0.5844 | 0.8432 | 0.8723 | 0.9010 | 0.9265 | 0.9612 |
| 0.6192 | 0.6192 | 0.6362 | 0.7425 | 0.6181 | 0.8358 | 0.8609 | 0.8853 | 0.9106 | 0.9352 |
| 0.6533 | 0.6533 | 0.6703 | 0.7408 | 0.6519 | 0.8255 | 0.8453 | 0.8616 | 0.8837 | 0.9036 |

| $z/W$ | 30 μm | $z/W$ | 564 μm | $z/W$ | 1696 μm | 2196 μm | 3196 μm | 4196 μm | 4926 μm |
|---|---|---|---|---|---|---|---|---|---|
| | $u/u_{max,FD}$ | | $u/u_{max,FD}$ | | $u/u_{max,FD}$ | $u/u_{max,FD}$ | $u/u_{max,FD}$ | $u/u_{max,FD}$ | $u/u_{max,FD}$ |
| 0.6873 | 0.6873 | 0.7043 | 0.7364 | 0.6856 | 0.8086 | 0.8254 | 0.8248 | 0.8492 | 0.8629 |
| 0.7214 | 0.7214 | 0.7384 | 0.7268 | 0.7194 | 0.7849 | 0.7974 | 0.7791 | 0.8066 | 0.8121 |
| 0.7554 | 0.7554 | 0.7724 | 0.7114 | 0.7531 | 0.7484 | 0.7543 | 0.7248 | 0.7576 | 0.7486 |
| 0.7895 | 0.7895 | 0.8065 | 0.6857 | 0.7868 | 0.7008 | 0.7020 | 0.6552 | 0.6899 | 0.6672 |
| 0.8235 | 0.8235 | 0.8406 | 0.6467 | 0.8206 | 0.6346 | 0.6357 | 0.5769 | 0.6080 | 0.5742 |
| 0.8576 | 0.8576 | 0.8746 | 0.5884 | 0.8543 | 0.5542 | 0.5601 | 0.4766 | 0.5110 | 0.4679 |
| 0.8916 | 0.8916 | 0.9087 | 0.5130 | 0.8881 | 0.4500 | 0.4620 | 0.3652 | 0.4044 | 0.3511 |
| 0.9257 | 0.9257 | 0.9427 | 0.4098 | 0.9218 | 0.3315 | 0.3461 | 0.2490 | 0.2848 | 0.2303 |
| 0.9598 | 0.9598 | 0.9768 | 0.2925 | 0.9556 | 0.2161 | 0.2286 | 0.1568 | 0.1787 | 0.1323 |
| 0.9938 | 0.9938 | | | 0.9893 | 0.1351 | 0.1376 | 0.0961 | 0.1125 | 0.0756 |

## A.2 Channel Centerline Velocity Development

Table A.13: Centerline Velocity, $D_h$ = 100 μm, Re = 0.476, Distilled Water

| $x/ReD_h$ | $u_{cl}/u_{cl,fd}$ | $x/ReD_h$ | $u_{cl}/u_{cl,fd}$ |
|---|---|---|---|
| 0.0905 | 0.5398 | 2.3214 | 1.0133 |
| 0.4092 | 0.7052 | 2.6401 | 1.0090 |
| 0.7279 | 0.8340 | 2.9588 | 1.0079 |
| 1.0466 | 0.9094 | 3.2775 | 1.0118 |
| 1.3653 | 0.9625 | 3.5962 | 1.0140 |
| 1.6840 | 0.9987 | 3.9149 | 1.0093 |
| 2.0027 | 1.0161 | 4.2337 | 1.0087 |

Table A.14: Centerline Velocity, $D_h$ = 100 µm, Re = 4.76, Distilled Water

| $x/ReD_h$ | $u_{cl}/u_{cl,fd}$ | $x/ReD_h$ | $u_{cl}/u_{cl,fd}$ | $x/ReD_h$ | $u_{cl}/u_{cl,fd}$ |
|---|---|---|---|---|---|
| 0.0090 | 0.1904 | 0.3278 | 0.9932 | 0.6299 | 1.0149 |
| 0.0409 | 0.3716 | 0.3596 | 0.9901 | 0.6617 | 1.0151 |
| 0.0728 | 0.6084 | 0.3915 | 0.9787 | 0.6936 | 1.0133 |
| 0.1047 | 0.8231 | 0.4234 | 0.9732 | 0.7255 | 1.0093 |
| 0.1365 | 0.9304 | 0.4386 | 1.0177 | 0.7574 | 1.0085 |
| 0.1684 | 0.9773 | 0.4705 | 1.0147 | 0.7892 | 1.0085 |
| 0.2003 | 0.9956 | 0.5024 | 1.0125 | | |
| 0.2321 | 0.9981 | 0.5343 | 1.0159 | | |
| 0.2640 | 0.9722 | 0.5661 | 1.0135 | | |
| 0.2959 | 0.9926 | 0.5980 | 1.0125 | | |

Table A.15: Centerline Velocity, $D_h$ = 100 µm, Re = 50, Distilled Water

| $x/ReD_h$ | $u_{cl}/u_{cl,fd}$ | $x/ReD_h$ | $u_{cl}/u_{cl,fd}$ | $x/ReD_h$ | $u_{cl}/u_{cl,fd}$ |
|---|---|---|---|---|---|
| 0.0009 | 0.3218 | 0.0478 | 0.9817 | 0.0978 | 0.9942 |
| 0.0039 | 0.5102 | 0.0509 | 0.9807 | 0.1009 | 0.9963 |
| 0.0069 | 0.6674 | 0.0539 | 0.9755 | 0.1039 | 1.0009 |
| 0.0100 | 0.7853 | 0.0569 | 0.9792 | 0.1069 | 1.0031 |
| 0.0130 | 0.8469 | 0.0600 | 0.9812 | 0.1100 | 1.0023 |
| 0.0160 | 0.8971 | 0.0630 | 0.9861 | 0.1130 | 1.0002 |
| 0.0191 | 0.9237 | 0.0660 | 0.9898 | 0.1160 | 0.9987 |
| 0.0221 | 0.9417 | 0.0691 | 0.9895 | 0.1191 | 0.9971 |
| 0.0251 | 0.9506 | 0.0721 | 0.9878 | 0.1221 | 0.9953 |
| 0.0282 | 0.9568 | 0.0751 | 0.9873 | 0.1251 | 0.9931 |
| 0.0312 | 0.9579 | 0.0782 | 0.9891 | 0.1282 | 0.9944 |
| 0.0327 | 0.9649 | 0.0812 | 0.9890 | 0.1312 | 0.9980 |
| 0.0357 | 0.9716 | 0.0847 | 0.9899 | 0.1342 | 1.0034 |
| 0.0387 | 0.9780 | 0.0881 | 0.9899 | 0.1373 | 1.0070 |
| 0.0418 | 0.9794 | 0.0918 | 0.9899 | 0.1403 | 1.0081 |
| 0.0448 | 0.9850 | 0.0948 | 0.9901 | | |

Table A.16: Centerline Velocity, $D_h$ = 100 μm, Re = 89, Distilled Water

| $x/ReD_h$ | $u_{cl}/u_{cl,fd}$ | $x/ReD_h$ | $u_{cl}/u_{cl,fd}$ | $x/ReD_h$ | $u_{cl}/u_{cl,fd}$ |
|---|---|---|---|---|---|
| 0.0005 | 0.2273 | 0.0269 | 0.8967 | 0.0533 | 0.9766 |
| 0.0022 | 0.2969 | 0.0286 | 0.8984 | 0.0550 | 0.9805 |
| 0.0039 | 0.4598 | 0.0303 | 0.8966 | 0.0567 | 0.9822 |
| 0.0056 | 0.6174 | 0.0320 | 0.8995 | 0.0584 | 0.9834 |
| 0.0073 | 0.7363 | 0.0337 | 0.9036 | 0.0601 | 0.9818 |
| 0.0090 | 0.7792 | 0.0354 | 0.9050 | 0.0618 | 0.9867 |
| 0.0107 | 0.8168 | 0.0371 | 0.9074 | 0.0635 | 0.9903 |
| 0.0124 | 0.8400 | 0.0388 | 0.9069 | 0.0652 | 0.9894 |
| 0.0141 | 0.8504 | 0.0405 | 0.9096 | 0.0669 | 0.9868 |
| 0.0158 | 0.8586 | 0.0422 | 0.9139 | 0.0686 | 0.9874 |
| 0.0175 | 0.8666 | 0.0439 | 0.9164 | 0.0703 | 0.9920 |
| 0.0183 | 0.8725 | 0.0447 | 0.9500 | 0.0720 | 0.9972 |
| 0.0201 | 0.8822 | 0.0464 | 0.9553 | 0.0737 | 0.9977 |
| 0.0218 | 0.8900 | 0.0481 | 0.9645 | 0.0754 | 1.0024 |
| 0.0235 | 0.8934 | 0.0498 | 0.9706 | 0.0771 | 1.0036 |
| 0.0252 | 0.8972 | 0.0516 | 0.9736 | 0.0788 | 1.0070 |

Table A.17: Centerline Velocity, $D_h$ = 200 μm, Re = 0.5, Distilled Water

| $x/ReD_h$ | $u_{cl}/u_{cl,fd}$ | $x/ReD_h$ | $u_{cl}/u_{cl,fd}$ | $x/ReD_h$ | $u_{cl}/u_{cl,fd}$ | $x/ReD_h$ | $u_{cl}/u_{cl,fd}$ |
|---|---|---|---|---|---|---|---|
| 0.0000 | 0.4226 | 3.0362 | 0.9941 | 6.0099 | 0.9891 | 8.9923 | 0.9947 |
| 0.1412 | 0.6979 | 3.1774 | 0.9906 | 6.1511 | 0.9838 | 9.1281 | 0.9946 |
| 0.2824 | 0.8799 | 3.2520 | 0.9914 | 6.2924 | 0.9832 | 9.2639 | 0.9954 |
| 0.4237 | 0.9439 | 3.3933 | 0.9892 | 6.4336 | 0.9819 | 9.3996 | 0.9914 |
| 0.5649 | 0.9517 | 3.5345 | 0.9875 | 6.5748 | 0.9877 | 9.5354 | 0.9906 |
| 0.7061 | 0.9595 | 3.6757 | 0.9867 | 6.7160 | 0.9909 | 9.6712 | 0.9934 |
| 0.8473 | 0.9673 | 3.8169 | 0.9850 | 6.8572 | 0.9944 | 9.8070 | 1.0010 |
| 0.9886 | 0.9751 | 3.9581 | 0.9746 | 6.9985 | 0.9992 | 9.9428 | 0.9983 |
| 1.0591 | 0.9829 | 4.0994 | 0.9715 | 7.1397 | 0.9981 | | |
| 1.2003 | 0.9908 | 4.2406 | 0.9744 | 7.2809 | 0.9972 | | |
| 1.3415 | 0.9986 | 4.3818 | 0.9907 | 7.4221 | 0.9940 | | |
| 1.4827 | 0.9945 | 4.5230 | 0.9922 | 7.5633 | 0.9943 | | |
| 1.6239 | 0.9959 | 4.6643 | 0.9922 | 7.6344 | 0.9813 | | |
| 1.7652 | 0.9968 | 4.8055 | 0.9853 | 7.7702 | 0.9864 | | |
| 1.9064 | 0.9970 | 4.9467 | 0.9815 | 7.9060 | 0.9924 | | |
| 2.0476 | 0.9923 | 5.0879 | 0.9742 | 8.0418 | 0.9923 | | |
| 2.1888 | 0.9864 | 5.2291 | 0.9822 | 8.1775 | 0.9827 | | |
| 2.3301 | 0.9803 | 5.3704 | 0.9855 | 8.3133 | 0.9742 | | |
| 2.4713 | 0.9753 | 5.4450 | 0.9890 | 8.4491 | 0.9797 | | |
| 2.6125 | 0.9787 | 5.5862 | 0.9892 | 8.5849 | 0.9910 | | |
| 2.7537 | 0.9847 | 5.7275 | 0.9908 | 8.7207 | 1.0001 | | |
| 2.8949 | 0.9898 | 5.8687 | 0.9907 | 8.8565 | 0.9988 | | |

Table A.18: Centerline Velocity, $D_h$ = 200 μm, Re = 5, Distilled Water

| $x/ReD_h$ | $u_{cl}/u_{cl,fd}$ | $x/ReD_h$ | $u_{cl}/u_{cl,fd}$ | $x/ReD_h$ | $u_{cl}/u_{cl,fd}$ | $x/ReD_h$ | $u_{cl}/u_{cl,fd}$ |
|---|---|---|---|---|---|---|---|
| 0.0000 | 0.3420 | 0.3018 | 0.9930 | 0.6042 | 1.0301 | 0.8992 | 1.0129 |
| 0.0155 | 0.5644 | 0.3173 | 0.9998 | 0.6196 | 1.0288 | 0.9146 | 1.0030 |
| 0.0310 | 0.6840 | 0.3328 | 0.9927 | 0.6351 | 1.0277 | 0.9301 | 1.0012 |
| 0.0464 | 0.7720 | 0.3483 | 0.9850 | 0.6506 | 1.0292 | 0.9456 | 1.0052 |
| 0.0619 | 0.8626 | 0.3565 | 0.9972 | 0.6661 | 1.0291 | 0.9611 | 1.0130 |
| 0.0774 | 0.9345 | 0.3720 | 0.9992 | 0.6743 | 1.0178 | 0.9766 | 1.0134 |
| 0.0929 | 0.9769 | 0.3874 | 1.0046 | 0.6897 | 1.0065 | 0.9920 | 1.0164 |
| 0.1084 | 0.9793 | 0.4029 | 1.0055 | 0.7052 | 0.9953 | 1.0075 | 1.0216 |
| 0.1238 | 0.9818 | 0.4184 | 1.0036 | 0.7207 | 0.9840 | 1.0230 | 1.0251 |
| 0.1393 | 0.9843 | 0.4339 | 0.9955 | 0.7362 | 0.9848 | 1.0385 | 1.0205 |
| 0.1548 | 0.9868 | 0.4494 | 1.0007 | 0.7517 | 0.9859 | 1.0540 | 1.0176 |
| 0.1703 | 0.9785 | 0.4648 | 1.0172 | 0.7671 | 0.9810 | 1.0694 | 1.0197 |
| 0.1858 | 0.9741 | 0.4803 | 1.0150 | 0.7826 | 0.9794 | 1.0849 | 1.0273 |
| 0.1935 | 0.9962 | 0.4958 | 1.0196 | 0.7981 | 0.9818 | 1.1004 | 1.0266 |
| 0.2090 | 0.9991 | 0.5113 | 1.0170 | 0.8136 | 0.9838 | 1.1159 | 1.0142 |
| 0.2244 | 0.9977 | 0.5268 | 1.0136 | 0.8291 | 0.9908 | 1.1314 | 0.9908 |
| 0.2399 | 1.0005 | 0.5422 | 1.0163 | 0.8372 | 0.9979 | 1.1468 | 0.9778 |
| 0.2554 | 0.9938 | 0.5577 | 1.0040 | 0.8527 | 1.0007 | | |
| 0.2709 | 0.9867 | 0.5732 | 1.0122 | 0.8682 | 1.0071 | | |
| 0.2864 | 0.9847 | 0.5887 | 1.0187 | 0.8837 | 1.0129 | | |

Table A.19: Centerline Velocity, $D_h$ = 200 μm, Re = 50, Distilled Water

| $x/ReD_h$ | $u_{cl}/u_{cl,fd}$ | $x/ReD_h$ | $u_{cl}/u_{cl,fd}$ | $x/ReD_h$ | $u_{cl}/u_{cl,fd}$ | $x/ReD_h$ | $u_{cl}/u_{cl,fd}$ |
|---|---|---|---|---|---|---|---|
| 0.0000 | 0.3131 | 0.0256 | 0.9107 | 0.0513 | 0.9522 | 0.0769 | 0.9714 |
| 0.0015 | 0.4809 | 0.0271 | 0.9197 | 0.0527 | 0.9462 | 0.0784 | 0.9754 |
| 0.0029 | 0.5938 | 0.0285 | 0.9227 | 0.0542 | 0.9539 | 0.0798 | 0.9818 |
| 0.0044 | 0.6787 | 0.0300 | 0.9197 | 0.0557 | 0.9594 | 0.0813 | 0.9911 |
| 0.0059 | 0.7483 | 0.0315 | 0.9177 | 0.0564 | 0.9658 | 0.0828 | 0.9924 |
| 0.0073 | 0.8054 | 0.0329 | 0.9210 | 0.0579 | 0.9692 | 0.0842 | 0.9886 |
| 0.0088 | 0.8336 | 0.0337 | 0.9143 | 0.0594 | 0.9725 | 0.0857 | 0.9873 |
| 0.0102 | 0.8533 | 0.0352 | 0.9210 | 0.0608 | 0.9715 | 0.0865 | 0.9862 |
| 0.0110 | 0.8398 | 0.0366 | 0.9317 | 0.0623 | 0.9637 | 0.0879 | 0.9856 |
| 0.0124 | 0.8437 | 0.0381 | 0.9364 | 0.0637 | 0.9601 | 0.0894 | 0.9970 |
| 0.0139 | 0.8512 | 0.0396 | 0.9321 | 0.0652 | 0.9638 | 0.0909 | 1.0063 |
| 0.0154 | 0.8567 | 0.0410 | 0.9258 | 0.0667 | 0.9724 | 0.0923 | 1.0117 |
| 0.0168 | 0.8595 | 0.0425 | 0.9272 | 0.0681 | 0.9709 | 0.0938 | 1.0151 |
| 0.0183 | 0.8683 | 0.0439 | 0.9317 | 0.0696 | 0.9617 | 0.0953 | 1.0080 |
| 0.0198 | 0.8828 | 0.0454 | 0.9390 | 0.0711 | 0.9553 | 0.0967 | 1.0015 |
| 0.0212 | 0.8964 | 0.0469 | 0.9468 | 0.0725 | 0.9554 | 0.0982 | 0.9972 |
| 0.0227 | 0.9004 | 0.0483 | 0.9549 | 0.0740 | 0.9645 | 0.0996 | 0.9987 |
| 0.0241 | 0.9022 | 0.0498 | 0.9553 | 0.0755 | 0.9705 | 0.1011 | 1.0019 |

| $x$/ReDh | $u_{cl}/u_{cl,fd}$ | $x$/ReDh | $u_{cl}/u_{cl,fd}$ | $x$/ReDh | $u_{cl}/u_{cl,fd}$ | $x$/ReDh | $u_{cl}/u_{cl,fd}$ |
|---|---|---|---|---|---|---|---|
| 0.1019 | 0.9946 | 0.1165 | 0.9983 | 0.1312 | 0.9830 | 0.1451 | 1.0060 |
| 0.1033 | 0.9969 | 0.1180 | 0.9962 | 0.1319 | 0.9912 | 0.1466 | 1.0059 |
| 0.1048 | 0.9999 | 0.1194 | 0.9978 | 0.1334 | 0.9837 | 0.1473 | 1.0048 |
| 0.1063 | 0.9996 | 0.1209 | 0.9916 | 0.1349 | 0.9932 | 0.1488 | 1.0030 |
| 0.1077 | 1.0021 | 0.1224 | 0.9884 | 0.1363 | 1.0114 | 0.1503 | 1.0000 |
| 0.1092 | 0.9946 | 0.1238 | 0.9821 | 0.1378 | 1.0199 | 0.1517 | 0.9975 |
| 0.1107 | 0.9889 | 0.1253 | 0.9798 | 0.1392 | 1.0233 | 0.1532 | 0.9940 |
| 0.1121 | 0.9892 | 0.1268 | 0.9781 | 0.1407 | 1.0201 | 0.1547 | 0.9949 |
| 0.1136 | 0.9945 | 0.1282 | 0.9823 | 0.1422 | 1.0169 | 0.1561 | 0.9897 |
| 0.1151 | 0.9947 | 0.1297 | 0.9816 | 0.1436 | 1.0117 | | |

Table A.20: Centerline Velocity, $D_h$ = 200 μm, Re = 200, Distilled Water

| $x$/ReDh | $u_{cl}/u_{cl,fd}$ | $x$/ReDh | $u_{cl}/u_{cl,fd}$ | $x$/ReDh | $u_{cl}/u_{cl,fd}$ | $x$/ReDh | $u_{cl}/u_{cl,fd}$ |
|---|---|---|---|---|---|---|---|
| 0.0000 | 0.2939 | 0.0106 | 0.8104 | 0.0214 | 0.9069 | 0.0320 | 0.9573 |
| 0.0004 | 0.4042 | 0.0110 | 0.8171 | 0.0218 | 0.9007 | 0.0322 | 0.9633 |
| 0.0008 | 0.4915 | 0.0113 | 0.8242 | 0.0221 | 0.8967 | 0.0326 | 0.9665 |
| 0.0011 | 0.5747 | 0.0117 | 0.8260 | 0.0223 | 0.9081 | 0.0329 | 0.9707 |
| 0.0015 | 0.6522 | 0.0121 | 0.8253 | 0.0227 | 0.9129 | 0.0333 | 0.9730 |
| 0.0019 | 0.7058 | 0.0125 | 0.8264 | 0.0231 | 0.9161 | 0.0337 | 0.9622 |
| 0.0023 | 0.7316 | 0.0129 | 0.8287 | 0.0235 | 0.9180 | 0.0341 | 0.9430 |
| 0.0026 | 0.7329 | 0.0132 | 0.8297 | 0.0238 | 0.9214 | 0.0344 | 0.9383 |
| 0.0028 | 0.7341 | 0.0136 | 0.8305 | 0.0242 | 0.9246 | 0.0348 | 0.9486 |
| 0.0032 | 0.7359 | 0.0140 | 0.8334 | 0.0246 | 0.9263 | 0.0352 | 0.9684 |
| 0.0036 | 0.7420 | 0.0144 | 0.8377 | 0.0250 | 0.9244 | 0.0356 | 0.9689 |
| 0.0040 | 0.7487 | 0.0147 | 0.8408 | 0.0254 | 0.9227 | 0.0360 | 0.9639 |
| 0.0043 | 0.7562 | 0.0151 | 0.8437 | 0.0257 | 0.9214 | 0.0363 | 0.9565 |
| 0.0047 | 0.7588 | 0.0155 | 0.8447 | 0.0261 | 0.9233 | 0.0367 | 0.9558 |
| 0.0051 | 0.7647 | 0.0159 | 0.8465 | 0.0263 | 0.9395 | 0.0371 | 0.9599 |
| 0.0055 | 0.7710 | 0.0163 | 0.8475 | 0.0267 | 0.9410 | 0.0375 | 0.9631 |
| 0.0059 | 0.7785 | 0.0165 | 0.8634 | 0.0271 | 0.9444 | 0.0378 | 0.9637 |
| 0.0062 | 0.7840 | 0.0168 | 0.8622 | 0.0274 | 0.9475 | 0.0380 | 0.9630 |
| 0.0066 | 0.7871 | 0.0172 | 0.8643 | 0.0278 | 0.9454 | 0.0384 | 0.9625 |
| 0.0070 | 0.7904 | 0.0176 | 0.8724 | 0.0282 | 0.9307 | 0.0388 | 0.9603 |
| 0.0074 | 0.7945 | 0.0180 | 0.8800 | 0.0286 | 0.9259 | 0.0392 | 0.9605 |
| 0.0077 | 0.7972 | 0.0184 | 0.8866 | 0.0290 | 0.9312 | 0.0396 | 0.9594 |
| 0.0081 | 0.7986 | 0.0187 | 0.8915 | 0.0293 | 0.9473 | 0.0399 | 0.9572 |
| 0.0085 | 0.8020 | 0.0191 | 0.8922 | 0.0297 | 0.9552 | 0.0403 | 0.9589 |
| 0.0089 | 0.8076 | 0.0195 | 0.8953 | 0.0301 | 0.9578 | 0.0407 | 0.9614 |
| 0.0093 | 0.8093 | 0.0199 | 0.8984 | 0.0305 | 0.9597 | 0.0411 | 0.9677 |
| 0.0096 | 0.8083 | 0.0202 | 0.9030 | 0.0308 | 0.9598 | 0.0414 | 0.9646 |
| 0.0100 | 0.8088 | 0.0206 | 0.9061 | 0.0312 | 0.9579 | 0.0418 | 0.9591 |
| 0.0104 | 0.8122 | 0.0210 | 0.9079 | 0.0316 | 0.9549 | 0.0422 | 0.9537 |

| $x/\mathrm{ReD_h}$ | $u_{cl}/u_{cl,fd}$ | $x/\mathrm{ReD_h}$ | $u_{cl}/u_{cl,fd}$ | $x/\mathrm{ReD_h}$ | $u_{cl}/u_{cl,fd}$ | $x/\mathrm{ReD_h}$ | $u_{cl}/u_{cl,fd}$ |
|---|---|---|---|---|---|---|---|
| 0.0426 | 0.9538 | 0.0570 | 0.9871 | 0.0712 | 0.9780 | 0.0855 | 0.9954 |
| 0.0430 | 0.9643 | 0.0573 | 0.9863 | 0.0715 | 0.9719 | 0.0859 | 0.9990 |
| 0.0433 | 0.9483 | 0.0575 | 0.9784 | 0.0719 | 0.9646 | 0.0863 | 0.9975 |
| 0.0437 | 0.9541 | 0.0579 | 0.9730 | 0.0723 | 0.9570 | 0.0867 | 0.9963 |
| 0.0439 | 0.9733 | 0.0583 | 0.9730 | 0.0727 | 0.9495 | 0.0869 | 0.9956 |
| 0.0443 | 0.9665 | 0.0587 | 0.9775 | 0.0731 | 0.9520 | 0.0873 | 0.9980 |
| 0.0447 | 0.9662 | 0.0591 | 0.9868 | 0.0733 | 0.9644 | 0.0876 | 0.9964 |
| 0.0450 | 0.9674 | 0.0594 | 0.9858 | 0.0736 | 0.9678 | 0.0880 | 0.9894 |
| 0.0454 | 0.9692 | 0.0598 | 0.9847 | 0.0740 | 0.9681 | 0.0884 | 0.9917 |
| 0.0458 | 0.9649 | 0.0602 | 0.9837 | 0.0744 | 0.9717 | 0.0888 | 0.9927 |
| 0.0462 | 0.9593 | 0.0606 | 0.9771 | 0.0748 | 0.9756 | 0.0892 | 0.9955 |
| 0.0466 | 0.9523 | 0.0609 | 0.9826 | 0.0751 | 0.9774 | 0.0895 | 0.9870 |
| 0.0469 | 0.9471 | 0.0613 | 0.9819 | 0.0755 | 0.9804 | 0.0899 | 0.9805 |
| 0.0473 | 0.9490 | 0.0615 | 0.9811 | 0.0759 | 0.9795 | 0.0903 | 0.9823 |
| 0.0477 | 0.9557 | 0.0619 | 0.9795 | 0.0763 | 0.9802 | 0.0907 | 0.9866 |
| 0.0481 | 0.9574 | 0.0623 | 0.9735 | 0.0767 | 0.9718 | 0.0910 | 0.9968 |
| 0.0484 | 0.9595 | 0.0627 | 0.9716 | 0.0770 | 0.9664 | 0.0914 | 1.0010 |
| 0.0488 | 0.9678 | 0.0630 | 0.9702 | 0.0774 | 0.9635 | 0.0918 | 1.0069 |
| 0.0492 | 0.9755 | 0.0634 | 0.9697 | 0.0778 | 0.9726 | 0.0922 | 1.0080 |
| 0.0496 | 0.9739 | 0.0638 | 0.9669 | 0.0782 | 0.9755 | 0.0926 | 1.0060 |
| 0.0500 | 0.9596 | 0.0642 | 0.9684 | 0.0785 | 0.9838 | 0.0928 | 1.0034 |
| 0.0503 | 0.9525 | 0.0645 | 0.9745 | 0.0789 | 0.9774 | 0.0931 | 1.0001 |
| 0.0505 | 0.9644 | 0.0649 | 0.9824 | 0.0791 | 0.9739 | 0.0935 | 0.9996 |
| 0.0509 | 0.9705 | 0.0653 | 0.9803 | 0.0795 | 0.9766 | 0.0939 | 1.0027 |
| 0.0513 | 0.9752 | 0.0657 | 0.9779 | 0.0799 | 0.9842 | 0.0943 | 1.0067 |
| 0.0517 | 0.9726 | 0.0661 | 0.9711 | 0.0803 | 0.9911 | 0.0946 | 1.0066 |
| 0.0520 | 0.9818 | 0.0664 | 0.9754 | 0.0806 | 0.9931 | 0.0950 | 1.0032 |
| 0.0524 | 0.9842 | 0.0668 | 0.9756 | 0.0810 | 0.9942 | 0.0954 | 0.9996 |
| 0.0528 | 0.9829 | 0.0672 | 0.9731 | 0.0814 | 1.0018 | 0.0958 | 1.0003 |
| 0.0532 | 0.9785 | 0.0674 | 0.9830 | 0.0818 | 1.0054 | 0.0962 | 1.0006 |
| 0.0536 | 0.9827 | 0.0678 | 0.9858 | 0.0821 | 1.0113 | 0.0965 | 1.0035 |
| 0.0539 | 0.9876 | 0.0681 | 0.9848 | 0.0825 | 1.0054 | 0.0969 | 1.0003 |
| 0.0543 | 0.9862 | 0.0685 | 0.9837 | 0.0829 | 0.9979 | 0.0973 | 0.9992 |
| 0.0547 | 0.9834 | 0.0689 | 0.9827 | 0.0833 | 0.9925 | 0.0977 | 0.9992 |
| 0.0551 | 0.9816 | 0.0693 | 0.9817 | 0.0837 | 0.9858 | 0.0980 | 0.9971 |
| 0.0555 | 0.9814 | 0.0697 | 0.9662 | 0.0840 | 0.9820 | 0.0984 | 0.9953 |
| 0.0558 | 0.9842 | 0.0700 | 0.9602 | 0.0844 | 0.9801 | | |
| 0.0562 | 0.9863 | 0.0704 | 0.9682 | 0.0848 | 0.9839 | | |
| 0.0566 | 0.9889 | 0.0708 | 0.9826 | 0.0852 | 0.9874 | | |

Table A.21: Centerline Velocity, $D_h$ = 500 µm, Re = 0.5, Distilled Water

| $x/ReD_h$ | $u_{cl}/u_{cl,fd}$ | $x/ReD_h$ | $u_{cl}/u_{cl,fd}$ | $x/ReD_h$ | $u_{cl}/u_{cl,fd}$ | $x/ReD_h$ | $u_{cl}/u_{cl,fd}$ |
|---|---|---|---|---|---|---|---|
| 0.0529 | 0.7621 | 2.1943 | 0.9968 | 4.3356 | 0.9876 | 6.4769 | 1.0199 |
| 0.1855 | 0.8279 | 2.3269 | 0.9998 | 4.4682 | 0.9914 | 6.6095 | 1.0166 |
| 0.3181 | 0.9054 | 2.4594 | 0.9982 | 4.6008 | 0.9953 | 6.7421 | 1.0100 |
| 0.4507 | 0.9514 | 2.5920 | 0.9966 | 4.7334 | 0.9995 | 6.8747 | 1.0085 |
| 0.5833 | 0.9782 | 2.7246 | 0.9972 | 4.8660 | 1.0001 | 7.0073 | 1.0164 |
| 0.7159 | 0.9882 | 2.8572 | 1.0033 | 4.9985 | 0.9986 | 7.1399 | 1.0307 |
| 0.8485 | 0.9879 | 2.9898 | 1.0064 | 5.1311 | 1.0057 | 7.2725 | 1.0353 |
| 0.9811 | 0.9862 | 3.1224 | 1.0050 | 5.2637 | 1.0074 | 7.4051 | 1.0334 |
| 1.1137 | 0.9931 | 3.2550 | 1.0024 | 5.3963 | 1.0048 | 7.5376 | 1.0306 |
| 1.2463 | 0.9947 | 3.3876 | 0.9984 | 5.5289 | 0.9967 | 7.6702 | 1.0263 |
| 1.2661 | 0.9901 | 3.5202 | 0.9913 | 5.5488 | 1.0110 | 7.8028 | 1.0203 |
| 1.3987 | 0.9917 | 3.6528 | 0.9808 | 5.6814 | 1.0173 | 7.9354 | 1.0189 |
| 1.5313 | 0.9944 | 3.6726 | 0.9873 | 5.8140 | 1.0250 | 8.0680 | 1.0185 |
| 1.6639 | 0.9919 | 3.8052 | 0.9873 | 5.9466 | 1.0232 | 8.2006 | 1.0231 |
| 1.7965 | 0.9914 | 3.9378 | 0.9923 | 6.0791 | 1.0183 | | |
| 1.9291 | 0.9891 | 4.0704 | 0.9923 | 6.2117 | 1.0148 | | |
| 2.0617 | 0.9932 | 4.2030 | 0.9892 | 6.3443 | 1.0161 | | |

Table A.22: Centerline Velocity, $D_h$ = 500 µm, Re = 5, Distilled Water

| $x/ReD_h$ | $u_{cl}/u_{cl,fd}$ | $x/ReD_h$ | $u_{cl}/u_{cl,fd}$ | $x/ReD_h$ | $u_{cl}/u_{cl,fd}$ | $x/ReD_h$ | $u_{cl}/u_{cl,fd}$ |
|---|---|---|---|---|---|---|---|
| 0.6682 | 0.0049 | 1.0001 | 0.2049 | 1.0090 | 0.4049 | 1.0047 | 0.6049 |
| 0.7397 | 0.0173 | 0.9954 | 0.2173 | 1.0058 | 0.4173 | 1.0035 | 0.6173 |
| 0.8210 | 0.0297 | 0.9926 | 0.2297 | 1.0051 | 0.4297 | 1.0040 | 0.6297 |
| 0.8882 | 0.0421 | 0.9914 | 0.2421 | 1.0063 | 0.4421 | 1.0014 | 0.6421 |
| 0.9373 | 0.0545 | 0.9929 | 0.2545 | 1.0082 | 0.4545 | 1.0026 | 0.6545 |
| 0.9702 | 0.0669 | 0.9937 | 0.2669 | 1.0079 | 0.4669 | 1.0017 | 0.6669 |
| 0.9841 | 0.0792 | 0.9890 | 0.2792 | 1.0070 | 0.4792 | 1.0051 | 0.6792 |
| 0.9876 | 0.0916 | 0.9884 | 0.2916 | 1.0085 | 0.4916 | 1.0063 | 0.6916 |
| 0.9945 | 0.1040 | 0.9831 | 0.3040 | 1.0078 | 0.5040 | 1.0060 | 0.7040 |
| 0.9956 | 0.1164 | 0.9809 | 0.3164 | 1.0040 | 0.5164 | 1.0049 | 0.7164 |
| 0.9908 | 0.1183 | 0.9935 | 0.3183 | 1.0070 | 0.5183 | 1.0005 | 0.7183 |
| 0.9915 | 0.1306 | 0.9937 | 0.3306 | 1.0045 | 0.5306 | 1.0020 | 0.7306 |
| 0.9923 | 0.1430 | 0.9952 | 0.3430 | 1.0045 | 0.5430 | 1.0046 | 0.7430 |
| 0.9919 | 0.1554 | 0.9953 | 0.3554 | 1.0006 | 0.5554 | 1.0051 | 0.7554 |
| 0.9923 | 0.1678 | 0.9972 | 0.3678 | 1.0008 | 0.5678 | 1.0052 | 0.7678 |
| 0.9980 | 0.1802 | 1.0008 | 0.3802 | 1.0000 | 0.5802 | 1.0059 | 0.7802 |
| 0.9995 | 0.1926 | 1.0070 | 0.3926 | 0.9991 | 0.5926 | 1.0000 | 0.7926 |

| $x$/ReDh | $u_{cl}/u_{cl,fd}$ | $x$/ReDh | $u_{cl}/u_{cl,fd}$ | $x$/ReDh | $u_{cl}/u_{cl,fd}$ | $x$/ReDh | $u_{cl}/u_{cl,fd}$ |
|---|---|---|---|---|---|---|---|
| 1.0082 | 0.8049 | 0.9890 | 0.9430 | 0.9849 | 1.0916 | 1.0045 | 1.2297 |
| 1.0058 | 0.8173 | 0.9838 | 0.9554 | 0.9818 | 1.1040 | 1.0043 | 1.2421 |
| 1.0066 | 0.8297 | 0.9836 | 0.9678 | 0.9785 | 1.1164 | 1.0068 | 1.2545 |
| 1.0017 | 0.8421 | 0.9834 | 0.9802 | 0.9991 | 1.1183 | 1.0048 | 1.2669 |
| 1.0054 | 0.8545 | 0.9832 | 0.9926 | 1.0109 | 1.1306 | 1.0034 | 1.2792 |
| 1.0034 | 0.8669 | 0.9830 | 1.0049 | 1.0085 | 1.1430 | 0.9947 | 1.2916 |
| 1.0024 | 0.8792 | 0.9829 | 1.0173 | 1.0056 | 1.1554 | 0.9905 | 1.3040 |
| 1.0048 | 0.8916 | 0.9841 | 1.0297 | 1.0049 | 1.1678 | 0.9977 | 1.3164 |
| 1.0080 | 0.9040 | 0.9830 | 1.0421 | 1.0064 | 1.1802 | 0.9970 | 1.3288 |
| 1.0088 | 0.9164 | 0.9855 | 1.0545 | 1.0083 | 1.1926 | 0.9889 | 1.3412 |
| 0.9878 | 0.9183 | 0.9860 | 1.0669 | 1.0089 | 1.2049 | 0.9826 | 1.3536 |
| 0.9905 | 0.9306 | 0.9867 | 1.0792 | 1.0052 | 1.2173 | 0.9809 | 1.3659 |

Table A.23: Centerline Velocity, $D_h$ = 500 μm, Re = 50, Distilled Water

| $x$/ReDh | $u_{cl}/u_{cl,fd}$ | $x$/ReDh | $u_{cl}/u_{cl,fd}$ | $x$/ReDh | $u_{cl}/u_{cl,fd}$ | $x$/ReDh | $u_{cl}/u_{cl,fd}$ |
|---|---|---|---|---|---|---|---|
| 0.0012 | 0.5880 | 0.0307 | 0.9259 | 0.0597 | 0.9677 | 0.0892 | 0.9900 |
| 0.0026 | 0.6341 | 0.0321 | 0.9299 | 0.0611 | 0.9728 | 0.0903 | 1.0008 |
| 0.0039 | 0.6813 | 0.0335 | 0.9327 | 0.0624 | 0.9645 | 0.0916 | 1.0035 |
| 0.0053 | 0.7254 | 0.0348 | 0.9341 | 0.0638 | 0.9621 | 0.0930 | 1.0034 |
| 0.0067 | 0.7639 | 0.0362 | 0.9337 | 0.0651 | 0.9671 | 0.0943 | 0.9984 |
| 0.0080 | 0.7901 | 0.0376 | 0.9329 | 0.0665 | 0.9792 | 0.0957 | 0.9944 |
| 0.0094 | 0.8105 | 0.0384 | 0.9336 | 0.0678 | 0.9853 | 0.0970 | 0.9952 |
| 0.0103 | 0.8292 | 0.0397 | 0.9362 | 0.0692 | 0.9865 | 0.0984 | 1.0015 |
| 0.0117 | 0.8325 | 0.0411 | 0.9396 | 0.0703 | 0.9764 | 0.0997 | 0.9998 |
| 0.0130 | 0.8380 | 0.0424 | 0.9373 | 0.0716 | 0.9758 | 0.1011 | 0.9987 |
| 0.0144 | 0.8478 | 0.0438 | 0.9376 | 0.0730 | 0.9780 | 0.1024 | 0.9957 |
| 0.0158 | 0.8582 | 0.0451 | 0.9373 | 0.0743 | 0.9820 | 0.1038 | 0.9983 |
| 0.0171 | 0.8661 | 0.0465 | 0.9423 | 0.0757 | 0.9863 | 0.1051 | 0.9980 |
| 0.0185 | 0.8759 | 0.0478 | 0.9463 | 0.0770 | 0.9893 | 0.1065 | 0.9956 |
| 0.0198 | 0.8830 | 0.0492 | 0.9486 | 0.0784 | 0.9860 | 0.1078 | 0.9938 |
| 0.0212 | 0.8920 | 0.0505 | 0.9503 | 0.0797 | 0.9836 | 0.1092 | 0.9939 |
| 0.0226 | 0.8969 | 0.0519 | 0.9517 | 0.0811 | 0.9806 | 0.1105 | 0.9972 |
| 0.0239 | 0.9012 | 0.0532 | 0.9550 | 0.0824 | 0.9850 | 0.1119 | 1.0004 |
| 0.0253 | 0.9075 | 0.0546 | 0.9582 | 0.0838 | 0.9886 | 0.1132 | 1.0006 |
| 0.0267 | 0.9122 | 0.0559 | 0.9584 | 0.0851 | 0.9920 | 0.1146 | 0.9967 |
| 0.0280 | 0.9177 | 0.0573 | 0.9582 | 0.0865 | 0.9919 | 0.1159 | 0.9912 |
| 0.0294 | 0.9216 | 0.0584 | 0.9676 | 0.0878 | 0.9913 | | |

Table A.24: Centerline Velocity, $D_h$ = 500 µm, Re = 200, Distilled Water

| $x$/ReD$_h$ | $u_{cl}/u_{cl,fd}$ | $x$/ReD$_h$ | $u_{cl}/u_{cl,fd}$ | $x$/ReD$_h$ | $u_{cl}/u_{cl,fd}$ | $x$/ReD$_h$ | $u_{cl}/u_{cl,fd}$ |
|---|---|---|---|---|---|---|---|
| 0.0003 | 0.4441 | 0.0109 | 0.7965 | 0.0216 | 0.8822 | 0.0323 | 0.9273 |
| 0.0006 | 0.4985 | 0.0113 | 0.7988 | 0.0220 | 0.8833 | 0.0326 | 0.9258 |
| 0.0010 | 0.5415 | 0.0116 | 0.8009 | 0.0223 | 0.8843 | 0.0330 | 0.9254 |
| 0.0013 | 0.5852 | 0.0120 | 0.8034 | 0.0226 | 0.8858 | 0.0333 | 0.9277 |
| 0.0017 | 0.6156 | 0.0123 | 0.8039 | 0.0230 | 0.8901 | 0.0336 | 0.9265 |
| 0.0020 | 0.6379 | 0.0126 | 0.8065 | 0.0233 | 0.8909 | 0.0340 | 0.9245 |
| 0.0023 | 0.6538 | 0.0130 | 0.8111 | 0.0236 | 0.8925 | 0.0343 | 0.9193 |
| 0.0027 | 0.6665 | 0.0133 | 0.8126 | 0.0240 | 0.8913 | 0.0326 | 0.9255 |
| 0.0030 | 0.6791 | 0.0136 | 0.8131 | 0.0243 | 0.8928 | 0.0329 | 0.9261 |
| 0.0034 | 0.6894 | 0.0140 | 0.8129 | 0.0226 | 0.8842 | 0.0332 | 0.9243 |
| 0.0037 | 0.6937 | 0.0143 | 0.8142 | 0.0229 | 0.8849 | 0.0336 | 0.9262 |
| 0.0040 | 0.6946 | 0.0126 | 0.8148 | 0.0232 | 0.8863 | 0.0339 | 0.9306 |
| 0.0044 | 0.6932 | 0.0129 | 0.8150 | 0.0236 | 0.8885 | 0.0343 | 0.9377 |
| 0.0026 | 0.6995 | 0.0132 | 0.8167 | 0.0239 | 0.8898 | 0.0346 | 0.9395 |
| 0.0029 | 0.7026 | 0.0136 | 0.8198 | 0.0243 | 0.8910 | 0.0349 | 0.9394 |
| 0.0033 | 0.7061 | 0.0139 | 0.8214 | 0.0246 | 0.8900 | 0.0353 | 0.9413 |
| 0.0036 | 0.7116 | 0.0143 | 0.8179 | 0.0249 | 0.8918 | 0.0356 | 0.9422 |
| 0.0039 | 0.7149 | 0.0146 | 0.8179 | 0.0253 | 0.8942 | 0.0359 | 0.9423 |
| 0.0043 | 0.7198 | 0.0149 | 0.8237 | 0.0256 | 0.8969 | 0.0363 | 0.9391 |
| 0.0046 | 0.7249 | 0.0153 | 0.8304 | 0.0259 | 0.8968 | 0.0366 | 0.9377 |
| 0.0050 | 0.7321 | 0.0156 | 0.8254 | 0.0263 | 0.8966 | 0.0370 | 0.9365 |
| 0.0053 | 0.7390 | 0.0159 | 0.8262 | 0.0266 | 0.8990 | 0.0373 | 0.9362 |
| 0.0056 | 0.7439 | 0.0163 | 0.8323 | 0.0270 | 0.9017 | 0.0376 | 0.9397 |
| 0.0060 | 0.7473 | 0.0166 | 0.8459 | 0.0273 | 0.9017 | 0.0380 | 0.9428 |
| 0.0063 | 0.7503 | 0.0170 | 0.8485 | 0.0276 | 0.9029 | 0.0383 | 0.9449 |
| 0.0067 | 0.7539 | 0.0173 | 0.8506 | 0.0280 | 0.9044 | 0.0386 | 0.9433 |
| 0.0070 | 0.7589 | 0.0176 | 0.8527 | 0.0283 | 0.9092 | 0.0390 | 0.9416 |
| 0.0073 | 0.7632 | 0.0180 | 0.8562 | 0.0286 | 0.9106 | 0.0393 | 0.9418 |
| 0.0077 | 0.7670 | 0.0183 | 0.8597 | 0.0290 | 0.9107 | 0.0376 | 0.9529 |
| 0.0080 | 0.7712 | 0.0186 | 0.8612 | 0.0293 | 0.9097 | 0.0379 | 0.9513 |
| 0.0084 | 0.7756 | 0.0190 | 0.8617 | 0.0276 | 0.9025 | 0.0382 | 0.9499 |
| 0.0087 | 0.7783 | 0.0193 | 0.8602 | 0.0279 | 0.9039 | 0.0386 | 0.9533 |
| 0.0090 | 0.7782 | 0.0176 | 0.8564 | 0.0282 | 0.9083 | 0.0389 | 0.9568 |
| 0.0094 | 0.7772 | 0.0179 | 0.8571 | 0.0286 | 0.9119 | 0.0393 | 0.9625 |
| 0.0076 | 0.7619 | 0.0182 | 0.8573 | 0.0289 | 0.9137 | 0.0396 | 0.9588 |
| 0.0079 | 0.7638 | 0.0186 | 0.8590 | 0.0293 | 0.9138 | 0.0399 | 0.9567 |
| 0.0082 | 0.7662 | 0.0189 | 0.8590 | 0.0296 | 0.9174 | 0.0403 | 0.9529 |
| 0.0086 | 0.7697 | 0.0193 | 0.8615 | 0.0299 | 0.9192 | 0.0406 | 0.9536 |
| 0.0089 | 0.7719 | 0.0196 | 0.8623 | 0.0303 | 0.9202 | 0.0409 | 0.9559 |
| 0.0093 | 0.7748 | 0.0199 | 0.8633 | 0.0306 | 0.9151 | 0.0413 | 0.9572 |
| 0.0096 | 0.7708 | 0.0203 | 0.8660 | 0.0309 | 0.9152 | 0.0416 | 0.9582 |
| 0.0099 | 0.7826 | 0.0206 | 0.8693 | 0.0313 | 0.9156 | 0.0420 | 0.9571 |
| 0.0103 | 0.7891 | 0.0209 | 0.8752 | 0.0316 | 0.9216 | 0.0423 | 0.9558 |
| 0.0106 | 0.7943 | 0.0213 | 0.8784 | 0.0320 | 0.9243 | 0.0426 | 0.9582 |

| $x$/ReDh | $u_{cl}/u_{cl,fd}$ | $x$/ReDh | $u_{cl}/u_{cl,fd}$ | $x$/ReDh | $u_{cl}/u_{cl,fd}$ | $x$/ReDh | $u_{cl}/u_{cl,fd}$ |
|---|---|---|---|---|---|---|---|
| 0.0430 | 0.9631 | 0.0536 | 0.9805 | 0.0643 | 0.9822 | 0.0729 | 0.9931 |
| 0.0433 | 0.9660 | 0.0540 | 0.9777 | 0.0626 | 0.9853 | 0.0732 | 0.9921 |
| 0.0436 | 0.9671 | 0.0543 | 0.9783 | 0.0629 | 0.9823 | 0.0736 | 0.9906 |
| 0.0440 | 0.9646 | 0.0526 | 0.9838 | 0.0632 | 0.9806 | 0.0739 | 0.9918 |
| 0.0443 | 0.9657 | 0.0529 | 0.9840 | 0.0636 | 0.9798 | 0.0743 | 0.9954 |
| 0.0426 | 0.9627 | 0.0532 | 0.9857 | 0.0639 | 0.9803 | 0.0746 | 0.9964 |
| 0.0429 | 0.9610 | 0.0536 | 0.9864 | 0.0643 | 0.9788 | 0.0749 | 0.9961 |
| 0.0432 | 0.9608 | 0.0539 | 0.9891 | 0.0646 | 0.9772 | 0.0753 | 0.9977 |
| 0.0436 | 0.9580 | 0.0543 | 0.9891 | 0.0649 | 0.9722 | 0.0756 | 1.0002 |
| 0.0439 | 0.9594 | 0.0546 | 0.9924 | 0.0653 | 0.9740 | 0.0759 | 1.0009 |
| 0.0443 | 0.9587 | 0.0549 | 0.9904 | 0.0656 | 0.9736 | 0.0763 | 0.9991 |
| 0.0446 | 0.9609 | 0.0553 | 0.9909 | 0.0659 | 0.9832 | 0.0766 | 0.9950 |
| 0.0449 | 0.9606 | 0.0556 | 0.9869 | 0.0663 | 0.9865 | 0.0770 | 0.9902 |
| 0.0453 | 0.9646 | 0.0559 | 0.9849 | 0.0666 | 0.9892 | 0.0773 | 0.9889 |
| 0.0456 | 0.9684 | 0.0563 | 0.9848 | 0.0670 | 0.9878 | 0.0776 | 0.9900 |
| 0.0459 | 0.9707 | 0.0566 | 0.9864 | 0.0673 | 0.9873 | 0.0780 | 0.9934 |
| 0.0463 | 0.9709 | 0.0570 | 0.9880 | 0.0676 | 0.9865 | 0.0783 | 0.9934 |
| 0.0466 | 0.9700 | 0.0573 | 0.9885 | 0.0680 | 0.9832 | 0.0786 | 0.9935 |
| 0.0470 | 0.9723 | 0.0576 | 0.9914 | 0.0683 | 0.9804 | 0.0790 | 0.9923 |
| 0.0473 | 0.9720 | 0.0580 | 0.9920 | 0.0686 | 0.9773 | 0.0793 | 0.9908 |
| 0.0476 | 0.9716 | 0.0583 | 0.9931 | 0.0690 | 0.9770 | | |
| 0.0480 | 0.9680 | 0.0586 | 0.9893 | 0.0693 | 0.9765 | | |
| 0.0483 | 0.9657 | 0.0590 | 0.9883 | 0.0676 | 0.9866 | | |
| 0.0486 | 0.9633 | 0.0593 | 0.9858 | 0.0679 | 0.9922 | | |
| 0.0490 | 0.9623 | 0.0576 | 0.9866 | 0.0682 | 0.9945 | | |
| 0.0493 | 0.9621 | 0.0579 | 0.9877 | 0.0686 | 0.9947 | | |
| 0.0476 | 0.9796 | 0.0582 | 0.9873 | 0.0689 | 0.9892 | | |
| 0.0479 | 0.9769 | 0.0586 | 0.9874 | 0.0693 | 0.9901 | | |
| 0.0482 | 0.9772 | 0.0589 | 0.9845 | 0.0696 | 0.9892 | | |
| 0.0486 | 0.9783 | 0.0593 | 0.9855 | 0.0699 | 0.9897 | | |
| 0.0489 | 0.9843 | 0.0596 | 0.9848 | 0.0703 | 0.9898 | | |
| 0.0493 | 0.9875 | 0.0599 | 0.9824 | 0.0706 | 0.9925 | | |
| 0.0496 | 0.9854 | 0.0603 | 0.9825 | 0.0709 | 0.9944 | | |
| 0.0499 | 0.9855 | 0.0606 | 0.9814 | 0.0713 | 0.9920 | | |
| 0.0503 | 0.9885 | 0.0609 | 0.9840 | 0.0716 | 0.9918 | | |
| 0.0506 | 0.9906 | 0.0613 | 0.9825 | 0.0720 | 0.9909 | | |
| 0.0509 | 0.9909 | 0.0616 | 0.9857 | 0.0723 | 0.9929 | | |
| 0.0513 | 0.9862 | 0.0620 | 0.9886 | 0.0726 | 0.9920 | | |
| 0.0516 | 0.9889 | 0.0623 | 0.9889 | 0.0730 | 0.9942 | | |
| 0.0520 | 0.9889 | 0.0626 | 0.9873 | 0.0733 | 0.9944 | | |
| 0.0523 | 0.9907 | 0.0630 | 0.9847 | 0.0736 | 0.9956 | | |
| 0.0526 | 0.9891 | 0.0633 | 0.9847 | 0.0740 | 0.9940 | | |
| 0.0530 | 0.9884 | 0.0636 | 0.9834 | 0.0743 | 0.9936 | | |
| 0.0533 | 0.9842 | 0.0640 | 0.9827 | 0.0726 | 0.9934 | | |

## A.3 Microchannel Entrance Length Data

Table A.25: Entrance Length Data, Distilled Water

| $D_h$ | Re | $Le/D_h$ |
|---|---|---|
| 100 µm | 0.476 | 0.7680 |
| | 4.76 | 0.9113 |
| | 50 | 3.9084 |
| | 89 | 6.4000 |
| 200 µm | 0.5 | 0.6842 |
| | 5 | 0.9566 |
| | 50 | 4.0655 |
| | 200 | 16.0520 |
| 500 µm | 0.5 | 0.4922 |
| | 5 | 0.5201 |
| | 50 | 4.2574 |
| | 200 | 14.5274 |

# Appendix B

# Experimental Data for the Thermal Entrance Region

## B.1 Microtube Turbulent Friction Factors

Table B.1: Friction Factor Data, FC-72

| $D$ | Re | $f_{exp}$ |
|---|---|---|
| 0.508 mm | 4717 | 0.0490 |
| | 6645 | 0.0398 |
| | 7912 | 0.0362 |
| | 8733 | 0.0386 |
| 1.067 mm | 5399 | 0.0422 |
| | 6287 | 0.0408 |
| | 8035 | 0.0421 |
| | 8926 | 0.0416 |

## B.2 Local Microtube Wall Temperatures

Table B.2: Wall Temperatures, $D = 0.508$ mm, Re = 4717, FC-72

| $x/D$ | $T_{w_x}$ (°C) | $x/D$ | $T_{w_x}$ (°C) | $x/D$ | $T_{w_x}$ (°C) | $x/D$ | $T_{w_x}$ (°C) |
|---|---|---|---|---|---|---|---|
| -1.2532 | 40.7904 | 3.3318 | 40.9586 | 7.9168 | 41.0071 | 12.5019 | 40.9404 |
| -1.1004 | 40.0321 | 3.4846 | 41.0054 | 8.0697 | 41.0819 | 12.6547 | 41.1083 |
| -0.9476 | 39.2340 | 3.6375 | 40.8605 | 8.2225 | 41.0018 | 12.8075 | 40.9132 |
| -0.7947 | 39.0606 | 3.7903 | 40.8534 | 8.3753 | 41.1352 | 12.9604 | 40.8714 |
| -0.6419 | 38.6520 | 3.9431 | 41.1730 | 8.5282 | 41.1427 | 13.1132 | 40.8173 |
| -0.4891 | 38.7788 | 4.0960 | 41.1241 | 8.6810 | 40.9047 | 13.2660 | 40.9433 |
| -0.3362 | 39.1198 | 4.2488 | 40.9022 | 8.8338 | 40.8722 | 13.4189 | 40.8233 |
| -0.1834 | 39.6118 | 4.4016 | 41.1168 | 8.9867 | 40.9335 | 13.5717 | 40.9515 |
| -0.0306 | 40.0563 | 4.5545 | 41.0908 | 9.1395 | 41.1428 | 13.7246 | 40.9937 |
| 0.1223 | 39.3871 | 4.7073 | 41.4722 | 9.2923 | 41.1637 | 13.8774 | 40.9388 |
| 0.2751 | 39.8133 | 4.8601 | 41.1008 | 9.4452 | 40.9964 | 14.0302 | 41.0165 |
| 0.4279 | 40.3408 | 5.0130 | 41.2109 | 9.5980 | 40.8322 | 14.1831 | 40.9695 |
| 0.5808 | 41.1892 | 5.1658 | 41.1989 | 9.7509 | 41.0961 | 14.3359 | 41.0244 |
| 0.7336 | 40.9434 | 5.3186 | 41.0798 | 9.9037 | 40.9351 | 14.4887 | 41.0162 |
| 0.8864 | 40.8493 | 5.4715 | 41.2041 | 10.0565 | 40.9873 | 14.6416 | 40.7849 |
| 1.0393 | 40.3926 | 5.6243 | 41.1591 | 10.2094 | 41.1440 | 14.7944 | 40.8344 |
| 1.1921 | 42.0012 | 5.7771 | 41.1962 | 10.3622 | 41.0897 | 14.9472 | 40.9120 |
| 1.3449 | 41.3091 | 5.9300 | 41.0342 | 10.5150 | 41.1027 | 15.1001 | 40.8695 |
| 1.4978 | 42.3461 | 6.0828 | 40.9269 | 10.6679 | 41.0676 | 15.2529 | 40.9999 |
| 1.6506 | 42.4918 | 6.2357 | 40.8810 | 10.8207 | 41.1360 | 15.4057 | 41.0186 |
| 1.8034 | 40.9761 | 6.3885 | 41.2465 | 10.9735 | 41.1474 | 15.5586 | 41.1751 |
| 1.9563 | 41.3233 | 6.5413 | 41.1523 | 11.1264 | 41.1234 | 15.7114 | 41.2076 |
| 2.1091 | 41.3095 | 6.6942 | 41.2130 | 11.2792 | 41.0832 | 15.8642 | 40.9276 |
| 2.2620 | 40.9223 | 6.8470 | 40.9336 | 11.4320 | 41.1001 | 16.0171 | 40.8834 |
| 2.4148 | 40.9788 | 6.9998 | 41.1476 | 11.5849 | 41.0122 | 16.1699 | 41.1266 |
| 2.5676 | 40.6458 | 7.1527 | 41.2647 | 11.7377 | 40.8683 | 16.3227 | 41.0834 |
| 2.7205 | 40.7209 | 7.3055 | 40.9958 | 11.8905 | 41.0451 | 16.4756 | 41.2959 |
| 2.8733 | 40.7445 | 7.4583 | 40.8914 | 12.0434 | 40.8950 | 16.6284 | 41.0460 |
| 3.0261 | 40.6688 | 7.6112 | 41.0287 | 12.1962 | 40.9503 | 16.7812 | 41.4509 |
| 3.1790 | 40.9709 | 7.7640 | 40.9312 | 12.3490 | 40.9252 | 16.9341 | 41.3933 |

Table B.3: Wall Temperatures, $D = 0.508$ mm, Re = 6645, FC-72

| $x/D$ | $Tw_x$ (°C) | $x/D$ | $Tw_x$ (°C) | $x/D$ | $Tw_x$ (°C) | $x/D$ | $Tw_x$ (°C) |
|---|---|---|---|---|---|---|---|
| -1.2532 | 41.2246 | 3.3318 | 41.9424 | 7.9168 | 42.1348 | 12.5019 | 41.7369 |
| -1.1004 | 40.1909 | 3.4846 | 41.9953 | 8.0697 | 42.1900 | 12.6547 | 41.9405 |
| -0.9476 | 39.6984 | 3.6375 | 41.9341 | 8.2225 | 41.9351 | 12.8075 | 41.7333 |
| -0.7947 | 39.1352 | 3.7903 | 42.2513 | 8.3753 | 42.1259 | 12.9604 | 41.8970 |
| -0.6419 | 39.0109 | 3.9431 | 42.1224 | 8.5282 | 42.3472 | 13.1132 | 41.6829 |
| -0.4891 | 40.3886 | 4.0960 | 42.0867 | 8.6810 | 42.0673 | 13.2660 | 41.6853 |
| -0.3362 | 40.5131 | 4.2488 | 41.9368 | 8.8338 | 42.1501 | 13.4189 | 42.1536 |
| -0.1834 | 40.5909 | 4.4016 | 41.9740 | 8.9867 | 41.8599 | 13.5717 | 41.8801 |
| -0.0306 | 41.2701 | 4.5545 | 42.4846 | 9.1395 | 41.9968 | 13.7246 | 42.1634 |
| 0.1223 | 41.5589 | 4.7073 | 42.3782 | 9.2923 | 41.7517 | 13.8774 | 42.1695 |
| 0.2751 | 41.7520 | 4.8601 | 42.1530 | 9.4452 | 41.9702 | 14.0302 | 42.2165 |
| 0.4279 | 42.0829 | 5.0130 | 42.1619 | 9.5980 | 41.9295 | 14.1831 | 42.2982 |
| 0.5808 | 42.0699 | 5.1658 | 42.3442 | 9.7509 | 41.9412 | 14.3359 | 41.9238 |
| 0.7336 | 42.5006 | 5.3186 | 42.2817 | 9.9037 | 42.0014 | 14.4887 | 41.9207 |
| 0.8864 | 42.3813 | 5.4715 | 42.3191 | 10.0565 | 41.7725 | 14.6416 | 41.9620 |
| 1.0393 | 42.2572 | 5.6243 | 42.1644 | 10.2094 | 41.8934 | 14.7944 | 41.7922 |
| 1.1921 | 43.6347 | 5.7771 | 42.2344 | 10.3622 | 41.9542 | 14.9472 | 41.7732 |
| 1.3449 | 42.6741 | 5.9300 | 42.5144 | 10.5150 | 41.6287 | 15.1001 | 42.1509 |
| 1.4978 | 43.1373 | 6.0828 | 42.6578 | 10.6679 | 41.6243 | 15.2529 | 42.0543 |
| 1.6506 | 43.2288 | 6.2357 | 42.5314 | 10.8207 | 41.7853 | 15.4057 | 41.8857 |
| 1.8034 | 42.5529 | 6.3885 | 42.2347 | 10.9735 | 41.8495 | 15.5586 | 42.0776 |
| 1.9563 | 42.2797 | 6.5413 | 42.4421 | 11.1264 | 41.9908 | 15.7114 | 41.9167 |
| 2.1091 | 42.4503 | 6.6942 | 42.6371 | 11.2792 | 42.0349 | 15.8642 | 41.9153 |
| 2.2620 | 42.3073 | 6.8470 | 42.4433 | 11.4320 | 42.0073 | 16.0171 | 41.7399 |
| 2.4148 | 42.0305 | 6.9998 | 42.2524 | 11.5849 | 41.9514 | 16.1699 | 41.6716 |
| 2.5676 | 41.9151 | 7.1527 | 42.4616 | 11.7377 | 41.8026 | 16.3227 | 41.9458 |
| 2.7205 | 41.7995 | 7.3055 | 42.7614 | 11.8905 | 41.5452 | 16.4756 | 42.1832 |
| 2.8733 | 41.8334 | 7.4583 | 42.3961 | 12.0434 | 41.4469 | 16.6284 | 42.6383 |
| 3.0261 | 41.9778 | 7.6112 | 42.3585 | 12.1962 | 41.6452 | 16.7812 | 42.1894 |
| 3.1790 | 41.7678 | 7.7640 | 42.3785 | 12.3490 | 41.9177 | 16.9341 | 42.2352 |

Table B.4: Wall Temperatures, $D$ = 0.508 mm, Re = 7912, FC-72

| $x/D$ | $Tw_x$ (°C) | $x/D$ | $Tw_x$ (°C) | $x/D$ | $Tw_x$ (°C) | $x/D$ | $Tw_x$ (°C) |
|---|---|---|---|---|---|---|---|
| -1.2532 | 40.4771 | 3.3318 | 40.5608 | 7.9168 | 40.5714 | 12.5019 | 40.5673 |
| -1.1004 | 39.8488 | 3.4846 | 40.5708 | 8.0697 | 40.4502 | 12.6547 | 40.5451 |
| -0.9476 | 39.7679 | 3.6375 | 40.5348 | 8.2225 | 40.5357 | 12.8075 | 40.6337 |
| -0.7947 | 39.2411 | 3.7903 | 40.7198 | 8.3753 | 40.6508 | 12.9604 | 40.7690 |
| -0.6419 | 38.7562 | 3.9431 | 40.9507 | 8.5282 | 40.7931 | 13.1132 | 40.5139 |
| -0.4891 | 39.1606 | 4.0960 | 40.8373 | 8.6810 | 40.6105 | 13.2660 | 40.4951 |
| -0.3362 | 38.6728 | 4.2488 | 40.6601 | 8.8338 | 40.7076 | 13.4189 | 40.9017 |
| -0.1834 | 39.1132 | 4.4016 | 40.7701 | 8.9867 | 40.6439 | 13.5717 | 40.8439 |
| -0.0306 | 38.6191 | 4.5545 | 40.8984 | 9.1395 | 40.6025 | 13.7246 | 40.7964 |
| 0.1223 | 38.5132 | 4.7073 | 41.0139 | 9.2923 | 40.7168 | 13.8774 | 40.7786 |
| 0.2751 | 39.1540 | 4.8601 | 40.9914 | 9.4452 | 40.6704 | 14.0302 | 40.7023 |
| 0.4279 | 39.3292 | 5.0130 | 40.8654 | 9.5980 | 40.6646 | 14.1831 | 40.9335 |
| 0.5808 | 39.7619 | 5.1658 | 40.6283 | 9.7509 | 40.7773 | 14.3359 | 40.6660 |
| 0.7336 | 40.2661 | 5.3186 | 40.8226 | 9.9037 | 40.6242 | 14.4887 | 40.5522 |
| 0.8864 | 39.7293 | 5.4715 | 40.5541 | 10.0565 | 40.5251 | 14.6416 | 40.5598 |
| 1.0393 | 39.7385 | 5.6243 | 40.4695 | 10.2094 | 40.5239 | 14.7944 | 40.3204 |
| 1.1921 | 40.9490 | 5.7771 | 40.6426 | 10.3622 | 40.5385 | 14.9472 | 40.5605 |
| 1.3449 | 40.4791 | 5.9300 | 40.6743 | 10.5150 | 40.3822 | 15.1001 | 40.6495 |
| 1.4978 | 40.7375 | 6.0828 | 40.7898 | 10.6679 | 40.6347 | 15.2529 | 40.5927 |
| 1.6506 | 41.8541 | 6.2357 | 40.4168 | 10.8207 | 40.7236 | 15.4057 | 40.6753 |
| 1.8034 | 41.1330 | 6.3885 | 40.4083 | 10.9735 | 40.5570 | 15.5586 | 40.8854 |
| 1.9563 | 40.9854 | 6.5413 | 40.5722 | 11.1264 | 40.5400 | 15.7114 | 40.7398 |
| 2.1091 | 40.7676 | 6.6942 | 40.8521 | 11.2792 | 40.5540 | 15.8642 | 40.7922 |
| 2.2620 | 40.6540 | 6.8470 | 40.6355 | 11.4320 | 40.3808 | 16.0171 | 40.9641 |
| 2.4148 | 40.5093 | 6.9998 | 40.6958 | 11.5849 | 40.6216 | 16.1699 | 40.7959 |
| 2.5676 | 39.7437 | 7.1527 | 40.7537 | 11.7377 | 40.4772 | 16.3227 | 40.9469 |
| 2.7205 | 40.1551 | 7.3055 | 40.6189 | 11.8905 | 40.5183 | 16.4756 | 41.1096 |
| 2.8733 | 40.1852 | 7.4583 | 40.4950 | 12.0434 | 40.5451 | 16.6284 | 41.1741 |
| 3.0261 | 40.6525 | 7.6112 | 40.8622 | 12.1962 | 40.6647 | 16.7812 | 40.9166 |
| 3.1790 | 40.5802 | 7.7640 | 40.5322 | 12.3490 | 40.5987 | 16.9341 | 41.0485 |

Table B.5: Wall Temperatures, $D = 0.508$ mm, Re = 8733, FC-72

| $x/D$ | $Tw_x$ (°C) | $x/D$ | $Tw_x$ (°C) | $x/D$ | $Tw_x$ (°C) | $x/D$ | $Tw_x$ (°C) |
|---|---|---|---|---|---|---|---|
| -1.2532 | 40.2862 | 3.3318 | 41.1588 | 7.9168 | 40.9190 | 12.5019 | 40.8054 |
| -1.1004 | 40.1623 | 3.4846 | 41.0131 | 8.0697 | 40.8031 | 12.6547 | 41.0426 |
| -0.9476 | 38.8843 | 3.6375 | 40.9602 | 8.2225 | 41.0294 | 12.8075 | 40.9118 |
| -0.7947 | 38.7181 | 3.7903 | 40.7591 | 8.3753 | 41.1667 | 12.9604 | 40.8226 |
| -0.6419 | 38.8441 | 3.9431 | 41.2641 | 8.5282 | 41.0734 | 13.1132 | 40.7277 |
| -0.4891 | 39.2263 | 4.0960 | 40.9951 | 8.6810 | 40.8135 | 13.2660 | 40.7355 |
| -0.3362 | 39.2191 | 4.2488 | 40.9751 | 8.8338 | 40.6426 | 13.4189 | 40.9269 |
| -0.1834 | 39.8594 | 4.4016 | 41.1602 | 8.9867 | 40.9196 | 13.5717 | 40.8804 |
| -0.0306 | 39.7914 | 4.5545 | 41.1190 | 9.1395 | 40.9738 | 13.7246 | 40.8795 |
| 0.1223 | 39.9140 | 4.7073 | 41.5047 | 9.2923 | 41.1686 | 13.8774 | 40.8927 |
| 0.2751 | 39.9216 | 4.8601 | 41.3748 | 9.4452 | 40.9456 | 14.0302 | 40.9722 |
| 0.4279 | 40.2695 | 5.0130 | 41.3775 | 9.5980 | 40.9570 | 14.1831 | 40.9942 |
| 0.5808 | 41.1794 | 5.1658 | 41.3723 | 9.7509 | 41.0601 | 14.3359 | 40.9769 |
| 0.7336 | 40.7987 | 5.3186 | 41.2372 | 9.9037 | 41.0340 | 14.4887 | 40.7783 |
| 0.8864 | 40.4138 | 5.4715 | 41.0959 | 10.0565 | 40.8859 | 14.6416 | 40.5666 |
| 1.0393 | 40.5916 | 5.6243 | 40.9884 | 10.2094 | 40.9775 | 14.7944 | 40.5874 |
| 1.1921 | 42.0992 | 5.7771 | 41.0977 | 10.3622 | 40.8952 | 14.9472 | 40.9496 |
| 1.3449 | 41.7832 | 5.9300 | 40.7777 | 10.5150 | 40.7722 | 15.1001 | 40.7877 |
| 1.4978 | 42.7845 | 6.0828 | 40.8299 | 10.6679 | 41.0799 | 15.2529 | 41.1539 |
| 1.6506 | 42.8186 | 6.2357 | 40.9179 | 10.8207 | 41.1539 | 15.4057 | 41.0266 |
| 1.8034 | 41.5881 | 6.3885 | 41.0789 | 10.9735 | 40.8935 | 15.5586 | 41.0525 |
| 1.9563 | 41.5551 | 6.5413 | 40.9148 | 11.1264 | 40.9034 | 15.7114 | 41.1392 |
| 2.1091 | 41.7552 | 6.6942 | 41.1741 | 11.2792 | 40.8447 | 15.8642 | 40.7726 |
| 2.2620 | 41.4273 | 6.8470 | 40.9980 | 11.4320 | 41.0058 | 16.0171 | 40.7302 |
| 2.4148 | 41.2035 | 6.9998 | 41.0971 | 11.5849 | 41.0829 | 16.1699 | 40.9708 |
| 2.5676 | 40.7364 | 7.1527 | 41.1705 | 11.7377 | 41.0840 | 16.3227 | 40.9649 |
| 2.7205 | 40.8100 | 7.3055 | 40.9472 | 11.8905 | 40.9318 | 16.4756 | 41.1721 |
| 2.8733 | 40.9913 | 7.4583 | 40.9419 | 12.0434 | 40.8416 | 16.6284 | 41.0714 |
| 3.0261 | 40.6046 | 7.6112 | 41.0534 | 12.1962 | 40.8797 | 16.7812 | 41.5255 |
| 3.1790 | 41.0417 | 7.7640 | 40.9587 | 12.3490 | 40.7926 | 16.9341 | 41.5262 |

Table B.6: Wall Temperatures, $D$ = 1.067 mm, Re = 5399, FC-72

| $x/D$ | $T_{W_x}$ (°C) | $x/D$ | $T_{W_x}$ (°C) | $x/D$ | $T_{W_x}$ (°C) | $x/D$ | $T_{W_x}$ (°C) |
|---|---|---|---|---|---|---|---|
| -1.4553 | 41.2942 | 0.5239 | 41.8535 | 2.5031 | 42.2623 | 4.4823 | 42.1382 |
| -1.3971 | 41.2826 | 0.5821 | 41.9085 | 2.5613 | 42.2273 | 4.5405 | 42.1302 |
| -1.3389 | 41.2666 | 0.6403 | 41.8508 | 2.6195 | 42.2139 | 4.5987 | 42.1399 |
| -1.2807 | 41.3310 | 0.6985 | 41.8463 | 2.6777 | 42.2636 | 4.6569 | 42.0088 |
| -1.2224 | 41.4121 | 0.7568 | 41.8918 | 2.7360 | 42.2504 | 4.7152 | 42.0758 |
| -1.1642 | 41.1561 | 0.8150 | 42.0556 | 2.7942 | 42.1843 | 4.7734 | 42.1651 |
| -1.1060 | 41.1461 | 0.8732 | 41.9077 | 2.8524 | 42.1846 | 4.8316 | 42.1038 |
| -1.0478 | 41.1421 | 0.9314 | 41.9608 | 2.9106 | 42.2230 | 4.8898 | 42.1945 |
| -0.9896 | 41.1284 | 0.9896 | 42.0029 | 2.9688 | 42.2629 | 4.9480 | 42.1966 |
| -0.9314 | 41.1461 | 1.0478 | 41.9646 | 3.0270 | 42.2187 | 5.0062 | 42.1425 |
| -0.8732 | 41.2102 | 1.1060 | 41.9466 | 3.0852 | 42.2958 | 5.0644 | 42.1717 |
| -0.8150 | 41.2409 | 1.1642 | 41.9177 | 3.1434 | 42.2311 | 5.1226 | 42.2263 |
| -0.7568 | 41.2821 | 1.2224 | 42.0228 | 3.2016 | 42.1913 | 5.1809 | 42.2982 |
| -0.6985 | 41.2237 | 1.2807 | 41.9939 | 3.2599 | 42.2297 | 5.2391 | 42.4089 |
| -0.6403 | 41.2781 | 1.3389 | 42.1130 | 3.3181 | 42.1618 | 5.2973 | 42.1696 |
| -0.5821 | 41.2770 | 1.3971 | 42.1113 | 3.3763 | 42.1460 | 5.3555 | 42.2966 |
| -0.5239 | 41.2913 | 1.4553 | 42.0825 | 3.4345 | 42.0187 | 5.4137 | 42.2939 |
| -0.4657 | 41.3522 | 1.5135 | 42.0952 | 3.4927 | 42.1571 | 5.4719 | 42.2120 |
| -0.4075 | 41.2470 | 1.5717 | 42.2427 | 3.5509 | 42.1680 | 5.5301 | 42.2800 |
| -0.3493 | 41.2643 | 1.6299 | 42.0141 | 3.6091 | 42.2092 | 5.5883 | 42.1613 |
| -0.2911 | 41.3133 | 1.6881 | 42.1444 | 3.6673 | 42.2368 | 5.6465 | 42.0568 |
| -0.2328 | 41.2882 | 1.7464 | 42.2299 | 3.7256 | 42.0012 | 5.7048 | 42.2314 |
| -0.1746 | 41.3260 | 1.8046 | 42.1071 | 3.7838 | 42.0771 | 5.7630 | 42.3573 |
| -0.1164 | 41.4605 | 1.8628 | 42.2829 | 3.8420 | 42.1088 | 5.8212 | 42.3914 |
| -0.0582 | 41.5115 | 1.9210 | 42.2404 | 3.9002 | 42.1109 | 5.8794 | 42.3127 |
| 0.0000 | 41.4701 | 1.9792 | 42.1645 | 3.9584 | 42.3188 | 5.9376 | 42.2060 |
| 0.0582 | 41.6247 | 2.0374 | 42.1255 | 4.0166 | 42.4158 | 5.9958 | 42.2736 |
| 0.1164 | 41.7087 | 2.0956 | 42.0786 | 4.0748 | 42.2820 | 6.0540 | 42.3283 |
| 0.1746 | 41.8196 | 2.1538 | 42.0967 | 4.1330 | 42.3101 | 6.1122 | 42.4454 |
| 0.2328 | 41.7343 | 2.2120 | 42.0244 | 4.1913 | 42.2974 | 6.1705 | 42.3695 |
| 0.2911 | 41.7598 | 2.2703 | 42.0398 | 4.2495 | 42.1966 | 6.2287 | 42.3484 |
| 0.3493 | 41.8449 | 2.3285 | 42.0797 | 4.3077 | 42.4082 | 6.2869 | 42.3351 |
| 0.4075 | 41.7670 | 2.3867 | 42.2097 | 4.3659 | 42.3382 | 6.3451 | 42.2960 |
| 0.4657 | 41.7469 | 2.4449 | 42.2424 | 4.4241 | 42.4245 | | |

Table B.7: Wall Temperatures, $D$ = 1.067 mm, Re = 6287, FC-72

| $x/D$ | $Tw_x$ (°C) | $x/D$ | $Tw_x$ (°C) | $x/D$ | $Tw_x$ (°C) | $x/D$ | $Tw_x$ (°C) |
|---|---|---|---|---|---|---|---|
| -1.4553 | 41.5584 | 0.5239 | 42.0042 | 2.5031 | 41.9965 | 4.4823 | 42.1345 |
| -1.3971 | 41.5349 | 0.5821 | 42.1151 | 2.5613 | 42.0617 | 4.5405 | 42.0219 |
| -1.3389 | 41.5582 | 0.6403 | 42.1079 | 2.6195 | 42.1390 | 4.5987 | 41.9733 |
| -1.2807 | 41.6211 | 0.6985 | 42.0288 | 2.6777 | 42.1284 | 4.6569 | 41.8909 |
| -1.2224 | 41.6117 | 0.7568 | 42.0208 | 2.7360 | 42.0880 | 4.7152 | 41.9215 |
| -1.1642 | 41.5538 | 0.8150 | 42.1901 | 2.7942 | 41.9495 | 4.7734 | 41.9776 |
| -1.1060 | 41.4722 | 0.8732 | 41.9622 | 2.8524 | 41.9539 | 4.8316 | 41.9991 |
| -1.0478 | 41.4780 | 0.9314 | 42.0054 | 2.9106 | 42.0073 | 4.8898 | 42.0645 |
| -0.9896 | 41.5354 | 0.9896 | 42.0888 | 2.9688 | 42.0950 | 4.9480 | 42.1775 |
| -0.9314 | 41.5673 | 1.0478 | 42.2181 | 3.0270 | 42.1758 | 5.0062 | 42.1057 |
| -0.8732 | 41.5605 | 1.1060 | 42.1188 | 3.0852 | 42.1601 | 5.0644 | 42.0021 |
| -0.8150 | 41.6759 | 1.1642 | 42.0383 | 3.1434 | 42.0943 | 5.1226 | 41.9954 |
| -0.7568 | 41.7875 | 1.2224 | 42.0938 | 3.2016 | 41.9550 | 5.1809 | 42.0882 |
| -0.6985 | 41.6854 | 1.2807 | 41.9535 | 3.2599 | 42.0337 | 5.2391 | 42.1860 |
| -0.6403 | 41.4998 | 1.3389 | 42.0423 | 3.3181 | 41.8857 | 5.2973 | 42.0680 |
| -0.5821 | 41.6182 | 1.3971 | 42.0943 | 3.3763 | 42.0179 | 5.3555 | 42.0711 |
| -0.5239 | 41.5734 | 1.4553 | 42.1075 | 3.4345 | 42.0065 | 5.4137 | 42.0922 |
| -0.4657 | 41.5482 | 1.5135 | 42.1554 | 3.4927 | 42.1311 | 5.4719 | 42.0769 |
| -0.4075 | 41.5262 | 1.5717 | 42.2119 | 3.5509 | 42.1258 | 5.5301 | 42.1855 |
| -0.3493 | 41.5435 | 1.6299 | 42.0088 | 3.6091 | 42.2539 | 5.5883 | 41.9916 |
| -0.2911 | 41.6700 | 1.6881 | 42.0522 | 3.6673 | 42.0511 | 5.6465 | 42.0473 |
| -0.2328 | 41.7883 | 1.7464 | 42.1924 | 3.7256 | 41.9780 | 5.7048 | 42.1444 |
| -0.1746 | 41.7906 | 1.8046 | 42.1434 | 3.7838 | 41.8799 | 5.7630 | 42.1364 |
| -0.1164 | 42.0552 | 1.8628 | 42.1731 | 3.8420 | 41.9489 | 5.8212 | 42.2623 |
| -0.0582 | 41.9226 | 1.9210 | 42.0703 | 3.9002 | 42.0308 | 5.8794 | 42.1934 |
| 0.0000 | 41.8666 | 1.9792 | 42.0697 | 3.9584 | 42.2790 | 5.9376 | 42.1592 |
| 0.0582 | 41.9881 | 2.0374 | 41.9964 | 4.0166 | 42.3550 | 5.9958 | 42.1767 |
| 0.1164 | 42.0008 | 2.0956 | 41.9374 | 4.0748 | 42.2780 | 6.0540 | 42.1604 |
| 0.1746 | 41.9959 | 2.1538 | 42.0591 | 4.1330 | 42.1619 | 6.1122 | 42.1968 |
| 0.2328 | 42.0596 | 2.2120 | 41.9658 | 4.1913 | 42.1260 | 6.1705 | 42.2774 |
| 0.2911 | 41.9211 | 2.2703 | 41.9087 | 4.2495 | 42.1111 | 6.2287 | 42.3039 |
| 0.3493 | 42.0497 | 2.3285 | 41.9413 | 4.3077 | 42.2473 | 6.2869 | 42.1671 |
| 0.4075 | 41.9255 | 2.3867 | 41.9442 | 4.3659 | 42.4245 | 6.3451 | 42.2636 |
| 0.4657 | 42.0431 | 2.4449 | 42.0949 | 4.4241 | 42.2892 | | |

Table B.8: Wall Temperatures, $D$ = 1.067 mm, Re = 8035, FC-72

| $x/D$ | $Tw_x$ (°C) | $x/D$ | $Tw_x$ (°C) | $x/D$ | $Tw_x$ (°C) | $x/D$ | $Tw_x$ (°C) |
|---|---|---|---|---|---|---|---|
| -0.7745 | 40.0408 | 0.6971 | 41.5300 | 2.1686 | 41.4555 | 3.6402 | 41.3052 |
| -0.7358 | 40.2939 | 0.7358 | 41.5531 | 2.2073 | 41.4131 | 3.6789 | 41.2584 |
| -0.6971 | 40.2282 | 0.7745 | 41.5903 | 2.2461 | 41.3293 | 3.7176 | 41.1811 |
| -0.6583 | 40.7263 | 0.8132 | 41.5903 | 2.2848 | 41.3564 | 3.7564 | 41.1445 |
| -0.6196 | 40.5906 | 0.8520 | 41.4081 | 2.3235 | 41.4174 | 3.7951 | 41.1957 |
| -0.5809 | 41.0235 | 0.8907 | 41.4838 | 2.3622 | 41.5111 | 3.8338 | 41.2500 |
| -0.5422 | 40.6335 | 0.9294 | 41.4570 | 2.4010 | 41.5289 | 3.8725 | 41.2693 |
| -0.5034 | 40.8616 | 0.9681 | 41.5113 | 2.4397 | 41.4740 | 3.9113 | 41.2492 |
| -0.4647 | 40.3069 | 1.0069 | 41.4954 | 2.4784 | 41.3935 | 3.9500 | 41.3141 |
| -0.4260 | 40.4957 | 1.0456 | 41.4988 | 2.5172 | 41.4611 | 3.9887 | 41.3581 |
| -0.3873 | 40.8188 | 1.0843 | 41.4877 | 2.5559 | 41.3746 | 4.0274 | 41.3090 |
| -0.3485 | 41.0312 | 1.1230 | 41.3311 | 2.5946 | 41.2769 | 4.0662 | 41.2579 |
| -0.3098 | 41.0235 | 1.1618 | 41.3344 | 2.6333 | 41.4052 | 4.1049 | 41.3005 |
| -0.2711 | 40.9914 | 1.2005 | 41.4121 | 2.6721 | 41.3770 | 4.1436 | 41.2647 |
| -0.2324 | 40.9368 | 1.2392 | 41.4908 | 2.7108 | 41.3515 | 4.1823 | 41.2692 |
| -0.1936 | 41.3293 | 1.2779 | 41.5029 | 2.7495 | 41.2774 | 4.2211 | 41.1663 |
| -0.1549 | 41.5261 | 1.3167 | 41.5116 | 2.7882 | 41.3636 | 4.2598 | 41.0831 |
| -0.1162 | 41.5847 | 1.3554 | 41.5245 | 2.8270 | 41.4008 | 4.2985 | 41.0968 |
| -0.0775 | 41.5931 | 1.3941 | 41.5861 | 2.8657 | 41.3949 | 4.3372 | 40.9902 |
| -0.0387 | 41.7288 | 1.4328 | 41.5896 | 2.9044 | 41.4091 | 4.3760 | 41.0250 |
| 0.0000 | 41.6815 | 1.4716 | 41.6109 | 2.9431 | 41.5178 | 4.4147 | 40.9920 |
| 0.0387 | 41.4326 | 1.5103 | 41.5285 | 2.9819 | 41.4834 | 4.4534 | 40.9920 |
| 0.0775 | 41.4240 | 1.5490 | 41.5518 | 3.0206 | 41.3672 | 4.4921 | 41.1660 |
| 0.1162 | 41.4750 | 1.5877 | 41.5482 | 3.0593 | 41.3614 | 4.5309 | 41.0894 |
| 0.1549 | 41.5041 | 1.6265 | 41.4545 | 3.0980 | 41.4155 | 4.5696 | 40.9599 |
| 0.1936 | 41.4655 | 1.6652 | 41.3627 | 3.1368 | 41.3785 | 4.6083 | 41.0108 |
| 0.2324 | 41.3895 | 1.7039 | 41.4196 | 3.1755 | 41.3865 | 4.6470 | 41.0880 |
| 0.2711 | 41.5953 | 1.7426 | 41.4455 | 3.2142 | 41.4291 | 4.6858 | 41.0638 |
| 0.3098 | 41.4803 | 1.7814 | 41.3797 | 3.2529 | 41.4069 | 4.7245 | 41.0434 |
| 0.3485 | 41.3940 | 1.8201 | 41.4054 | 3.2917 | 41.3271 | 4.7632 | 41.0662 |
| 0.3873 | 41.5832 | 1.8588 | 41.4104 | 3.3304 | 41.2699 | 4.8019 | 41.0393 |
| 0.4260 | 41.5742 | 1.8975 | 41.4009 | 3.3691 | 41.2489 | 4.8407 | 41.0117 |
| 0.4647 | 41.5645 | 1.9363 | 41.3949 | 3.4078 | 41.2344 | 4.8794 | 41.1509 |
| 0.5034 | 41.4022 | 1.9750 | 41.4606 | 3.4466 | 41.2464 | 4.9181 | 41.1318 |
| 0.5422 | 41.5237 | 2.0137 | 41.3980 | 3.4853 | 41.3106 | 4.9569 | 41.1658 |
| 0.5809 | 41.6679 | 2.0524 | 41.3502 | 3.5240 | 41.4519 | 4.9956 | 41.2176 |
| 0.6196 | 41.4465 | 2.0912 | 41.4225 | 3.5627 | 41.4585 | | |
| 0.6583 | 41.3711 | 2.1299 | 41.4772 | 3.6015 | 41.3380 | | |

Table B.9: Wall Temperatures, $D$ = 1.067 mm, Re = 8926, FC-72

| $x/D$ | $Tw_x$ (°C) | $x/D$ | $Tw_x$ (°C) | $x/D$ | $Tw_x$ (°C) | $x/D$ | $Tw_x$ (°C) |
|---|---|---|---|---|---|---|---|
| -0.7745 | 40.8032 | 0.6971 | 41.5311 | 2.1686 | 41.4041 | 3.6402 | 41.2639 |
| -0.7358 | 40.2878 | 0.7358 | 41.4858 | 2.2073 | 41.4448 | 3.6789 | 41.2483 |
| -0.6971 | 39.9641 | 0.7745 | 41.4942 | 2.2461 | 41.4138 | 3.7176 | 41.1021 |
| -0.6583 | 40.6408 | 0.8132 | 41.5480 | 2.2848 | 41.3055 | 3.7564 | 41.1183 |
| -0.6196 | 40.4714 | 0.8520 | 41.5759 | 2.3235 | 41.3222 | 3.7951 | 41.2707 |
| -0.5809 | 39.9013 | 0.8907 | 41.4816 | 2.3622 | 41.3393 | 3.8338 | 41.2486 |
| -0.5422 | 40.3206 | 0.9294 | 41.6586 | 2.4010 | 41.2900 | 3.8725 | 41.2954 |
| -0.5034 | 40.7640 | 0.9681 | 41.6819 | 2.4397 | 41.3614 | 3.9113 | 41.2472 |
| -0.4647 | 40.5109 | 1.0069 | 41.6933 | 2.4784 | 41.3567 | 3.9500 | 41.2099 |
| -0.4260 | 40.9090 | 1.0456 | 41.6620 | 2.5172 | 41.3236 | 3.9887 | 41.1080 |
| -0.3873 | 40.4817 | 1.0843 | 41.6011 | 2.5559 | 41.3003 | 4.0274 | 41.1022 |
| -0.3485 | 40.8902 | 1.1230 | 41.6383 | 2.5946 | 41.2571 | 4.0662 | 41.1615 |
| -0.3098 | 41.0568 | 1.1618 | 41.6300 | 2.6333 | 41.3312 | 4.1049 | 41.1444 |
| -0.2711 | 41.3316 | 1.2005 | 41.5990 | 2.6721 | 41.3595 | 4.1436 | 41.1612 |
| -0.2324 | 41.3090 | 1.2392 | 41.4886 | 2.7108 | 41.3702 | 4.1823 | 41.2004 |
| -0.1936 | 41.0560 | 1.2779 | 41.5984 | 2.7495 | 41.3110 | 4.2211 | 41.2019 |
| -0.1549 | 40.8194 | 1.3167 | 41.5961 | 2.7882 | 41.2821 | 4.2598 | 41.1883 |
| -0.1162 | 41.1179 | 1.3554 | 41.6008 | 2.8270 | 41.4023 | 4.2985 | 41.1198 |
| -0.0775 | 41.1265 | 1.3941 | 41.4409 | 2.8657 | 41.4020 | 4.3372 | 41.0125 |
| -0.0387 | 41.3746 | 1.4328 | 41.4134 | 2.9044 | 41.3927 | 4.3760 | 41.1108 |
| 0.0000 | 41.4483 | 1.4716 | 41.4937 | 2.9431 | 41.3338 | 4.4147 | 41.0526 |
| 0.0387 | 41.3570 | 1.5103 | 41.4558 | 2.9819 | 41.3531 | 4.4534 | 40.9898 |
| 0.0775 | 41.3529 | 1.5490 | 41.4859 | 3.0206 | 41.3204 | 4.4921 | 41.0199 |
| 0.1162 | 41.6292 | 1.5877 | 41.4198 | 3.0593 | 41.2900 | 4.5309 | 41.0830 |
| 0.1549 | 41.6533 | 1.6265 | 41.4555 | 3.0980 | 41.2945 | 4.5696 | 41.1529 |
| 0.1936 | 41.6600 | 1.6652 | 41.3335 | 3.1368 | 41.2952 | 4.6083 | 41.2565 |
| 0.2324 | 41.5752 | 1.7039 | 41.4329 | 3.1755 | 41.2142 | 4.6470 | 41.2411 |
| 0.2711 | 41.3124 | 1.7426 | 41.4460 | 3.2142 | 41.1836 | 4.6858 | 41.1450 |
| 0.3098 | 41.2789 | 1.7814 | 41.3400 | 3.2529 | 41.1844 | 4.7245 | 41.1898 |
| 0.3485 | 41.3511 | 1.8201 | 41.3501 | 3.2917 | 41.2489 | 4.7632 | 41.2016 |
| 0.3873 | 41.3539 | 1.8588 | 41.3051 | 3.3304 | 41.2149 | 4.8019 | 41.1675 |
| 0.4260 | 41.4376 | 1.8975 | 41.1698 | 3.3691 | 41.2669 | 4.8407 | 41.1805 |
| 0.4647 | 41.5251 | 1.9363 | 41.0930 | 3.4078 | 41.2896 | 4.8794 | 41.2451 |
| 0.5034 | 41.5173 | 1.9750 | 41.1370 | 3.4466 | 41.3233 | 4.9181 | 41.2405 |
| 0.5422 | 41.6068 | 2.0137 | 41.1935 | 3.4853 | 41.2006 | 4.9569 | 41.1619 |
| 0.5809 | 41.6119 | 2.0524 | 41.3902 | 3.5240 | 41.2757 | 4.9956 | 41.1751 |
| 0.6196 | 41.4861 | 2.0912 | 41.4210 | 3.5627 | 41.2737 | | |
| 0.6583 | 41.5389 | 2.1299 | 41.4331 | 3.6015 | 41.2434 | | |

# B.3 Local Nusselt Values

Table B.10: Nusselt Values, $D = 0.508$ mm, Re = 4717, FC-72

| $x/D$ | $Nu_x$ | $x/D$ | $Nu_x$ | $x/D$ | $Nu_x$ | $x/D$ | $Nu_x$ |
|---|---|---|---|---|---|---|---|
| -1.2532 | 74.5737 | 3.3318 | 59.1578 | 7.9168 | 58.6767 | 12.5019 | 61.0027 |
| -1.1004 | 87.1095 | 3.4846 | 58.6985 | 8.0697 | 58.1595 | 12.6547 | 59.3531 |
| -0.9476 | 119.9879 | 3.6375 | 60.2782 | 8.2225 | 58.9734 | 12.8075 | 61.9585 |
| -0.7947 | 173.5755 | 3.7903 | 61.6806 | 8.3753 | 57.9799 | 12.9604 | 61.6951 |
| -0.6419 | 173.9853 | 3.9431 | 56.2132 | 8.5282 | 57.1784 | 13.1132 | 62.4178 |
| -0.4891 | 88.9748 | 4.0960 | 57.2865 | 8.6810 | 59.9272 | 13.2660 | 60.7644 |
| -0.3362 | 111.3440 | 4.2488 | 59.2288 | 8.8338 | 63.5731 | 13.4189 | 62.6629 |
| -0.1834 | 89.1014 | 4.4016 | 56.6405 | 8.9867 | 60.3248 | 13.5717 | 60.6080 |
| -0.0306 | 78.2553 | 4.5545 | 57.4104 | 9.1395 | 57.6415 | 13.7246 | 60.1887 |
| 0.1223 | 110.4299 | 4.7073 | 54.2170 | 9.2923 | 56.7446 | 13.8774 | 61.4005 |
| 0.2751 | 83.5399 | 4.8601 | 57.4531 | 9.4452 | 59.1453 | 14.0302 | 59.9376 |
| 0.4279 | 71.0935 | 5.0130 | 55.8714 | 9.5980 | 78.5451 | 14.1831 | 62.2789 |
| 0.5808 | 57.9060 | 5.1658 | 56.0562 | 9.7509 | 57.6969 | 14.3359 | 59.9597 |
| 0.7336 | 67.7344 | 5.3186 | 57.3022 | 9.9037 | 60.8592 | 14.4887 | 61.0811 |
| 0.8864 | 67.1389 | 5.4715 | 56.7167 | 10.0565 | 59.4616 | 14.6416 | 63.6634 |
| 1.0393 | 69.4922 | 5.6243 | 57.1796 | 10.2094 | 59.3819 | 14.7944 | 63.2468 |
| 1.1921 | 48.5230 | 5.7771 | 56.1595 | 10.3622 | 58.4054 | 14.9472 | 61.9652 |
| 1.3449 | 56.2361 | 5.9300 | 58.2109 | 10.5150 | 58.5517 | 15.1001 | 62.5210 |
| 1.4978 | 44.5822 | 6.0828 | 59.6175 | 10.6679 | 58.6536 | 15.2529 | 61.1732 |
| 1.6506 | 43.7686 | 6.2357 | 60.0761 | 10.8207 | 57.7667 | 15.4057 | 60.3516 |
| 1.8034 | 62.0362 | 6.3885 | 56.1967 | 10.9735 | 57.3628 | 15.5586 | 58.1459 |
| 1.9563 | 56.0221 | 6.5413 | 57.0215 | 11.1264 | 57.7358 | 15.7114 | 58.2789 |
| 2.1091 | 54.9070 | 6.6942 | 56.0498 | 11.2792 | 58.2520 | 15.8642 | 62.2773 |
| 2.2620 | 60.3982 | 6.8470 | 59.3980 | 11.4320 | 58.5702 | 16.0171 | 63.3323 |
| 2.4148 | 59.4986 | 6.9998 | 57.0497 | 11.5849 | 59.7792 | 16.1699 | 59.6241 |
| 2.5676 | 64.0499 | 7.1527 | 55.9837 | 11.7377 | 61.7986 | 16.3227 | 59.8543 |
| 2.7205 | 61.6733 | 7.3055 | 58.6718 | 11.8905 | 59.7736 | 16.4756 | 57.6871 |
| 2.8733 | 62.1472 | 7.4583 | 60.6343 | 12.0434 | 60.8617 | 16.6284 | 60.1274 |
| 3.0261 | 63.4111 | 7.6112 | 58.1479 | 12.1962 | 60.1830 | 16.7812 | 55.8051 |
| 3.1790 | 59.2315 | 7.7640 | 59.9665 | 12.3490 | 60.9139 | 16.9341 | 56.5741 |

Table B.11: Nusselt Values, $D = 0.508$ mm, Re = 6645, FC-72

| $x/D$ | $Nu_x$ | $x/D$ | $Nu_x$ | $x/D$ | $Nu_x$ | $x/D$ | $Nu_x$ |
|---|---|---|---|---|---|---|---|
| -1.2532 | 72.4820 | 3.3318 | 56.0583 | 7.9168 | 54.7080 | 12.5019 | 59.5409 |
| -1.1004 | 94.4511 | 3.4846 | 55.5264 | 8.0697 | 54.5916 | 12.6547 | 58.0872 |
| -0.9476 | 105.8352 | 3.6375 | 55.9955 | 8.2225 | 57.1120 | 12.8075 | 60.4955 |
| -0.7947 | 135.9243 | 3.7903 | 53.2608 | 8.3753 | 55.5835 | 12.9604 | 57.9146 |
| -0.6419 | 194.3726 | 3.9431 | 54.1215 | 8.5282 | 53.2587 | 13.1132 | 59.8923 |
| -0.4891 | 80.8242 | 4.0960 | 54.4542 | 8.6810 | 55.6327 | 13.2660 | 60.6724 |
| -0.3362 | 76.6658 | 4.2488 | 55.7995 | 8.8338 | 54.8124 | 13.4189 | 56.2499 |
| -0.1834 | 78.2046 | 4.4016 | 55.6074 | 8.9867 | 57.5973 | 13.5717 | 58.5092 |
| -0.0306 | 64.1781 | 4.5545 | 51.3448 | 9.1395 | 56.9778 | 13.7246 | 55.7606 |
| 0.1223 | 67.5721 | 4.7073 | 53.5371 | 9.2923 | 58.6988 | 13.8774 | 55.4184 |
| 0.2751 | 63.9351 | 4.8601 | 54.6673 | 9.4452 | 56.9298 | 14.0302 | 55.2405 |
| 0.4279 | 23.7684 | 5.0130 | 54.7035 | 9.5980 | 57.1425 | 14.1831 | 54.3171 |
| 0.5808 | 55.7015 | 5.1658 | 52.7921 | 9.7509 | 57.0060 | 14.3359 | 58.1040 |
| 0.7336 | 54.5383 | 5.3186 | 53.3492 | 9.9037 | 56.8728 | 14.4887 | 58.7910 |
| 0.8864 | 53.5052 | 5.4715 | 53.3733 | 10.0565 | 58.5499 | 14.6416 | 57.6911 |
| 1.0393 | 54.0191 | 5.6243 | 54.4660 | 10.2094 | 57.7334 | 14.7944 | 59.5250 |
| 1.1921 | 42.7453 | 5.7771 | 53.9348 | 10.3622 | 57.0454 | 14.9472 | 59.4958 |
| 1.3449 | 50.8732 | 5.9300 | 51.6891 | 10.5150 | 60.6730 | 15.1001 | 56.3573 |
| 1.4978 | 46.4473 | 6.0828 | 50.5325 | 10.6679 | 60.5815 | 15.2529 | 57.7496 |
| 1.6506 | 45.4388 | 6.2357 | 51.7347 | 10.8207 | 58.6841 | 15.4057 | 59.0100 |
| 1.8034 | 51.3750 | 6.3885 | 53.6439 | 10.9735 | 57.7524 | 15.5586 | 56.6383 |
| 1.9563 | 56.5893 | 6.5413 | 51.8358 | 11.1264 | 56.3809 | 15.7114 | 58.2709 |
| 2.1091 | 51.5010 | 6.6942 | 50.7296 | 11.2792 | 56.1655 | 15.8642 | 58.5056 |
| 2.2620 | 53.6921 | 6.8470 | 52.0217 | 11.4320 | 56.8591 | 16.0171 | 60.2815 |
| 2.4148 | 55.1039 | 6.9998 | 53.6168 | 11.5849 | 57.2279 | 16.1699 | 60.7968 |
| 2.5676 | 56.3182 | 7.1527 | 51.7073 | 11.7377 | 59.0110 | 16.3227 | 57.6688 |
| 2.7205 | 57.5041 | 7.3055 | 49.5197 | 11.8905 | 61.5031 | 16.4756 | 56.6731 |
| 2.8733 | 56.6279 | 7.4583 | 52.7081 | 12.0434 | 62.7672 | 16.6284 | 51.7273 |
| 3.0261 | 55.4437 | 7.6112 | 52.7372 | 12.1962 | 60.4514 | 16.7812 | 55.9247 |
| 3.1790 | 57.6809 | 7.7640 | 52.4992 | 12.3490 | 57.8742 | 16.9341 | 56.3649 |

Table B.12: Nusselt Values, $D = 0.508$ mm, Re = 7912, FC-72

| $x/D$ | $Nu_x$ | $x/D$ | $Nu_x$ | $x/D$ | $Nu_x$ | $x/D$ | $Nu_x$ |
|---|---|---|---|---|---|---|---|
| -1.2532 | 75.8588 | 3.3318 | 68.6099 | 7.9168 | 67.5596 | 12.5019 | 65.6078 |
| -1.1004 | 92.9179 | 3.4846 | 70.0732 | 8.0697 | 69.1358 | 12.6547 | 66.2656 |
| -0.9476 | 96.2131 | 3.6375 | 68.7263 | 8.2225 | 66.9321 | 12.8075 | 65.6966 |
| -0.7947 | 70.6582 | 3.7903 | 64.9225 | 8.3753 | 65.6252 | 12.9604 | 62.3454 |
| -0.6419 | 123.5772 | 3.9431 | 61.3016 | 8.5282 | 64.8146 | 13.1132 | 68.4466 |
| -0.4891 | 123.6852 | 4.0960 | 61.9476 | 8.6810 | 65.4205 | 13.2660 | 68.8708 |
| -0.3362 | 95.6253 | 4.2488 | 65.3296 | 8.8338 | 63.4311 | 13.4189 | 62.4751 |
| -0.1834 | 78.2925 | 4.4016 | 62.9324 | 8.9867 | 64.1901 | 13.5717 | 62.6096 |
| -0.0306 | 108.4266 | 4.5545 | 62.7758 | 9.1395 | 65.5752 | 13.7246 | 64.2461 |
| 0.1223 | 152.9878 | 4.7073 | 63.3086 | 9.2923 | 62.4176 | 13.8774 | 63.0350 |
| 0.2751 | 144.5645 | 4.8601 | 61.0678 | 9.4452 | 63.7342 | 14.0302 | 64.8775 |
| 0.4279 | 148.5900 | 5.0130 | 63.2299 | 9.5980 | 65.9268 | 14.1831 | 60.8225 |
| 0.5808 | 136.1914 | 5.1658 | 70.5209 | 9.7509 | 61.9014 | 14.3359 | 64.5533 |
| 0.7336 | 90.9393 | 5.3186 | 61.5382 | 9.9037 | 64.8628 | 14.4887 | 67.1025 |
| 0.8864 | 123.5583 | 5.4715 | 66.6624 | 10.0565 | 67.1206 | 14.6416 | 66.5473 |
| 1.0393 | 114.1828 | 5.6243 | 69.0337 | 10.2094 | 68.6772 | 14.7944 | 74.0931 |
| 1.1921 | 81.2428 | 5.7771 | 65.9018 | 10.3622 | 67.6339 | 14.9472 | 66.9189 |
| 1.3449 | 134.3594 | 5.9300 | 70.8686 | 10.5150 | 69.7988 | 15.1001 | 66.3901 |
| 1.4978 | 92.5207 | 6.0828 | 66.8098 | 10.6679 | 64.5581 | 15.2529 | 69.1312 |
| 1.6506 | 54.4226 | 6.2357 | 73.7049 | 10.8207 | 63.4530 | 15.4057 | 64.7151 |
| 1.8034 | 91.5187 | 6.3885 | 71.4243 | 10.9735 | 66.7056 | 15.5586 | 61.4993 |
| 1.9563 | 91.8398 | 6.5413 | 67.4976 | 11.1264 | 67.3038 | 15.7114 | 65.4983 |
| 2.1091 | 79.4865 | 6.6942 | 63.8077 | 11.2792 | 66.3756 | 15.8642 | 64.0778 |
| 2.2620 | 82.2250 | 6.8470 | 65.8773 | 11.4320 | 83.0387 | 16.0171 | 61.1901 |
| 2.4148 | 75.0801 | 6.9998 | 65.1814 | 11.5849 | 65.3588 | 16.1699 | 62.7093 |
| 2.5676 | 90.2459 | 7.1527 | 63.7664 | 11.7377 | 68.0727 | 16.3227 | 60.9447 |
| 2.7205 | 78.9621 | 7.3055 | 66.6236 | 11.8905 | 66.4911 | 16.4756 | 58.9529 |
| 2.8733 | 77.8438 | 7.4583 | 68.4005 | 12.0434 | 66.0922 | 16.6284 | 57.5705 |
| 3.0261 | 69.3485 | 7.6112 | 63.9097 | 12.1962 | 64.2234 | 16.7812 | 61.2883 |
| 3.1790 | 70.0825 | 7.7640 | 67.2624 | 12.3490 | 66.5550 | 16.9341 | 59.8140 |

Table B.13: Nusselt Values, $D = 0.508$ mm, Re = 8733, FC-72

| $x/D$ | $Nu_x$ | $x/D$ | $Nu_x$ | $x/D$ | $Nu_x$ | $x/D$ | $Nu_x$ |
|---|---|---|---|---|---|---|---|
| -1.2532 | 114.2259 | 3.3318 | 75.2560 | 7.9168 | 76.1638 | 12.5019 | 78.9139 |
| -1.1004 | 115.3111 | 3.4846 | 76.2413 | 8.0697 | 79.4758 | 12.6547 | 75.9295 |
| -0.9476 | 134.7586 | 3.6375 | 76.6717 | 8.2225 | 74.1462 | 12.8075 | 77.8199 |
| -0.7947 | 149.3656 | 3.7903 | 112.5476 | 8.3753 | 74.7791 | 12.9604 | 78.2237 |
| -0.6419 | 163.8086 | 3.9431 | 70.5700 | 8.5282 | 74.5006 | 13.1132 | 80.2023 |
| -0.4891 | 160.2359 | 4.0960 | 74.8559 | 8.6810 | 77.8318 | 13.2660 | 80.1986 |
| -0.3362 | 157.8591 | 4.2488 | 74.1585 | 8.8338 | 82.2009 | 13.4189 | 78.1773 |
| -0.1834 | 156.7430 | 4.4016 | 71.9243 | 8.9867 | 76.1141 | 13.5717 | 77.0940 |
| -0.0306 | 157.2115 | 4.5545 | 72.9209 | 9.1395 | 74.9902 | 13.7246 | 78.0467 |
| 0.1223 | 117.1749 | 4.7073 | 68.3752 | 9.2923 | 71.0448 | 13.8774 | 78.3915 |
| 0.2751 | 133.1833 | 4.8601 | 69.8294 | 9.4452 | 75.2943 | 14.0302 | 76.6232 |
| 0.4279 | 104.7791 | 5.0130 | 69.0091 | 9.5980 | 74.7041 | 14.1831 | 75.6104 |
| 0.5808 | 83.2759 | 5.1658 | 68.6131 | 9.7509 | 73.0976 | 14.3359 | 75.5384 |
| 0.7336 | 109.0721 | 5.3186 | 70.1154 | 9.9037 | 75.2618 | 14.4887 | 80.3211 |
| 0.8864 | 101.8467 | 5.4715 | 74.7364 | 10.0565 | 76.7741 | 14.6416 | 85.0919 |
| 1.0393 | 89.3920 | 5.6243 | 83.3799 | 10.2094 | 107.9243 | 14.7944 | 85.1333 |
| 1.1921 | 62.2741 | 5.7771 | 73.2788 | 10.3622 | 79.0172 | 14.9472 | 79.1133 |
| 1.3449 | 67.3852 | 5.9300 | 88.6800 | 10.5150 | 80.4753 | 15.1001 | 80.2073 |
| 1.4978 | 52.5692 | 6.0828 | 78.1800 | 10.6679 | 73.7810 | 15.2529 | 74.9543 |
| 1.6506 | 52.7258 | 6.2357 | 76.5591 | 10.8207 | 73.2363 | 15.4057 | 75.3209 |
| 1.8034 | 79.5104 | 6.3885 | 73.8150 | 10.9735 | 76.6401 | 15.5586 | 74.5672 |
| 1.9563 | 70.4087 | 6.5413 | 76.1248 | 11.1264 | 76.1428 | 15.7114 | 73.9448 |
| 2.1091 | 65.0600 | 6.6942 | 71.1944 | 11.2792 | 77.2277 | 15.8642 | 81.0024 |
| 2.2620 | 71.5769 | 6.8470 | 73.9577 | 11.4320 | 75.1122 | 16.0171 | 81.5971 |
| 2.4148 | 73.5293 | 6.9998 | 72.7689 | 11.5849 | 74.6053 | 16.1699 | 76.4062 |
| 2.5676 | 79.3281 | 7.1527 | 73.3009 | 11.7377 | 75.5142 | 16.3227 | 76.1359 |
| 2.7205 | 77.7041 | 7.3055 | 76.0460 | 11.8905 | 76.5393 | 16.4756 | 73.2447 |
| 2.8733 | 75.6597 | 7.4583 | 76.7907 | 12.0434 | 77.4396 | 16.6284 | 74.1113 |
| 3.0261 | 83.0670 | 7.6112 | 74.2137 | 12.1962 | 77.2061 | 16.7812 | 67.8452 |
| 3.1790 | 76.0998 | 7.7640 | 76.6132 | 12.3490 | 79.6861 | 16.9341 | 68.2670 |

Table B.14: Nusselt Values, $D = 1.067$ mm, Re = 5399, FC-72

| $x/D$ | $Nu_x$ | $x/D$ | $Nu_x$ | $x/D$ | $Nu_x$ | $x/D$ | $Nu_x$ |
|---|---|---|---|---|---|---|---|
| -1.4553 | 72.8576 | 0.5094 | 59.1928 | 2.4740 | 50.3956 | 4.4387 | 51.9359 |
| -1.3825 | 71.7673 | 0.5821 | 56.8515 | 2.5468 | 52.2424 | 4.5114 | 52.8260 |
| -1.3098 | 77.4429 | 0.6549 | 59.2181 | 2.6195 | 50.7585 | 4.5842 | 53.8027 |
| -1.2370 | 67.3995 | 0.7276 | 58.7174 | 2.6923 | 50.9129 | 4.6569 | 56.1729 |
| -1.1642 | 77.7524 | 0.8004 | 56.3645 | 2.7651 | 50.2465 | 4.7297 | 54.1542 |
| -1.0915 | 79.0824 | 0.8732 | 56.4528 | 2.8378 | 51.6955 | 4.8025 | 52.6314 |
| -1.0187 | 77.8542 | 0.9459 | 55.9807 | 2.9106 | 50.8490 | 4.8752 | 51.9289 |
| -0.9459 | 77.1123 | 1.0187 | 54.1511 | 2.9834 | 51.0960 | 4.9480 | 52.4467 |
| -0.8732 | 76.0189 | 1.0915 | 56.5580 | 3.0561 | 50.6233 | 5.0208 | 52.4361 |
| -0.8004 | 73.1773 | 1.1642 | 56.8641 | 3.1289 | 50.3395 | 5.0935 | 51.0645 |
| -0.7276 | 74.6374 | 1.2370 | 54.7783 | 3.2016 | 51.5574 | 5.1663 | 50.9040 |
| -0.6549 | 74.3107 | 1.3098 | 53.2428 | 3.2744 | 50.3751 | 5.2391 | 48.0379 |
| -0.5821 | 73.5795 | 1.3825 | 53.8705 | 3.3472 | 51.2615 | 5.3118 | 49.8663 |
| -0.5094 | 72.4066 | 1.4553 | 53.7988 | 3.4199 | 53.7924 | 5.3846 | 49.3879 |
| -0.4366 | 73.7455 | 1.5281 | 52.3309 | 3.4927 | 52.7807 | 5.4574 | 51.8380 |
| -0.3638 | 75.0689 | 1.6008 | 55.5375 | 3.5655 | 49.9627 | 5.5301 | 50.4357 |
| -0.2911 | 72.6034 | 1.6736 | 52.3349 | 3.6382 | 52.6710 | 5.6029 | 54.0990 |
| -0.2183 | 74.1347 | 1.7464 | 50.2906 | 3.7110 | 54.7226 | 5.6757 | 51.3476 |
| -0.1455 | 70.8846 | 1.8191 | 50.7606 | 3.7838 | 53.8880 | 5.7484 | 48.9965 |
| -0.0728 | 66.9300 | 1.8919 | 50.3525 | 3.8565 | 50.5044 | 5.8212 | 48.4194 |
| 0.0000 | 68.2446 | 1.9646 | 54.4512 | 3.9293 | 50.4461 | 5.8939 | 50.7495 |
| 0.0728 | 63.4302 | 2.0374 | 53.1442 | 4.0021 | 47.8866 | 5.9667 | 51.4048 |
| 0.1455 | 59.7861 | 2.1102 | 51.8788 | 4.0748 | 50.0426 | 6.0395 | 49.1497 |
| 0.2183 | 61.5205 | 2.1829 | 55.0452 | 4.1476 | 49.8416 | 6.1122 | 47.3828 |
| 0.2911 | 60.3975 | 2.2557 | 54.0996 | 4.2204 | 50.4261 | 6.1850 | 49.4464 |
| 0.3638 | 59.4133 | 2.3285 | 53.6946 | 4.2931 | 48.2543 | 6.2578 | 49.9548 |
| 0.4366 | 61.0356 | 2.4012 | 49.1564 | 4.3659 | 49.0682 | 6.3305 | 50.9389 |

Table B.15: Nusselt Values, $D = 1.067$ mm, Re = 6287, FC-72

| $x/D$ | $Nu_x$ | $x/D$ | $Nu_x$ | $x/D$ | $Nu_x$ | $x/D$ | $Nu_x$ |
|---|---|---|---|---|---|---|---|
| -1.4553 | 89.3125 | 0.5094 | 67.6264 | 2.4740 | 74.6196 | 4.4387 | 67.1270 |
| -1.3825 | 90.8903 | 0.5821 | 66.8721 | 2.5468 | 72.8080 | 4.5114 | 71.3811 |
| -1.3098 | 89.1874 | 0.6549 | 64.2346 | 2.6195 | 64.2448 | 4.5842 | 70.0798 |
| -1.2370 | 87.6795 | 0.7276 | 68.5732 | 2.6923 | 66.3660 | 4.6569 | 77.5893 |
| -1.1642 | 89.1161 | 0.8004 | 64.6691 | 2.7651 | 70.5764 | 4.7297 | 75.4129 |
| -1.0915 | 92.6215 | 0.8732 | 72.0774 | 2.8378 | 70.7837 | 4.8025 | 72.1904 |
| -1.0187 | 92.2384 | 0.9459 | 68.2890 | 2.9106 | 69.4330 | 4.8752 | 68.7726 |
| -0.9459 | 88.7688 | 1.0187 | 63.0376 | 2.9834 | 66.2549 | 4.9480 | 65.9650 |
| -0.8732 | 89.1899 | 1.0915 | 69.7833 | 3.0561 | 68.1142 | 5.0208 | 67.6840 |
| -0.8004 | 79.7691 | 1.1642 | 68.2527 | 3.1289 | 67.1107 | 5.0935 | 69.8300 |
| -0.7276 | 81.6166 | 1.2370 | 71.5144 | 3.2016 | 71.6647 | 5.1663 | 70.3586 |
| -0.6549 | 91.5596 | 1.3098 | 69.7880 | 3.2744 | 72.1770 | 5.2391 | 65.2790 |
| -0.5821 | 85.5222 | 1.3825 | 69.4664 | 3.3472 | 72.0061 | 5.3118 | 68.1314 |
| -0.5094 | 88.1794 | 1.4553 | 65.7104 | 3.4199 | 69.3259 | 5.3846 | 67.7640 |
| -0.4366 | 92.5238 | 1.5281 | 64.8719 | 3.4927 | 67.5227 | 5.4574 | 68.7022 |
| -0.3638 | 92.2493 | 1.6008 | 67.4664 | 3.5655 | 59.8451 | 5.5301 | 63.0508 |
| -0.2911 | 84.6220 | 1.6736 | 68.3156 | 3.6382 | 63.2888 | 5.6029 | 77.6885 |
| -0.2183 | 76.9407 | 1.7464 | 62.4722 | 3.7110 | 76.7320 | 5.6757 | 66.8358 |
| -0.1455 | 72.0558 | 1.8191 | 61.0395 | 3.7838 | 76.3355 | 5.7484 | 66.0609 |
| -0.0728 | 74.6408 | 1.8919 | 66.3641 | 3.8565 | 68.6931 | 5.8212 | 61.9197 |
| 0.0000 | 76.1278 | 1.9646 | 68.4457 | 3.9293 | 61.7055 | 5.8939 | 62.1008 |
| 0.0728 | 72.7553 | 2.0374 | 73.4243 | 4.0021 | 59.1154 | 5.9667 | 65.5517 |
| 0.1455 | 69.9079 | 2.1102 | 69.2720 | 4.0748 | 59.7376 | 6.0395 | 64.6022 |
| 0.2183 | 68.9168 | 2.1829 | 73.8407 | 4.1476 | 67.4233 | 6.1122 | 63.7628 |
| 0.2911 | 72.6547 | 2.2557 | 77.7294 | 4.2204 | 69.1443 | 6.1850 | 65.9635 |
| 0.3638 | 64.9778 | 2.3285 | 73.9474 | 4.2931 | 63.1673 | 6.2578 | 61.2300 |
| 0.4366 | 73.7240 | 2.4012 | 70.2234 | 4.3659 | 55.2167 | 6.3305 | 64.1345 |

Table B.16: Nusselt Values, $D$ = 1.067 mm, Re = 8035, FC-72

| $x/D$ | $Nu_x$ | $x/D$ | $Nu_x$ | $x/D$ | $Nu_x$ | $x/D$ | $Nu_x$ |
|---|---|---|---|---|---|---|---|
| -0.7745 | 144.4323 | 0.6971 | 115.9026 | 2.1686 | 118.1682 | 3.6402 | 121.4308 |
| -0.7358 | 137.3592 | 0.7358 | 115.6437 | 2.2073 | 118.8159 | 3.6789 | 122.2544 |
| -0.6971 | 139.8173 | 0.7745 | 115.0572 | 2.2461 | 120.3741 | 3.7176 | 123.6064 |
| -0.6583 | 130.0791 | 0.8132 | 115.0838 | 2.2848 | 119.7596 | 3.7564 | 124.2683 |
| -0.6196 | 132.1218 | 0.8520 | 118.0156 | 2.3235 | 118.8226 | 3.7951 | 123.4988 |
| -0.5809 | 124.4819 | 0.8907 | 116.9348 | 2.3622 | 117.1824 | 3.8338 | 122.5398 |
| -0.5422 | 133.1563 | 0.9294 | 117.2603 | 2.4010 | 116.9762 | 3.8725 | 122.4129 |
| -0.5034 | 127.2542 | 0.9681 | 116.3404 | 2.4397 | 117.8773 | 3.9113 | 122.6733 |
| -0.4647 | 138.8873 | 1.0069 | 116.5911 | 2.4784 | 119.0901 | 3.9500 | 121.4571 |
| -0.4260 | 134.0105 | 1.0456 | 116.5927 | 2.5172 | 118.0554 | 3.9887 | 120.7689 |
| -0.3873 | 129.6317 | 1.0843 | 117.1817 | 2.5559 | 119.6131 | 4.0274 | 121.6200 |
| -0.3485 | 124.0444 | 1.1230 | 120.6216 | 2.5946 | 121.2449 | 4.0662 | 122.5228 |
| -0.3098 | 124.0492 | 1.1618 | 120.8530 | 2.6333 | 119.1876 | 4.1049 | 121.8915 |
| -0.2711 | 124.9305 | 1.2005 | 118.1125 | 2.6721 | 119.5600 | 4.1436 | 122.4522 |
| -0.2324 | 126.0059 | 1.2392 | 116.7825 | 2.7108 | 119.9400 | 4.1823 | 122.9785 |
| -0.1936 | 118.8815 | 1.2779 | 116.7254 | 2.7495 | 121.2367 | 4.2211 | 124.7744 |
| -0.1549 | 115.5195 | 1.3167 | 116.6053 | 2.7882 | 119.8572 | 4.2598 | 125.9549 |
| -0.1162 | 114.5610 | 1.3554 | 116.3787 | 2.8270 | 119.2374 | 4.2985 | 125.8507 |
| -0.0775 | 114.4459 | 1.3941 | 115.4414 | 2.8657 | 119.4287 | 4.3372 | 127.8444 |
| -0.0387 | 112.4732 | 1.4328 | 115.4479 | 2.9044 | 119.2186 | 4.3760 | 127.0497 |
| 0.0000 | 113.1363 | 1.4716 | 115.1546 | 2.9431 | 117.4226 | 4.4147 | 127.6853 |
| 0.0387 | 117.9481 | 1.5103 | 116.4370 | 2.9819 | 118.0299 | 4.4534 | 127.6859 |
| 0.0775 | 117.8857 | 1.5490 | 116.1696 | 3.0206 | 119.9938 | 4.4921 | 124.7283 |
| 0.1162 | 116.5760 | 1.5877 | 116.2010 | 3.0593 | 120.1420 | 4.5309 | 126.0814 |
| 0.1549 | 116.3025 | 1.6265 | 117.7201 | 3.0980 | 119.2670 | 4.5696 | 128.3649 |
| 0.1936 | 116.7006 | 1.6652 | 119.1994 | 3.1368 | 119.8478 | 4.6083 | 127.6367 |
| 0.2324 | 117.8084 | 1.7039 | 118.3294 | 3.1755 | 119.7603 | 4.6470 | 126.2187 |
| 0.2711 | 114.7185 | 1.7426 | 117.9086 | 3.2142 | 119.1109 | 4.6858 | 126.5845 |
| 0.3098 | 116.7082 | 1.7814 | 119.0532 | 3.2529 | 119.4568 | 4.7245 | 126.8596 |
| 0.3485 | 117.9434 | 1.8201 | 118.6447 | 3.2917 | 120.8371 | 4.7632 | 126.4777 |
| 0.3873 | 114.8436 | 1.8588 | 118.6050 | 3.3304 | 121.8629 | 4.8019 | 126.8699 |
| 0.4260 | 115.0210 | 1.8975 | 118.7398 | 3.3691 | 122.2426 | 4.8407 | 127.3090 |
| 0.4647 | 115.2297 | 1.9363 | 118.8855 | 3.4078 | 122.7985 | 4.8794 | 125.0733 |
| 0.5034 | 117.8191 | 1.9750 | 117.8603 | 3.4466 | 122.7777 | 4.9181 | 125.3423 |
| 0.5422 | 116.2080 | 2.0137 | 118.8493 | 3.4853 | 121.6413 | 4.9569 | 124.6655 |
| 0.5809 | 113.8649 | 2.0524 | 119.5755 | 3.5240 | 118.9872 | 4.9956 | 123.8695 |
| 0.6196 | 117.3613 | 2.0912 | 118.5110 | 3.5627 | 118.8942 | | |
| 0.6583 | 118.5630 | 2.1299 | 117.6894 | 3.6015 | 120.8071 | | |

Table B.17: Nusselt Values, $D = 1.067$ mm, Re = 8926, FC-72

| $x/D$ | $Nu_x$ | $x/D$ | $Nu_x$ | $x/D$ | $Nu_x$ | $x/D$ | $Nu_x$ |
|---|---|---|---|---|---|---|---|
| -0.7745 | 143.2138 | 0.6971 | 129.7550 | 2.1686 | 133.1661 | 3.6402 | 136.9547 |
| -0.7358 | 160.3251 | 0.7358 | 130.5045 | 2.2073 | 132.4063 | 3.6789 | 137.3034 |
| -0.6971 | 165.9414 | 0.7745 | 130.4582 | 2.2461 | 133.2416 | 3.7176 | 140.0286 |
| -0.6583 | 147.7325 | 0.8132 | 129.7450 | 2.2848 | 135.2942 | 3.7564 | 139.8699 |
| -0.6196 | 155.4539 | 0.8520 | 129.2719 | 2.3235 | 134.9164 | 3.7951 | 137.1826 |
| -0.5809 | 165.2209 | 0.8907 | 130.8158 | 2.3622 | 134.4377 | 3.8338 | 137.5820 |
| -0.5422 | 154.6693 | 0.9294 | 127.8060 | 2.4010 | 135.4596 | 3.8725 | 136.6091 |
| -0.5034 | 144.3108 | 0.9681 | 127.4114 | 2.4397 | 134.0717 | 3.9113 | 137.5829 |
| -0.4647 | 151.0529 | 1.0069 | 127.2119 | 2.4784 | 134.2072 | 3.9500 | 138.3865 |
| -0.4260 | 141.9345 | 1.0456 | 127.7740 | 2.5172 | 134.9866 | 3.9887 | 140.2370 |
| -0.3873 | 151.1974 | 1.0843 | 128.9331 | 2.5559 | 135.4963 | 4.0274 | 140.4428 |
| -0.3485 | 143.1508 | 1.1230 | 128.3708 | 2.5946 | 136.1352 | 4.0662 | 139.3459 |
| -0.3098 | 139.5844 | 1.1618 | 128.4422 | 2.6333 | 134.7459 | 4.1049 | 139.6487 |
| -0.2711 | 133.3421 | 1.2005 | 129.1357 | 2.6721 | 134.2819 | 4.1436 | 139.3533 |
| -0.2324 | 133.6544 | 1.2392 | 130.9750 | 2.7108 | 134.0385 | 4.1823 | 139.3434 |
| -0.1936 | 138.9085 | 1.2779 | 129.0324 | 2.7495 | 135.3455 | 4.2211 | 138.9144 |
| -0.1549 | 142.7772 | 1.3167 | 129.0683 | 2.7882 | 135.8561 | 4.2598 | 139.0399 |
| -0.1162 | 137.5121 | 1.3554 | 129.0050 | 2.8270 | 133.6752 | 4.2985 | 140.5364 |
| -0.0775 | 137.6689 | 1.3941 | 131.9382 | 2.8657 | 133.5864 | 4.3372 | 142.7322 |
| -0.0387 | 132.8767 | 1.4328 | 132.5818 | 2.9044 | 133.8199 | 4.3760 | 140.9220 |
| 0.0000 | 131.0222 | 1.4716 | 131.0524 | 2.9431 | 134.9565 | 4.4147 | 142.0501 |
| 0.0387 | 132.5401 | 1.5103 | 131.7350 | 2.9819 | 134.7263 | 4.4534 | 143.4465 |
| 0.0775 | 132.6310 | 1.5490 | 131.2632 | 3.0206 | 135.4708 | 4.4921 | 142.9071 |
| 0.1162 | 127.8724 | 1.5877 | 132.4031 | 3.0593 | 136.0905 | 4.5309 | 141.6187 |
| 0.1549 | 127.4456 | 1.6265 | 131.9017 | 3.0980 | 136.0018 | 4.5696 | 140.0880 |
| 0.1936 | 127.3340 | 1.6652 | 134.0677 | 3.1368 | 135.9413 | 4.6083 | 138.1546 |
| 0.2324 | 128.9258 | 1.7039 | 132.3067 | 3.1755 | 137.3883 | 4.6470 | 138.2802 |
| 0.2711 | 133.9485 | 1.7426 | 132.0452 | 3.2142 | 138.0851 | 4.6858 | 140.2458 |
| 0.3098 | 134.7362 | 1.7814 | 134.1089 | 3.2529 | 138.1948 | 4.7245 | 139.3466 |
| 0.3485 | 133.4717 | 1.8201 | 133.8880 | 3.2917 | 137.2787 | 4.7632 | 139.0678 |
| 0.3873 | 133.0282 | 1.8588 | 134.9284 | 3.3304 | 138.5181 | 4.8019 | 139.7882 |
| 0.4260 | 131.3383 | 1.8975 | 137.6056 | 3.3691 | 137.0802 | 4.8407 | 139.5614 |
| 0.4647 | 129.9229 | 1.9363 | 139.1439 | 3.4078 | 136.6074 | 4.8794 | 138.4387 |
| 0.5034 | 130.0460 | 1.9750 | 138.1087 | 3.4466 | 135.9612 | 4.9181 | 138.5696 |
| 0.5422 | 128.4442 | 2.0137 | 137.0373 | 3.4853 | 138.2953 | 4.9569 | 140.0999 |
| 0.5809 | 128.3793 | 2.0524 | 133.3090 | 3.5240 | 136.5836 | 4.9956 | 139.8338 |
| 0.6196 | 131.4384 | 2.0912 | 132.8088 | 3.5627 | 136.6736 | | |
| 0.6583 | 129.8045 | 2.1299 | 132.5813 | 3.6015 | 137.3448 | | |